ScuDo
Scuola di Dottorato ~ Doctoral School
WHAT YOU ARE, TAKES YOU FAR

Doctoral Dissertation
Doctoral Program in Physics (33^{th}cycle)

Electron-phonon interactions in low-dimensional carbon systems:
superconductivity and charge-density waves

By

Davide Romanin

******

Supervisor(s):
Prof. Dario Daghero, Polytechnic University of Turin
Prof. Matteo Calandra, University of Trento

Doctoral Examination Committee:
Prof. P. Barone, Referee, University of Roma La Sapienza
Prof. A. Ruini, Referee, University of Modena and Reggio Emilia

Politecnico di Torino
2021

Declaration

I hereby declare that, the contents and organization of this dissertation constitute my own original work and does not compromise in any way the rights of third parties, including those relating to the security of personal data. Parts of the work collected in this Doctoral Dissertation have been appeared previously in these publications:

- E. Piatti, D. Romanin, R. S. Gonnelli and D. Daghero, "Anomalous screening of an electrostatic field at the surface of a BCS superconductor", *Appl. Surf. Sci.* **461**, 17 (2018)
- G. A. Ummarino and D. Romanin, "Proximity two bands Eliashberg theory of electrostatic field-effect-doping in a superconducting film of MgB2", *J. Phys.: Condens. Matter* **31**, 024001 (2018)
- E. Piatti, D. Romanin and R. S. Gonnelli, "Mapping multi-valley Lifshitz transitions induced by field-effect doping in strained MoS2 nanolayers", *J. Phys.: Condens. Matter* **31**, 114002 (2019)
- D. Romanin, Th. Sohier, D. Daghero, F. Mauri, R. S. Gonnelli and M. Calandra, "Electric field exfoliation and high-TC superconductivity in field-effect hole-doped hydrogenated diamond (111)", *Appl. Surf. Sci.* **496**, 143709 (2019)
- E. Piatti, D. Romanin, D. Daghero and R. S Gonnelli, "Two-dimensional hole transport in ion-gated diamond surfaces", *Low Temp. Phys.* **45**, 11 (2019)
- G. A. Ummarino and D. Romanin, "Theoretical explanation of electric field-induced superconductive critical temperature shifts in Indium thin films", *Phys. Status. Solidi B* **257**, 1900651 (2020)

- D. Romanin, Th. Brumme, D. Daghero, R. S. Gonnelli and E. Piatti, "Strong band-filling-dependence of the scattering lifetime in gated MoS2 nanolayers induced by the opening of intervalley scattering channels", *Journal of Applied Physics* **128**, 063907 (2020)
- D. Romanin, "Field-effect induced superconductivity in surfaces of tetrahedrally coordinated semiconductors: the case of (111) hydrogenated silicon", *Il Nuovo Cimento C* **43**, 115 (2020)
- D. Romanin, G. A Ummarino and E. Piatti, "Migdal-Eliashberg theory of multiband high-temperature superconductivity in field-effect-doped hydrogenated (111) diamond", *Appl. Surf. Sci.* **536**, 147723 (2021)

Computational resources were provided by hpc@polito,which is a project of Academic Computing within the Department of Control and Computer Engineering at the Politecnico di Torino (http://hpc.polito.it), and by the facilities of CINECA through the ISCRA projects HP10BB2RVB, HP10C8P1FI and HP10CY4S13.

Davide Romanin
2021

* This dissertation is presented in partial fulfillment of the requirements for **Ph.D. degree** in the Graduate School of Politecnico di Torino (ScuDo).

I would like to dedicate this thesis to my Anxiety.

Acknowledgements

I define myself as ‘eternally unsatisfied’.

As such, at the beginning, I wasn’t completely pleased with my work. However, while I was writing down my thesis, I finally had a ‘bird’s-eye view’ of the last three years, from both a scientific and personal point of view. In the end, I must admit that I learnt a lot and I have to thank different people for that.

First of all, I would like to acknowledge my two tutors. Dario was really patient with me, undergoing all my rapidly-fluctuating mood swings: not only he supported me scientifically (even if he is keen to emphasize that DFT is not his field), but he also became a sort of psychologist helping me go through most of my crises. Matteo taught me everything I know regarding density functional theory and, even though I had to give up doing my PhD in Paris, he still agreed to follow me at a distance and I am really grateful. They have both trusted my capabilities, which is something that I am not able to do myself.

I cannot forget to thank my mother and my sister (and my cat) who have “patiently” endured all my madness and believed in me during these three years: I think they deserve some kind of sanctification for this! Jokes apart, I really love them with all my heart ♡

Next I must thank both the Italian and french groups I worked with. In particular, from the group of Torino, I thank Renato, Erik and Simona (my second unofficial psychologist after Dario and chocolate dealer!). Then I have to thank ‘Les ritals’, the french group, that is Cesare (who has also helped me with my troubles with french assurance), Marco and Oliviero.

Finally, but not least, I have to thank my friends, Bruno, Betta, Titty, Pi, Siro, Angi, Momi and Roux. We might end up in different places but we will always stay together no matter what.

Abstract

In this thesis work I investigated the effects of the electron-phonon interactions in low-dimensional carbon allotropes from first principles. In particular I focused on the emergence of superconductive phase transitions when doping systems via field effect and the occurrence of charge-density waves (CDW) due to the reduced dimensionality. In order to do so, I exploited density functional theory (DFT) and its linear response extension (DFPT), taking also into account electronic correlations via hybrid exchange-correlation functionals and the GW approximation. Furthermore, when studying the CDW transition, I also took into account the anharmonic phonon-phonon interaction via the stochastic self-consistent harmonic approximation (SSCHA).

Chapter 1 gives a short review of the different carbon allotropes, since they represent the core of the present work. In particular I give a classification based on their dimensionalities, describing how they affect their electronic and vibrational properties, focusing more on the allotropes of interest for this thesis.

Chapter 2 reviews the electron-phonon interactions from a many-body point of view. I discuss the implication of the Migdal approximation to the electron-phonon vertex and the random phase approximation (RPA) to the phonon propagator. Finally I briefly derive the multi-band Migdal-Eliashberg theory of superconductivity and I discuss its main approximations.

Chapter 3 presents a general description of the field-effect (FET) doping technique from both the experimental and the theoretical point of view, discussing also the theoretical models for FET architectures implemented in plane-wave ab-initio codes. Finally, I investigate the field-effect induction of superconductive proximity effect in three phonon-mediated superconductors.

Chapter 4 studies if it is possibile to induce a superconductive phase transition in diamond thin films via field-effect doping using both a semi-empirical approach (McMillan/Allen-Dynes equation) and a many-body approach (solving the multi-band Migdal-Eliashberg equations). I first analyze how FET doping affects both the electronic and the vibrational properties of the system. Electron-phonon interactions are then computed ab-initio over all the Brillouin zone through a Wannier interpolation scheme. High temperature superconductivity ($T_c \sim 40$ K) is expected for relatively high doping ($n_{2D} \sim 6 \times 10^{14}$ cm^{-2}).

Chapter 5 deals with a possibile superconductive phase transition in few-layers graphene when stacked in a rhombohedral configuration induced via field-effect doping for sufficiently high values of the induced charge density. Due to flat bands at the Fermi level, electronic correlations are expected to play a key role also for electron-phonon interactions. Therefore, electron-phonon matrix elements are computed through finite differences by also taking into account different percentages of exact exchange interaction among electrons (i.e. with hybrid functionals). Standard DFPT severely underestimates the deformation potential in this case and the inclusion of electronic correlation boosts the electron-phonon coupling constant approximately by a factor 2. Nevertheless, no phonon-mediated superconductive phase transition is observed.

Chapter 6 focuses on the lattice instability of the linear acetylenic carbon chain. The Landau-Peierls distortion of carbyne from an ordered metallic to a distorted insulating phase is re-investigated, departing from the harmonic description of lattice dynamics and taking into account electronic correlations. Moreover, thanks to the stochastic self-consistent harmonic approximation (SSCHA), the temperature dependent free energy landscape is studied by including phonon-phonon anharmonic interactions in a non-perturbative way. Finally, I also perform ab-initio computation of the optical properties of polyyne both in the G_0W_0 approximation and solving the Bethe-Salpeter equation.

Contents

Symbols

Physical Constants

$\hbar$	Reduced Plank constant
k_B	Boltzmann's constant
m_e	Electron mass

Variables and Functions

σ	Spin
$\mathbf{k}$ ($\mathbf{q}$)	Electron (Phonon) momentum
$\varepsilon_{\mathbf{k}j}$ ($\varepsilon^0_{\mathbf{k}j}$)	Screened (unscreened) energy of an electron of momentum $\mathbf{k}$ in band j
$\omega_{\mathbf{q}\nu}$ ($\omega^0_{\mathbf{q}\nu}$)	Screened (unscreened) frequency of a phonon of momentum $\mathbf{q}$ and mode ν
$c^\dagger_{\mathbf{k}j\sigma}$ ($c_{\mathbf{k}j\sigma}$)	Creation (Destruction) operator for an electron of spin σ and momentum $\mathbf{k}$ at band j
$b^\dagger_{\mathbf{q}\nu}$ ($b_{\mathbf{q}\nu}$)	Creation (Destruction) operator for a phonon of frequency $\omega_{\mathbf{q}\nu}$ at mode ν and momentum $\mathbf{q}$
$e^{A\alpha}_{\mathbf{q}\nu}$	Phonon eigenvectors for momentum $\mathbf{q}$ and mode ν
$u^{\mathbf{q}}_{A\alpha}$	Fourier transformed displacement of atom A along cartesian direction α
$g^{\nu}_{\mathbf{k}j,\mathbf{k}+\mathbf{q}j'}$	Electron-Phonon matrix elements

$\mathcal{G}(\mathbf{k},\omega_n)$ $\left(\mathcal{G}^0(\mathbf{k},\omega_n)\right)$	Interacting (free) electron Green's function
$\mathcal{D}(\mathbf{q},\nu_n)$ $\left(\mathcal{D}^0(\mathbf{q},\nu_n)\right)$	Interacting (free) phonon Green's function
$\Sigma(\mathbf{k},\omega_n)$	Electron self-energy
$\Pi(\mathbf{q},\nu_n)$	Phonon self-energy
$\mathcal{J}(\mathbf{k},\mathbf{q};\omega_n,\nu_m)$	Electron-phonon vertex function
T $(\beta = 1/k_B T)$	Temperature (inverse temperature)
v_F	Fermi velocity
$f(\varepsilon_k)$	Fermi distribution
$\chi_0(\mathbf{q},\omega)$	Lindhard function

Indices

j, j'	Electronic bands
ν, μ	Vibrational modes
α, α'	Cartesian coordinates {x,y,z}
A, A'	Atom
ω_n (ν_n)	Electron (phonon) Matsubara's frequencies

Acronyms

DFT	Density Functional Theory
DFPT	Density Functional Perturbation Theory
SSCHA	Stochastic Self Consistent Harmonic Approximation
ARPES	Angle-Resolved PhotoEmission Spectroscopy
DOS	Density Of States
FET	Field Effect Transistor
RPA	Random Phase Approximation

Chapter 1

Carbon allotropes

Carbon, apart from providing the basis for life on Earth, nowadays plays a critical role in many aspects of technological development, (i.e. drug delivery, solar cells, opto-electronics, nano-electronics, etc.) [1, 2]. Thanks to its valency and the possibility of forming hybrid orbitals, carbon can give rise to many allotropes, i.e. structurally different forms of the same element. Indeed, single, double and triple bonds can be formed leading to 3D systems (e.g. diamond or graphite) as well as low dimensional ones, i.e. 2D (e.g. graphene), 1D (e.g. carbon nanotubes or polymers) and 0D (e.g. fullerenes) [3], which display very different chemical and physical properties.

The aim of this chapter is to briefly summarize the properties of carbon allotropes, since they represent the key topic of this thesis. As a matter of fact, the present work focuses on the ab-initio investigation of three carbon allotropes with reduced dimensionality: quasi-2D diamond thin films, 2D multilayer graphene with rhombohedral stacking and 1D carbyne. These three case studies are exploited to highlight the effect of low dimensionality on the electron-phonon interaction, in particular on the emergence of superconductivity and charge-density waves (CDW).

First of all, in Sec. 1.1 I will describe the hybridization process for the case of the carbon atom. Then I will illustrate the main carbon allotropes resulting from the orbital hybridization, dividing them according to their effective dimensionality. In particular in Sec. 1.2 I will discuss the 3D forms of carbon, i.e. diamond and graphite. In Sec. 1.3 I will consider 2D graphene in its different geometries, i.e. monolayer, multilayer, rhombohedral and twisted. Then, in Sec. 1.4 the focus will

pass on the 1D forms of carbon, i.e. carbon nanotubes (CNTs) and carbynes. Finally, the 0D fullerenes will be investigated in Sec. 1.5.

1.1 Orbital Hybridization and Carbon Allotropes

Carbon allotropes, as well as atoms belonging to the carbon group (e.g. silicon and germanium), belong to the class of *covalent materials*: the atoms taking part to the formation of the solid form bonds by sharing the unpaired valence electrons between them and reaching the stable electronic configuration for both atoms [4]. Therefore a *covalent bond* is such that it contains two electrons, which will be localized in space and will not contribute to the electrical conductivity. As a matter of fact diamond, bulk silicon and gallium arsenide are typical examples of covalent solids and are insulating because they do not have free carriers available for conduction: completely filled electronic bands will be separated from empty bands by an energy gap of few eV. Moreover, we distinguish between bonds formed between same atoms (as in the case of carbon allotropes) and bonds formed with different atoms (as in the case of GaAs): the first one will be called *homopolar bond* and it is a symmetric bond (Fig. 1.1 (a)), while the latter is called *heteropolar bond* or simply *polar bond* and it is asymmetric (Fig. 1.1 (b)). The covalent structure will be thus unstable if the covalent bond does not contain two electrons, if the bonding energy is too small or if the bond is too polar (in such case the structure might collapse to a denser system such as a ionic crystal) [5].

In its ground state, carbon's electronic configuration is $1s^2 2s^2 2p^2$ and, therefore, only the two electrons in the 2p orbitals seem to be available to form covalent bonds. Nevertheless, carbon is actually tetravalent and it can easily bond to both electropositive and electronegative elements. Moreover, it can easily form single (average bond energy of ~ 3.627 eV), double (average bond energy of ~ 6.322 eV) or triple (average bond energy of ~ 8.706 eV) bonds [6]. This is due to the possibility of exciting one of the electrons from the $2s$ shell to the free $2p$ orbital, thus obtaining a final electronic configuration of $1s^2 2s^1 2p^3$: for the isolated carbon this would cost ~ 4.2 eV, however forming covalent bonds lowers the total energy of the carbon allotrope making it energetically favorable [7].

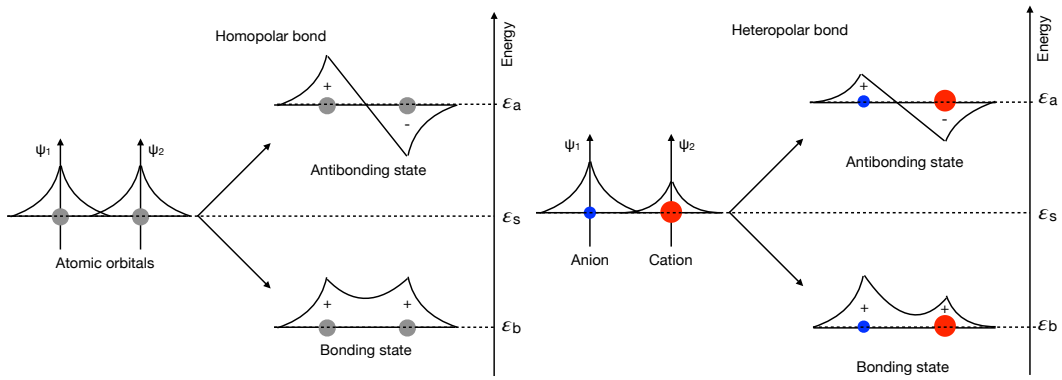

Fig. 1.1 Bonding and antibonding states for a (a) homopolar and (b) heteropolar diatomic molecule. The energy ε_b (ε_a) of the bonding (antibonding) state is always smaller (bigger) than the sum of the energies of the isolated atoms ε_s. Figure adapted from Ref. 5.

Consider now a diatomic molecule formed by two carbon atoms positioned along the x axis: their orbitals are depicted in Fig. 1.2. According to the theory of linear combination of atomic orbitals (LCAO), when the wavefunctions of the two atoms overlap we obtain a *bonding state* with spatial symmetry and lower energy and an *antibonding state* antisymmetric in space and with higher energy (Fig. 1.1 (a)). The bonding states will be the first ones to be occupied, however if the number of carriers exceeds the number of bonding states then the antibonding orbitals have to be occupied raising the energy as a consequence: in this latter case if the total energy is too high, then it is not convenient to form a bond. When orbitals overlap on the same line joining electrons, bonding σ and antibonding σ^* states are formed: in the situation depicted in Fig. 1.2, this can happen between the $2s$ orbitals, between the $2p_x$ orbitals or between the $2s$ orbital of atom 1 and $2p_x$ orbital of atom 2 (or vice versa). The remaining $2p_y$ orbitals couple only between them, as well as the $2p_z$, forming the bonding π and antibonding π^* states: the electron density will therefore lie in front and in back, or above and below, the bonding axis [5, 8].

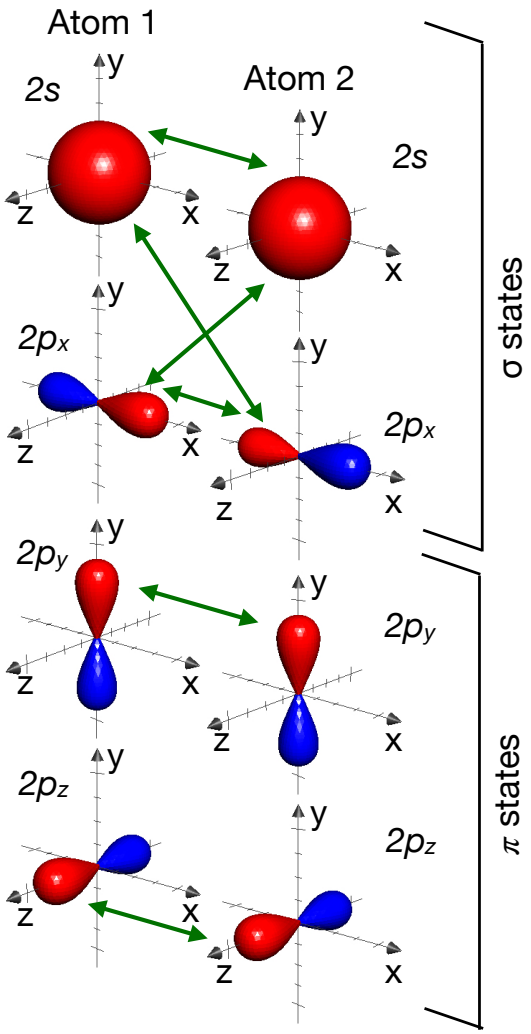

Fig. 1.2 Modulus squared atomic orbitals' wavefunctions for two carbon atoms with their phases: red (blue) colored lobes represent positive (negative) phases, which will give rise to constructive (destructive) overlap between orbitals when forming bonds. Green arrows represent the possible overlaps when two atoms along the x direction are allowed to form a bond. In particular, in this case, σ (and σ^*) bonds will be formed among $2s$ and $2p_x$ orbitals, while π (and π^*) bonds will be formed between $2p_y$ and between $2p_z$. Figure adapted from Ref. 5.

While the $2s$ orbital have a spherical symmetry, the $2p$ ones are directed along the axis of an orthonormal euclidean space and therefore it might seem that carbon atoms can form bonds only with bonding angles of 90°. However, as we will discuss below, this is not true because carbon allotropes show geometrical structures quite different from the simple cubic one thanks to the possibility of mixing its electronic orbitals.

The process of mixing different orbitals is called *orbital hybridization*. In particular, since carbon mixes the $2s^1$ and the $2p$ orbitals, three types of hybridizations are possible depending on the number of $2p$ states that are mixed with the $2s^1$: linear sp ($2s^1+2p$), trigonal planar sp^2 ($2s^1+2p+2p$) and tetrahedral sp^3 ($2s^1+2p+2p+2p$).

In the sp hybridization (Fig. 1.3 (a)) the hybrid orbital results from the mixing of the $2s^1$ and one of the $2p$ atomic orbitals of carbon. Since the spatial distribution of the modulus squared of the $2s^1$ wavefunction is isotropic while the $2p$ is directed either on the x, y or z direction, the sp^1 hybrid orbital will lie along a straight line (the same of the original $2p$ orbital) with oppositely phased lobes, allowing for linear molecular geometries with bonding angles of 180° between neighboring carbon atoms. The remaining unhybridized $2p$ lobes will be perpendicular to the two sp^1 hybrid orbitals and to each other: as a consequence we can have one sp^1 σ bond along the bonding axis joining the two carbon atoms (Fig. 1.3 (b)) and two π bonds with the remaining $2p$ orbitals (Fig. 1.3 (c)). This kind of hybridization can give rise to single+triple bonds or to double+double bonds and is typical of 1D linear chains and polymers.

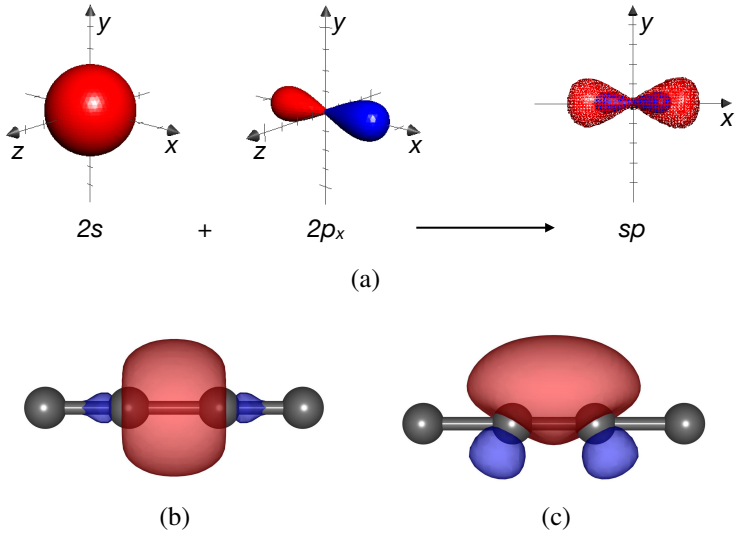

Fig. 1.3 (a) Schematic representation of the sp^1 hybridization. The positive (red) lobes of the hybrid orbitals have been made semi-transparent in order to show the inner smaller negative (blue) lobes; (b) σ bond between sp^1 hybrid orbitals in the linear carbon chain oriented along the x axis; (c) π bond between $2p_z$ orbitals in the linear carbon chain oriented along the x axis. (b) and (c) have been obtained by interpolating valence bands through maximally localized Wannier functions. Positive (negative) lobes are colored in red (blue).

If we now mix two $2p$ atomic orbitals with the $2s^1$ we obtain the sp^2 hybrid orbitals, which has a trigonal planar geometry (Fig. 1.4 (a)). Indeed, we can identify a plane passing through the $2p$ orbitals taking part to the hybridization process and, therefore, bonds will form in such plane with 120° bond angles. Therefore, three σ bonds with the sp^2 hybrid orbitals will be formed on the plane (Fig. 1.4 (b)), while the remaining $2p$ orbital will be used for a π bond above and below the carbon-carbon line or they will take part to a (long-range) van der Waals interaction (e.g. in layered systems, Fig. 1.4 (c)). This is typical of aromatic molecules (e.g. benzene C_6H_6), layered graphite and graphene.

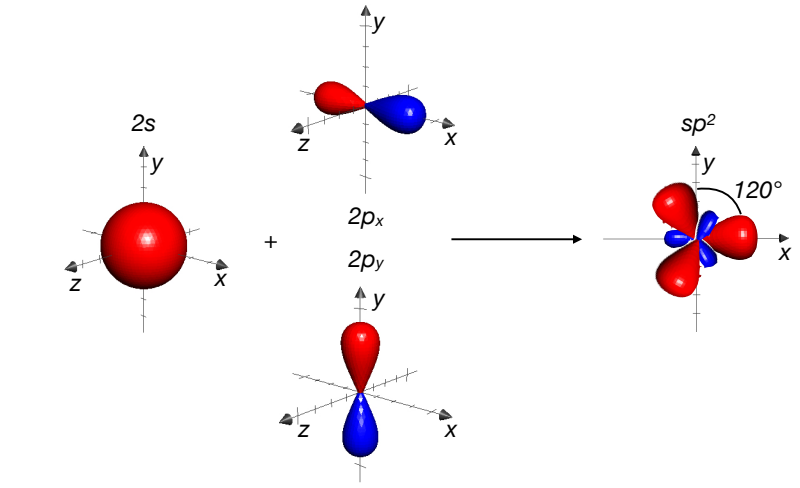

(a)

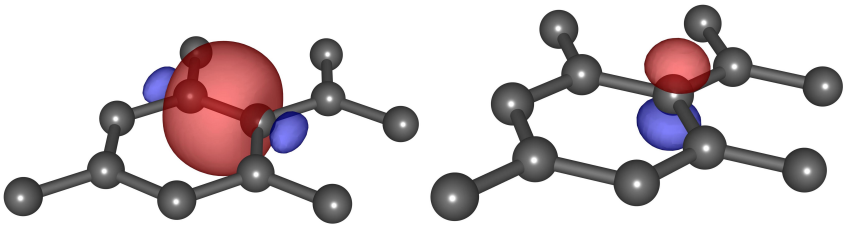

(b) (c)

Fig. 1.4 (a) Schematic representation of the sp^2 hybridization; (b) σ bond between sp^2 hybrid orbitals in the hexagonal graphene lattice; (c) Unpaired $2p_z$ orbital in the hexagonal graphene lattice. (b) and (c) have been obtained by interpolating valence bands through maximally localized Wannier functions. Positive (negative) lobes are colored in red (blue).

Finally, by mixing all of the $2p$ orbitals with the $2s^1$ we get the sp^3 orbitals, which are oriented in 3D space since they result from a linear combination of orbitals lying in all three spatial directions (Fig. 1.5 (a)). Indeed, the geometry of the resulting orbitals is tetrahedral with bonding angles of 109.5°, typical of diamond. The sp^3 hybridization will give rise only to single σ bonds (Fig. 1.3 (b)).

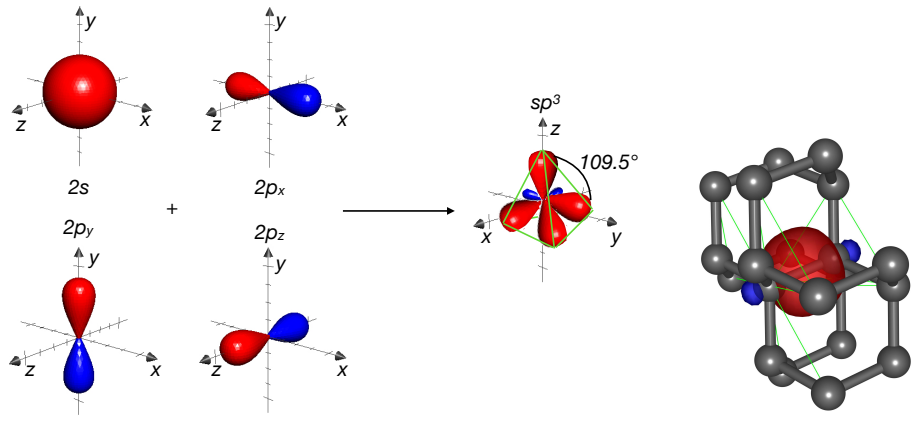

(a) (b)

Fig. 1.5 (a) Schematic representation of the sp^3 hybridization; (b) σ bond between sp^3 hybrid orbitals in diamond. (b) has been obtained by interpolating valence bands through maximally localized Wannier functions. Positive (negative) lobes are colored in red (blue). Green lines identify the tetrahedral structure.

As a final remark, by connecting together the dangling bonds of graphene sheets, they can be rolled up into carbon nanotubes (Fig. 1.13) or fullerenes (Fig. 1.16). However, by doing so, the electronic structure is altered since bond lengths and bond angles between overlapping orbitals are stretched and/or curved. This gives rise to a mixture of sp^2 and sp^3 hybrid orbitals in such allotropes making the hybridization no longer purely sp^2, which represents the phenomenon of *rehybridization* [9–12].

In Fig. 1.6 a summary of the main carbon allotropes is given, with a division based on the type of hybridization that gives rise to their crystal structure. I would like to stress that, while diamond, graphite, graphene, CNTs and fullerenes are all existing allotropes, the actual existence of carbyne is still debated, since linear carbon chains are subject to Landau-Peierls instabilities. This latter topic will be the heart of the last chapter.

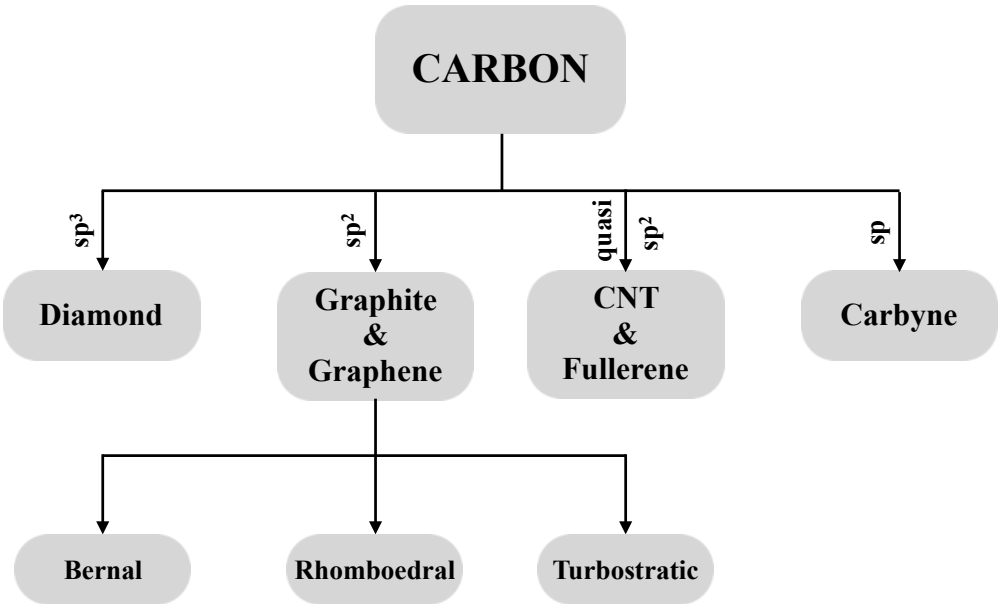

.

Fig. 1.6 Family tree of the main carbon allotropes grouped according to their hybridization, as described in this chapter. Notice that the stability of the *sp* carbon allotrope is still a source of debate.

1.2 3D: Diamond and Graphite

Diamond crystal structure (Fig. 1.7 (a)) can be viewed as two intersecting face-centered cubic lattices (space group $Fd\bar{3}m$), with a spacing of $1/4$ of the lattice parameter ($a = 3.56$ Å) in all the directions [3]. Due to its strong covalent sp^3 σ bonds, σ electrons are strongly localized in between the carbon atoms making this material an electrical insulator whose electronic energy gap is ~ 5.5 eV [13]. This is also the reason behind its optical transparency since the wavelength that we need for exciting an electron from the valence to the conduction band doesn't lie in the optical spectrum [13]. Diamond, which is among the hardest materials [13], has a ultrahigh thermal conductivity [13] and it represents the thermodynamically stable form of carbon for pressures greater than 6×10^9 Pa [1].

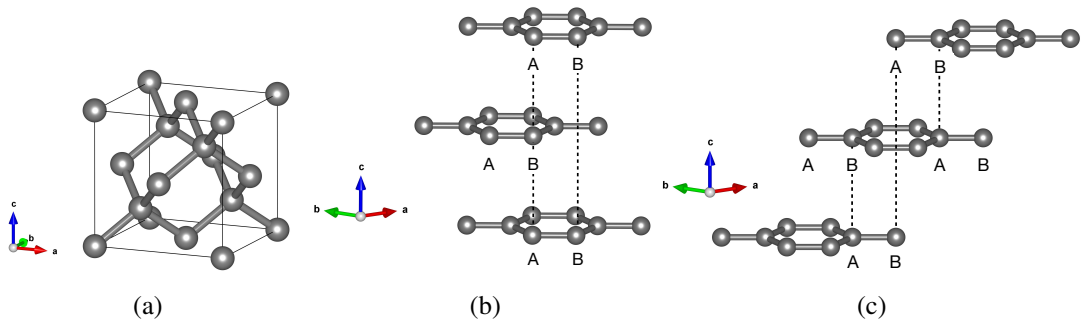

(a) (b) (c)

Fig. 1.7 3D carbon allotropes: (a) sp^3 hybridized diamond; (b) sp^2 hybridized Bernal (AB) graphite; (c) sp^2 hybridized rhombohedral (ABC) graphite.

Ultrahard materials have high-energy phonons and this is in principle beneficial for the possible occurrence of an insulator-to-metal (IM) and a superconductive (SC) phase transition in the case of phonon-mediated superconductors, as it will be explained in the next chapter. However, in order for this to happen, a sizeable number of electrons at the Fermi energy is required and this is not the case for intrinsic diamond due to the insulating nature of the covalent bonds. Therefore, one key problem is the possibility of adding carriers without degrading excessively the intrinsic properties of this carbon allotrope.

In 2004 it was shown by E. A. Ekimov et al. [14] that by chemically doping diamond with boron (with a concentration n_B) it is indeed possible to induce first an insulator-to-metal phase transtion ($n_B \approx 10^{20}$ cm^{-3}) and then the appearance of a superconductive phase for $T < T_c \sim 4$ K [15–17] and $n_B \approx 4-5\times10^{21}$ cm^{-3}. Later it was theoretically confirmed via density functional theory analysis that boron-doped bulk diamond is a conventional superconductor (i.e. phonon-mediated) and that, in principle, if sufficiently large B contents could be attained, it would be possible to enhance the superconductive transition temperature up to ~ 40 K. [18–23]. However there is a limit (*solubility limit*) to the amount of boron that can be chemically incorporated in the closely packed structure of diamond [24], which hinders the possibility of actually raising T_c to such high values, limiting it to $\approx 8-10$ K in thin films [17]. It is important to underlie that there are non-equilibrium doping techniques which can be exploited in order to induce dopants, as in the case of Q-carbon [25] or silicon [26], however the crystal structure of diamond might be severely compromised and, as a consequence, the vibrational properties would be substantially modified. Another possibility to introduce carriers without adding

boron atoms is through electrochemical doping [27], but this possibility will be accurately discussed in the next chapters as it represents one of the main topics of this work.

At lower pressures, the thermodynamically stable allotrope of carbon is graphite. It crystallizes in the hexagonal crystal structure (space group $P63mc$) where carbon atoms are arranged in layers: in each layer atoms are bonded together through sp^2 σ bonds, thus forming the characteristic honeycomb lattice, while in the out-of-plane direction the unpaired $2p_z$ accomodate the remaining fourth electron that is shared among all the others carbons on the plane. Weaker van der Waals forces keep together the graphene layers at a distance of 3.35Å [3, 28]. Due to low-energy bonds in the out-of-plane direction, the various layers can slide on top of each other giving graphite lubricant properties. Moreover, the shared unpaired $2p_z$ electron allows graphite to be a good thermal and electrical in-plane conductor, while it has poor electrical and thermal properties in the out-of-plane direction. As a consequence, the electronic band structure of graphite doesn't show a gap typical of insulators but it is actually a semi-metal with linearly dispersive bands forming Dirac cones at the Fermi level [29–32]. The absence of an optical gap in the electronic dispersion relation is the reason behind its black color.

Another important property of graphite is that, thanks to its lubricant properties, the various layers can be stacked in many different ways [33]. Consider one single layer, then in the unitary cell we can identify two inequivalent atoms that we can call A and B. The first common form of graphite is the Bernal or AB stacking shown in Fig. 1.7 (b), where A atoms always have a neighbor B atom in the first layer on top or below it while B atoms only have neighbor B atoms in a second layer. Another possibility consists in the rhombohedral or ABC graphite (Fig. 1.7 (c)), whose stacking has a period of three layers: in this case A atoms will have a neighbor B atom in the first layer on top of it and two layers below, while B atoms will have a neighbor A atom in the first layer below it and two layers above. Nevertheless, rhombohedral graphite doesn't exist in nature and up to now only multilayer samples (up to ~ 50 layers [34, 35]) have been obtained: Bernal stacked graphene is energetically favored with respect to ABC graphene [36] and, therefore, the latter is quite difficult to isolate [37, 38]. Finally, relative translations or rotations of layers lead to non-trivial stacking geometries and this form is called turbostratic graphite [39, 40].

1.3 2D: Graphene - Monolayer, Multilayer and Twisted

A single layer of carbon atoms with sp^2 hybridization is called graphene (Fig. 1.8 (a)) and it is charaterized by a hexagonal unit cell (space group $P6/mmm$). This 1-atom thick allotrope can be considered a 2D material since it extends far more in the in-plane direction than in the out-of-plane one. However, for a very long time, it was a general belief that strictly 2D materials (as well as 1D materials) could not exist due to quantum and thermal fluctuations as stated first by Landau [41, 42] and Peierls [43] and then by Mermin [44]. Indeed, it can be shown [8] that the finite-temperature mean square atom displacement diverges for $T > 0$ K: as a consequence the melting temperature of 2D crystals can be considered as the absolute zero. Therefore according to the Mermin-Wagner-Hohenberg theorem [45, 46], two (or lower) dimensional systems that are invariant only for discrete translations cannot be stable for any $T \neq 0$ K: the reason behind it is the presence of acoustic phonon modes (i.e. Goldstone modes [47]) which disrupt the crystalline order at any finite temperature.

Nevertheless, Andre Geim and Konstantin Novoselov showed that it was actually possible to obtain free standing graphene layers by exfoliating graphite using a simple Scotch tape [48]. Its stability, contrarily to what was stated before, has to be linked to its three dimensional environment: indeed, while its electronic properties are those of an effective 2D material, it is still a system which lives in three dimensions. The absence of atoms on top and below it, reduces the out-of-plane interatomic forces leading to a flexural phonon [49] mode whose energy goes quadratically to zero as the excitation wavelength goes to zero. This flexural mode, which is protected by rotational symmetry, gives rise to ripples in the ideally flat graphene, leading to an increase in elastic energy and suppressing thermal fluctuations thus minimizing the total free energy. Moreover, even if according to harmonic theory, such flexural phonon should prevent graphene from propagating sound waves, authors in Ref. 50 showed that if we take into account phonon-phonon anharmonic interactions sound propagation does coexists with the quadratic flexural phonon.

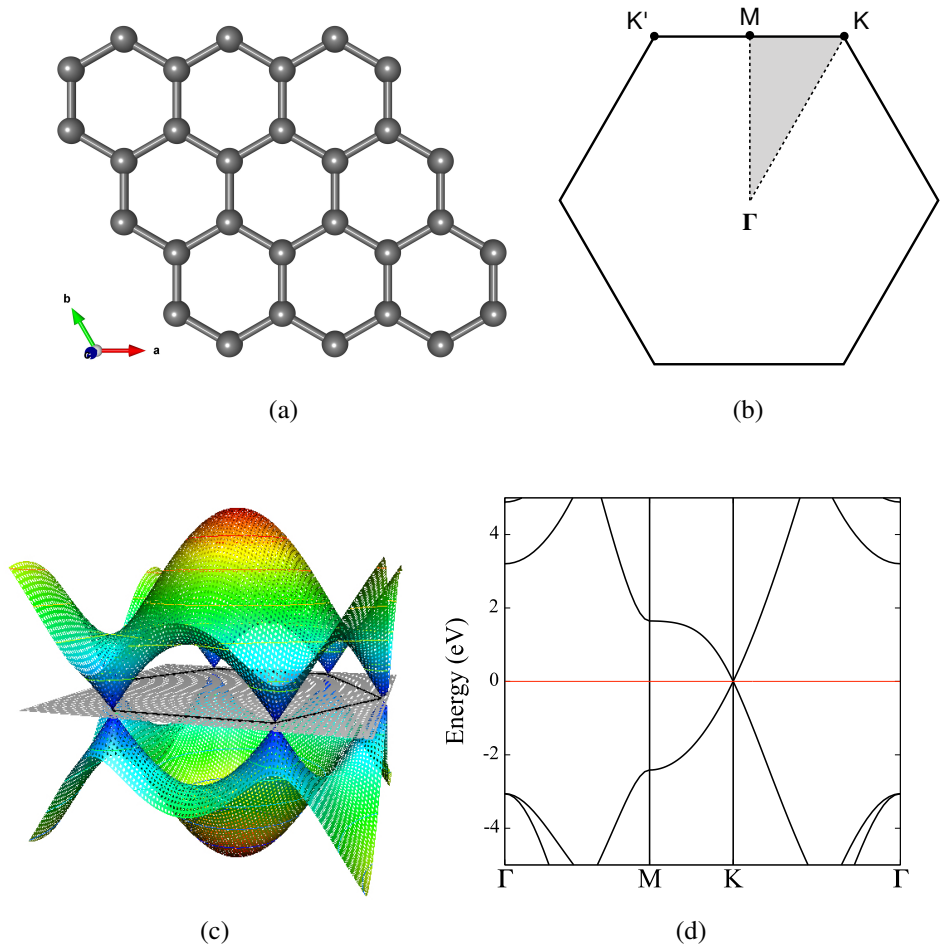

(a) (b)

(c) (d)

Fig. 1.8 (a) 2D sp^2 carbon allotrope: monolayer graphene; (b) Graphene Brillouin zone (BZ): the high symmetry points $\mathbf{\Gamma}$, $\mathbf{M}$ and $\mathbf{K}$ ($\mathbf{K}'$) are highlighted. The grey shaded region represents the irreducible Brillouin zone (IBZ); (c) 3D plot of the low energy graphene dispersion relation, highlighting the Dirac cones touching at the corners of the hexagonal BZ; (d) Electronic band structure of graphene along lines in the BZ connecting high symmetry points ($\mathbf{\Gamma}-\mathbf{M}-\mathbf{K}-\mathbf{\Gamma}$.)

Monolayer graphene seemed to be very promising for technological applications thanks to its high-quality transport properties at ambient condition (without any doping or charge transfer) [51] and its flexibility, making it a promising material for touch screens or wearable technology [52]. The most striking aspect of its electronic dispersion relation is its linearity near the corners of the Brillouin zone ($\mathbf{K}$ and $\mathbf{K}'$, Fig. 1.8 (b)): two cones are formed, touching at the charge neutrality point where the Fermi level lies, thus completely filling the lower cone and leaving completely empty the upper one (Fig. 1.8 (c)). As such, graphene represents a semimetal or a zero-gap

semiconductor with a twofold valley degeneracy [53, 54] (Fig. 1.8 (d)). The two cones formed by the linearly dispersive bands are called Dirac cones because in the vicinity of such high-symmetry points it is possible to show that the fermions obey the massless chiral Dirac equation [55].

Indeed, since two inequivalent atoms are required to describe the unit cell of graphene, electrons acquire a new twofold degree of freedom that is called *pseudospin* and, consequently, they acquire a chirality: if we look at the **K** point, in the upper cone the direction of pseudospin is parallel to the electron wavevector **k**, whereas in the lower cone it is antiparallel. On the other hand, it is possible to observe an opposite picture for the $\mathbf{K}'$ symmetry point [56]. Therefore, thanks to its very simple geometrical structure, graphene has become a prototypical toy model for theoreticians in order to study a condensed-matter analogue of quantum electrodynamics in $(2+1)$-dimensions [57, 58].

However, even if the low energy model of graphene predicts (as a first approximation) linearly dispersive electronic bands near **K** and $\mathbf{K}'$ (i.e. the Dirac cones as described before), electron-electron interactions modify such picture: indeed, close to the charge neutrality point the conventional Landau theory of strongly interacting Fermi liquid is no more valid and renormalization group analysis predicts a logarithmically divergent Fermi velocity. This peculiarity has been experimentally proven through cyclotron mass measurements on suspended graphene, as reported in Ref. 59.

Thanks to angular-resolved photoemission spectroscopry (ARPES), it is possible to directly extract the electronic dispersion relation of a material near the Fermi level by shining a sample with photons and then measuring the kinetic energy of out-coming electrons [60]. Therefore, by exploiting this technique it was possible to measure the linear dispersion relation of single-layer graphene deposited on a silicon carbide substrate [61–63]. However, the measured Fermi velocity (which is proportional to the slope of the electronic band at the Fermi level) is actually larger than the one obtained by standard density functional theory computations by about $\sim 10-20\%$ [64], which is another consequence of the many-body nature of electron-electron interaction.

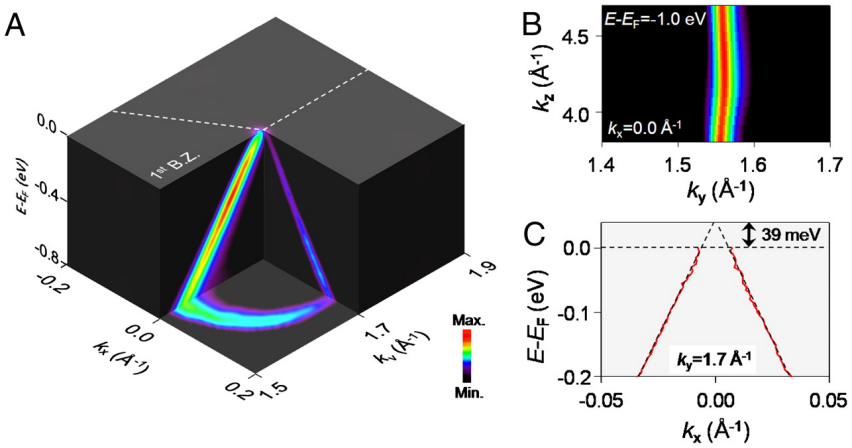

Fig. 1.9 From "*Many-body interactions in quasi-freestanding graphene*, D. A. Siegel, C.-H. Park, C. Hwang, J. Deslippe, A. V. Fedorov, S. G. Louie and A. Lanzara, PNAS July 12, 2011 108 (28) 11365-11369": "(A) ARPES spectra of monolayer graphene, showing several slices through the Dirac cone of monolayer graphene. (B) The kz dependence of photoemission intensity shows a single line, signature of monolayer graphene. (C) The red solid line shows the peak positions of the MDC fits, and the dotted red line represents the linear fit of the dispersion. The position of the Dirac point is slightly above the Fermi level." .

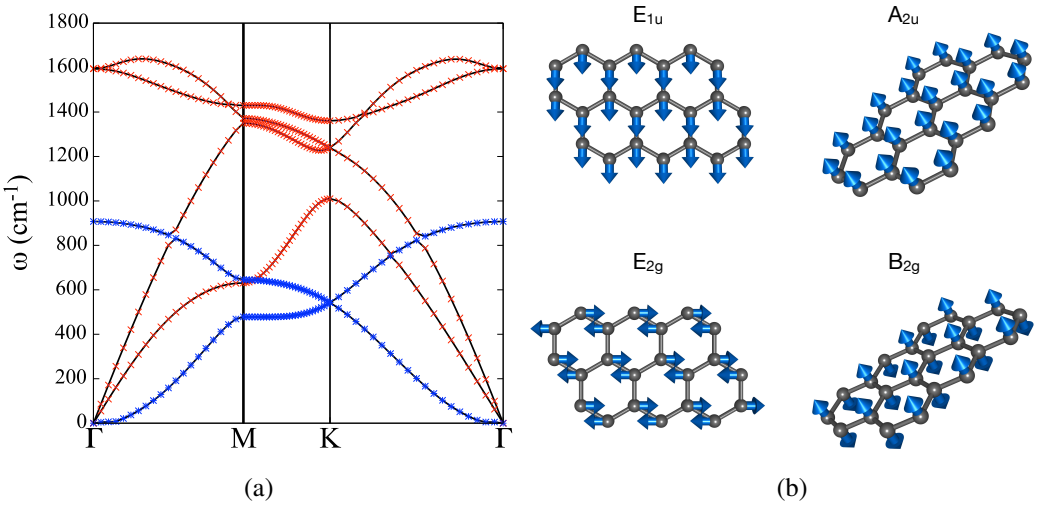

Fig. 1.10 (a) Phonon dispersion relation of monolayer graphene along lines in the BZ connecting high symmetry points ($\mathbf{\Gamma} - \mathbf{M} - \mathbf{K} - \mathbf{\Gamma}$.). Red (blue) dots represent the in-plane (out-of-plane) character of the mode; (b) Phonon eigenmodes of monolayer graphene computed at $\mathbf{q} = \mathbf{\Gamma}$, obtained by diagonalizing the dynamical matrix.

As for phonons (Fig. 1.10 (b)), there are two infrared-active in-plane doubly degenerate acoustic modes E_{1u}, the out-of-plane acoustic flexural phonon A_{2u}, two doubly degenerate in-plane Raman-active optical modes E_{2g} and an out-of-plane optical mode B_{2g} [65]. The notation used for the vibrational modes comes from the German and is such that g stands for *gerade* (symmetric), while u stand for *ungerade* (antisymmetric): indeed, if we make a spatial inversion transformation in direct space such that $\mathbf{r}$ is transformed into $-\mathbf{r}$, the representations will be symmetric (g) or antisymmetric (u) under such transformation.

The most interesting aspect of the phonon dispersion relation of graphene (Fig. 1.10 (a)) is the sharp discontinuity of the highest optical branches, i.e. the E_{2g} mode at the center of the Brillouin zone ($\mathbf{\Gamma}$) and the A_1' mode at the corner of the Brillouin zone $\mathbf{K}$ [66]. This is can be directly linked to the effect of the electronic band-structure of Graphene on the electron-phonon couplings [67], which leads to the breakdown of the Born-Oppenheimer approximation [68, 69] and to the appearance of non-adiabatic Kohn anomalies [70] (i.e. to a sharp discontinuity of the phonon branches) that is also strictly linked to the 2D nature of the material and to the divergence of the Lindhard function at $2k_F$ (k_F being the Fermi momentum). The presence of Kohn anomalies and the effects on the electron-phonon interactions represent another important topic of the present thesis and are going to be discussed later on in this work.

Moreover, from ARPES measurements it is also possible to observe two kinks in the electronic dispersion relation [63]: the first is at ~ 160 meV below the Fermi energy (remaining unchanged upon doping), while the second one is closer to the charge neutrality point and its position is doping-dependent. All these effects can be linked to many-body interactions, in particular to the electron-phonon and electron-electron interaction. More precisely, the first kink is linked to the interaction between electrons and the vibrating lattice [63], the second is due to a plasmon [71]. Finally, the authors of Ref. 72 showed that it is possible to induce superconductivity in monolayer graphene by depositing alkaline metal adatoms on its surface, similarly to what happens in intercalated graphite [73, 74].

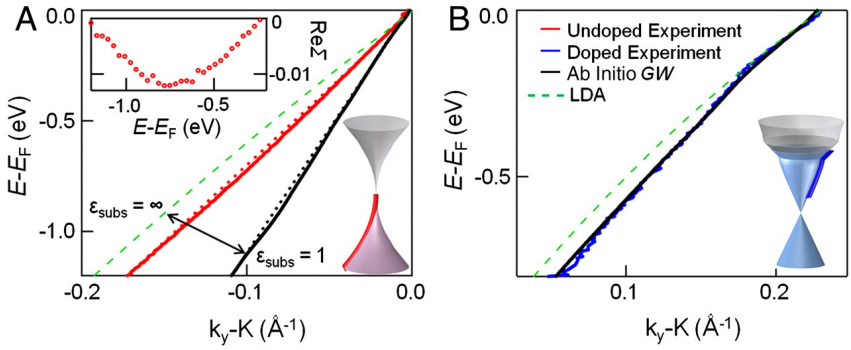

Fig. 1.11 From "*Many-body interactions in quasi-freestanding graphene*, D. A. Siegel, C.-H. Park, C. Hwang, J. Deslippe, A. V. Fedorov, S. G. Louie and A. Lanzara, PNAS July 12, 2011 108 (28) 11365-11369": "(A) Extracted dispersions from as-grown C-face graphene (red), and from ab initio GW plus el-ph calculations including electron-phonon (el-ph) and electron-electron (el-el) interactions in suspended graphene (black). Straight red and black dashed lines are given as guides to the eye, which intersect the dispersions at -1.2 eV and -0.2 eV, to show how the experimental dispersions (solid lines) deviate from linearity (straight dotted lines). The LDA (local density approximation) band is given as a green dashed line. (Inset) Deviation of the experimental dispersion from linearity (red dotted line subtracted from the solid red experimental dispersion). (B) Extracted dispersions for highly doped graphene (blue). Doping is obtained by K deposition and the resulting charge density is more than three orders of magnitude higher than undoped graphene. Black solid line shows the ab initio GW plus el-ph calculated dispersion. The LDA band is shown by the green dashed line." .

Graphene can be stacked both in the Bernal and Rhombohedral pattern with different number of layers [75]. As a consequence we can obtain two-, three- or few-layers graphene (or in general a multi-layer system) and thanks to Raman's spectroscopy it is possible to distinguish the number of layers and its stacking. Indeed the electronic structure and the electron-phonon interactions are directly affected on how many layers are involved in the multylayered sample and on the Bernal or rhombohedral stacking [76, 77].

In the case of bilayer graphene, the only possible non-trivial stacking is the AB or Bernal. Such system is particularly interesting because, without taking into account electron-electron interactions, it remains a gapless semiconductor with electronic bands touching at the **K** and **K′** high symmetry points quadratically. Moreover, when an external electric field is applied in a perpendicular direction, an energy gap is opened between the two degenerate electronic bands: the magnitude of such energy gap can be tuned by varying the intensity of the applied electric field, making

this system appealing for optoelectronic applications since it is possible to directly control the wavelength of the excitation energy [78].

However multilayer Bernal-stacked graphene samples show an interesting property if we now take into account electron-electron interactions as it has been experimentally measured on ultra-clean suspended samples [79]: an energy gap opens at temperatures smaller than a certain critical value T_c. More precisely, bilayer graphene shows a second order phase transition into an insulating gapped state for $T < T_c = 12K$ and the same happens for multilayer Bernal-stacked graphene samples with an even number of layers: in this latter case the critical temperature T_c and the value of the energy gap Δ_0 increases linearly with the number of layer following the mean-field ratio $\Delta_0/k_B T_c = 1.76$. On the other hand, a second order phase transition also occurs in Bernal-stacked multilayers samples with an odd number of layers but the system remains metallic: this is because an energy gap divides the two quadratically dispersive bands, but a third linearly dispersive one is crossed by the Fermi level.

If we now take into account a three-layer systems, the other possible stacking is the rhombohedral (ABC) one as described before in Sec. 1.2. Rhombohedrally stacked multilayer graphene shows an extremely flat band (2 meV of bandwidth [80, 81, 75]) at the corner of the Brillouin zone (i.e. **K**), whose extension is incremented upon adding more layers to the system up to ~ 8 layers (with a maximum extension of ~ 13 Å^{-1}). The presence of dispersionless electronic states is very appealing, since it might lead to correlated states of matter, such as magnetism, high-T_c superconductivity, charge density waves or spin density waves: indeed the flatness of the electronic band at the Fermi energy is linked with a reduction of the electron kinetic energy, consequently enhancing the role of electron-electron interactions.

While standard DFT computations predict a zero-gap semiconductor, experiments prove the presence of a small energy gap (~ 42 meV) at very low temperatures [80, 82]. As a matter of fact the authors of Ref. 83 showed that, by including some percentage of exact-exchange interaction via hybrid functionals, it is possible to link the opening of such energy gap to an antiferromagnetic ground state. The peculiarity of such magnetic state is that it can be tuned via field-effect doping [84] and according to the number of layers [75]. With the disappearance of a magnetically stable state, the Fermi level is located on a very flat band leaving the possibility for

a superconductive state [85–88] or a CDW ordered state. The possible occurrence of a phonon-mediated superconductive phase transition in few-layer rhombohedral graphene via field-effect doping will be investigated in the following chapter of this work, since a gate-tunable superconducting state was recently found in ABC graphene on top of hexagonal boron nitride [89]. The superconductive properties of ABC stacking represent a second topic of this thesis and will be further investigated in the next chapters.

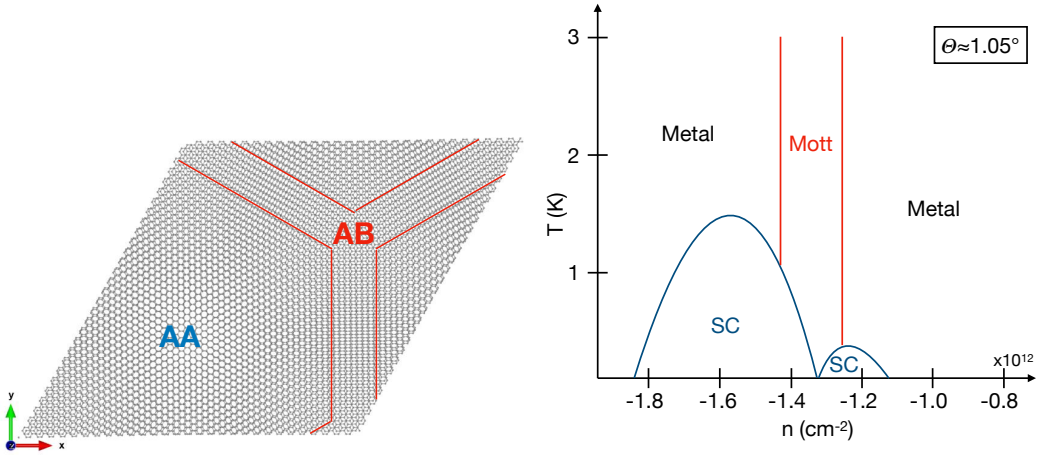

(a) (b)

Fig. 1.12 (a) Twisted bilayer graphene (TBG) at the *magic angle* $\theta = 1.05°$ responsible for superconductivity. It is possible to recognize an hexagonal region with a majority of AA stacking and a border with mainly AB stacking; (b) Phase diagram of TBG at the magic angle $\theta = 1.05°$ as a function of temperature (T) and electron doping (n). The figure is adapted from Ref. 90.

Finally it is worth mentioning that if we take two graphene layers and we twist them relatively to each other, the electronic band structure is drastically modified and two very flat bands appear at the charge neutrality point [91–94]. As a consequence, in 2018 P. Jarillo-Herrero et al. experimentally [95, 90] showed that, close to the *magic angle* of $\theta \approx 1.05°$ (Fig. 1.12 (a)), these flat bands give rise to a Mott-like insulating phase resulting from electron localization in the Moiré superlattice [96] (i.e. the supercell required to recover the in-plane periodicity due to the lattice mismatch induced by the rotation). Moreover, upon doping, the insulating phase is destroyed and a superconductive phase transition appears with a critical temperature T_c up to $\sim$ 1.7 K. The resulting phase diagram (Fig. 1.12 (b)) of twisted bilayer graphene (TBG) is very similar to those of cuprates, with superconducting domes, Mott-insulating

phases [97] and magnetically ordered states induced by electron-electron interactions of the highly localized electrons [98, 99]. The strongly correlated phases that appear in TBG make this system the first purely carbon-based superconducting material with a 2D geometry with a tunable electron-electron interaction [100, 101]. The nature of the superconducting phase is still being debated: as a matter of fact there are some suggestion that it might be phonon-mediated superconductivity [97, 102], but there are other possible exotic explanation such as topological superconductivity [103].

1.4 1D: Carbon nanotubes and Carbyne

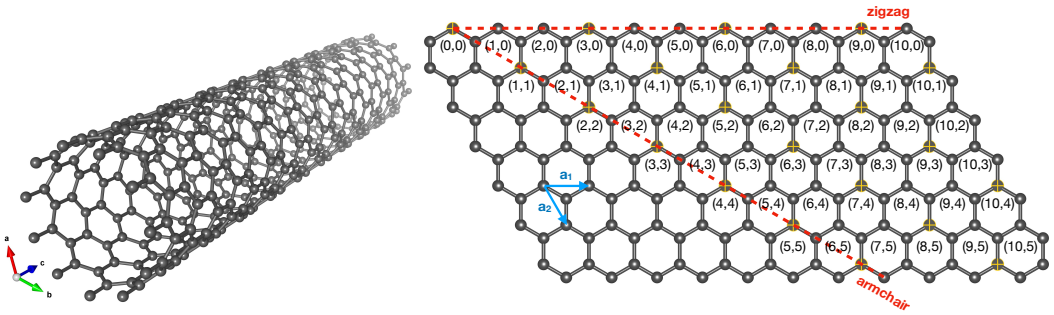

(a) (b)

Fig. 1.13 (a) 1D quasi-sp^2 carbon allotrope: single-walled carbon nanotubes (CNTs); (b) Possible helicities of CNTs: the carbon atoms highlighted in yellow represent the suitable (n,m) combinations that lead to a metallic carbon nanotube.

Carbon nanotubes (CNTs, Fig. 1.13 (a)) were first synthesized in 1991 through evaporation of graphite [104] and later on other through techniques, such as chemical vapor deposition [105]. As we described before, a carbon nanotube can be pictured as a single rolled-up graphene layer with a quasi-sp^2 hybridization. CNTs, depending on the number of tubes forming the system, can be single- or multi-walled: in the multi-walled case there are two or more concentric CNTs. Carbon nanotubes can be considered 1D systems since their diameter has a typical size of $\sim 1-2$ nm, while their lengths can be $\gtrsim 1$ mm [2]. Thanks to their electronic and vibrational properties, these systems have a vast potential in nanoelectronics [106], biological applications [107] or hydrogen storage [108].

Carbon nanotubes are specified by the *chiral vector* [109] $\mathbf{C}_h = n\mathbf{a}_1 + m\mathbf{a}_2 = (n,m)$, with $\mathbf{a}_1$ and $\mathbf{a}_2$ being the primitive vectors of a graphene sheet (Fig. 1.13 (b)): depending on the couple of integers (n,m), i.e. the helicity, CNTs can attain either a semiconducting or a metallic behavior [110]. When $\mathbf{C}_h$ and the x-axis form an angle $\theta = 0°$the structure is called *zigzag*, while for $\theta = 30°$we have the *armchair* structure. Notice that is also possible to have a general $0° < \theta < 30°$. Moreover all of the armchair CNTs are metallic, whereas the general condition for obtaining a metallic carbon nanotube is that $3q = 2n + m$ (with q an integer number) [111, 112]. Finally, thanks to the reduced dimensionality, electrons and phonons couple strongly giving rise to resonant Raman spectra and peculiar features in Stokes and anti-Stokes scattering [113].

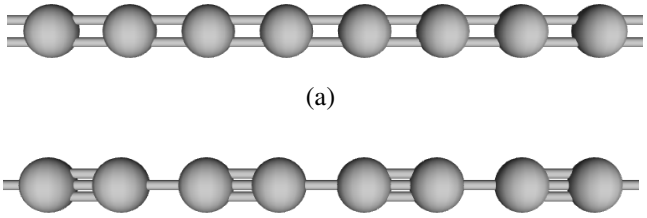

(a)

(b)

Fig. 1.14 1D *sp* carbon allotrope: (a) cumulene, characterized by equidistant carbon atoms with cumulated double bonds; (b) polyyne, characterized by alternating triple and single bonds.

Strictly speaking, a prototypical 1D carbon system is the linear acetylenic carbon or carbyne (Fig. 1.14 (a)) with chemical structure $(=C=C=)_\infty$: it is a linear chain of carbon atoms in the purely *sp* hybridization, linked among them by double bonds. Due to the cumulative presence of double bonds, such system is also called *cumulene*. The existence of cumulene is still controversial [114, 115] and it has been hypothesized that it is present significantly in the interstellar clouds [116, 117]. Indeed, the Mermin-Wagner-Hohenberg [45, 46] prevents the stability of a long-range ordered phase in 1D at finite temperatures due to thermal fluctuations and the Coleman theorem [118] also denies its stability at $T = 0$ K due to quantum fluctuations (i.e. the zero-point motion of atoms [119]). As such, linear chains undergo the Landau-Peierls [41, 43, 120] transition which breaks the long-range order: atoms are no more equally spaced, but we find couples of *sp*-hybridized carbon atoms linked by triple bonds; these units are connected to one another by single bonds giving a chemical structure $(-C \equiv C-)_\infty$ as depicted in Fig. 1.14 (b). Following

chemistry nomenclature, the distorted infinite linear carbon chain takes the name *polyyne*, showing alternating triple and single bonds. While cumulene is metallic and half filled (i.e. with the Fermi level crossing exactly in the middle of a band), polyyne is insulating: indeed, in order to reduce the total energy of the system, the equally spaced atoms get closer and closer forming triply-bonded couples until the minimum of the Free energy is reached and, by doing so, an energy gap is opened in the electronic structure, separating a completely filled band from an empty one [121–124]. As a matter of fact, according to the Landau-Peierls theory, the instability of the metallic cumulenic structure is directly linked to an imaginary longitudinal optical phonon at $2k_F$ (where k_F is the Fermi momentum) which becomes stable by distorting the lattice [125, 126]: therefore, carbyne represents the prototypical example of a charge density wave (CDW) system. Finally, mechanical distortion (i.e. stretching or twisting) can alter the electronic band-gap [127] and can make the system become a magnetic semiconductor [128]. On the other hand, even if polyyne also shows a long-range order due to repeated carbon dimers, it has been synthesized in laboratory and isolated inside carbon nanotubes [129–131].

Due to the light mass of carbon atoms and due to the low dimensionality of such linear systems, zero-point (ZP) lattice motions are particularly relevant. As a matter of fact, the ZP motion of atoms in one-dimensional Peierls systems at $T = 0$ K and their thermal lattice distortion ($T \neq 0$ K) are comparable in magnitude: as a consequence, the electronic band-gap is further reduced and this in principle can be measured in optical experiments as a subgap [132, 133], i.e the absorption peak appears at an energy value smaller than the energy gap. Another consequence of the strong zero point lattice motion, which is a pure quantum effect, combined with the reduced dimensionality is that the harmonic picture is no longer optimal for describing the vibrational properties and anharmonic phonon-phonon interactions have to be taken into account [134, 127].

From the application point of view, the interest in being able to synthesize carbyne first of all lies in its mechanical properties since it is thought to be the strongest material known, with a specific tensile strength of $6.0 - 7.5 \times 10^7$ Nm/kg [128], making it potentially optimal for molecular wires [135]. Indeed diamond has a specific tensile strength of $2.5 - 6.5 \times 10^7$ Nm/kg, graphene has $4.7 - 5.5 \times 10^7$ Nm/kg and carbon nanotubes have $4.3 - 5.0 \times 10^7$ Nm/kg. Moreover, the Young's modulus per density is assumed to be twice as large as that of graphene [128] and the linear acetylenic carbon can be also employed in energy applications as it can

be potentially decorated with other elements such as calcium in order to obtain reversible storage of hydrogen [136]. Relatively long polyyne chains (comprising ~ 6000 atoms) have been observed inside multi-walled carbon nanotubes [129–131]: this has been experimentally confirmed through resonance Raman spectroscopy, as well as transmission electron microscopy and X-ray diffraction. By doing so it was possible to measure the electronic band gap, which were reported in the energy range $E_g \sim [1.848; 2.253]$ eV. However, the measured electronic and optical properties could be affected by the interaction with the CNTs. Nevertheless, while free pure linear carbon chains have still not been synthesized, finite polyyenic systems [137] (e.g. polyacetylene) or end-capped oligoynes [138] (e.g. organometallic polyynes) can be realized in laboratory and therefore the study of their electronic and vibrational properties is fundamental.

The first principle investigation of the electronic and vibrational properties of the linear acetylenic carbon will be the topic of the last chapter of this thesis. We will take into account electron-electron correlation with different degrees of approximations and we will also consider the anharmonic effects of the phonon-phonon interaction self-consistently. Moreover, we will study the free energy profiles as a function of temperature in order to understand the nature of the Peierls phase transition between the cumelene and the polyyne structure.

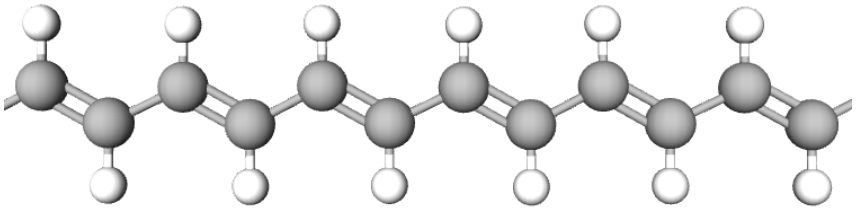

Fig. 1.15 Stick-and-ball structure of polyacetylene $(C_2H_2)_\infty$. Grey (white) balls represent carbon (hydrogen) atoms.

Among the class of 1D carbon system, polyacetylene (Fig. 1.15) is worth being mentioned as it is directly linked to carbyne. This 1D system comes from the polymerization of acetylene $(C_2H_2)_\infty$ and its high conductivity upon doping (discovered first by H. Shirakawa, A. Heeger and A. MacDiarmid [137]) gave rise to the field of organic conducting polymers and organic semiconductors. Moreover, due to the distortion of the carbon bonds, this simple system has proven to be an accurate toy model for correlated electrons as first discussed in 1979 by W. P. Su, J. R. Schrieffer,

and A. J. Heeger [139]. Indeed polyacetylene can support topological excitations (solitons) with fractional charge, a Peierls and a Mott insulating phase and is related to one-dimensional topological insulators [140–143].

1.5 0D: Fullerene

Fullerenes are closed-cage molecules with a spherical or nearly-spherical surface made of a network of quasi-sp^2 hybridized carbon atoms [144]. They were first observed by H. Kroto et al. [145] in 1985 and, subsequently, they were synthesized massively in 1990 by W. Krätschmer et al. [146]. The most famous one is depicted in Fig. 1.16 and it is called Buckminsterfullerene or C_{60}, being made of 60 carbon atoms disposed in twelve pentagonal and twenty hexagonal rings so as to form a truncated icosahedral structure. However, in general a fullerene can be made of n carbon atoms, so that they are generally expressed as C_n. Fullerenes can also incorporate other atoms (i.e. rare earths, alkaline earths or alkali metals) inside the carbon cage, and are therefore called *endohedral*, or they can be functionalized by external adsorption of other molecules, and thus are called *exohedral* [147]. Their application is related to energy storage (e.g. in organic solar cells [148]) or to the biological field (e.g. in drug delivery [149]).

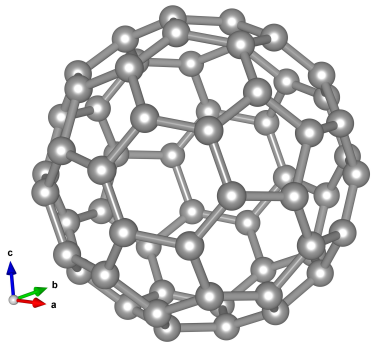

Fig. 1.16 0D quasi-sp^2 carbon allotrope: fullerene.

Since fullerenes are closed-cage molecules, their electronic structure is close to that of an isolated molecule [150]: in this sense, we say that fullerenes are the 0D carbon allotropes. For example in the case of C_{60} narrow bands with a bandwidth of $\sim 0.4 - 0.6$ eV is predicted from DFT computations, with a band gap of ~ 1.5

eV. As in the case of rhombohedral graphene, such flat band can be responsible for strongly correlated states of matter.

As a matter of fact, C_{60}-related materials show high-temperature superconductivity, with a critical temperature $T_c \sim 30$ K in the case of Rb_3C_{60} [151] and $T_c \sim 33$ K in the case of $Rb_xCs_yC_{60}$ [152]. Indeed, it has been shown that the strong electron-electron interaction due to the dispersionless band in doped Fullerenes is responsible for an enhancement of the electron-phonon matrix elements [153] and such characteristic is supposed to be a universal feature of phonon-mediated high-temperature superconductors [154]. Therefore, if suitably engineered in order to enhance the Coulomb boost to the electron-phonon interaction, doped fullerenes could potentially attain transition temperatures of the order of ~ 100 K [155, 156]. The phonon modes which couple more to the electrons are the Jahn-Teller intramolecular ones, however they can also be responsible for another strongly-correlated phase in C_{60} fullerene such as the Mott-Jahn-Teller insulator when the electron-electron interaction is too strong: in this case the on-site Coulomb repulsion block the conduction between molecules, suppressing magnetism and optical excitations [157].

Summary

- Carbon atoms can have three different types of hybridization leading to structures with different geometries and dimensionalities;
- In some allotropes, flat bands can appear in the electronic dispersion relation leading to strongly-correlated phases of matter (i.e. magnetism, high-T_c superconductivity, Mott insulators, etc.);
- The lightness of the carbon atoms together with reduced dimensionality give rise to strong anharmonic effects that can be responsible for the insurgence of charge density waves;

Chapter 2

Electron-Phonon Interactions and Superconductivity

Together with the Coulomb electron-electron interaction, the coupling between the collective motion of atoms in a solid (i.e. phonons) and the electronic degrees of freedom plays an important role on many physical properties. Indeed, it can alter the transport properties (both electrical and thermal) in a metal, while in doped semiconductors it is responsible for the recombination of thermally activated carriers (i.e. their lifetime) and their mobility [158, 159]. In some materials, it can lead to an effective electron-electron attraction at sufficiently low temperatures and this gives rise to the phonon-mediated superconductivity, as first theoretically described by the BCS theory [160]. It can also lead to the instauration of charge density waves [161].

The strength of the interaction can be experimentally investigated. As a matter of fact, the many-body nature of the interaction gives rise to screened electron and phonon quasiparticles which renormalizes many fundamental properties such as the electronic bands (which can be experimentally probed via the angle-resolved photoemission spectroscopy (ARPES) [162]), the vibrational spectra [163] (which can be obtained via neutron spectroscopy or x-ray scattering [164]) and optical absorptions [165–167].

First of all, in this chapter I briefly discuss the Born-Oppenheimer approximation and how both the electron and lattice problem are tackled (Sec. 2.1). Then, I present the many-body formulation of the electron-phonon interaction (Sec. 2.2) and the random phase approximation to the phonon self-energy (Sec. 2.3). Finally,

I will focus on the strong-coupling theory of phonon-mediated superconductivity (Sec. 2.4).

2.1 The Born-Oppenheimer Approximation

Consider electrons moving in a thermally vibrating lattice. Their Hamiltonian is given by:

$$H = H_{ion} + H_{el} + H_{el-ion} \tag{2.1}$$

i.e. it is the sum of a purely ionic, a purely electron and an interaction hamiltonian. The first term is made up of the kinetic energy of the ions and the mutual interactions among them:

$$H_{ion} = \sum_{L,A} \frac{\mathbf{P}_{LA}^2}{2M_A} + V_i(\mathbf{R}) = \sum_{L,A} \frac{\mathbf{P}_{LA}^2}{2M_A} + \frac{e^2}{2} \sum_{L,A \neq M,B} \frac{Z_A Z_B}{|\mathbf{R}_{LA} - \mathbf{R}_{\mathbf{MB}}|} \tag{2.2}$$

where L is the index of the unit cell, A labels atoms inside the unit cell, $\mathbf{P}$ is the ionic momentum, M_A and Z_A are the A-th ionic mass and charge respectively and $\mathbf{R}_{LA}$ is the A-th ionic position inside the L-th unit cell. As for the electronic hamiltonian, it depends only on the electronic coordinates and it is the sum of the electron kinetic energy and the mutual interaction among them:

$$H_{el} = \sum_i \frac{\mathbf{p}_i^2}{2m_e} + V_e(\mathbf{r}) = \sum_i \frac{\mathbf{p}_i^2}{2m_e} + \frac{e^2}{2} \sum_{i \neq j} \frac{1}{|\mathbf{r}_i - \mathbf{r}_j|} \tag{2.3}$$

where i runs over the number of electrons, $\mathbf{p}_i$ and $\mathbf{r}_i$ are respectively the momentum and position of the i-th electron and m_e is the electron mass. Finally, the bare electron-ion hamiltonian is given by:

$$H_{el-ion} = V_{ie}(\mathbf{r}, \mathbf{R}) = -\sum_{i,LA} \frac{Z_A e^2}{|\mathbf{R_{LA}} - \mathbf{r_i}|} \tag{2.4}$$

Since electrons and ions degrees of freedom are coupled to each other, the problem of finding eigenvalues and eigenvectors of Eq. 2.1 is very complicated (or impossible in most cases). However due to the very low inertia of electrons with respect to ions (i.e. $m_e/M \to 0$), the Born-Oppneheimer (or adiabatic) approximation [168] allows us to decouple such problems neglecting the electron-ion

interactions: due to their light mass, electrons move inside a lattice which is frozen, whereas ions follow their motion adiabatically moving in an effective potential due to the faster electrons. As a consequence, the ansatz is that we can expand the complicated crystal wavefunction over a complete set of electronic states evaluated at a frozen-ion configuration:

$$\Psi(\mathbf{r},\mathbf{R}) = \sum_n \Phi_n(\mathbf{R})\phi_n(\mathbf{r};\mathbf{R}) \tag{2.5}$$

where $\Phi_n(\mathbf{R})$ and $\phi_n(\mathbf{r};\mathbf{R})$ are respectively the ionic and electronic part of the wave-function. Notice that, while $\Phi_n(\mathbf{R})$ explicitly depends on the ionic positions, $\phi_n(\mathbf{r};\mathbf{R})$ depends on them only implicitly because it is calculated for a fixed lattice configuration. Then, diagonalizing the crystal hamiltonian with such ansatz for the total wavefunction (i.e. $H\Psi(\mathbf{r},\mathbf{R}) = E\Psi(\mathbf{r},\mathbf{R})$), we obtain two equations, one for the electron and one for the ion parts. In particular, the electronic problem at clamped ions is solved through:

$$\Big[\sum_i \frac{\mathbf{p}_i^2}{2m_e} + V_e(\mathbf{r}) + V_i(\mathbf{R}) + V_{ie}(\mathbf{r},\mathbf{R}) - \varepsilon_n(\mathbf{R})\Big]\phi_n(\mathbf{r};\mathbf{R}) = 0 \tag{2.6}$$

where $\varepsilon_n(\mathbf{R})$ are the eigenvalues of the electron problem at clamped ions. On the other hand, the ionic equation is given by:

$$\Big[\sum_{LA} \frac{\mathbf{P}_{LA}^2}{2M_A} + E(\mathbf{R}) - \xi(\mathbf{R})\Big]\Phi_n(\mathbf{R}) + \sum_m \sum_{LA}\Big[\frac{A_{mn}^{LA}\mathbf{P}_{LA}}{M_A} + \frac{B_{mn}^{LA}}{M_A}\Big]\Phi_m(\mathbf{R}) = 0 \tag{2.7}$$

where $\xi(\mathbf{R})$ are the eigenvalues of the ionic problem and $E(\mathbf{R}) = \langle\phi_n|H_{el} + V_i(\mathbf{R}) + V_{ie}(\mathbf{r},\mathbf{R})|\phi_n\rangle$ is called *Born-Oppenheimer energy surface*, which is the ground state energy at fixed nuclei of the interacting electrons (i.e the lowest $\varepsilon_n(\mathbf{R})$). The last two terms of Eq. 2.7 represent non-diagonal ($n \neq m$) interactions among electrons and ions and can be neglected according to the Born-Oppenheimer approximation:

$$A_{mn}^{LA} = \int d\mathbf{r}\phi_m^*(\mathbf{r};\mathbf{R})\mathbf{P}_{LA}\phi_n(\mathbf{r};\mathbf{R}) \tag{2.8}$$

$$B_{mn}^{LA} = \frac{1}{2}\int d\mathbf{r}\phi_m^*(\mathbf{r};\mathbf{R})\mathbf{P}_{LA}^2\phi_n(\mathbf{r};\mathbf{R}) \tag{2.9}$$

However, while B_{mn}^{LA} represents the *non-linear electron-phonon coupling* term and can (almost) always be neglected, A_{mn}^{LA} represents the *linear electron-phonon coupling*

term and cannot be neglected since it is responsible for many relevant physical phenomena (e.g. conventional superconductivity, the intrinsic resistivity of metals, temperature dependence of band gaps, etc.).

2.1.1 The electron problem

In this work, I will solve the electron problem through the Kohn-Sham (KS) formulation of Density Functional Theory (DFT), which can be applied to any system of interacting particles in an external potential and represents an exact theory of many-body systems.

In 1964, P. Hohenberg and W. Kohn [169] showed that the equilibrium properties of a system of interacting electrons are completely determined solely by its ground-state density $n_0(\mathbf{r})$, which can be retrieved after minimization of an energy functional of the electron density $E[n] = F_{HK}[n] + E_{ext}$: $F_{HK}[n]$ is a universal functional containing the electron kinetic and potential energy and E_{ext} is the energy associated to any external perturbation, such as the potential generated by the lattice, an electric field or a magnetic field.

Even if exact from the theoretical point of view, the original Hohenberg-Kohn formulation of DFT is impractical from the computational point of view. Therefore, in 1965 W. Kohn and L. J. Sham [170] showed that it is possible to map the complicated problem of an interacting electron gas into a simpler non-interacting one with the only restriction that the electronic ground state density has to be the same of the original problem (i.e. $n_{0,\mathrm{HK}} = n_{0,KS}$). With this ansatz they obtained a set of independent particle equations to be solved self-consistently:

$$H_{KS}\phi_n(\mathbf{r};\mathbf{R}) = \left[\sum_i \frac{\mathbf{p}_i^2}{2m_e} + V_{KS}(\mathbf{r};\mathbf{R})\right]\phi_n(\mathbf{r};\mathbf{R}) = \varepsilon_n^0(\mathbf{R})\phi_n(\mathbf{r};\mathbf{R}) \tag{2.10}$$

$$V_{KS}(\mathbf{r};\mathbf{R}) = V_{ext}(\mathbf{r};\mathbf{R}) + V_{\mathrm{Hartree}}(\mathbf{r}) + V_{XC}(\mathbf{r}) \tag{2.11}$$

$$n(\mathbf{r};\mathbf{R}) = 2\sum_i |\phi_n(\mathbf{r};\mathbf{R})|^2 \tag{2.12}$$

where $V_{KS}(\mathbf{r};\mathbf{R})$ is the Kohn-Sham potential, $\varepsilon_n^0(\mathbf{R})$ and $\phi_n(\mathbf{r};\mathbf{R})$ are the Kohn-Sham eigenvalues and eigenvectors respectively, $V_{\mathrm{Hartree}}(\mathbf{r})$ is the classical electrostatic repulsion between independent electrons and $V_{XC}(\mathbf{r})$ contains all of the complicated correlation effects of the original interacting electron gas and it is called *exchange-*

correlation potential. Notice that these equations are free of any approximation and, therefore, are exact: if the exchange-correlation functional (and consequently the exchange-correlation potential) was known, these equations would lead to the exact ground state density. However, from the practical point of view, it is impossible to know its exact analytical form therefore approximations are made (e.g. LDA, GGA, hybrid functionals, etc.). Finally, we recall that any other perturbation to the electronic gas (such as the lattice potential, an external electric or magnetic field, etc.) is taken into account through the external potential $V_{ext}(\mathbf{r};\mathbf{R})$.

2.1.2 The lattice problem

Once we have solved the electron problem, we can turn our attention to the thermally vibrating lattice. We will neglect the non-diagonal term of Eq. 2.7 and we will also employ the harmonic approximation, i.e. we will expand the Born-Oppnheimer energy surface $E(\mathbf{R})$ up to the second order.

Consider a periodic lattice made of N unit cells and N_{at} atoms in the unit cell, such that the position of the I-th atom is given by:

$$\mathbf{R}_{LA} = \mathbf{R}_L + \boldsymbol{\tau}_A \tag{2.13}$$

with $\mathbf{R}_L$ the position of the L-th unit cell ($L = 1,\dots,N$) and $\boldsymbol{\tau}_A$ is the position of the A-th atom inside the cell ($A = 1,\dots,N_{at}$). The ionic position at equilibrium ($\mathbf{R}^0_{LA}$) are found for vanishing interatomic forces:

$$\mathbf{F}_{LA} = -\left.\frac{\partial E(\mathbf{R})}{\partial \mathbf{R}_{LA}}\right|_{\mathbf{R}_{LA}=\mathbf{R}^0_{LA}} = 0 \quad \forall\{L,A\} \tag{2.14}$$

Then, if we allow atoms to slightly displace from their equilibrium position (i.e. $\mathbf{R}_{LA} = \mathbf{R}^0_{LA} + \mathbf{u}_{LA}(t)$, where $\mathbf{u}_{LA}(t)$ is the time-dependent ion displacement), we can Taylor-expand the BO energy surface up to the second order (harmonic approximation):

$$\begin{aligned} E(\mathbf{R}) &= E(\mathbf{R}^0) + \frac{1}{2}\sum_{LA\alpha}\sum_{MB\beta} C_{A\alpha,B\beta}(\mathbf{R}_L,\mathbf{R}_M)u_{LA\alpha}u_{MB\beta} + O(u^3) = \\ &= E(\mathbf{R}^0) + \frac{1}{2}\sum_{LA\alpha}\sum_{MB\beta} \sqrt{M_A M_B} D_{A\alpha,B\beta}(\mathbf{R}_L,\mathbf{R}_M)u_{LA\alpha}u_{MB\beta} + O(u^3) \end{aligned} \tag{2.15}$$

where $\alpha = x, y, z$ is the label for cartesian coordinates and we have omitted the time dependence of the ion displacement.

We have here defined the *force constant matrix* as:

$$C_{A\alpha,B\beta}(\mathbf{R}_L, \mathbf{R}_M) = \frac{\partial^2 E}{\partial u_{LA\alpha} \partial u_{MB\beta}} \tag{2.16}$$

and the *dynamical matrix* as:

$$D_{A\alpha,B\beta}(\mathbf{R}_L, \mathbf{R}_M) = \frac{C_{A\alpha,B\beta}(\mathbf{R}_L, \mathbf{R}_M)}{\sqrt{M_A M_B}} \tag{2.17}$$

Notice that, thanks to the translational invariance property of the crystal we can write $C_{A\alpha,B\beta}(\mathbf{R}_L - \mathbf{R}_M)$ and we can set, without loss of generality, $\mathbf{R}_M = 0$. Moreover, we are neglecting the anharmonic terms that, as we will see later on in this work, can have a drastic impact on the dynamical properties of the system and, as an example, are responsible for thermal expansion of solids or phonon lifetimes.

The Fourier transform of the force constant matrix is defined as $C_{A\alpha,B\beta}(\mathbf{q}) = \sum_L C_{A\alpha,B\beta}(\mathbf{R}_L) e^{-i\mathbf{q}\cdot\mathbf{R}_L}$. Then diagonalizing the dynamical matrix in reciprocal space, we can obtain its eigenvalues (i.e. the screened phonon frequencies, $\omega_{\mathbf{q}\nu}$) and its eigenvectors (i.e. the phonon polarizations, $\mathbf{e}_{\mathbf{q},\nu}$) for each phonon momentum $\mathbf{q}$:

$$\det\left| D_{A\alpha,B\beta}(\mathbf{q}) - \omega_{\mathbf{q}\nu} \mathbb{I} \right| = 0 \tag{2.18}$$

where the index $\mu = 1, \ldots, 3N_{at}$ is the phonon branch index. Moreover, ionic displacements and phonon polarizations (that give information on the atoms movement pattern) are linked by:

$$u_{LA\alpha} = \sum_q \frac{e^{i\mathbf{q}\cdot\mathbf{R}_L}}{\sqrt{M_A}} (e^{A\alpha}_{\mathbf{q}\nu})^* \mathbf{e}_{\mathbf{q}\nu} \tag{2.19}$$

The force constant matrix can be computed within linear response theory [171].

In the framework of plane-wave density functional theory [172] they can be written as:

$$C_{A\alpha,B\beta}(\mathbf{R}_L;T) = 2\sum_{\mathbf{k}j,\mathbf{k}'j'}^{N_k(T)} \frac{(f_{\mathbf{k}j}(T)-f_{\mathbf{k}'j'}(T))}{\varepsilon^0_{\mathbf{k}j}-\varepsilon^0_{\mathbf{k}'j'}+i\eta} \left\langle \mathbf{k}'j' \right| \frac{\delta V_{KS}(\mathbf{r};\mathbf{R})}{\delta \mathbf{u}_{LA}} \left|\mathbf{k}i\right\rangle \left\langle \mathbf{k}i \right| \frac{\delta V_{ext}(\mathbf{r};\mathbf{R})}{\delta \mathbf{u}_{0B}} \left|\mathbf{k}'j'\right\rangle + \int d\mathbf{r} n_0(\mathbf{r};\mathbf{R}) \frac{\delta^2 V_{ext}(\mathbf{r};\mathbf{R})}{\delta \mathbf{u}_{LA}\delta \mathbf{u}_{0B}} \tag{2.20}$$

where the factor 2 accounts for spin degeneracy, $\mathbf{k},\mathbf{k}'$ are the electron momenta, j,j' are the band indices, T is the electronic temperature, $f_{\mathbf{k}j}(T)$ is the Fermi distribution, $\eta \to 0^+$ and $N_k(T)$ is the number of k-points summed at a temperature T (which is a number to be converged numerically). Finally $|\mathbf{k}j\rangle$ is the Bloch-periodic part of the Kohn-Sham eigenfunction. This formulation is the one which is typically implemented in codes making use of density functional perturbation theory (DFPT) [172].

At the same time, the linear electron-phonon matrix elements in a DFPT framework represent the scattering of an electron from a state with momentum $\mathbf{k}$ to a state with momentum $\mathbf{k}\pm\mathbf{q}$ through absorption (emission) of a phonon of momentum $\mathbf{q}$ $(-\mathbf{q})$ and screened frequency $\omega_{\mathbf{q}\nu}$ and describe the interaction strength between electrons and phonons. They are defined as:

$$g^{\nu}_{\mathbf{k}j,\mathbf{k}\pm\mathbf{q}j'} = \sum_{A\alpha} \sqrt{\frac{\hbar}{2M_A\omega^0_{\mathbf{q}\nu}}} e^{A\alpha}_{\mathbf{q}\nu} \left\langle \mathbf{k}j \right| \frac{\delta v_{\mathrm{KS}}}{\delta u^{\mathbf{q}}_{A\alpha}} \left| j'\mathbf{k}\pm\mathbf{q} \right\rangle \tag{2.21}$$

where $v_{KS} = e^{-i\mathbf{q}\cdot\mathbf{r}}V_{KS}$ is the periodic part of the Kohn-Sham potential, $u^{\mathbf{q}}_{A\alpha}$ denotes the Fourier-transformed displacement of atom A of mass M_A along the cartesian coordinate $\alpha = \{x,y.z\}$, normalized on the unit cell.

2.2 Many-body treatment of the electron-phonon interaction

On the basis of the Kohn-Sham wavefunctions, the electron-phonon hamiltonian In the second-quatized form corresponds to the Frölich hamiltonian [173]:

$$\begin{aligned}\hat{H}_{\text{tot}} &= \hat{H}_{\text{KS}} + \hat{H}_{\text{ph}} + \hat{H}_{\text{el-ph}} = \\ &= \sum_{\mathbf{k}j\sigma} \varepsilon^0_{\mathbf{k}j} c^\dagger_{\mathbf{k}j\sigma} c_{\mathbf{k}j\sigma} + \sum_{\mathbf{q}\nu} \hbar\omega^0_{\mathbf{q}\nu} \left(b^\dagger_{\mathbf{q}\nu} b_{\mathbf{q}\nu} + \frac{1}{2} \right) \\ &+ \sum_{\mathbf{k}jj'\sigma} \sum_{\mathbf{q}\nu} g^\nu_{\mathbf{k}j,\mathbf{k}+\mathbf{q}j'} c^\dagger_{\mathbf{k}j\sigma} c_{\mathbf{k}+\mathbf{q}j'\sigma} \left[b_{\mathbf{q}\nu} + b^\dagger_{-\mathbf{q}\nu} \right]\end{aligned} \tag{2.22}$$

where $c^\dagger_{\mathbf{k}j\sigma}$ ($c_{\mathbf{k}j\sigma}$) is the creation (destruction) operator for a fermion of spin $\sigma = \{\uparrow,\downarrow\}$ at band j and momentum $\mathbf{k}$ with energy $\varepsilon^0_{\mathbf{k}j}$ (i.e the Kohn-Sham eigenvalue measured with respect to the chemical potential, which is the Fermi level E_F at $T = 0$ K), while $b^\dagger_{\mathbf{q}\nu}$ ($b_{\mathbf{q}\nu}$) is the creation (destruction) operator for a phonon of unscreened frequency $\omega^0_{\mathbf{q}\nu}$ at mode ν and momentum $\mathbf{q}$.

We now group the momentum and band indices for the electron $k = (\mathbf{k}, j)$, while for the phonon we group the momentum and mode indices $q = (\mathbf{q}, \nu)$. In order to understand how observables are renormalized by the electron-phonon interaction we need to find a way to compute the screened quasiparticles. In order to do so, we follow the imaginary-time Matsubara approach [174] and we define an imaginary time variable $-\hbar\beta < \tau < \hbar\beta$, with $\beta = 1/k_B T$ (k_B is the Boltzmann constant). The exact (or interacting) single-particle temperature Green's functions for the electrons, $\mathcal{G}(k, \omega_n)$, and phonons, $\mathcal{D}(q, \nu_n)$, are defined as [175, 176]:

$$\mathcal{G}(k,\tau) = -\langle T_\tau c_{k\sigma}(\tau) c^\dagger_{k\sigma}(0) \rangle \tag{2.23a}$$

$$\mathcal{D}(q,\tau) = -\langle T_\tau (b_q(\tau) + b^\dagger_{-q}(\tau))(b_{-q}(0) + b^\dagger_q(0)) \rangle \tag{2.23b}$$

where T_τ is the time-ordering Wick's operator, which orders field operators by keeping on the left the highest τ. The time-dependence of the operators is obtained in the Heisenberg picture: $\Psi_{\mathbf{k}}(\tau) = e^{\hat{K}\tau} \Psi_{\mathbf{k}} e^{-\hat{K}\tau}$, where $\hat{K} = \hat{H} - \mu\hat{N}$ is the Grand-canonical hamiltonian, $\hat{H}$ is the normal hamiltonian, μ is the chemical potential and $\hat{N}$ is the particle number operator. We are assuming that the electron-phonon

interaction doesn't mix spin components: as a consequence, the electron Green's function will be diagonal in the spin indices and we can suppress them. The expected value is to be performed in a Grand-canonical ensemble, that is:

$$\langle \hat{O} \rangle = \mathrm{Tr}\{\hat{\rho}_G \hat{O}\} \tag{2.24}$$

where the statistical operator $\hat{\rho}_G$ is defined as $\hat{\rho}_G = e^{-\beta \hat{K}}/Z_G$ and the Grand-canonical partition function is given by $Z_G = e^{-\beta\Omega} = Tr\{e^{-\beta \hat{K}}\}$, where Ω is the Grand-potential and the trace runs over states with all values of N.

Both the electron and phonon Matsubara's Green functions are periodic with period 2β and may be expanded in Fourier series:

$$\mathcal{G}(k,\tau) = \frac{1}{\hbar\beta}\sum_n e^{-i\omega_n\tau}\mathcal{G}(k,i\omega_n) \qquad \omega_n = (2n+1)\pi/\beta\hbar \tag{2.25a}$$

$$\mathcal{D}(q,\tau) = \frac{1}{\hbar\beta}\sum_n e^{-i\nu_n\tau}\mathcal{D}(q,i\nu_n) \qquad \nu_n = 2n\pi/\beta\hbar \tag{2.25b}$$

where ω_n (ν_n) are discrete odd (even) Matsubara's frequencies and the Fourier coefficients are given by:

$$\mathcal{G}(k,i\omega_n) = \tfrac{1}{2}\textstyle\int_{-\hbar\beta}^{+\hbar\beta} d\tau e^{i\omega_n\tau}\mathcal{G}(k,\tau) \tag{2.26a}$$

$$\mathcal{D}(q,i\nu_n) = \tfrac{1}{2}\textstyle\int_{-\hbar\beta}^{+\hbar\beta} d\tau e^{i\nu_n\tau}\mathcal{D}(q,\tau) \tag{2.26b}$$

The Feynman-Dyson many-body perturbation theory [177, 178] gives a practical way to compute the exact Green's function via the formal summation of infinite diagrams, which is accomplished by the Dyson equation:

$$\mathcal{G}^{-1}(k,i\omega_n) = [\mathcal{G}^0(k,i\omega_n)]^{-1} - \Sigma(k,i\omega_n) \tag{2.27a}$$

$$\mathcal{D}^{-1}(q,i\nu_n) = [\mathcal{D}^0(q,i\nu_n)]^{-1} - \Pi(q,i\nu_n) \tag{2.27b}$$

where $\Sigma(k,i\omega_n)$ is the irreducible band-resolved total electron self-energy and $\Pi(q,i\nu_n)$ is the irreducible mode-resolved phonon self-energy. The free (or non-interacting) Green's functions for the electrons, $\mathcal{G}^0(k,i\omega_n)$, and phonons, $\mathcal{D}^0(q,i\nu_n)$, are computed using the non-interacting hamiltonian $\hat{H}_0 = \hat{H}_{\mathrm{KS}} + \hat{H}_{\mathrm{ph}}$ and Eq. 2.23

and are given by:

$$\mathcal{G}^0(k,i\omega_n) = \frac{1}{i\omega_n - \varepsilon_k^0/\hbar} \qquad \omega_n = (2n+1)\pi/\beta\hbar \tag{2.28a}$$

$$\mathcal{D}^0(q,i\nu_n) = \frac{2\omega_q^0}{(i\nu_n^2) - (\omega_q^0)^2} \qquad \nu_n = 2n\pi/\beta\hbar \tag{2.28b}$$

Hereafter, we will set $\hbar = 1$ for lightness of the equation. The electron-phonon contribution to the irreducible electron self-energy ($\Sigma_{ep}(k,i\omega_n)$), the irreducible phonon self-energy and the proper electron-phonon vertex function ($\mathcal{J}(k,q;i\omega_n,i\nu_m)$),whose diagrams are shown in Fig. 2.1, can be written as [179, 180]:

$$\Sigma_{ep}(k,i\omega_n) = -\frac{1}{\beta N_q}\sum_{q,\nu,m} g^{\nu}_{\mathbf{k}j,\mathbf{k}-\mathbf{q}j'}\mathcal{D}(q,i\nu_m)\mathcal{G}(k-q,i\omega_n-i\nu_m)\cdot \\ \cdot\mathcal{J}(k,q;i\omega_n,i\nu_m) \tag{2.29a}$$

$$\Pi(q,i\nu_n) = \frac{2}{\beta N_k}\sum_{k,m} g^{\nu}_{\mathbf{k}j,\mathbf{k}-\mathbf{q}j'}\mathcal{G}(k,i\omega_m)\mathcal{G}(k-q,i\omega_m-i\nu_n)\cdot \\ \cdot\mathcal{J}(k,k-q;i\omega_m,i\omega_m-i\nu_n) \tag{2.29b}$$

$$\mathcal{J}(k,q;i\omega_n,i\nu_m) = g^{\nu}_{\mathbf{k}-\mathbf{q}j',\mathbf{k}j}\left[1+\mathcal{J}^{(1)}(k,q;i\omega_n,i\nu_m)+\ldots\right] \tag{2.29c}$$

$\mathcal{J}^{(1)}(k,q;i\omega_n,i\nu_m)$ denotes the first-order vertex correction and, using Feynman diagrams (Fig. 2.2), can be computed as:

$$g^{\nu}_{\mathbf{k}-\mathbf{q}j',\mathbf{k}j}\mathcal{J}^{(1)}(k,q;i\omega_n,i\nu_m) = -\frac{1}{\beta N_p}\sum_{p,l}\sum_{\nu',y,y'} g^{\nu}_{\mathbf{k}-\mathbf{q}-\mathbf{p}y,\mathbf{k}-\mathbf{p}y'}\cdot \\ \cdot\mathcal{G}(k-q-p,i\omega_n-i\nu_m-i\nu_l)\mathcal{G}(k-p,i\omega_n-i\nu_l)\cdot \\ \cdot g^{\nu'}_{\mathbf{k}-\mathbf{q}j',\mathbf{k}-\mathbf{q}-\mathbf{p}y'}\mathcal{D}(p,i\nu_l)g^{\nu'}_{\mathbf{k}-\mathbf{p}y,\mathbf{k}j}\Big]$$

where ν' and $\{y,y'\}$ are, respectively, the internal mode and band indices, while p and $i\nu_n$ are the internal momentum and Matsubara's frequency.

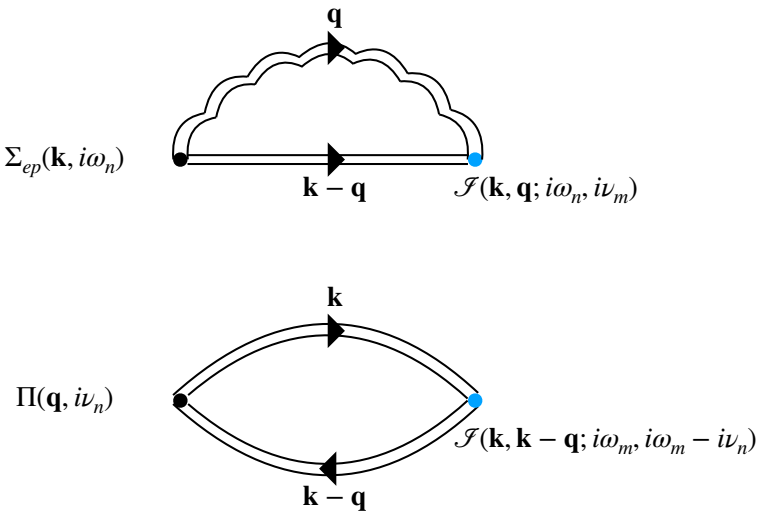

.

Fig. 2.1 Electron-phonon contribution to the electron self-energy ($\Sigma_{ep}(k, i\omega_n)$) and phonon self-energy ($\Pi(q, i\nu_n)$). The solid double straight black lines denotes the exact single-particle temperature Green's functions for the electrons ($\mathcal{G}(k, i\omega_n)$), while the solid double wiggle black lines stands for the exact single-particle temperature Green's functions for phonons ($\mathcal{D}(q, i\nu_n)$). The blue circle denotes the electron-phonon vertex function ($\mathcal{J}(k, q; i\omega_n, i\nu_m)$). The black dots correspond to the zero-order correction for the electron-phonon vertex function ($\mathcal{J}^{(0)}(k, q; i\omega_n, i\nu_m)$).

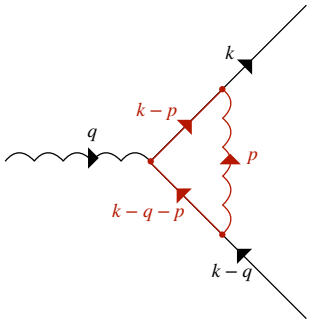

.

Fig. 2.2 First-order vertex correction (highlighted in red) $\mathcal{J}^{(1)}(k, q; i\omega_n, i\nu_m)$. Solid straight lines denotes the single-particle temperature Green's function for the electrons ($\mathcal{G}(k, i\omega_n)$) and wiggle solid lines stands the single-particle temperature Green's functions for phonons ($\mathcal{D}(q, i\nu_n)$). The black and red dots correspond to the zero-order correction for the electron-phonon vertex function ($\mathcal{J}^{(0)}(k, q; i\omega_n, i\nu_m)$).

According to Migdal's theorem [181], the first-order vertex correction contributes with a factor of order $\sim O[(m_e/M_A)^{1/2}]$ for electrons in a normal metal, that is it depends on the ratio between the electron mass m_e and the atom mass M_A. As a consequence, for systems with sufficiently high atomic mass we can consider only the zero-order term in Eq. 2.29 (c): $\mathcal{J}(k,q;i\omega_n,i\nu_m) = g^{\nu}_{\mathbf{k}-\mathbf{q}j',\mathbf{k}j}$ and the blue dots in Fig. 2.1 can be replaced by simple black dots. Migdal's theorem is valid only when $\omega_D/E_F << 1$, i.e. when the ratio between the typical phonon energy (represented by the Debye frequency ω_D) and the typical electron energy at the Fermi level (i.e E_F) is small. This criterion is violated for small phonon momenta, for one-dimensional materials [182], for highly anharmonic systems or in the presence of van Hove singularities [183].

From the knowledge of the exact Green's functions we can retrieve the Grand-potential Ω, from which we can obtain the equilibrium thermodynamic properties of our systems by means of statistical mechanics. Moreover, according to a finite temperature generalization of the Lehmann representation of Green's functions [184], we can also get information on energies and lifetimes of excited states by analitically continuing the exact Green's functions from the imaginary axis to the real axis (i.e. $i\omega_n \to \varepsilon_k + i\delta$ and $i\nu_n \to \omega_q + i\delta$ with $\delta \to 0^+$) and then looking for their poles.

As a consequence, for the electrons (phonons) we can write $\varepsilon_k = \tilde{\varepsilon}_k - i/2\Gamma_k$ ($\omega_q = \tilde{\omega}_q - i/2\gamma_q$) [185, 182]:

$$\begin{cases} \tilde{\varepsilon}_k = \varepsilon_k^0 + \mathfrak{Re}\{\Sigma_{ep}(k,\tilde{\varepsilon}_k)\} \\ 1/2\Gamma_k = -\mathfrak{Im}\{\Sigma_{ep}(k,\tilde{\varepsilon}_k)\} \end{cases} \tag{2.30a}$$

$$\begin{cases} \tilde{\omega}_q^2 = (\omega_q^0)^2 + 2\omega_q^0 \mathfrak{Re}\{\Pi(k,\tilde{\omega}_q)\} \\ 1/2\gamma_q = -\mathfrak{Im}\{\Pi(q,\tilde{\omega}_q)\} \end{cases} \tag{2.30b}$$

provided that the (full width at half maximum) linewidths are sufficiently small with respect to the time variable, i.e. $|\tau|\Gamma_k \lesssim 1$ ($|\tau|\gamma_q \lesssim 1$). In order to experimentally study the strength of the coupling between electrons and phonons in proximity of the Fermi energy (we set $E_F = 0$) we define the mass-enhancement parameter [185, 182]:

$$\lambda_k = -\left.\frac{\partial \mathfrak{Re}\{\Sigma_{ep}(k,\tilde{\varepsilon}_k)\}}{\partial \varepsilon_k}\right|_{\varepsilon_{k=0}} \tag{2.31}$$

which renormalizes the Fermi velocity $\tilde{v}_f = v_f/(1+\lambda_k)$ (thus implying a renormalized electron mass $\tilde{m}_e = m_e(1+\lambda_k)$), whose effect can be observed by means of ARPES measurements.

2.3 The Random Phase Approximation to the phonon propagator

We now assume that Migdal's theorem is valid. We want to evaluate the exact phonon propagator $\mathcal{D}(q, i\nu_n)$, from whose poles we can obtain the dressed phonon frequencies. In order to do so we can recognize that the phonon-exchange mechanism between two electrons can be mapped onto an effective spin-independent electron-electron interaction (Fig. 2.3). Indeed the analytic continuation of the phonon self-energy onto the positive real axis ($i\nu_n \to \omega_q + i\delta$, $\delta \to 0^+$), i.e. the retarded phonon self-energy $\bar{\Pi}^R(q,\omega_q)$, can be viewed as a polarization of the medium due to the interaction between electrons and the collective motion of the lattice:

$$\bar{U}^R(k,q,\omega_q) = \left|g^{\nu}_{\mathbf{k}j,\mathbf{k}-\mathbf{q}j'}\right|^2 \bar{D}^R(q,\omega_q) = \left|g^{\nu}_{\mathbf{k}j,\mathbf{k}-\mathbf{q}j'}\right|^2 \frac{\bar{D}^{0,R}(q,\omega_q)}{1-\bar{D}^{0,R}(q,\omega_q)\bar{\Pi}^R(q,\omega_q)} \tag{2.32}$$

where $\bar{D}^R(q,\omega_q)$ ($\bar{D}^{0,R}(q,\omega_q)$) is the retarded exact (free) phonon propagator and $\bar{U}^R(k,q,\omega_q)$ is the effective electron-phonon interaction. Here we have implicitly assumed that $g^{\nu}_{\mathbf{k}j,\mathbf{k}-\mathbf{q}j'} = g^{\nu}_{\mathbf{k}j,\mathbf{k}+\mathbf{q}j'}$.

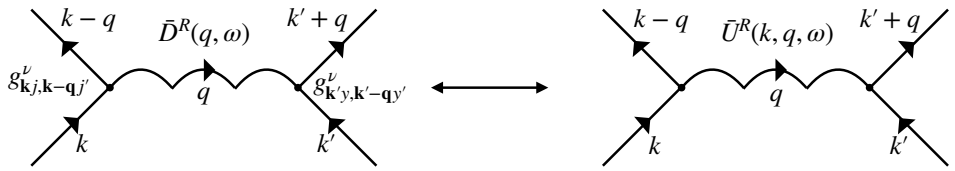

Fig. 2.3 Mapping of the electron-phonon interaction onto the effective electron-electron interaction. $\bar{D}^R(q,\omega)$ ($\bar{U}^R(k,q,\omega)$) is the retarded phonon propagator (effective electron-electron interaction).

Therefore we just need to evaluate the phonon self-energy and then analytically continue it. The lowest order contributions to $\Pi(q,i\nu_n)$, i.e. $\Pi^{(0)}(q,i\nu_n)$, is shown in Fig. 2.4 (a), which is obtained by simply substituting the exact electron Green's

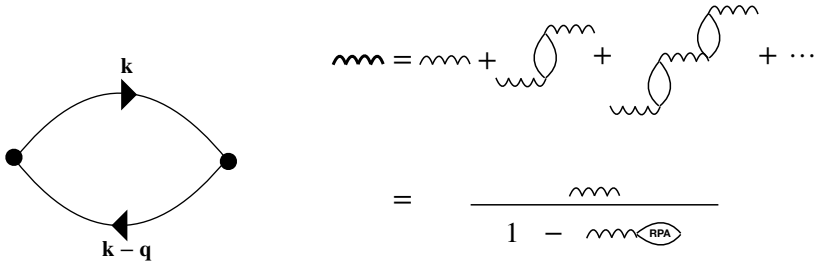

(a) (b)

Fig. 2.4 (a) Lowest order contribution to the phonon self-energy, $\Pi^{(0)}(q, i\nu_n)$: the *bubble* or *ring* diagram; (b) Random phase approximation of the effective electron-electron interaction. Thick black wiggle line represents the exact phonon propagator, while light black straight (wiggle) line represents the free electron (phonon) Green's function.

functions with their free-particle counterpart. They are called *bubble* or *ring* diagrams. The summation of ring diagrams represents the random phase approximation (RPA) to the polarization of the medium and the effective electron-electron interaction (compare Fig. 2.3 with Fig. 2.4 (b)), as explained before, and in Eq. 2.32 this corresponds to set $\bar{\Pi}^{R}(q, \omega_q + i\delta) = \bar{\Pi}^{0,R}(q, \omega_q + i\delta)$.

Therefore, the analytic continuation of the RPA phonon self-energy can be computed as:

$$\begin{aligned}\bar{\Pi}^{0,R}(q, \omega_q + i\delta) &= \frac{2}{N_k}\sum_k \left|g^{\nu}_{\mathbf{k}j,\mathbf{k}-\mathbf{q}j'}\right|^2 \frac{1}{\beta}\sum_m \mathcal{G}^0(k, i\omega_m)\mathcal{G}^0[k-q, i\omega_m - (\omega_q + i\delta)] \\ &= -\frac{2}{N_k}\sum_k \left|g^{\nu}_{\mathbf{k}j,\mathbf{k}-\mathbf{q}j'}\right|^2 \frac{f(\varepsilon_{k-q}) - f(\varepsilon_k)}{\omega_q - (\varepsilon^0_{k-q} - \varepsilon^0_k) + i\delta}\end{aligned} \tag{2.33}$$

where $f(\varepsilon_k) = \{\exp(\beta\varepsilon_k) + 1\}^{-1}$ is the Fermi-Dirac distribution, which tends to the step-function $\Theta(k_F - |k|)$ as $T \to 0$.

The phonon linewidth (i.e. the imaginary part of the phonon self-energy) in the RPA approximation is given by:

$$\begin{aligned}\gamma_q^{-1} &= -2\Im\mathfrak{m}\{\bar{\Pi}^{0,R}(q, \omega_q + i\delta)\} = \\ &= \frac{2\pi}{N_k}\sum_k \left|g^{\nu}_{\mathbf{k}j,\mathbf{k}-\mathbf{q}j'}\right|^2 (f(\varepsilon_{k-q}) - f(\varepsilon_k))\delta[\omega_q + (\varepsilon^0_{k-q} - \varepsilon^0_k)]\end{aligned} \tag{2.34}$$

Usually phonon energies are small when compared to the electronic ones (i.e. $\omega_q << \varepsilon_k$), therefore $\varepsilon^0_{k-q} - \varepsilon^0_k \approx \omega_q$ and $f(\varepsilon_{k-q}) - f(\varepsilon_k) \to \frac{\partial f(\varepsilon_k)}{\partial \varepsilon}$, which tends to $\frac{\partial f}{\partial \varepsilon} \to -\delta(\varepsilon_k)$ as $T \to 0$ K. Therefore [164]:

$$\gamma_q^{-1} = \frac{2\pi\omega_q}{N_k} \sum_k \left| g^{\nu}_{\mathbf{k}j,\mathbf{k}-\mathbf{q}j'} \right|^2 \delta(\varepsilon_k)\delta(\varepsilon_{k-q}) \tag{2.35}$$

and from this we can see that the imaginary part of the phonon self-energy is directly related to the strength of the electron-phonon matrix elements, which can be measured from x-ray or inelastic neutron spectroscopy.

On the other hand, from Eq. 2.33, if we now make the assumption of constant electron-phonon matrix elements and we consider a single mode ν (i.e. $\left| g^{\nu}_{\mathbf{k}j,\mathbf{k}-\mathbf{q}j'} \right|^2 = g^2$), we can recognize the Lindhard function [186], i.e the density-density response function of a homogeneous electron-gas:

$$\chi_0(\mathbf{q},\omega) = \frac{1}{N_k} \sum_k \frac{f(\varepsilon_{k-q}) - f(\varepsilon_k)}{\omega_q - (\varepsilon^0_{k-q} - \varepsilon^0_k) + i\delta} \tag{2.36}$$

This approximation is rather rough, nevertheless it provides a useful model to understand how the phonon self-energy affects the dynamical properties of the lattice. In the parabolic band approximation ($\varepsilon^0_k = \hbar^2 k^2 / 2m_e$) and in its staticl limit ($\omega = 0$), the Lindhard function is purely real and shows a divergency at $|\mathbf{q}| = 2k_F$ (i.e. where we have perfect nesting of the Fermi surface) as it is shown in Fig 2.5 (a)[187]. In particular, in the 3D and 2D cases we have a divergence in its first derivative, while in 1D the divergence appears in $\chi_0(\mathbf{q},0)$. Such singularities are responsible for the origin of the Kohn anomaly [163] in the phonon dispersion relation (that is a change in the slope of the phonon branches as a function of $\mathbf{q}$) and to the spontaneous appearance of a charge density wave (CDW) with the subsequent deformation of the lattice as suggested by Peierls [120] (Fig 2.5 (b)). As we will show in the last chapter of this work, this interpretation of the charge density wave instability as a purely electron-phonon effect is not completely correct: indeed both the electron-phonon and the electron-electron interactions are required, together with the anharmonic phonon-phonon interactions.

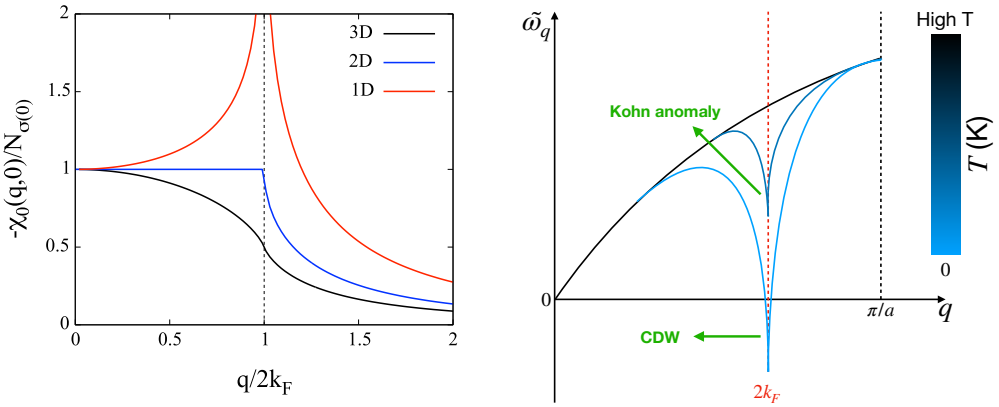

Fig. 2.5 (a) Negative normalized static Lindhard function $-\chi_0(\mathbf{q},0)/N_\sigma(0)$ as a function of the phonon momentum $\mathbf{q}$ for 3D, 2D and 1D systems at $T = 0K$. $N_\sigma(0)$ is the total electron density of states per spin at the Fermi level ($E_F = 0$); (b) Screened phonon frequency ($\tilde{\omega}_q$) for a 1D chain as a function of the electronic temperature (T): at $q = 2k_F$ the system develops first a Kohn anomaly and then a negative frequency that corresponds to a distortion of the lattice (i.e. a charge density wave, CDW).

When we consider the full frequency dependence of the Lindhard function, it acquires a complex structure: $\chi_0(\mathbf{q},\omega) = \mathfrak{Re}\{\chi_0(\mathbf{q},\omega)\} + i\mathfrak{Im}\{\chi_0(\mathbf{q},\omega)\}$. The imaginary part will be different from zero only in a limited part of the $(|\mathbf{q}|,\omega)$-plane, which is called the electron-hole continuum (Fig. 2.6) that depends on the shape of the Fermi surface and on the dimensionality of the system. This range of frequencies describes the possible excitation energies of the electron gas for a selected $\mathbf{q}$ vector: in this regions the collective excitations (i.e the plasmons or the electron-hole excitations) acquire a lifetime (i.e. an imaginary part) and are damped in time.

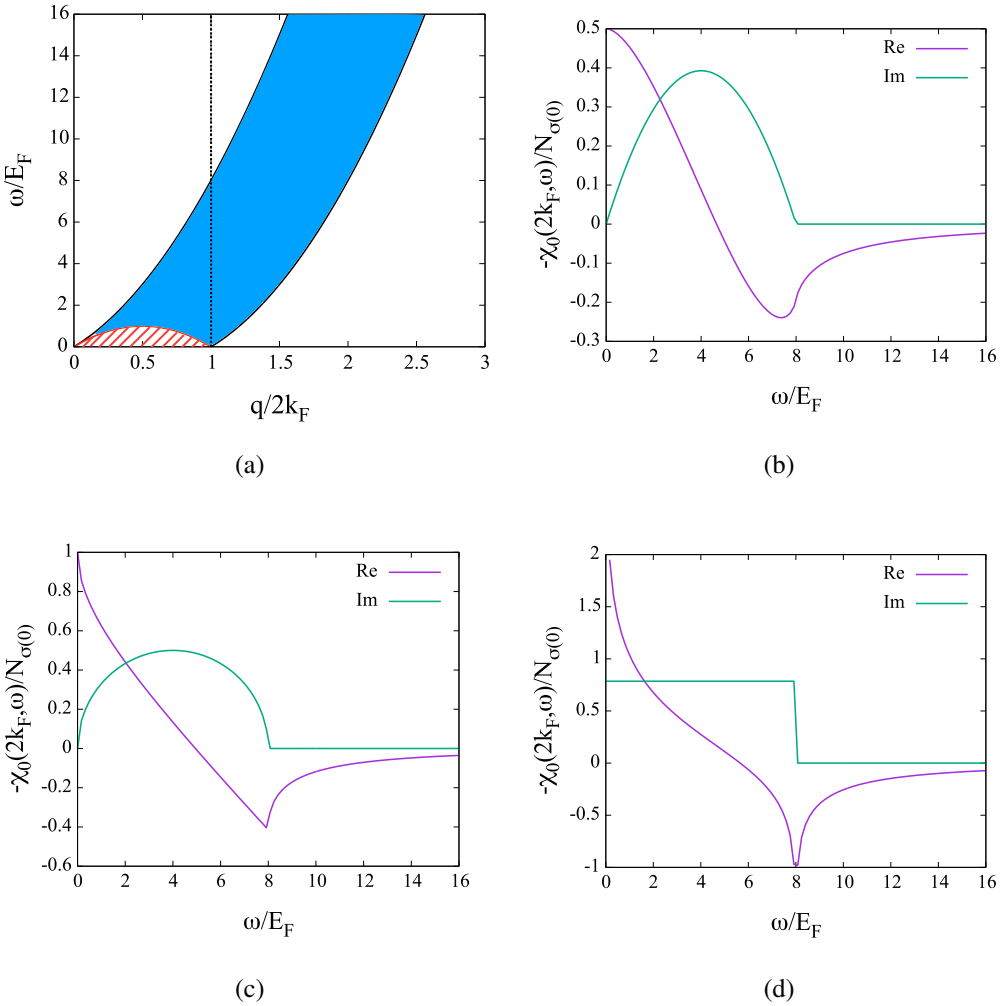

Fig. 2.6 (a) The blu shaded region plus the red dashed part of the graph depict the electron-hole continuum in the 3D and 2D case, while the latter is not present for a 1D system; Real and imaginary parts of the negative normalized dynamical Lindhard function evaluated for $q = 2k_F$, i.e. $-\chi_0(\mathbf{q},\omega)/N_\sigma(0)$, as a function of the frequency ω for (b) 3D, (c) 2D and (d) 1D system at $T = 0K$.

2.4 Imaginary-axis Migdal-Eliashberg theory of superconductivity

For electrons near the Fermi surface, when the temperature is sufficiently low ($T < T_c$, where we denote the critical temperature as T_c) the exchange of a phonon can lead to an effective attractive electron-electron interaction, thus leading to the formation of Cooper pairs [188]. As a consequence the system undergoes a second order phase transition, characterized by a discontinuity in the specific heat, and the new superconducting ground-state will be made of a condensate of non interacting quasiparticles (i.e. the Cooper pairs), with a gapped dispersion relation: a finite amount of energy will be required to break the electron pair and bring the material back to the normal state. The superconducting phase of a phonon-mediated superconductor has some peculiar properties:

- zero resistivity: once a current starts flowing inside a superconductor, no energy dissipation occurs and there is no need to have an external potential difference which maintains the electric current;
- Meissner-Ochsenfeld effect: a (sufficiently weak) magnetic field cannot penetrate inside the superconductor or, if already present in the normal state, is expelled;
- Isotope effect: the superconducting critical temperature depends on the atomic mass according to $T_c \sim 1/\sqrt{M}$;

J. Bardeen, L. N. Cooper and J. R. Schrieffer in 1957 proposed the first microscopic theory of phonon-mediated superconductivity [160]. This theory describes well materials in the weak-coupling regime, i.e. with a not too strong electron-phonon interaction. For the BCS theory the superconductive energy gap Δ and the transition temperature T_c are given by:

$$\Delta = 2\omega_D \frac{e^{-1/\lambda}}{1-e^{-1/\lambda}} \tag{2.37a}$$

$$T_c = 1.13\omega_D e^{-1/\lambda} \tag{2.37b}$$

where the strength of the electron-phonon interaction is represented by the electron-phonon coupling constant λ, while ω_D is the Debye frequency (which is material-

dependent). Moreover, the BCS theory provides a universal result, which is independent of the details of the system under study:

$$\frac{2\Delta}{k_B T_c} = 3.54 \tag{2.38}$$

However, in the strong-coupling regime, the BCS theory fails to correctly predict actual transition temperatures [189]: indeed, the problem lies in the assumption of an instantaneous non-local pairwise interaction between electrons. Nevertheless, the theory given by G. M. Eliashberg [190, 191] and further extended by D. J. Scalapino, J. R. Schrieffer and J. W. Wilkins[192], takes care for strong electron-phonon interactions using a many-body formulation that can naturally incorporate retardation effects in the coupling between electrons and phonons.

In the Nambu-Gor'kov [193–195] formalism we introduce a 2-component spinor for the electron:

$$\Psi_{j\mathbf{k}} = \begin{pmatrix} c_{\mathbf{k}j\uparrow} \\ c^\dagger_{-\mathbf{k}j\downarrow} \end{pmatrix} \qquad \Psi^\dagger_{j\mathbf{k}} = \begin{pmatrix} c^\dagger_{\mathbf{k}j\uparrow} & c_{-\mathbf{k}j\downarrow} \end{pmatrix} \tag{2.39}$$

As a consequence we can write the electron hamiltonian with the Frölich interaction (Eq. 2.22) in the basis of the 2×2 Pauli matrices $\{\mathbb{I}, \hat{\tau}_1, \hat{\tau}_2, \hat{\tau}_3\}$ as:

$$\begin{aligned} \hat{H}_{\text{tot}} = &\sum_{\mathbf{k}j} \varepsilon^0_{\mathbf{k}j} \Psi^\dagger_{j\mathbf{k}} \tau_3 \Psi_{j\mathbf{k}} + \frac{1}{2} \sum_{\mathbf{k}\mathbf{k}'\mathbf{k}'' jj'} v(\mathbf{k}'') (\Psi^\dagger_{\mathbf{k}'-\mathbf{k}''j'} \tau_3 \Psi_{\mathbf{k}j}) (\Psi^\dagger_{\mathbf{k}+\mathbf{k}''j} \tau_3 \Psi_{\mathbf{k}'j'}) \\ &+ \sum_{\mathbf{q}\nu} \hbar\omega^0_{\mathbf{q}\nu} \left(b^\dagger_{\mathbf{q}\nu} b_{\mathbf{q}\nu} + \frac{1}{2} \right) \\ &+ \sum_{\mathbf{k}jj'} \sum_{\mathbf{q}\nu} g^\nu_{\mathbf{k}j,\mathbf{k}+\mathbf{q}j'} (\Psi^\dagger_{\mathbf{k}j} \tau_3 \Psi_{\mathbf{k}+\mathbf{q}j'}) \left[b_{\mathbf{q}\nu} + b^\dagger_{-\mathbf{q}\nu} \right] \end{aligned} \tag{2.40}$$

where:

$$\mathbb{I} = \begin{pmatrix} 1 & 0 \\ 0 & 1 \end{pmatrix} \qquad \hat{\tau}_1 = \begin{pmatrix} 0 & 1 \\ 1 & 0 \end{pmatrix} \qquad \hat{\tau}_2 = \begin{pmatrix} 0 & -i \\ i & 0 \end{pmatrix} \qquad \hat{\tau}_3 = \begin{pmatrix} 1 & 0 \\ 0 & -1 \end{pmatrix} \tag{2.41}$$

We group again the momentum and band indices for the electron $k = (\mathbf{k}, j)$, while for the phonon we group the momentum and mode indices $q = (\mathbf{q}, \nu)$.

Next, we introduce a 2×2 electron Green's function matrix in order to describe both electron quasi-particles and Cooper pairs at the same time:

$$\begin{aligned}\hat{\mathcal{G}}(k,\tau) &= -\begin{pmatrix} \langle T_\tau c_{k\uparrow}(\tau) c^\dagger_{k\downarrow}(0)\rangle & \langle T_\tau c_{k\uparrow}(\tau) c_{-k\downarrow}(0)\rangle \\ \langle T_\tau c^\dagger_{-k\downarrow}(\tau) c^\dagger_{\mathbf{k}\uparrow}(0)\rangle & \langle T_\tau c^\dagger_{-k\downarrow}(\tau) c_{-k\uparrow}(0)\rangle \end{pmatrix} \\ &= \begin{pmatrix} \mathcal{G}(k,\tau) & \mathcal{F}(k,\tau) \\ \bar{\mathcal{F}}(k,\tau) & -\mathcal{G}(-k,-\tau) \end{pmatrix}\end{aligned} \tag{2.42}$$

where the diagonal terms ($\mathcal{G}(k,\tau)$) represent the standard single-particle electronic excitations, while the off-diagonal terms ($\mathcal{F}(k,\tau)$) represent the Gor'kov anomalous Green's functions describing Cooper pairs, which are therefore non-zero only below T_c. In Matsubara's space, the generalized Green's function takes the form:

$$\hat{\mathcal{G}}(k,i\omega_n) = \begin{pmatrix} \mathcal{G}(k,i\omega_n) & \mathcal{F}(k,i\omega_n) \\ \bar{\mathcal{F}}(k,i\omega_n) & -\mathcal{G}(-k,-i\omega_n) \end{pmatrix} \tag{2.43}$$

and the Green's function can be evaluated exploiting Dyson's equation:

$$\hat{\mathcal{G}}^{-1}(k,i\omega_n) = [\hat{\mathcal{G}}^0(k,i\omega_n)]^{-1} - \hat{\Sigma}(k,i\omega_n) \tag{2.44}$$

where the electron's Green's function in the normal state coincides with the non-interacting electron Green's function $[\hat{\mathcal{G}}^0(k,i\omega_n)]^{-1} = i\omega_n \mathbb{I} - \varepsilon_k \hat{\tau}_3$, while $\hat{\Sigma}(k,i\omega_n)$ is the 2×2 total electron self-energy matrix. In evaluating the free-electron propagator, we will consider the screened single particle electron energies ε^0_k computed via DFT, which are measured with respect to the chemical potential.

Moreover, in a DFPT framework we obtain phonon frequencies that are already screened and dressed by the electron-phonon interaction. As a consequence, we can neglect the phonon self-energy $\Pi(q,i\nu_n)$ and assume that the exact phonon Green's function coincides with the non-interacting propagator evaluated using DFPT phonon frequencies $\omega_{\mathbf{q}\nu}$: $\mathcal{D}(q,i\nu_n) = \mathcal{D}^0(q,i\nu_n) = 2\omega_q \left[(i\nu_n^2) - (\omega_q)^2\right]^{-1}$. Finally we assume that Migdal's theorem is valid and, consequently, we keep only the first order vertex correction for the electron-phonon interaction, which will be taken to be coincident with the screened electron-phonon matrix elements computed via DFPT (Eq. 2.21).

The total electron self-energy is composed by two parts $\hat{\Sigma}(k,i\omega_n) = \hat{\Sigma}_{\rm ep}(k,i\omega_n) + \hat{\Sigma}_{\rm C}(k,i\omega_n)$, i.e. the electron-phonon self-energy $\hat{\Sigma}_{\rm ep}(k,i\omega_n)$ and the electron-electron Coulomb self-energy $\hat{\Sigma}_{\rm C}(k,i\omega_n)$. As for the latter, it can be shown [182] that it enters the total electron-self energy only in the off-diagonal elements, $\hat{\mathcal{G}}^{\rm od}(k,i\omega_n)$, in order to avoid the double counting of Coulomb interactions already included in $\hat{\mathcal{G}}_0(k,i\omega_n)$. This is because the diagonal elements concern the normal state and since we are taking ε_k^0 to be coincident with the DFT eigenvalues, they are already screened by electron-electron interactions.

In order to write the electron-phonon self energy, we first define the band-resolved Eliashberg spectral function $\alpha^2F_{jj'}(\omega)$, which describes the frequency-dependence of the e-ph interaction [196]:

$$\alpha^2F_{j\mathbf{k},j'\mathbf{k}'}(\omega) = N_\sigma(0)\sum_\nu \delta(\omega-\omega_{\mathbf{q}\nu})\left|g^\nu_{\mathbf{k}j,\mathbf{k}'j'}\right|^2 \tag{2.45}$$

where $\mathbf{k}' = \mathbf{k}\pm\mathbf{q}$ and $N_{j\sigma}(0)$ is the electron-density of states (DOS) of band j at the Fermi energy (here we have set $E_F = 0$). Next we define the electron-phonon coupling constant, which is a measure of the average strength of the interaction between electrons and phonons:

$$\lambda_{j\mathbf{k},j'\mathbf{k}'}(\omega_n-\omega_{n'}) = \int_0^{\omega_{\rm max}} d\omega \frac{2\omega}{(\omega_n-\omega_{n'})^2+\omega^2}\cdot\alpha^2F_{j\mathbf{k},j'\mathbf{k}'}(\omega) \tag{2.46}$$

where $\omega_{\rm max}$ is the maximum phonon frequency. Therefore, the electron-phonon self energy can be written as:

$$\hat{\Sigma}_{ep}(k,i\omega_n) = \frac{1}{\hbar\beta N_\sigma(0)}\sum_{\mathbf{k}'j'n'}\hat{\tau}_3\hat{\mathcal{G}}(k,i\omega_n)\hat{\tau}_3\lambda_{j\mathbf{k},j'\mathbf{k}'}(\omega_n-\omega_{n'}) \tag{2.47}$$

There remains a direct Coulomb repulsion between electrons which contributes negatively to the pairing interaction. In an analogous way to the electron-phonon coupling constant, we can define a parameter $\mu^*_{jj'}$ which measures the effective screened Coulomb repulsion averaged over the Fermi surface between electrons on the j-th band and those on the j'-th band. The total Coulomb pseudopotential $\mu^*_{\rm tot}$ can then be computed as:

$$\mu^*_{\rm tot} = \frac{\sum_{jj'}N_{\sigma,j}(0)\mu^*_{jj'}}{\sum_j N_{\sigma,j}(0)} \tag{2.48}$$

As a consequence, the Coulomb contribution to the total self-energy will be:

$$\hat{\Sigma}_{\mathrm{C}}(k,i\omega_n) = -\frac{1}{\hbar\beta N_\sigma(0)} \sum_{\mathbf{k}' j' n'} \hat{\tau}_3 \hat{\mathcal{G}}^{\mathrm{od}}(k,i\omega_n)\hat{\tau}_3 \mu^*_{jj'} \tag{2.49}$$

I would like to stress that the band label j is no longer needed in the single-band case, thus $\mu^*_{jj'} = \mu^*$.

By writing the total electron self-energy in its most general form using the basis of Pauli matrices and the general functions $Z_k(i\omega_n)$, $\chi_k(\omega_n)$, $\phi_k(i\omega_n)$ and $\bar{\phi}_k(\omega_n)$ as:

$$\hat{\Sigma}(k,i\omega_n) = i\omega_n[1 - Z_k(i\omega_n)]\hat{\tau}_0 + \chi_k(\omega_n)\hat{\tau}_3 + \phi_k(i\omega_n)\hat{\tau}_1 + \bar{\phi}_k(\omega_n)\hat{\tau}_2 \tag{2.50}$$

we can retrieve the multi-band fully-anisotropic **k**-resolved Eliashberg equations on the imaginary axis [190, 191, 182, 197, 198]. They consist in a set of $3j$ non-linear coupled equations which have to be solved self-consistently:

$$Z_k(i\omega_n) = 1 + \frac{1}{\beta N_\sigma(0)\omega_n} \sum_{\mathbf{k}' j' n'} \frac{\omega_{n'} Z_{k'}(i\omega_{n'})}{\Xi^2_{k'}(i\omega_{n'})} \cdot \lambda_{j\mathbf{k},j'\mathbf{k}'}(\omega_n - \omega_{n'}) \tag{2.51a}$$

$$\phi_k(i\omega_n) = \frac{1}{\beta N_\sigma(0)} \sum_{\mathbf{k}' n' j'} \frac{\phi_{k'}(i\omega_{n'})}{\Xi^2_{k'}(i\omega_{n'})} \cdot [\lambda_{j\mathbf{k},j'\mathbf{k}'}(\omega_n - \omega_{n'}) - \mu^*_{jj'}] \tag{2.51b}$$

$$\chi_k(i\omega_n) = -\frac{1}{\beta N_\sigma(0)} \sum_{\mathbf{k}' n' j'} \frac{\varepsilon_{k'} + \chi_{k'}(i\omega_{n'})}{\Xi^2_{k'}(i\omega_{n'})} \cdot \lambda_{j\mathbf{k},j'\mathbf{k}'}(\omega_n - \omega_{n'}) \tag{2.51c}$$

where $\bar{\phi}_k(\omega_n) = 0$ thanks to gauge invariance and $\Xi^2_j(\mathbf{k}, i\omega_n)$ is defined as:

$$\Xi^2_k(i\omega_n) = \omega_n^2 Z_k^2(i\omega_n) + (\varepsilon_k + \chi_k(i\omega_n))^2 + \phi_k^2(i\omega_n) \tag{2.52}$$

The divergence in the sums over n in Eq. 2.51 can be avoided by limiting the number of Matsubara's frequencies through a cut-off energy ω_c which is typically in the range $\omega_c \sim [4\omega_{\max}; 10\omega_{\max}]$. Moreover, the Fermi level has to be re-computed self-consistently so that the number of electrons in the system is preserved:

$$N = 1 - \frac{2}{\beta} \sum_{\mathbf{k}nj} \frac{\varepsilon_k + \chi_k(i\omega_n)}{\Xi^2_k(i\omega_n)} \tag{2.53}$$

thus, a non-linear set of $3j+1$ coupled equations has to be actually solved.

Finally, the SC energy gap (i.e. the order parameter) for each band can be defined as:

$$\Delta_k(i\omega_n) = \frac{\phi_k(i\omega_n)}{Z_k(i\omega_n)} \tag{2.54}$$

which has to be computed self-consistently for different values of the temperature T. The SC critical temperature T_c will be the highest temperature for which all of the j energy gaps are zero, i.e. when $\Delta_k(i\omega_n; T_c) = 0 \; \forall j$.

2.4.1 Isotropic Migdal-Eliashberg equations

The effective attractive interaction that lead to the formation of Cooper Pairs occurs typically in an energy range of $2\hbar\omega_{\max}$ (where $\omega_{\max}$ is the maximum phonon frequency) around the Fermi energy. Therefore, as a first approximation it is possible to restrict the solution of the Eliashberg equations to electronic bands that fall in such energy range, where we also consider a constant density of states $N_\sigma(0) = \text{const.}$. As a consequence the number of equations to be solved self-consistently is reduced to a set of $2j$ non-linear coupled equations, since Eq. 2.51c is exactly zero and Eq. 2.53 can be neglected.

For smooth and well-behaved (i.e non-crossing and isotropic) Fermi surfaces or in the presence of strong disorder, we can average Eq. 2.51a and Eq. 2.51b over the the Fermi surface. As a consequence, the **k**-resolved picture is replaced with an energy description, leading to the set of $2j$ coupled non-linear isotropic Migdal-Eliashberg equations [199]:

$$Z_j(i\omega_n) = 1 + \frac{\pi}{\beta\omega_n}\sum_{n'j'}\frac{\omega_{n'}}{\Xi_{j'}(i\omega_{n'})}\cdot\lambda_{jj'}(i\omega_n, i\omega_{n'}) \tag{2.55a}$$

$$Z_j(i\omega_n)\Delta_j(i\omega_n) = \frac{\pi}{\beta}\sum_{n'j'}\frac{\Delta_{j'}(i\omega_{n'})}{\Xi_{j'}(i\omega_{n'})}\cdot\left[\lambda_{jj'}(i\omega_n, i\omega_{n'}) - \mu^*_{jj'}\right] \tag{2.55b}$$

where the isotropic electron-phonon coupling constant and Eliashberg spectral function are respectively defined as:

$$\lambda_{jj'}(\omega_n, \omega_{n'}) = \int_0^{\omega_{\max}} d\omega \frac{2\omega}{(\omega_n - \omega_{n'})^2 + \omega^2}\cdot\alpha^2F_{jj'}(\omega) \tag{2.56a}$$

$$\alpha^2F_{jj'}(\omega) = \frac{1}{N_\sigma(0)N_kN_q}\sum_{\mathbf{k}\mathbf{k}',\nu}\delta(\omega - \omega_{\mathbf{q}\nu})\left|g^{\nu}_{j\mathbf{k}j'\mathbf{k}'}\right|^2\delta(\varepsilon_{j\mathbf{k}})\delta(\varepsilon_{j'\mathbf{k}'}) \tag{2.56b}$$

Once we have $\Delta_j(i\omega_n)$, we can analitically continue the order parameter (Fig. 2.7) from the imaginary axis to the real axis $\Delta_j(i\omega_n) \rightarrow \Delta_j(\omega + io^+)$ thanks to Padé approximants [200] (see Appendix B for the detaiils) or through iterative analytic continuation [201].

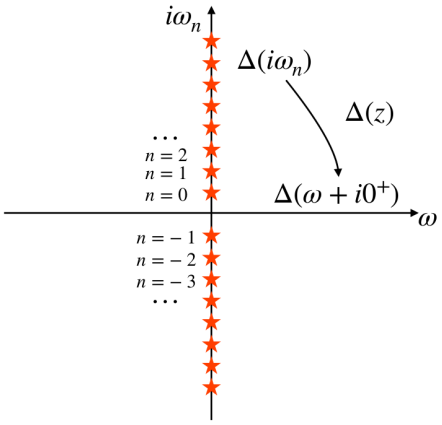

Fig. 2.7 Analytic continuation of the superconducting energy gap from the imaginary axis ($\Delta(i\omega_n)$) to the real axis ($\Delta(\omega + i0^+)$). Orange stars denotes the values of $\Delta(i\omega_n)$ for $n = \ldots, -2, -1, 0, 1, 2, \ldots$.

From the superconducting gap along the real axis, it is possible to extract the quasiparticle DOS in the SC phase $N_{S,j\sigma}(\omega)$ through:

$$\frac{N_{S,j\sigma}(\omega)}{N_{j\sigma}(0)} = \mathfrak{Re}\left[\frac{\omega}{\sqrt{\omega^2 - \Delta_j^2(\omega)}}\right] \tag{2.57}$$

2.4.2 Semi-empirical McMillan/Allen-Dynes T_c formula

Even if the superconducting critical temperature obtained by solving the Migdal-Eliashberg equations is more accurate, it may become computationally heavy in some cases even in its isotropic formulation due to the large number of Matsubara's frequencies required for convergence. A rougher estimate of T_c can be found using a semi-empirical formula first proposed in 1968 by W. L. McMillan[202] starting from the Migdal-Eliashberg equations and further improved by P. B. Allen and R. C. Dynes[203] in 1975:

$$T_c = \frac{\omega_{\log}}{1.2} \exp\left\{-\frac{1.04(1+\lambda)}{\lambda - \mu^*(1+0.62\lambda)}\right\} \tag{2.58}$$

Here λ is the total electron-phonon coupling constant, given by:

$$\lambda = 2\int d\omega \frac{\alpha^2 F(\omega)}{\omega} \tag{2.59}$$

where the Eliashberg function is defined as:

$$\alpha^2 F(\omega) = \frac{1}{N_\sigma(0) N_k N_q} \sum_{jj',\mathbf{kq},\nu} \delta(\omega - \omega_{\mathbf{q}\nu}) \left| g^{\nu}_{j\mathbf{k}j'\mathbf{k}+\mathbf{q}} \right|^2 \delta(\varepsilon_{j\mathbf{k}}) \delta(\varepsilon_{j'\mathbf{k}+\mathbf{q}}) \tag{2.60}$$

here N_k (N_q) is the total number of $\mathbf{k}$-points ($\mathbf{q}$-points) used in the sum and the Dirac-delta $\delta(\varepsilon_{j\mathbf{k}})$ and $\delta(\varepsilon_{j'\mathbf{k}+\mathbf{q}})$ limit the scattering events to the Fermi surface. Notice that, when we decompose λ over the bands, we obtain a symmetric $N_{\text{bands}} \times N_{\text{bands}}$ matrix (where N_{bands} is the number of bands) where intra-band ($j \leftrightarrow j$) and inter-band ($j \leftrightarrow j'$) couplings are described respectively by the diagonal and off-diagonal elements. The logarithmic-averaged phonon frequency $\omega_{\log}$ represents the typical frequency of the system:

$$\omega_{\log} = \exp\left[\frac{2}{\lambda}\int \log(\omega) \frac{\alpha^2 F(\omega)}{\omega} d\omega\right] \tag{2.61}$$

Finally, μ^* is the Morel-Anderson pseudopotential [204], i.e. a measure of the effective e-e interaction, which is an ad-hoc parameter whose value is usually set in order to reproduce the experimentally measured critical temperature. This parameter differs from the effective electron-electron interaction which appears in the Migdal-Eliashberg equations [197] and it is usually smaller.

Summary

- The many-body nature of the electron-phonon interaction modifies both electronic and vibrational properties;
- The strength of the electron-phonon coupling can be measured by ARPES or neutron or x-ray scattering;
- The divergency of the Lindhard function describes Kohn anomalies and charge density wave;
- The critical temperature of strong-coupling superconductors can be obtained from Migdal-Eliashberg equations on the imaginary axis.

Chapter 3

Electrochemical Doping

The possibility of controlling transport properties of semiconductors by means of an external electric field goes back to the invention of the field-effect transistor (FET) in 1960 and in particular to its modern implementation, the metal-oxide-semiconductor field-effect transistor (MOSFET) [205]. Indeed, as it will be explained in more detail, this device allows for an electrostatic modulation of the charge carriers at the interface between a dielectric and the material under study by switching on and off an electric field, rapidly going from a low- to a high-conducting system.

In the same year, R.E. Glover, III and M. D. Sherrill [206], by taking indium and tin thin-films as test-cases, showed that also the conductivity of metals can be modified thanks to the field effect and that it is possible to achieve both positive and negative shifts in the transition temperature of superconductors via electrostatic doping. After that, other authors showed that, thanks to electrostatic modulation of the carrier density, it is also possible to modify the conductivity of thin films of noble metals [207, 208] and to tune other strongly correlated phenomena, such as Mott-Hubbard transition [209], charge-density-waves [210, 211], insulator-to-metal transition [212, 213] and ferromagnetism [214].

As for the control of physical properties of superconductive materials via electrostatic fields, in the last decade the field-effect doping technique has emerged as a powerful tool. More specifically, the ionic gating technique allowed for an efficient tunability of properties of transition-metal dichalcogenides (TMDs) [211, 215–217], metallic superconductors [218–223], cuprates [224–232] and iron-based superconductors [233–239]. In order to describe these situations and try to compare the

experimental outcomes to theoretical predictions, it is important to properly take into account the FET geometry in density functional theory calculations and, in the framework of plane-wave basis expansion of the electronic wave-function, new routines have been developed in the last years to allow for the computation of both the electronic [240, 241] and vibrational [242] properties.

In this chapter I will describe the field-effect configuration in both its standard solid state configuration and in its electrochemical version (Sec. 3.1), the density functional perturbation theory for 2D materials and surfaces in the FET geometry (Sec. 3.3) and, finally, I will discuss the superconducting proximity effect in phonon-mediated superconductors (Sec. 3.2) with some DFT examples on metallic thin films.

3.1 Field-effect configuration

3.1.1 Metal-oxide-semiconductor field-effect transistor (MOS-FET)

A metal-oxide-semiconductor field-effect transistor (MOS-FET) is schematically represented in Fig. 3.1. The gate electrode is electrically separated from the semiconductor via an oxide layer, giving rise to an asymmetric capacitor: when a positive or negative voltage is applied to this electrode, an electric field is generated between the two plates (i.e. the gate and the semiconductor). By doing so, it is possible to tune the Fermi level of the semiconductor which will cross either its surface valence or conduction bands, forming at the oxide-semiconductor interface a layer of electrons or holes depending on the applied gate voltage.

This layer of charges will connect two heavily-doped islands of the semiconductor, thus forming a conduction channel: these two islands are connected to other two metallic electrodes, the drain and the source, through which we can apply a voltage difference and create a charge current. As a consequence, in a MOSFET we can alter in an almost continuous way the conduction properties of a semiconducting device by transverse electrostatic fields going from the gate to the semiconductor, i.e we can rapidly pass from a low-resistance metallic state to a high-resistance insulating one without any modification of the crystal structure (e.g. pressure or chemical doping).

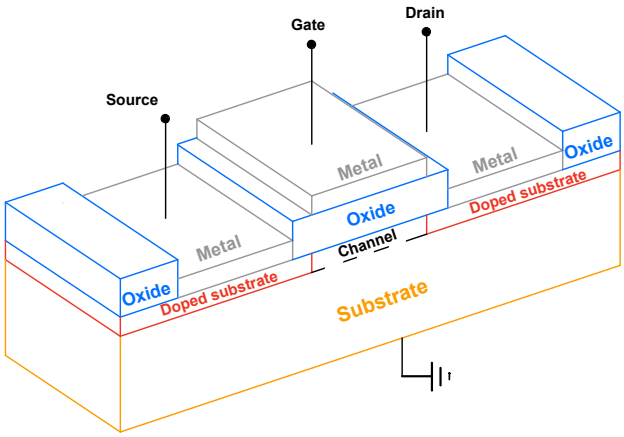

Fig. 3.1 Schematic representation of a metal-oxide-semiconductor field-effect transistor (MOS-FET). The gray blocks represent the three metallic electrodes: the gate, the drain and the source. The orange block represents the semiconductor. The gate electrode and the semiconductor are electrically isolated via an oxide layer, here depicted by blue blocks. Depending on the sign of the applied gate voltage, either electrons or holes are accumulated at the oxide-semiconductor interfaces connecting two heavily-doped islands of the substrate, thus forming a conduction channel. A voltage difference between the source and the drain then leads to an electric current in the conduction channel.

The main limitation of such devices lies in the breakdown field of solid-state dielectrics, which limits the maximum electric field that can be applied to $E_{max} \approx 10^8$ V/m: as a consequence the maximum induced charge density at the oxide-semiconductor interface is limited to $n_{2D} \approx 10^{13}$ cm^{-2}. Indeed, the amount of charges which can be induced at the oxide-semiconductor device for a given voltage difference depends on the gate capacitance per unit area, which is given by $C_g = \varepsilon_0 \varepsilon_r / d$ for a parallel-plate capacitor (here ε_0 is the vacuum permittivity, ε_r is the dielectric constant and d is the distance between the two plates). The maximum value of n_{2D} in solid-state dielectric technology is not a drawback for standard FET applications if the material under study is a small-gap semiconductor, however the magnitude of n_{2D} is not enough to alter the conduction properties of metals or to lead to the formation of correlated states of matter (e.g. superconductivity, antiferromagnetism, charge-density-waves, etc.). A possible way to overcome this problem is to increase ε_r as much as possible by suitably choosing the dielectric. For example, hafnium oxide (HfO_2) allows to increase ε_r by a factor 7 with respect to SiO_2, but the latter is obviously much more convenient in Si-based electronic devices [243].

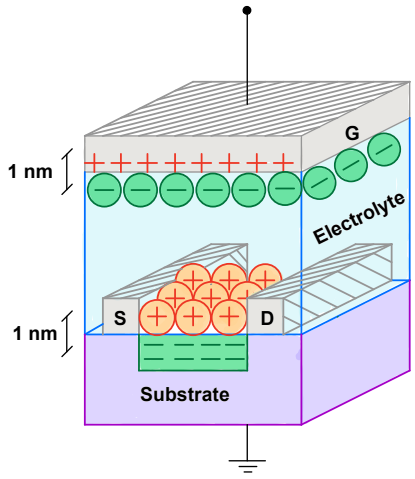

Fig. 3.2 Schematic representation of an electric-double-layer field-effect transistor (EDL-FET). The gray blocks represent the three metallic electrodes: the gate (G), the drain (D) and the source (S). The violet block represents the semiconductor under study. The blue block is the electrolyte in which cations and anions (respectively the orange and green spheres) are free to move. If we apply, for example, a positive voltage to the gate electrode, cations accumulate at the electrolyte-semiconductor interface, thus inducing a charge distribution of opposite sign in the first few layers of the material under study . A voltage difference between the source and the drain then leads to an electric current in the conduction channel.

3.1.2 Electric-double-layer field-effect transistor (EDL-FET)

In the electric-double-layer (EDL) field-effect transistor (FET) architecture, the solid-state dielectric is substituted with a liquid or gel electrolyte, i.e. an electrically conducting solution made of anions and cations uniformly dispersed into a polar solvent. In Fig. 3.2 the EDL-FET is schematically shown: if, for example, we apply a positive voltage to the gate electrode (G), cations will accumulate near the electrolyte-gate interface while anions will move towards the electrolyte-semiconductor interface in order to ensure global neutrality. Such accumulation of ions forms the so-called electric double layer (or Helmholtz layer) [244]: the spacing between ions and the metal gate or the substrate will be of the order of ≈ 1 nm (depending on the choice of the electrolyte), effectively representing a nano-capacitor.

In this way we are directly reducing the distance between the plates d and, as a consequence, the dielectric constant ε_r [245] with respect to standard solid-state devices, thus increasing the value of the capacitance and, as a consequence, the induced charge density inside the first few layers of the semiconductor: indeed, with this new architecture the maximum electric field becomes $E_{max} \approx 10^9 - 10^{10}$

V/m and the maximum induced surface charge density will be of the order of $n_{2D} \approx 10^{14} - 10^{15}$ cm^{-2}, depending on the material under study [207, 246].

Notice that, in this case, we do not have a possible dielectric breakdown because there is no actual exchange of electrons between the semiconductor and the electrolyte. One possible drawback of the EDL-FET architecture is rather that, with sufficiently high applied voltage differences, chemical reactions might happen to the electrolyte (modifying its chemical-physical properties). Moreover such high electric field can drastically modify the material under study [232, 247–249] and, in some cases, lead to ion intercalation inside the semiconductor crystal structure [210, 227, 250]. However, while such effect might represent a drawback to the EDL-FET doping, it can still be useful to achieve ultrahigh doping in the material via ionic intercalation.

3.2 Superconducting proximity effect

Consider a junction made of a superconductor (S) and a normal metal (N). In this configuration, it is possible to observe a superconductive proximity effect due to the leaking of Cooper pairs from the superconducting region to the normal one [251, 252]. Indeed, at the N-S interface, Andreev reflections [253] can occur: it is possible to transfer an incident electron with spin up (down) coming from the normal metal into the superconductor if its energy ε is higher than the superconductive energy gap Δ and there are vacant state for that excitation, however if $\varepsilon < \Delta$ the transfer can occur only if another electron with spin up (down) is also injected with the simultaneous reflection of a hole with spin down (up) from S to N.

As a consequence of this latter situation, a Cooper pair is formed in the superconductor. Moreover, by doing so, the reflected hole still carries memory of the complex macroscopic phase of the Cooper pair: therefore information of S leaks into N. Notice however that the Andreev reflection is not abrupt in space, but happens on a typical length scale of the order of the coherence length ξ of the Cooper pair, therefore modifying the local density of state of N. Superconductive proximity effect can therefore be seen as an interplay between the Andreev reflection phenomenon and long-range coherence in the normal state.

Morevoer, the superconductive proximity effect can be also observed in a superconductor-superconductor interface. Consider for example a superconductor S_1, with critical temperature $T_{c,1}$ and order parameter Δ_1, coupled to a second superconductor S_2, with critical temperature $T_{c,2}$ and order parameter Δ_2. Assume that $T_{c,1} < T_{c,2}$ and $\Delta_1 < \Delta_2$: when $T < T_{c,1}$ the local densities of states of S_1 and S_2 are significantly modified with respect to the values they had in the isolated superconductor, leading to a substantially different macroscopic transition temperature. However when $T_{c,1} < T < T_{c,2}$, a finite energy gap Δ_1' is opened in S_1 while the existing order parameter in S_2 is reduced, thus leading to an interface superconductivity induced by the proximity effect [251, 252].

As we have discussed at the beginning of the chapter, it was shown experimentally that the superconductive critical temperature can be enhanced or suppressed reversibly by field-effect doping. However the effective doping of the thin film does not involve the sample as a whole. As a matter of fact, when an electrostatic potential $\phi(\mathbf{r})$ is present (with a resulting potential energy $-e\phi(\mathbf{r})$, with e the Coulomb charge) the valence electrons will spatially reorganize themselves in order to effectively screen such perturbation. If the electrostatic potential is sufficiently small (i.e. $|e\phi(\mathbf{r})| << E_F$ and E_F is the Fermi energy), then the induced charge density will be equal to $\rho_{ind}(\mathbf{r}) = -2e^2\phi(\mathbf{r})N_\sigma(E_F)$ (where $N_\sigma(E_F)$ is the total density of states per spin at the Fermi level E_F). Then, according to the linear Thomas-Fermi theory of electronic screening, such induced charge distribution will screen the external potential over a typical length scale λ_{TF} which is called Thomas-Fermi screening length [254]:

$$\lambda_{TF} = \sqrt{\frac{\varepsilon_r \varepsilon_0}{2e^2 N(E_F)}} \tag{3.1}$$

where ε_0 and ε_r are respectively the vacuum permittivity and the dielectric constant. For a good metal, such screening length is of the order of $\lambda_{TF} \approx 1$Å, i.e. it involves only the first few layers of a thin film.

Notice that, on the other hand, the general treatment of electrostatic screening in a superconducting material is quite cumbersome and requires the theory on non-equilibrium superconductivity [255]. Nevertheless, when $T \sim T_c$ the screening is dominated by electrons which are not taking part to the formation of Cooper pairs, since the density of the superfluid is still small when the phase transition occurs. As a matter of fact, it has been shown by Ovchinnikov [256], whose theory exploits a two-fluid model for the screening of paired electrons, that the effective screening

length in sufficiently clean superconductors is only $\sim 5\%$ bigger than the normal state counterpart.

As a consequence, in a field-effect architecture only a small part of the material under study, which directly faces the electrolyte, will be in principle affected by the transverse electric field and thus experience charge accumulation, while the underlying bulk will be unaffected. Therefore, we will have a perturbed superconductor on top of an undoped one and, as we have discussed above, they will be coupled by superconductive proximity effect. In order to analytically study the spatially induced modulation of the order parameter along the direction of the applied electric field, we can model the system as two units [257]: one perturbed surface layer of thickness d_s and an unperturbed bulk of thickness $d_b = d - d_s$, with d being the total film thickness. The two subsystems are coupled to each other by superconductive proximity effect and in order to treat the phenomenon within the multi-band Migdal-Eliasberg theory of superconductivity we need to generalize the set of equations. Denoting by (s) the quantity referring to the surface layer and by (b) those of the bulk, in the case of an s-wave superconductor we have to solve the non linear set of coupled equations [220, 258–261]:

$$Z_j^{(b)}(i\omega_n) = 1 + \frac{\pi}{\beta\omega_n}\sum_{n'j'}\left\{\frac{\omega_{n'}}{\Xi_{j'}^{(b)}(i\omega_{n'})}\lambda_{jj'}^{(b)}(i\omega_n, i\omega_{n'}) + \Gamma_{(b)}\frac{\omega_n}{\Xi_{j'}^{(s)}(i\omega_n)}\right\} \tag{3.2a}$$

$$Z_j^{(s)}(i\omega_n) = 1 + \frac{\pi}{\beta\omega_n}\sum_{n'j'}\left\{\frac{\omega_{n'}}{\Xi_{j'}^{(s)}(i\omega_{n'})}\lambda_{jj'}^{(s)}(i\omega_n, i\omega_{n'}) + \Gamma_{(s)}\frac{\omega_n}{\Xi_{j'}^{(b)}(i\omega_n)}\right\} \tag{3.2b}$$

$$Z_j^{(b)}(i\omega_n)\Delta_j^{(b)}(i\omega_n) = \frac{\pi}{\beta}\sum_{n'j'}\left\{\frac{\Delta_{j'}^{(b)}(i\omega_{n'})}{\Xi_{j'}^{(b)}(i\omega_{n'})}\left[\lambda_{jj'}^{(b)}(i\omega_n, i\omega_{n'}) - \mu_{jj'}^{*(b)}\right] + \Gamma_{(b)}\frac{\Delta_{j'}^{(s)}(i\omega_n)}{\Xi_{j'}^{(s)}(i\omega_n)}\right\} \tag{3.2c}$$

$$Z_j^{(s)}(i\omega_n)\Delta_j^{(s)}(i\omega_n) = \frac{\pi}{\beta}\sum_{n'j'}\left\{\frac{\Delta_{j'}^{(s)}(i\omega_{n'})}{\Xi_{j'}^{(s)}(i\omega_{n'})}\left[\lambda_{jj'}^{(s)}(i\omega_n, i\omega_{n'}) - \mu_{jj'}^{*(s)}\right] + \Gamma_{(s)}\frac{\Delta_{j'}^{(b)}(i\omega_n)}{\Xi_{j'}^{(b)}(i\omega_n)}\right\} \tag{3.2d}$$

where $\Gamma_{(\alpha)} = \pi|t|^2 A d_\alpha N_{\sigma,\alpha}(0)$ ($\alpha = \{b,s\}$) and $\Gamma_{(b)}/\Gamma_{(s)} = d_b N_{\sigma,b}(0)/d_s N_{\sigma,s}(0)$, A is the cross-sectional area of the junction, $|t|^2$ is the the transmission matrix which will be set equal to 1 since at the interface the have the same material and $N_{\sigma,\alpha}(0)$ is the density of states at the Fermi level ($E_F = 0$) for the surface and bulk material.

As for the Coulomb pseudopotential of the surface $\mu^{*(s)}$, it can be calculated as a first approximation in the Thomas-Fermi model as described in Ref. 258:

$$\mu^{*(s)}(\omega_c) = \frac{\mu^{(s)}}{1+\mu^{(s)}\log\{[E_{F,(b)}+\Delta E_F]/\omega_c\}} \tag{3.3}$$

where:

$$\begin{aligned} &\mu^{(s)} = (a_s^2/2)\log\{1+a_s^{-2}\} \\ &a_s^2 = (2k_{TF,(b)}/k_{F,(b)})^2 \cdot (N_{\sigma,s}(0)/N_{\sigma,b}(0))/[(1+\Delta E_F)/E_{F,(b)}] \end{aligned} \tag{3.4}$$

Here $k_{TF,(b)}$ and $k_{F,(b)}$ are, respectively, the moduli of the Thomas-Fermi and the Fermi wave-vectors, $\Delta E_F = E_{F,(s)} - E_{F,(b)}$ is the Fermi level shift occurring in the surface layer. However, notice that usually the effect of electrostatic doping on the effective Coulomb interaction $\mu^{*(s)}$ is small and can be neglected [258].

In order to solve the set of equations Eqs. 3.2 we need many input parameters, which can be computed ab-initio via density functional theory: the Eliashberg spectral functions for the surface layer and the bulk $\alpha^2 F^{(\alpha)}_{jj'}(\omega)$ (which are needed for the computation of the electron-phonon coupling constants $\lambda^{(\alpha)}_{jj'}(i\omega_n, i\omega_{n'})$), the densities of states at the Fermi level $N_{\sigma,\alpha}(0)$, the Fermi energy shift ΔE_F. The total film thickness d and the cross-sectional area of the junction A are given by the experiment. Finally, the thickness of the surface layer d_s is not known a priori and can be left as a free parameter (or we can make suitable ansatz for its values, depending on the material under study). In the next two subsections I will show how such equations can be solved for a one-band (indium) and two-band (magnesium diboride) phonon-mediated superconductors and I will also discuss how such theory can help us studying the validity of linear Thomas-Fermi screening using as a test case niobium nitride.

3.2.1 Indium (In) and Magnesium Diboride (MgB_2)

In the introduction of this chapter I discussed how R.E. Glover, III and M. D. Sherrill [206], in 1960, showed that, by pure electrostatic doping via solid-state FET architecture, it is possible to modify the conductivity of metals and the transition temperature of two superconductors, namely indium and tin. In particular, in the case of indium ($T_c = 3.4$ K [262, 263]), they considered films of thickness ranging from 60 to 120 Å and, by doping the system electrostatically with $\sim 3 \times 10^{-5}$ electrons per atom (i.e with a field of $\sim 2.6 \times 10^7$ V/m), they showed that the transition temperature could be shifted both upwards and downwards by $\approx 10^{-4}$ K.

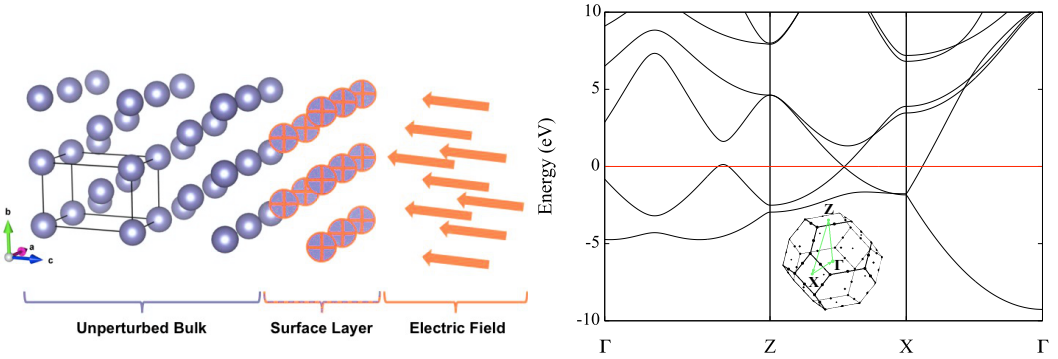

(a) (b)

Fig. 3.3 (a) Stick-and-ball structure of gated In thin film used for modelling the superconducting proximity effect. Figure is adapted from Ref. 259. (b) Electronic band structure of bulk In. The red line represents the Fermi level ($E_F = 0$). The inset shows the first Brillouin zone with highlighted high-symmetry points.

In Ref. 259 I wanted to give a theoretical explanation of such critical temperature shifts due to a static electric field by solving the generalized one band s-wave Eliashberg equations with proximity effect, with the model discussed above (Fig. 3.3 (a)). The input parameters of these equations were computed ab-initio via density functional theory (DFT) and the computational details are given in Appendix A. As already discussed, the only free parameters of such theory are the effective Coulomb interaction and the thickness of the surface layer d_s which is affected by the electric field. In order to fix μ^*, I solved the Eliashberg equations for the undoped bulk Indium imposing that the transition temperature was the one observed experimentally.

From DFT computations on the undoped bulk, I found an electron-phonon coupling $\lambda_b = 0.8728$ and an averaged logarithmic phonon frequency $\omega_{log} = 6.4177$ meV. As a result, by solving the Eliashberg equation, I fixed $\mu^{*(b)} = 0.170807$. As for the thickness of the surface layer, for sufficiently low electric fields (i.e for sufficiently low values of doping) a good approximation [220] is to set this length scale equal to the Thomas-Fermi screening length, i.e. $d_s = \lambda_{TF}$. In the case of Indium a $\lambda_{TF} = 0.182$ nm was found, using density of states at the Fermi level 0.42390 states/eV/spin/cell, unit cell volume 27.2839 Å^3 and relative dielectric constant $\varepsilon_r = 9.3$ [264]. Moreover, since I was dealing with sufficiently small electric fields, I was able to set $\mu^{*(s)} = \mu^{*(b)}$.

Subsequently, I investigated the effects of increasing doping (i.e. $x = 3 \times 10^{-5}$, 3×10^{-4}, 3×10^{-3} and 3×10^{-2} e$^-$/atom) on the electronic and vibrational properties of bulk indium. While at the beginning a decrease of the electron-phonon coupling constant λ and a slight increase of ω_{ln} can be observed, for higher carrier densities, the value of ω_{ln} decreases while that of λ increases (Fig. 3.4 (b) and (c)). The density of states at the Fermi level has the same doping dependence as ω_{ln} (Fig. 3.4 (d)). As a consequence, there is a net reduction of the superconductive critical temperature $T_{c,s}$ (Fig. 3.4 (a)), since λ decreases more than the ω_{ln} increment.

These results couldn't be directly compared to the experiments, because they were obtained in the case of uniformly doped indium. Thereofre, I subsequently applied the proximity model, where the junction was made of a perturbed surface layer ($T_{c,s}$) and an unperturbed bulk ($T_{c,b}$). In order to exactly reproduce the experimentally measured shifts of the superconductive critical temprature [206], the thickness of the doped surface layer had to be tuned to the value of $d_s = 0.165$ nm, which is in agreement with the theoretical value of λ_{TF} and thus justifies the Thomas-Fermi approximation.

As a further analysis, I computed critical temperature shifts ΔT_c as a function of increasing electron doping x and for three different total film thicknesses $d = 3, 5, 7$ nm, with a junction area [260] of $A = 10^{-6}$ m^2. The results coming from the solution of proximity-coupled Eliashberg calculations are shown in Fig. 3.5. From a qualitative point of view, it was possible to observe that T_c decreases as x increases for any film thickness d. On the other hand, from a quantitative point of view, ΔT_c is greatly suppressed with increasing film thickness: this is due to the coupling between the perturbed surface and the unperturbed bulk arising from the superconductive

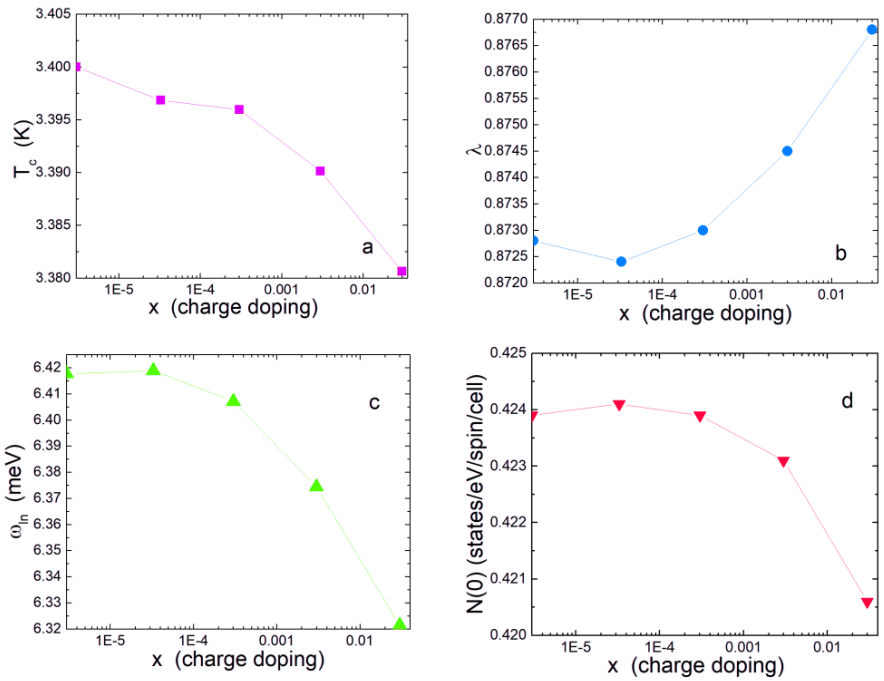

Fig. 3.4 (a): Superconductive critical temperature T_c vs. charge doping x for a system without proximity effect. (b): Electron-phonon coupling constant λ vs. charge doping x. (c): logarithmic averaged phonon frequency ω_{ln} vs. charge doping x. (d): normal density of states at the Fermi level $N(0)$ (we set $E_F = 0$) vs. charge doping x. The graphs are in logarithmic scale with $x + 3 \cdot 10^{-6}$ for graphic reasons. Figures are adapted from Ref. 259

proximity effect, thus leading to a strong dependence of T_c shown in the field-effect doped thin films.

Notice that, in single-band superconductors, such as indium (Fig. 3.3 (b)), field-effect doping directly affects the total density of states at the Fermi level $N(0)$ ($E_F = 0$). As a consequence, it is possible to directly affect the superconductive critical temperature T_c since it is a monotonic function of the electron-phonon coupling constant λ (which is proportional to $N(0)$, see Eq. 2.60). Therefore, if $N(0)$ decreases/increases, so does the T_c [258]. On the other hand, in a multi-band superconductor we have a more complex situation: the electric field can affect the bands crossing the Fermi level in different ways and, consequently, the superconductive critical temperature may have a stronger dependence on one particular band with respect to another one.

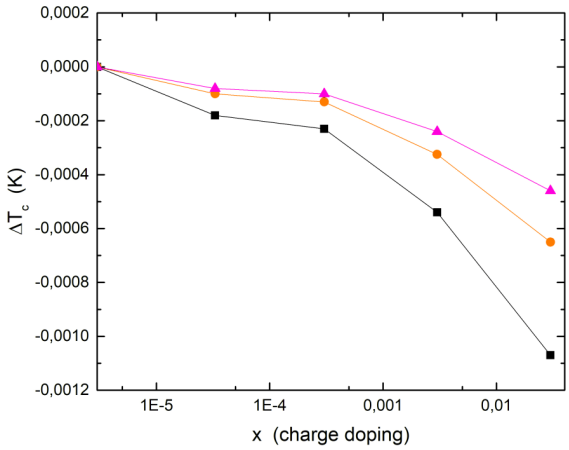

Fig. 3.5 Critical temperature shifts (ΔT_c) vs. charge doping x with surface layer thickness $d_s = 0.165$ nm for three different values of film thickness $d = 3$ nm (black squares), $d = 5$ nm (orange circles), $d = 7$ nm (magenta triangles). All lines act as guides to the eye. The graphs are in logarithmic scale with $x + 3 \cdot 10^{-6}$ for graphic reasons. Figure is adapted from Ref. 259

In order to show how proximity effect works in a multi-band superconductor, in Ref. [260] I studied the effect of an electrostatic field on MgB_2 thin films (Fig. 3.6 (a)), which is a two-band superconductor (Fig. 3.6 (b)), by solving the generalized two band s-wave Eliashberg equations with proximity effect, with the model discussed above. The input parameters of these equations were computed ab-initio via density functional theory (DFT) and the computational details are given in Appendix A. In particular, the effect of doping on the densities of states of band σ (responsible for in-plane bonding) and band π (responsible for out-of-plane bonding) is similar, however the critical temperature depends more on variations of the electron-phonon coupling constant due to $\sigma - \sigma$ scattering (i.e. $\lambda_{\sigma\sigma}$), while it is quite insensitive to variations of the $\pi - \pi$ channel (i.e. $\lambda_{\pi\pi}$). In principle there might be also interband contributions (i.e. $\lambda_{\sigma\pi}$ and $\lambda_{\pi\sigma}$), however it has been shown that they have negligible effects [265].

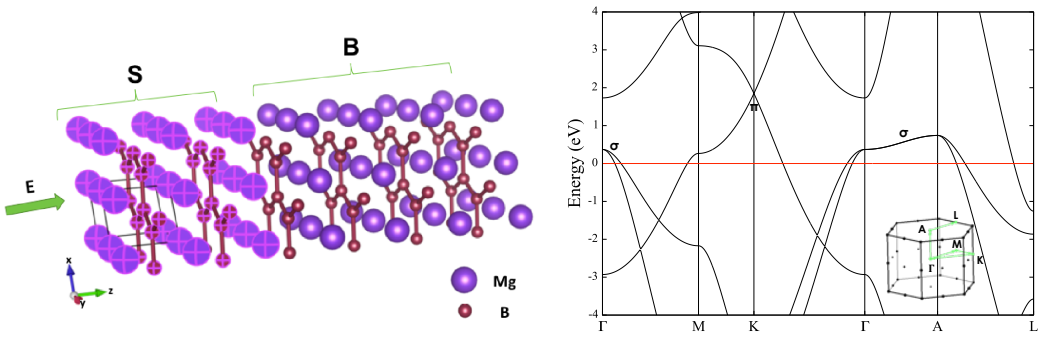

(a) (b)

Fig. 3.6 (a) Stick-and-ball structure of gated MgB_2 thin film used for modelling the superconducting proximity effect. B (S) is the label for the bulk (surface) layer. E indicates the electric field directed perpendicularly to the sample surface. Figure is adapted from Ref. 260. (b) Electronic band structure of bulk MgB_2: σ and π bands crossing the Fermi energy are explicitly labelled. The red line represents the Fermi level ($E_F = 0$). The inset shows the first Brillouin zone with highlighted high-symmetry points.

As for the Coulomb pseudopotential, it can be calculated analytically in the bulk, as shown in literature [266–268]. In principle, the value of μ^* in the surface layer would be different from that of the bulk, however the corrections can be linked only to the different densities of states at the Fermi level. Therefore, it is possible to write:

$$\mu_{jj'}^{*(\alpha)} = \mu_0\{N_{\sigma 1,\alpha}(0) + N_{\sigma 2,\alpha}(0)\} \cdot \begin{pmatrix} 2.23/N_{\sigma,\alpha}^{(\sigma)}(0) & 1/N_{\sigma,\alpha}^{(\sigma)}(0) \\ 1/N_{\sigma,\alpha}^{(\pi)}(0) & 2.48/N_{\sigma,\alpha}^{(\pi)}(0) \end{pmatrix} \tag{3.5}$$

where $\alpha = s, b$ refers either to the surface layer (s) or the bulk (b), $N_{\sigma,\alpha}^{(\sigma)}$ is the density of states per spin for band σ and $N_{\sigma,\alpha}^{(\pi)}$ is the density of states per spin for band π. The coefficient $\mu_0 = 0.033281$ is found by solving the unperturbed two-band s-wave Eliashberg equations for the bulk and forcing the resulting critical temperature to be equal to its experimental value $T_c = 39.4$ K.

From Fig. 3.7 (a) it is evident that by simultanously decreasing the total film thickness d and increasing the surface layer thickness d_s, the variation of critical temperature increases. However, as already pointed out, while the first is a property of the system that can be controlled, the second one is an intrinsic property of the material under study. The Thomas-Fermi model could be no longer valid for strong applied electric field and, as a consequence, the thickness of the surface layer which is affected by the field-effect doping could be larger than λ_{TF} [220, 269].

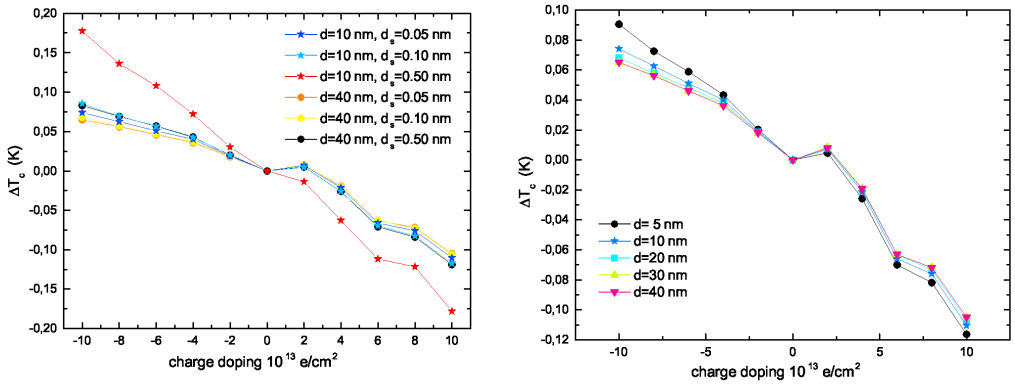

(a) (b)

Fig. 3.7 (a) Superconducting critical temperature shifts ΔT_c vs. charge doping for two different values of film thickness $d = 10$ nm and $d = 40$ nm and three different surface layer thickness $d_s \approx \lambda_{TF} = 0.05$ nm, $d_s = 0.1$ nm and $d_s = 0.5$ nm. (b) Superconducting critical temperature shifts ΔT_c vs. charge doping for six different values of film thickness $d = 5, 10, 20, 30, 40$ nm (black circles, blue stars, light-blue squares, green up triangles and magenta down triangle) with surface layer thickness $d_s \approx \lambda_{TF} = 0.05$ nm. Figures are adapted from Ref. 260.

This last point will be evident in the next section, when I will study the screening properties of NbN. As a consequence, for MgB_2 I performed calculations of ΔT_c for varying values of d_s: indeed, ΔT_c strongly depends on d_s and it does increase with it. However, since MgB_2 can be considered a "good" metal, for not too high values of the electric field $d_s \approx \lambda_{TF} = 0.05$ nm. In Fig. 3.7 (b) I plotted the resulting critical temperature shifts for a surface layer thickness coincident with the Thomas-Fermi screening length and for varying total thicknesses of the film d: ΔT_c decreases when d is increased.

In the end, thanks to superconductive proximity effect, it is possible to explain measured variations of the superconductive critical temperature of gated phonon-mediated superconductors and to identify optimal ratios between d_s and d for future studies.

3.2.2 Niobium Nitride (NbN)

I have largely discussed the fact that for good metals and not too large applied electric fields, the thickness of the surface layer involved in the field-effect doping is of the order of the Thomas-Fermi screening length, i.e $d_s \approx \lambda_{TF} \sim 1$Å. However, in many experimental measurements of electrostatic doping on superconducting systems [219, 220, 229, 270, 271], the effective screening length was found to increase after a certain doping value ($\sim \Delta n_{2D} \gg 10^{13}$ cm^{-2}, where Δn_{2D} is the magnitude of the induced surface charge density), with a resulting surface thickness much bigger than the Thomas-Fermi screening length (i.e. $d_s \gg \lambda_{TF}$). This observation is obviously against what is expected by linear Thomas-Fermi theory of screening, whose screening length is inversely proportional to the amount of carriers available at the Fermi level (Eq. 3.1).

In Ref. 220, the authors experimentally measured reversible critical temperature shifts in NbN thin films induced by proximity effect: indeed the values of ΔT_c were computed by solving Eqs. 3.2 providing experimental data of the thin films. More precisely they:

- considered two different subsystems, a perturbed (doped) one an an unperturbed (undoped) one;
- they computed the critical temperatures for both subsystems separately;
- they solved the generalized Eliashberg equations (Eqs. 3.2) with proximity effect, for the two coupled subsystems;

In particular, in order to theoretically reproduce the measured critical temperatures as a function of doping, the value of the thickness of the surface layer d_s was left as a free parameter: they showed that the effective screening length depends on the induced charge density and, moreover, it becomes bigger than the Thomas-Fermi screening length for sufficiently high electric fields. In order to explain such experimental evidence, they applied the theory of electronic screening beyond the linear regime [254] which is equivalent to the linear Thomas-Fermi theory for values of the induced charge density $\Delta n_{2D} \lesssim 10^{14}$ cm^{-2} and allows to exactly reproduce the experimental data up to $\Delta n_{2D} \sim 5 \times 10^{14}$ cm^{-2}. However, for higher values of Δn_{2D} such theory cannot reproduce the measured ΔT_c.

Therefore in Ref. 269 I addressed the problem of the anomalous screening of the electric field at the surface of niobium nitride when doped electrostatically from a density functional theory point of view. In order to do so I performed ab-initio calculations of charge density profile in NbN when electrochemically doped in the EDL field-effect configuration (Fig. 3.8 (a)) as described in Refs. 240 - 241. The computational details are given in Appendix A. Such EDL-FET model is implemented in the plane-wave formalism and has three main assumptions:

- the electrolyte is completely removed in order to reduce the computational cost of the simulation. Indeed, if we had to take into account the microscopic details of the electrolyte, this would require the presence of more atoms and a bigger supercell which will necessarily make the computation heavier;
- the ions that accumulate near the electrolyte/semiconductor interface are modelled with a uniform planar distribution of point-like charges of the same value Δn_{2D}, which is called monopole in Refs. 240 - 241. Such uniform sheet of charges generates an out-of-plane electric field, which enters the slab and will be screened after a certain penetration length modifying the charge density profile of the substrate;
- the spacing of ≈ 1 nm between the charge accumulation and the material surface is guaranteed by a potential barrier, which also prevents charge spilling from the semiconductor towards the planar charge distribution.

Notice that the plane-wave formalism exploits periodic boundary conditions. However in a 2D system or a surface we have periodicity only along the $[x,y]$ plane parallel to the surface, while along the z direction the system is no longer periodic. In DFT this is easily achievable by adding vacuum along the non-periodic direction, so that periodically repeated images do no interact with each other. However, in the EDL-FET geometry, the monopole is also periodically repeated along z and the presence of a long-range Coulomb potential along the z direction is such that it interacts with the system: as a matter of fact, in the vacuum region (i.e the one which does not face the electrolyte) there should not be any electrostatic potential. Therefore, in order to get rid of this spurious interaction, a dipole of opposite polarity is added near the monopole so that it exactly cancels out the Coulomb potential in the vacuum region due to periodically-repeated images along z. The scheme of such EDL-FET configuration is depicted in Fig. 3.8 (a), along with the various potential

energies contributions. In this way, the ground-state charge density of the surface and its electronic properties will be computed by taking into account self-consistently the presence of an electric field along the non-periodic direction.

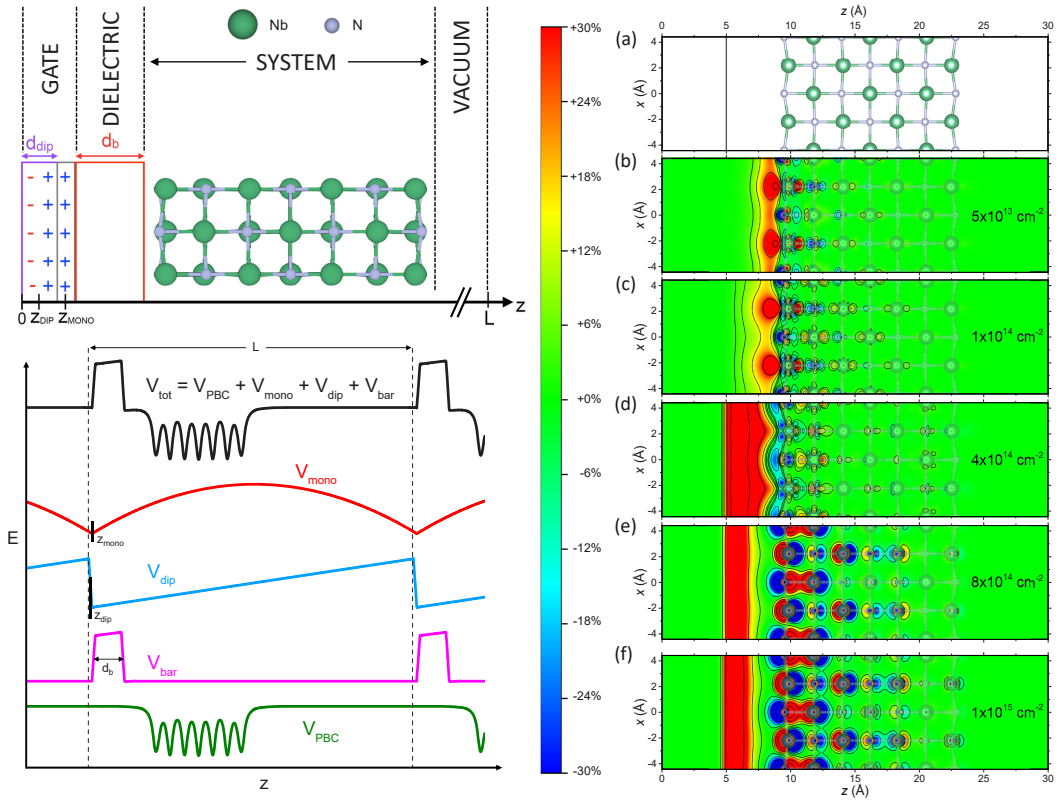

(a) (b)

Fig. 3.8 (a) **top**: Ball-and-stick model of the NbN 7-layer system in the FET configuration as described in Refs. 240 - 241; **bottom**: planar averaged total Kohn-Sham potential (black line) for the periodically repeated supercell. Its components are also depicted and are not in scale: monopole potential (red line), dipole potential (blue line), potential barrier (magenta line), ionic potential (green line). (b) Color maps of differences between the total charge density in doped and undoped NbN slab along the (x,z) plane. Plots are in linear scale between $\pm 30\%$ of the maximum magnitude of the density difference in the accumulation layer. Figures are taken from Ref. 269.

In Fig. 3.8 (b) I plotted color maps of the charge density distribution on a cut along a plane parallel to the $[x,z]$ plane, normalized to the maximum value reached in the accumulation layer. First of all it is possible to observe that the screening charge accumulates in the d_{z^2} orbitals of the outermost Nb atoms for moderate electric fields ($\Delta n_{2D} \leq 10^{14}$ cm^{-2}, Fig. 3.8 (b) panels b and c), while the p_z orbitals

of the outermost N mostly takes part to the formation of a charge dipole. Finally, between the Nb atoms of the first layer and the N atoms of the second one, a second row of dipoles appears. On the other hand, if large electric fields are considered ($\Delta n_{2D} \geq 8 \times 10^{14}$ cm^{-2}, Fig. 3.8 (b) panels e and f), an accumulation layer across the $[x,y]$ plane is formed, detached from the Nb orbitals with the simultaneous formation of dipoles (in counterphase) involving the Nb and N atoms at least up to the third atomic layer. As a consequence, for large electric fields, the effective screening length goes well beyond the first atomic layer (i.e. is way larger than $\sim$ 1Å) and it increases with increasing values of Δn_{2D}.

While this qualitatively agrees with the esperimental evidence of Ref. 220, a more quantitative analysis is more problematic. Indeed, only the conduction band is probed by transport measurements (i.e. the carriers that lay in an energy window of about $k_B T$ around the chemical potential [272]), which is difficult to identify from the DFT analysis of a surface due to folding of multiple bands. Moreover this problem is harder for systems with pre-existing mobile charges. Another problem lies in the definition of the screening length from DFT computations, which however has to agree with simpler models such as the linear Thomas-Fermi theory. Indeed this latter shows an exponentially screened electric field on a typical length-scale equal to the Thomas-Fermi screening length λ_{TF}. However, from an experimental point of view, the penetration length is computed assuming a step-like model for the screening charge density [270, 271, 220]. Moreover, in both cases the atomistic details are missing, while the charge density profiles obtained by DFT take them into account.

As a consequence, I considered a layer as perturbed when the electronic charge density in its proximity is modified by $\pm$30% of its value in the accumulation layer and the effective screening length will be equal to the number of perturbed layers. In Fig. 3.9 I have plotted the DFT results, together with the experimental measurements and the d_s computed through the non-linear screening model in units of the spacing between two layers in the bulk. From a qualitative point of view, the DFT esteems of d_s are clearly in agreement with the experimental ones. However from a quantitative point of view, they may be vary a little bit according to the threshold we used for defining the number of perturbed layers.

Moreover, the values extracted from transport measurements are based on a step-like model for the induced charge density. However, from this ab-initio analysis it is possible to see that:

- for low to moderate electric fields, the screening charges are localized around the first atomic layer;
- for large electric fields, the induced charge density distribution extends beyond the first unitary cell.

reproducing the anomalous screening behavior observed experimentally [220].

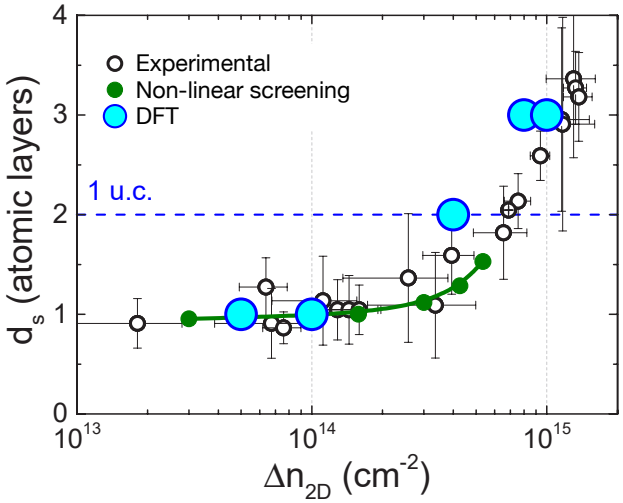

Fig. 3.9 Number of atomic layers involved in the screening of the electric field, as a function of the induced charge density Δn_{2D}. DFT computations are represented by blue dots, experimental measurements by black dots [220] and screening lengths computed via non-linear Thomas-Fermi model by green dots [220]. Figure is taken from Ref. 269

3.3 Ab-initio treatment of gated 2D materials and surfaces

In recent years, a lot of effort has been put in correctly modelling 2D materials in a density functional theory framework [273–275]: as a matter of fact, such systems are particularly sensitive to external perturbations (e.g. an applied electric field, as discussed above for the FET experiments) due to their reduced dimensionality. Moreover, as for the dynamical properties of the lattice, 2D systems show a different phonon dispersion with respect to their 3D counterparts. Indeed the presence of vacuum along the non periodic direction, i.e. the one perpendicular to the sample surface, is such that out-of-plane forces and stresses are smaller with respect to in-plane ones. As a consequence, this will lead to different phonon modes when dimensionality is reduced.

We call z the non-periodic direction. As a consequence, the out-of-plane modes will be labelled with Z. On the other hand, in-plane phonons will still be labelled with L (longitudinal modes) or with T (transverse modes). Moreover, we denote with A the acoustic modes, while O will be used for optical modes. Therefore, a 2D system with N atoms in the unit cell will shows 1 out-of-plane acoustic mode (ZA), 2 in-plane-acoustic modes (TA and LA), $N-1$ out-of-plane optical modes (ZO) and $2(N-1)$ in-plane optical modes (evenly distributed between LO and TO).

Let us consider in more detail the acoustic modes and analyze their dispersion relations in a 2D system, as compared to a bulk 3D one. In a 3D bulk system, we have three acoustic modes which tend to zero linearly as $\mathbf{q} \to \Gamma$ and therefore $\omega = v_s|\mathbf{q}|$ (where v_s is the sound velocity). However, in the 2D counterpart only the LA and TA modes have this linear dependence between the phonon frequency and the phonon momentum $\mathbf{q}$. Due to rotational symmetry, the ZA mode of a 2D system has a quadratic dispersion relation [49] as $\mathbf{q} \to \Gamma$, i.e. $\omega = \alpha|\mathbf{q}|^2$ (with $\alpha = \sqrt{k_0/\rho_0}$, k_0 being the bending rigidity of the material and ρ_0 its mass density). This mode generates out-of-plane ripples in the 2D structure and, as a consequence, it is called flexural phonon mode. As an example I show in Fig. 3.10 (a) the phonon dispersion relation for a monolayer of hexagonal boron nitride (hBN), while in Fig. 3.10 (b) the phonon eigenmodes computed at the center of the Brillouin zone (i.e. $\mathbf{q} = \mathbf{\Gamma}$).

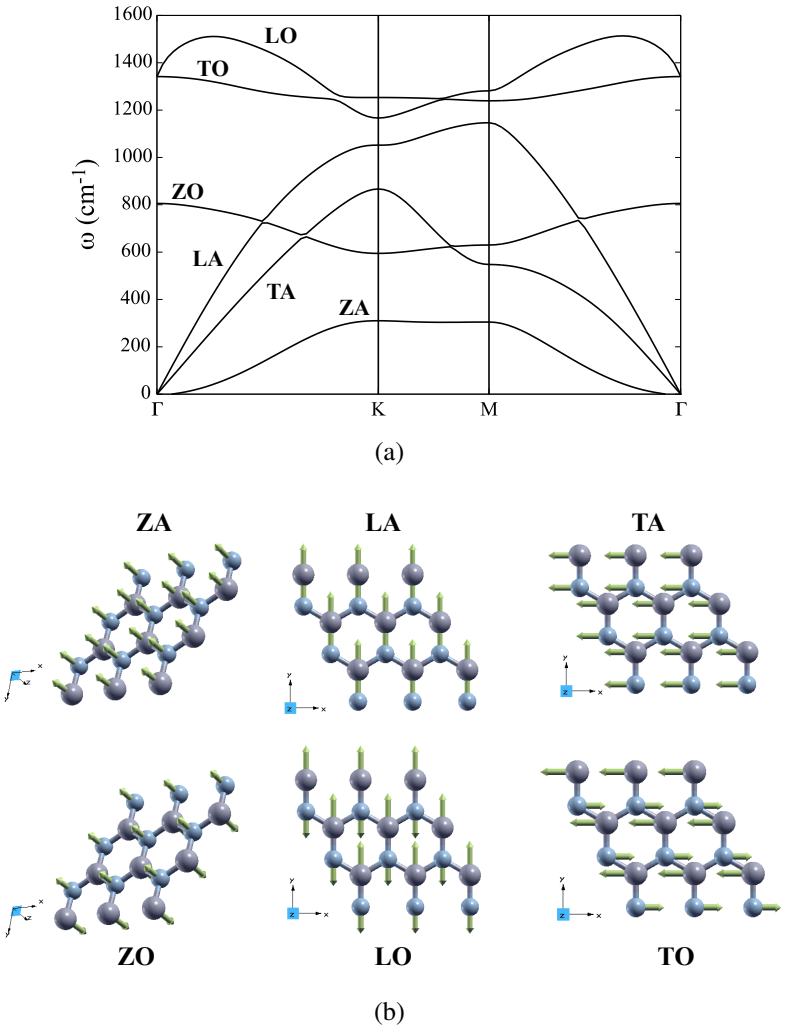

Fig. 3.10 (a) Phonon dispersion relation for a monolayer of hexagonal boron nitride (hB). (b) Phonon eigenmodes of monolayer hBN computed at $\mathbf{q} = \Gamma$.

If we now consider field-effect doping experiments, the re-distribution of the electronic charge density and the presence of an out-of-plane electric field not only modifies electronic properties (such as electronic dispersion relations, density of states, effective masses, etc.) but it can also have a strong impact on lattice dynamical properties. As a matter of fact, the authors of Ref. 242 showed that, in the case of isolated single layer graphene, the mirror symmetry of flexural phonons is broken due to the presence of the electric field leading to a finite electron-phonon coupling linked to a non-zero phonon frequency. Nevertheless, such interaction is negligible

with respect to the in-plane modes and, as such, cannot be detected in transport measurements.

Therefore, a suitable DFT model for both electronic and vibrational properties is required for correctly dealing with 2D or quasi-2D materials in the FET geometry. As I have discussed before in the case of NbN thin films, a method has already been implemented [241, 240] in a plane-wave formalism which gets rid of spurious interaction in the non-periodic direction through a dipole correction. Nevertheless, linear response theory was not developed in such framework, limiting its applicability only for the analysis of the electronic properties. This problem has been solved in Ref. 242, where a density functional perturbation theory approach for gated 2D materials and heterostructures was developed.

The main problem of gated systems lies in the correct representation of the total potential in the out-of-plane direction, at least in a region whose spatial extension is equal to the slab thickness. For this potential it is required that:

- in the vacuum region that does not face the metallic gate, the electrostatic field has to be zero (while the potential has to be constant);
- in the space between the ions forming the electric double layer and the substrate, the electric field is constant (while the potential is linear, with a slope of $\pm 4\pi\Delta n_{2D}$);
- there is a resulting out-of-plane dipolar moment that induces a constant shift in the Kohn-Sham potential;

Therefore, the ions distribution at the electrolyte-semiconductor interface is replaced by a uniform planar distribution of charges of value Δn_{2D} and its potential is included in the external potential of Kohn-Sham equations. Moreover, the dielectric is substituted with a potential barrier between the charge sheet and the (quasi-)2D material in order to prevent charge spilling when doping with electrons: indeed, in this case, the potential does increase linearly from the planar distribution to the substrate causing a possible leakage of carriers from the doped materials, which is unphysical. Finally, the presence of the barrier also prevents the collapsing of the gated 2D material towards the planar charge distribution, since an attractive electrostatic force is present as in between the plates of a capacitor: therefore, a relaxation run of the charged slab will be needed before starting the DFT analysis, so that we can find both its relaxed

structure and its equilibrium position with respect to the potential barrier under the application of an electric field.

Up to this point, the model has the same characteristics of the one we described when dealing with NbN thin films. However, the main difference between the two approaches is in how they deal with periodic boundary conditions required by plane-wave density functional theory. Indeed, while periodicity is preserved along the plane parallel to the surface, this is not true in the out-of-plane direction: as a consequence spurious interactions appear due to repeated images of the charged supercell, in particular the appearence of a dipolar shift in the vacuum region where there should be no electric field. The solution proposed by Refs. 240 - 241 is to add a dipolar correction of opposite polarity which removes this constant shift in the total potential. However, the problem here is that this dipole correction has to be recalculated in a self-consistent way and this approach has not been extended to linear response theory.

In Ref. 242 instead, in order to have effective 2D systems which mathematically fulfill 3D periodic boundary conditions, the authors employed the Coulomb cutoff technique [276–278]: by doing so, all the various terms contributing to the total energy and its derivatives are calculated including a cut-off in the out-of-plane dierection, effectively isolating each slab. In practice, the spurious potentials due to periodic images are set to zero outside a physical region equal to the slab thickness centered around the 2D material: by doing so no other terms such as the dipole correction are needed to be recomputed self consistently and the simple analytical form of the total Kohn-Sham potential allows for a straightforward generalization of the equations of density functional perturbation theory in a 2D framework. The details of the derivation and implementation of such equations are given in Ref. 242.

Summary

- Field-effect (FET) doping allows for an investigation of correlated phases of matter without the inclusion of external dopants;
- Electrochemical gating can induce surface charge densities Δn_{2D} which are ~ 2 orders of magnitudes bigger than solid-state dielectric FET architectures;
- FET doping can generate two different spatial regions in a thin film which are coupled via superconducting proximity effect, leading to non-trivial variations of T_c;
- It is possible to perform ab-initio simulations of (quasi-)2D materials in the FET geometry, by taking fully into account self-consistently the presence of the electric field for the computation of both the electronic and vibrational properties.

Chapter 4

High-T_c Superconductivity in Field-Effect Doped Hydrogenated (111)-Diamond thin films

Generally speaking, superconductivity may arise from the metallization of 3D covalent materials as I discussed in Chap. 1 for the case of boron-doped diamond, but other examples include MgB_2 [279] and H_3S [280]. However, the low solubility limit of boron into the closely packed structure of diamond hinders the possibility of obtaining the high transition temperatures theoretically predicted. An alternative to the pure chemical doping is represented by field-effect doping and in particular by electrochemical doping, which can be used to induce surface charges of the order of $\sim 10^{14} - 10^{15}$ cm^{-2} (depending on the material and on the elctrolyte) as discussed in Chap. 3.

Therefore, in Refs. 281 and 282, using ab-initio techniques [242], I have studied if it was possible to induce a superconductive phase transition in hydrogenated (111)-diamond thin films by means of electrochemical doping. The electric field, acting perpendicularly to the diamond surface, is screened after the first few layers of the sample and affects in a non-trivial way both the electronic and the vibrational properties, thus having an impact also on the electron-phonon interactions.

First of all in Sec. 4.2 I will show how the FET architecture induces a structural relaxation of the system.Then in Sec. 4.3 I will analyze the effect of electrochemical doping on the electronic structure and in Sec. 4.4 I will describe how it affects the vibrational properties of the diamond surface. Then, in Sec. 4.5 I will analyze the possible superconductive phase transition via the McMillan/Allen-Dynes formula: first of all I will employ a simple superconductive model requiring the electron-phonon matrix elements only at the center of the Brillouin zone (i.e. $\mathbf{q} = \mathbf{\Gamma}$) and then I will perform more accurate computations by a finer sampling of the Brillouin zone via a Wannier-interpolation scheme. Finally, in Sec. 4.6 I will study the possible occurrence of a superconductive phase transition more accurately via the self-consistent solution of the single- and multi-band Migdal-Eliashberg equations. Computational details are given in Appendix A.

4.1 Introduction

Since field-effect experiments are applied to surfaces, it is important to understand what is the crystallographic orientation of the sample as it can drastically affect the electronic and vibrational properties due to the presence of surface states even in the undoped case. In general a surface is labelled using three Miller indices (hkl), which designate in the direct space a vector perpendicular to the lattice plane along which the surface is cleaved. Indeed, when we realize a surface starting from a covalent material, bonds are broken leading to *dangling bonds* with unpaired electrons [283]: in such case the surface is metallic but becomes unstable and, as a consequence, it undergoes a *reconstruction* in order to reduce the total free energy. As a consequence the surface will show a reduced symmetry with respect to that of the bulk. This is the case, for example, of the Pandey [284, 285] reconstruction of the diamond surface. When a surface undergoes a reconstruction, its unit cell must be expanded in suitable directions in order to preserve periodicity: this is specified by two additional indices (n$\times$m), such that the lattice constant in the x (y) direction will be multiplied by n (m).

The three possible crystallographic orientations of a diamond surface are the (100), (110) and (111) [27]. Moreover, the dangling bonds can be saturated by hydrogen and this avoids the reconstruction process described above, so that the surface can be studied in the (1$\times$1) supercell. The problem of inducing superconductivity

in diamond surfaces via field-effect doping was already studied for the case of the hydrogenated (110) surface in Refs. 286 and287. In that case, ab-initio computations showed that for increasing doping values (i.e. increasing values of n_{2D}) the Fermi surface is composed first by one and then by two concentric hole pockets centered on the Gamma point: the charge distribution is localized in the first few layers of the material and exceeds the corresponding charge density introduced by boron doping in the bulk counterpart. Employing the McMillan/Allen-Dynes equation (with a Morel-Anderson pseudopotential of $\mu^* \sim 0.1$), the authors predicted that a superconductive phase transition with a critical temperature of $T_c \sim 1$ K can be induced for doping values $n_{2D} > 2.3 \cdot 10^{13}$ cm^{-2} with an electron-phonon constant of $\lambda \sim 0.3$: this happens in correspondence of the crossing of the second band, giving a boost in the electronic density of states at the Fermi level.

When polycrystalline diamond films are grown by chemical vapor deposition (CVD), the natural crystal facets are the (100) and the (111) [288]. Moreover, it has been experimentally shown that the hydrogenated (100) diamond has a surface capacitance of $2.1 - 2.8$ μF/cm^2, while that of hydrogenated diamond (111) is $2.6 - 4.6$ μF/cm^2 [289–291]: as a consequence, the (111) crystallographic orientation allows accumulating larger charge densities, which translates in more carriers at the Fermi level. Therefore, in Refs. 281 and 282 I have studied the effects of electrochemical gating on the electronic and vibrational properties of hydrogenated diamond (111) thin films (Fig. 4.1) using density functional theory (computational details can be found in App. A). I have focused our attention on three doping values: low (i.e. $n_{2D,1} = 2.84 \cdot 10^{13}$ cm^{-2}), medium (i.e. $n_{2D,2} = 1.96 \cdot 10^{13}$ cm^{-2}) and high (i.e. $n_{2D,3} = 6.00 \cdot 10^{13}$ cm^{-2}).

In order to study the superconductive properties in Refs. 281 and 282, I first used the McMillan/Allen-Dynes formula (Eq. 2.58) and then the solution of the multiband isotropic Migdal-Eliashberg equations (Eqs. 2.55). Notice that, as I will show in the next sections, the higher is the induced charge density inside the sample the more the system goes toward a quasi-2D situation, where the use of Eq. 2.58 may not be completely justified: indeed, bidimensional electron gases have large fluctuations [292] that can destroy the long-range order of the electron-phonon interaction, and other mechanisms might in principle arise [293]. Nevertheless, I assumed that Eq. 2.58 is still valid and I considered the computed value as an upper bound for the true critical temperature.

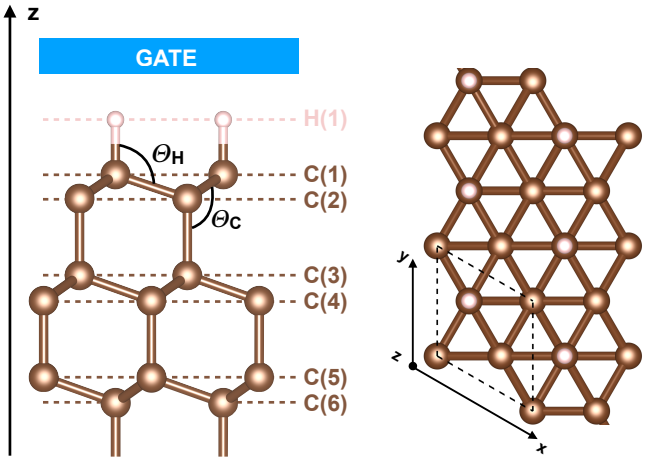

(a) (b)

Fig. 4.1 Ball-and-stick model of the atomic structure of the hydrogenated (111) diamond surface: (a) side view, (b) top view. H atoms are represented by pink spheres while C atoms by the brown ones. The unitary cell is identified by black dashed line. The angle between H and C(2) atoms is labelled by Θ_H, while Θ_C is the angle between C(1) and C(3) atoms. Figure taken from Ref. 281.

4.2 Structure relaxation and the induced charge density

First of all it is interesting to understand if the presence of the electric field affect the structure of the system. For the lowest possible doping value ($n_{2D,1}$), only the bond between hydrogen and the first carbon layer (H-C(1), see Fig. 4.1) is affected, being shortened by 0.14% with respect to the undoped case. All the other interatomic distances vary only by $\sim 0.03-0.05\%$. The angles $H\widehat{C(1)C(2)}$ and $C(1)\widehat{C(2)C(3)}$, i.e. Θ_H and Θ_C respectively, are also unaffected. Moving to medium doping ($n_{2D,2}$) the H-C(1) bond length is shortened by 0.72% while the distances between carbon atoms of the first and second layer (C(1)-C(2)) are elongated by 0.37%, while the interatomic length C(2)-C(3) is slightly reduced by 0.25%. Consequently, Θ_H and Θ_C increase repectively of by 0.57%. Finally, when the highest doping value ($n_{2D,3}$) is reached, the electric field mainly affect the first three carbon layers: the H-C(1) distance is shortened by 0.97%, the C(1)-C(2) bond length increases by 0.85% and the C(2)-C(3) one is reduced by 0.45%. Consequently, also Θ_H and Θ_C are greatly modified, being increased by 1.26%. The variations of the bond distances and angles are summarized in Tab. 4.1.

n_{2D} (cm^{-2})	0	$2.84 \cdot 10^{13}$	$1.96 \cdot 10^{14}$	$6 \cdot 10^{14}$
H - C(1)	1.109Å	1.107Å	1.101Å	1.098Å
C(1) - C(2)	1.536Å	1.537Å	1.542Å	1.549Å
C(2) - C(3)	1.554Å	1.555Å	1.550Å	1.547Å
Θ_H	108.55°	108.64°	109.18°	109.92°
Θ_C	108.55°	108.64°	109.18°	109.92°

Table 4.1 Structural parameters of the hydrogenated (111) diamond surface in FET geometry the three doping values considered, labelled according to Fig. 4.1. Table taken from Ref. 281.

It is clear that structural modifications are more pronounced as the magnitude of the electric field (and also of the induced charge density as a consequence) increases. The bond between hydrogen and the first carbon layer is the most affected in all three cases, while the underlying second and third layers undergo structural modifications only for medium to high doping. The changes in bond lengths suggest a redistribution of the electronic charge density due to the presence of the electric field inside the material. In order to understand if there was a correlation between the structural variations and the charge redistribution, I studied the profile of the charge density induced by the field in the FET geometry. Indeed charges redistribute inside the material in order to screen the electric field which is penetrating inside the slab. The induced charge density is defined as:

$$\rho_{||}^{\mathrm{ind}}(z) = \rho_{||}^{\mathrm{h}}(z) - \rho_{||}^{0}(z) \tag{4.1}$$

where $\rho_{||}^{\mathrm{h}}(z)$ and $\rho_{||}^{0}(z)$ are the planar-averaged charge densities for the hole-doped and undoped cases respectively.:

$$\rho_{||}^{\mathrm{i}}(z) = \frac{1}{\Omega_{2D}} \int_{\Omega_{2D}} \rho_{3D}^{\mathrm{i}}(x,y,z)dxdy \tag{4.2}$$

with Ω_{2D} the area of the unitary cell and $\rho_{3D}^{\mathrm{i}}(x,y,z)$ is the 3D charge density for the hole-doped (i = h) and undoped (i = 0) cases, both computed for the slab with relaxed atomic positions in the FET geometry.

On the other hand, the 3D charge density is defined as:

$$\rho^{\mathrm{i}}_{3D}(x,y,z) = \frac{e}{N_k} \sum_{\sigma,\mathbf{k}\in \mathrm{FBZ}} \sum_{n=0}^{E_F} \left|\psi^{\sigma}_{\mathbf{k},n}(x,y,z)\right|^2 \tag{4.3}$$

where e is the electron charge, N_k is the number of k points belonging to the first Brillouin zone (FBZ), σ is the spin index, n is the band index, E_F is the Fermi energy and $\psi^{\sigma}_{\mathbf{k},n}(x,y,z)$ is the Bloch wavefunction for band n, spin σ and k-point $\mathbf{k}$. The planar-averaged induced charge density profiles are shown in Fig. 4.2, together with the normalized cumulative integral of the absolute value of the planar-averaged charge density:

$$\frac{1}{\int_0^L \left|\rho^{\mathrm{i}}_{||}(z)\right| dz} \cdot \int_0^c \left|\rho^{\mathrm{i}}_{||}(z)\right| dz \quad \text{for } c \in [0;L] \tag{4.4}$$

where L is the size of the cell.

The induced charge density profiles contain information on both the re-arrangement of the pre-existing valence electrons and the added electrons due to field-effect doping, which contribute together to the screening of the electric field [269]. Negative (positive) values of $\rho^{\mathrm{ind}}_{||}(z)$ correspond to electron depletion (accumulation). For low doping ($n_{2D,1}$), the pre-existing charge plus the added one is not sufficient to screen the electric field to short distances and, consequently, six layers are affected by charge redistribution: indeed 70% of the integrated charge is reached after three atomic layers (i.e. 6 carbon layers). However, the higher is the value of n_{2D} the more peaked are the charge fluctuations comprising the first four (for $n_{2D,2}$) or two (for $n_{2D,3}$) carbon layers: an effective 2D electron gas confined at the surface of the system is obtained.

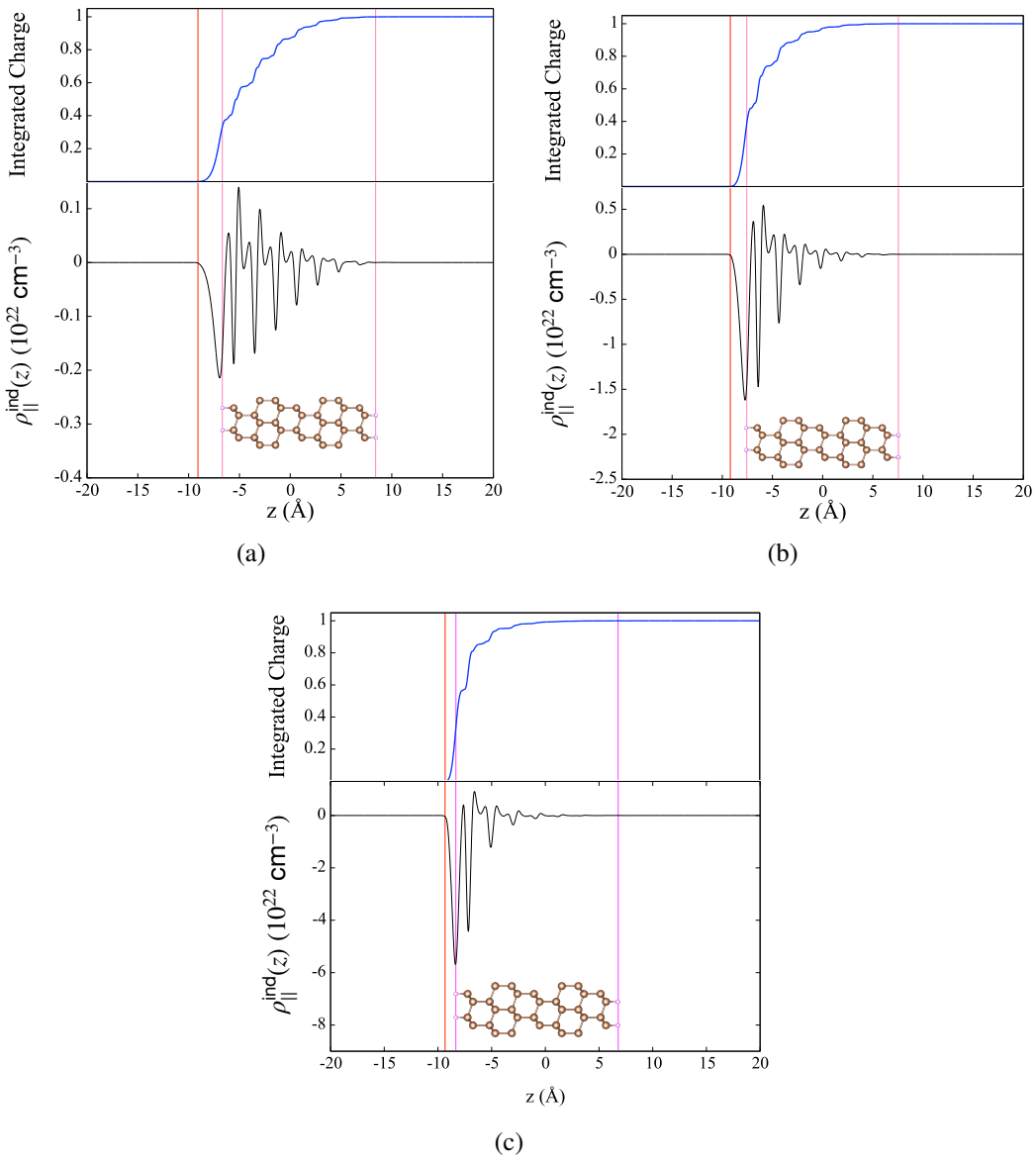

Fig. 4.2 Planar-averaged induced charge density ($\rho_{||}^{\mathrm{ind}}(z)$) and normalized cumulative integral of the absolute value of the planar-averaged charge density (integrated charge): (a) $n_{2D,1}$, (b) $n_{2D,2}$ and (c) $n_{2D,3}$. The pink lines locates the hydrogen layer (showing also the beginning and the end of the surface), while the red lines locates the potential barrier that prevents charge spilling. Figure taken from Ref. 281.

4.3 Electronic structure and electric field exfoliation of surface states

I will now present the electronic properties of the hydrogenated diamond-(111) surface as a function of doping. First of all in Fig. 4.3 I have plotted the electronic band structure for the three different values of n_{2D} when computed both via the FET model (black solid line) and via the jellium model (blue dashed line). The latter is a doping model where added charges are spread uniformly inside the slab with an oppositely charged background that makes the system neutral and avoids the $\mathbf{k} \to 0$ divergence of the Coulomb interaction.

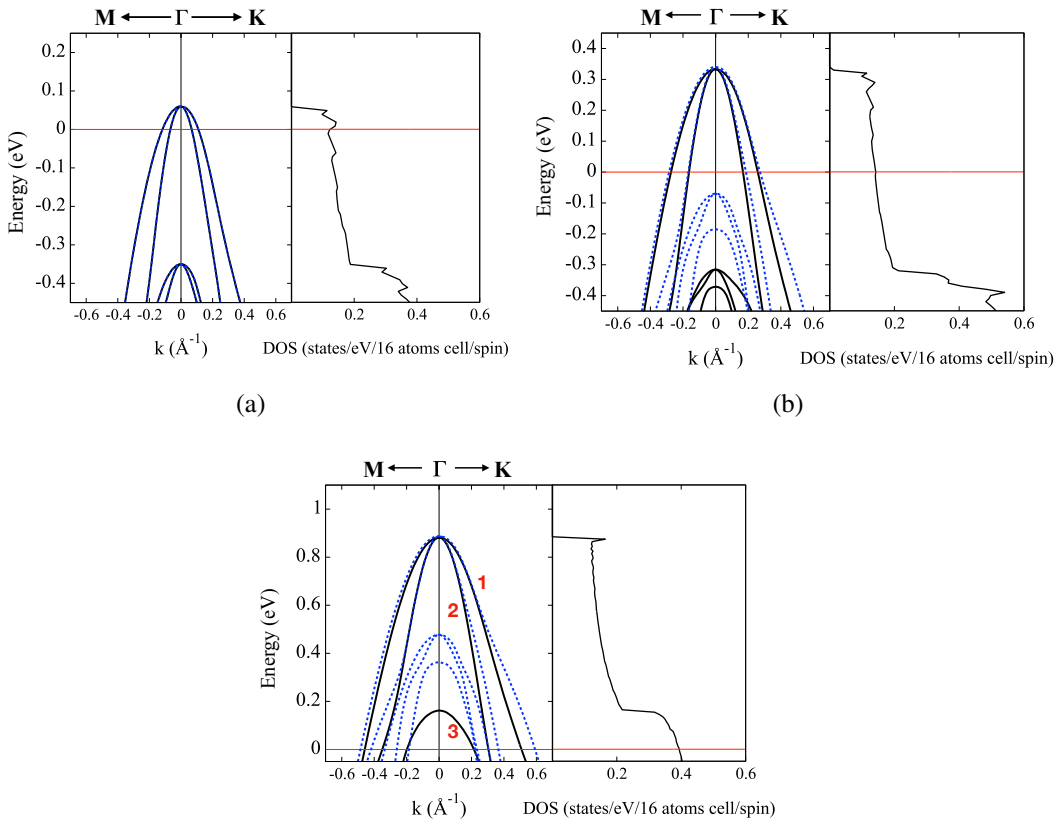

Fig. 4.3 Electronic band structure (black solid lines) and density of states (DOS) of the hydrogenated (111) diamond surface with (a) $n_{2D,1}$, (b) $n_{2D,2}$ and (c) $n_{2D,3}$. We also plot the electronic structure obtained from the uniform doping (i.e. the jellium model, blue dashed lines) as a reference. The red line represents the Fermi level. Figure taken from Ref. 281.

As soon as the system is doped, the Fermi level ($E_F = 0$, red line) appears crossing the valence bands. Hereafter, I will refer to the crossed bands according to the labels of Fig. 4.6 (c). For $n_{2D,1}$ E_F is just below the top of the first two valence bands. However when the doping value is increased, the Fermi level lowers crossing a third band for $n_{2D,3}$. Moreover, for medium to high doping the effect of the electric field is so intense that it removes the double degeneracy at $\mathbf{k} = \mathbf{\Gamma}$ (i.e. the center of the Brillouin zone) of the third band: indeed the static perturbation acting along the z direction breaks the inversion symmetry, lifting any degeneracy among eigenvalues resulting from simple group theoretical considerations.

From this consideration it is possible to understand that while the first two bands have an in-plane character (i.e. planar $[xy]$), the third one has an out-of-plane character (i.e. z). As a final remark, the energy gap is also reduced upon increasing the magnitude of the doping due to the fact that valence bands are shifted upward, while the conduction band (not shown) downward. Comparing the FET and jellium model it is clear that the latter is unable to catch all of these effects: indeed it would roughly correspond to a rigid shift of the occupied bands, preserving the various degeneracies among eigenvalues. These results are summarized in Tab. 4.2.

n_{2D} (cm^{-2})	E_G	$\Delta E_{V,1}$	$\Delta E_{V,2}$	$\Delta E_{V,3}$
$2.84 \cdot 10^{13}$	3.516 eV	58.6 meV	58.6 meV	Not Crossed
$1.96 \cdot 10^{14}$	2.525 eV	331.7 meV	331.7 meV	Not Crossed
$6 \cdot 10^{14}$	1.717 eV	880.2 meV	880.2 meV	161.6 meV

Table 4.2 Energy gaps (E_G) and energy difference between the Fermi energy and the top of valence bands ($\Delta E_{V,i}$, $i = 1,3$) for three different doping values (n_{2D}). Table taken from Ref. 281.

The right-hand panels of Fig. 4.3 a-c show the density of states as a function of energy. In all cases, the DOS is almost constant around the Fermi level, i.e. $\mathrm{DOS}(\varepsilon) \sim$ const., which is the typical energy dependency of 2D systems. For $n_{2D,1}$ a relatively high DOS at E_F is immediately reached, which is due to two bands crossing, but it almost becomes three times larger when crossing the third band (Tab. 4.3). This system has a multiband nature, therefore I had to quantify the contribution to the total density of states from each single energy band: indeed, this information is important for understanding the origin of the electron-phonon

interactions, being directly proportional to the density of states per spin per band. While band 2 and 3 contribute similarly to the total DOS (Tab. 4.3), the contribution of band 1 is $\sim 2-3$ times bigger for all three doping values. As a consequence, the electron-phonon interactions is expected to prevalently concern electrons hosted by the first band.

n_{2D} (cm^{-2})	$N_\sigma(0)$	$N_\sigma(0)$	$N_{2\sigma}(0)$	$N_{3\sigma}(0)$
$2.84\cdot10^{13}$	0.1319	0.0956	0.0363	None
$1.96\cdot10^{14}$	0.1427	0.1052	0.0375	None
$6\cdot10^{14}$	0.3930	0.1783	0.1088	0.1059

Table 4.3 Total density of states per spin $N_\sigma(0)$ and band contributions to the total density of states $N_{i\sigma}(0)$ (i $= 1,3$) at the Fermi level ($E_F = 0$) for the hydrogenated (111) diamond surface, in units of states/eV/16 atoms cell/spin. Bands are labeled according to Fig. 4.6 (c). Table taken from Ref. 281.

It is possible to extract more details regarding the nature of the electronic bands from the projected density of states on atomic orbitals (PDOS). First of all it is interesting to see that the in-plane ([xy]) and out-of-plane ([z]) components of the total DOS (Fig. 4.4, central panels). Band 1 and 2 come from eigenvalues whose symmetry group is related to in-plane rotations and translations, while band 3 is connected with out-of-plane transformations: that is why the last crossed band is the most affected by the presence of the electric field along the out-of-plane direction. Moreover the PDOS contribution at the Fermi level of band 3 is always much smaller than that of band 1 and 2 for $n_{2D,1}$ and $n_{2D,2}$, while they all become comparable when high doping values are reached.

Finally, it has been shown that the induced charge density gets more and more localized at the surface upon increment of the doping: this aspect can be also linked to the projected density of states over the carbon atoms of the slab (Fig. 4.4, right-hand panels). For low doping, charge fluctuations are spread well inside the slab and indeed this is mirrored by the high contribution to the total DOS from C(3). However, this latter quantity gets smaller and smaller with respect to the C(1) and C(2) PDOS as I go from intermediate to high doping values, confirming that in such situations carriers are being confined on the first few layers of the sample.

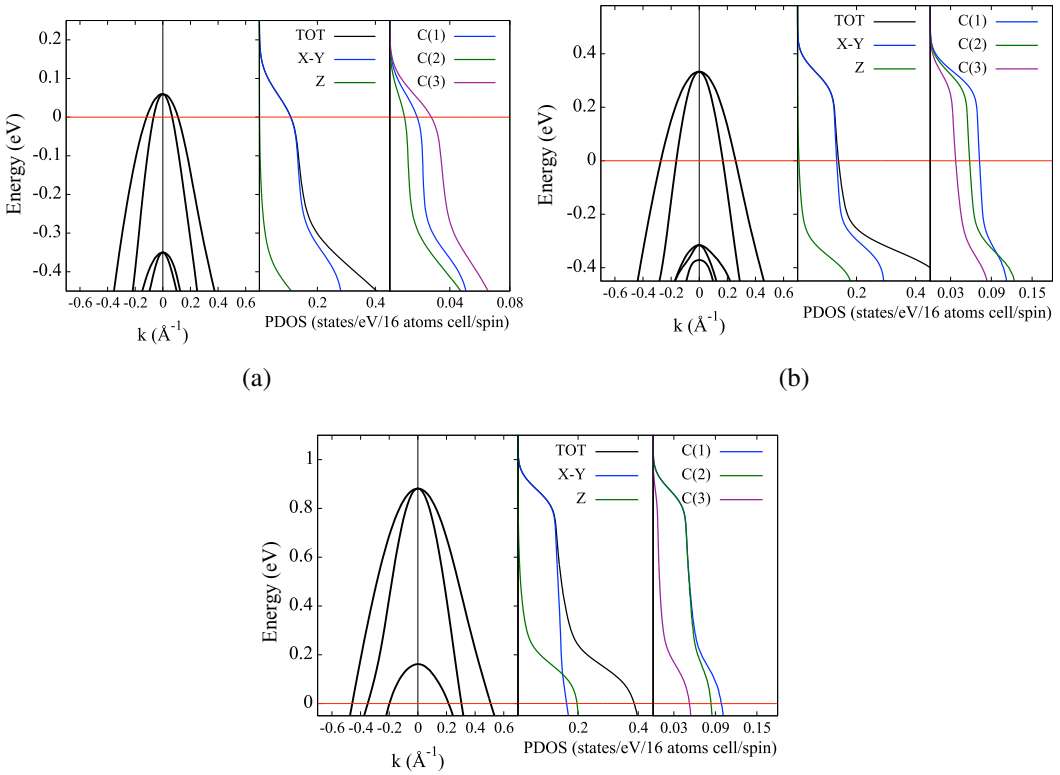

Fig. 4.4 Electronic band structure and projected density of states (PDOS) of the hydrogenated (111) diamond surface with (a) $n_{2D,1}$, (b) $n_{2D,2}$ and (c) $n_{2D,3}$. The red line represents the Fermi Energy. Central panel: in-plane ([xy]) and out-of-plane ([z]) components of the PDOS. Right panel: DOS projected onto C(1), C(2) and C(3) carbon atoms. Figure taken from Ref. 281.

It is therefore important to distinguish between surface and bulk electronic states. In order to do so, in Fig. 4.5 I have plotted the electronic band structure of the hydrogenated (111)-diamond slab and the surface-projected bulk-diamond electronic bands on top of each other. The latter can be obtained by computing the band structure of diamond oriented along the (111) crystallographic direction in its bulk form keeping fixed $\mathbf{k}_{||}=(k_x,k_y)$ along paths parallel to $\mathbf{\Gamma}$-M-K-$\mathbf{\Gamma}$ and at the same time varying k_z between 0 and π/c (where c is the height of the primitive cell): as a consequence, for an infinite discretization of the $[0;\pi/c]$ range, a continuum of bulk bands is obtained, which can be seen in Fig. 4.5 and Fig. 4.6 as gray-shaded regions. When the band structure of the slab is superimposed to this continuum, electronic

states that fall outside represent surface states while the others are considered bulk states.

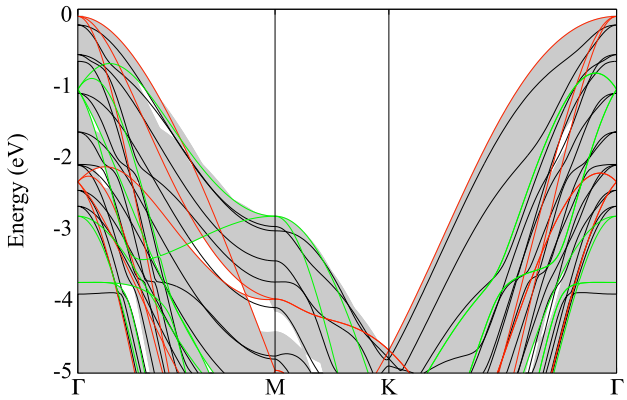

Fig. 4.5 Band structure of the undoped hydrogenated (111)-diamond surface (black lines) on top of the surface-projected bulk-diamond electronic structure (grey shaded regions). Red (green) lines correspond to the bulk band structure computed for $k_z = 0.0$ ($k_z = 0.5$) in crystal coordinates. Figure taken from Ref. 281.

Notice that the bulk and surface band structure have to be properly aligned in energy when superimposed: indeed, the surface can be seen as a perturbation to the charge distribution as it represents an interface between vacuum and the system and, as such, it generates a discontinuity in the electrostatic potential. This is similar to what happens at the interface between two semiconductors or between a metal and a semiconductor: these situations generate a Schottky barrier and the valence band discontinuity across the interface is related to the height of such barrier. If the electrostatic potential on the two different sides of the interface is aligned, it is possible to compute the *band offset*, i.e. the energy difference between the top of the valence band of the bulk and that of the surface.

In order to do so, first of all we define the planar-averaged electrostatic potential similarly to the planar-averaged charge distribution:

$$V_{||}(z) = \frac{1}{\Omega_{2D}} \int_{\Omega_{2D}} V_{3D}(x,y,z)dxdy \tag{4.5}$$

where $V_{3D}(x,y,z)$ is the 3D electrostatic potential. After that, I computed its *macroscopic average* [294] in order to extract the phenomena only relevant to the interface. The macroscopic average is just an average of the 3D electrostatic potential performed in a spatial window of width a, whose size has to be selected in order to filter

out the microscopic details of the system:

$$\tilde{V}_{||}(z) = \frac{1}{a}\int_{z-a/2}^{z+a/2} V_{||}(s)ds \tag{4.6}$$

Then, the computational scheme for finding the band alignment, both for the undoped and doped surface, proceeds as follows:

- Compute the macroscopic average of the planar-averaged electrostatic potential for the hydrogenated (111)-diamond. The reference energy for the surface will be taken to be coincident with its value in the bulk-like region of the slab ($\varepsilon_{\mathrm{RS}}$). Then, define $\Delta\varepsilon^{\mathrm{S}} = \varepsilon^{\mathrm{S}}_{\mathrm{VB}} - \varepsilon_{\mathrm{RS}}$ as the energy difference between the top of the valence band ($\varepsilon^{\mathrm{S}}_{\mathrm{VB}}$) and the reference energy of the slab;
- Compute the macroscopic average of the planar-averaged electrostatic potential for bulk diamond. The reference energy for the bulk system will be taken to be coincident with its mean value ($\varepsilon_{\mathrm{RB}}$). Then, define $\Delta\varepsilon^{\mathrm{B}} = \varepsilon^{\mathrm{B}}_{\mathrm{VB}} - \varepsilon_{\mathrm{RB}}$ as the energy difference between the top of the valence band ($\varepsilon^{\mathrm{B}}_{\mathrm{VB}}$) and the reference energy of the bulk;
- The band offset between the electronic dispersion relations of the slab and that of the surface-projected bulk is given by $\Delta\varepsilon^{\mathrm{SB}} = \Delta\varepsilon^{\mathrm{S}} - \Delta\varepsilon^{\mathrm{B}}$: This quantity represents the energy shift of the surface bands when plotted on top of the bulk projected bands.

From this analysis it is possible to see from Fig. 4.5 that, when the undoped surface is considered, all electronic bands are bulk states since they fall inside the gray-shaded regions. Nevertheless, for increasing doping values, the band shift increases. For $n_{2D,1}$ there is still a bulk-like situation (Fig. 4.6(a)) and this corresponds to a charge distribution that spreads well-inside the slab (Fig. 4.2(a)): as a consequence it is not possible to distinguish the surface from the bulk from an electronic point of view. However, for $n_{2D,2}$ and $n_{2D,3}$ the Fermi level crosses bands which fall outside the bulk-continuum and therefore they acquire a surface-like character as illustrated in Fig. 4.6(b) and Fig. 4.6(c): as a consequence the charge density profile will be strongly localized on the first few layers of the system (Fig. 4.2(b)-(c)). In Ref. 281, I referred to this phenomenon as *electric exfoliation*.

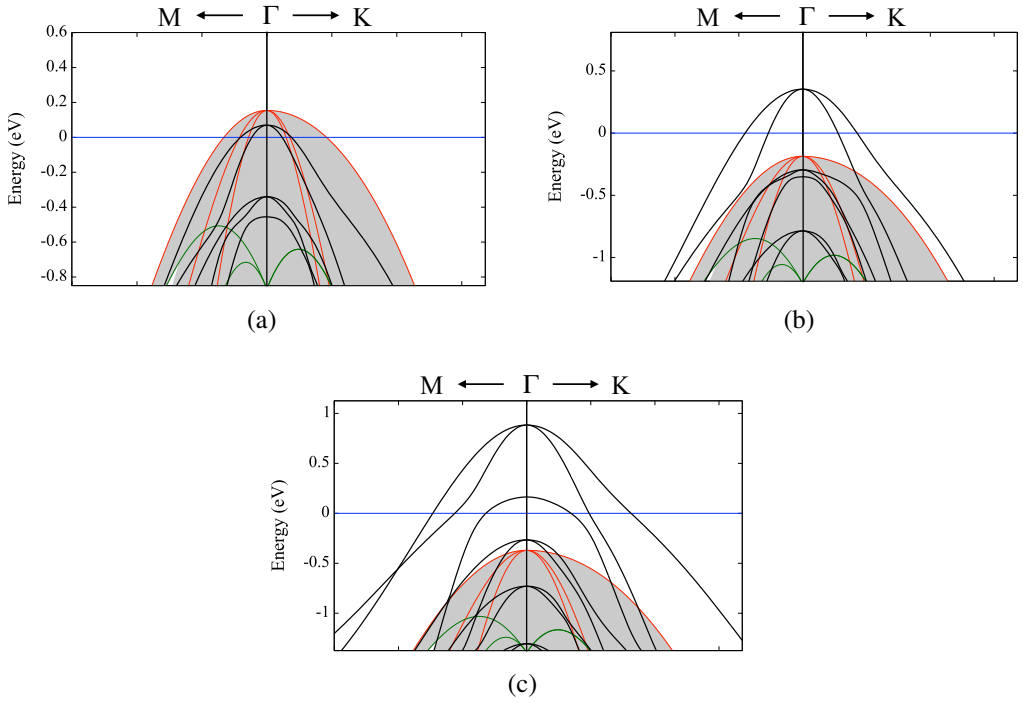

Fig. 4.6 Band structure of the doped hydrogenated (111)-diamond surface (black lines) on top of the surface-projected bulk-diamond electronic structure (grey shaded regions). The three doping regimes are: (a) $n_{2D,1}$, (b) $n_{2D,2}$ and (c) $n_{2D,3}$. Red (green) lines correspond to the bulk band structure computed for $k_z = 0.0$ ($k_z = 0.5$) in crystal coordinates. The blue line is the Fermi level. Figure taken from Ref. 281.

As a final remark, I studied the evolution of the Fermi surface as a function of n_{2D}: the various Fermi sheets are labelled according to Fig. 4.7, where the first band correspond to the blue line and will be labelled FS1, FS2 stands for band 2 and is associated to the green line and the band 3, called FS3, to the aqua line. Indeed, as soon as charges are induced on the first few layers of our systems, these get metallic and, consequently, a Fermi surface appears. Its extension is dependent on the charge doping and, as a matter of fact, it occupies a bigger and bigger region of the Brillouin zone as we pass from low to high doping values. In particular for $n_{2D,1}$ two small concentric hole pockets (FS1 and FS2) around the center of the Brillouin zone (i.e. $\mathbf{k} = \mathbf{\Gamma}$) appear: the system is a "bad" metal, in the sense that it has poor conduction properties due to low carrier concentration at the Fermi level. This situation has been observed by Yamaguchi et al. [289, 290], who were able to lead their sample of the verge of an insulator-to-metal transition at the same doping level. However, going to medium and high doping, the extension of the Fermi surfaces increases and at $n_{2D,3}$ a third concentric hole pocket appears.

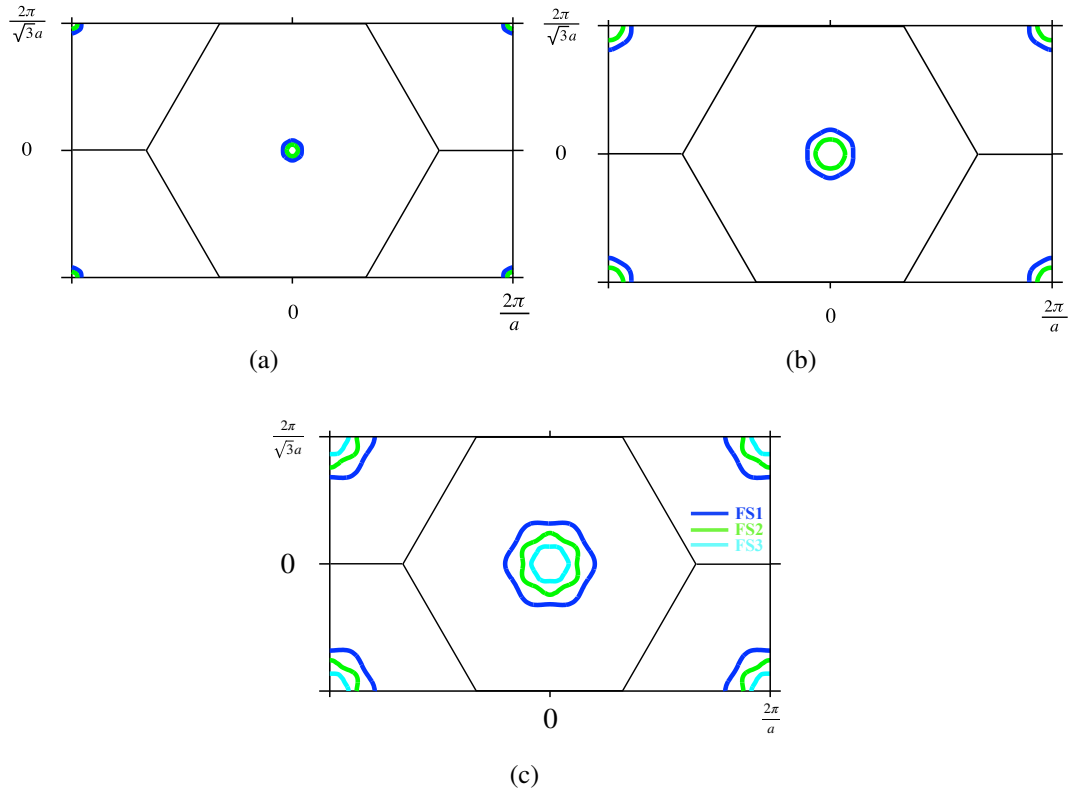

Fig. 4.7 2D Fermi surfaces with (a) $n_{2D,1}$, (b) $n_{2D,2}$ and (c) $n_{2D,3}$. FS1 $\rightarrow$ blue line, FS2 $\rightarrow$ green line and FS3 $\rightarrow$ aqua line. Figure taken from Ref. 281.

4.4 Phonon dispersion and Kohn anomalies

After the discussion of the electronic properties, we can move to the analysis of the dynamical properties of the lattice as a function of doping. In particular I am going to discuss the effects of the electrochemical doping on the phonon dispersion relation and density of states, shown in Fig. 4.8. Notice that the phonon modes are divided into in-plane (red dots) and out-of-plane (blue dots), with the size of the dots dependent on the percentage of the $[xy]$ (in-plane) and $[z]$ (out-of-plane) character at a specific $\mathbf{q}$ point.

First of all, at $n_{2D,1}$, the two degenerate out-of-plane modes of hydrogen are very flat and located at ~ 3000 cm^{-1}, giving two singularities in the phonon density of states. However, moving to medium and high doping values such degeneracy is lifted and the phonon branches acquire more dispersion, smoothing the singularities in the PHDOS. On the other hand the in-plane phonon modes of hydrogen correspond to two degenerate branches at ~ 1132.40 cm^{-1} and other two degenerate branches at 1136.69 cm^{-1}.

As for carbon atoms, their frequencies have a wider range (from 0 to ~ 1400 cm^{-1}) with a very rich and articulate dispersion relation. For all values of the induced charge density, the PHDOS is strongly concentrated around high-energy modes with a dominance of nearly flat in-plane bands (giving a high number of van Hove singularities). On the other hand, the low-frequency part of the phonon dispersion relation is less populated and more smooth from the PHDOS point of view.

Another important aspect that emerges from the phonon dispersion relation is the appearance of a Kohn anomaly [163] (Fig. 4.9, green circles) as a function of doping for an in-plane phonon mode: as we go from low to high values of the induced charge density, the frequencies of such phonon branch are softened more and more (i.e. they get lower and lower). Indeed, such strong renormalization of the phonon frequency is a signature of strong electron-phonon interactions having place in the system, which has already been observed in boron-doped diamond [20, 295] and p-doped graphane [296].

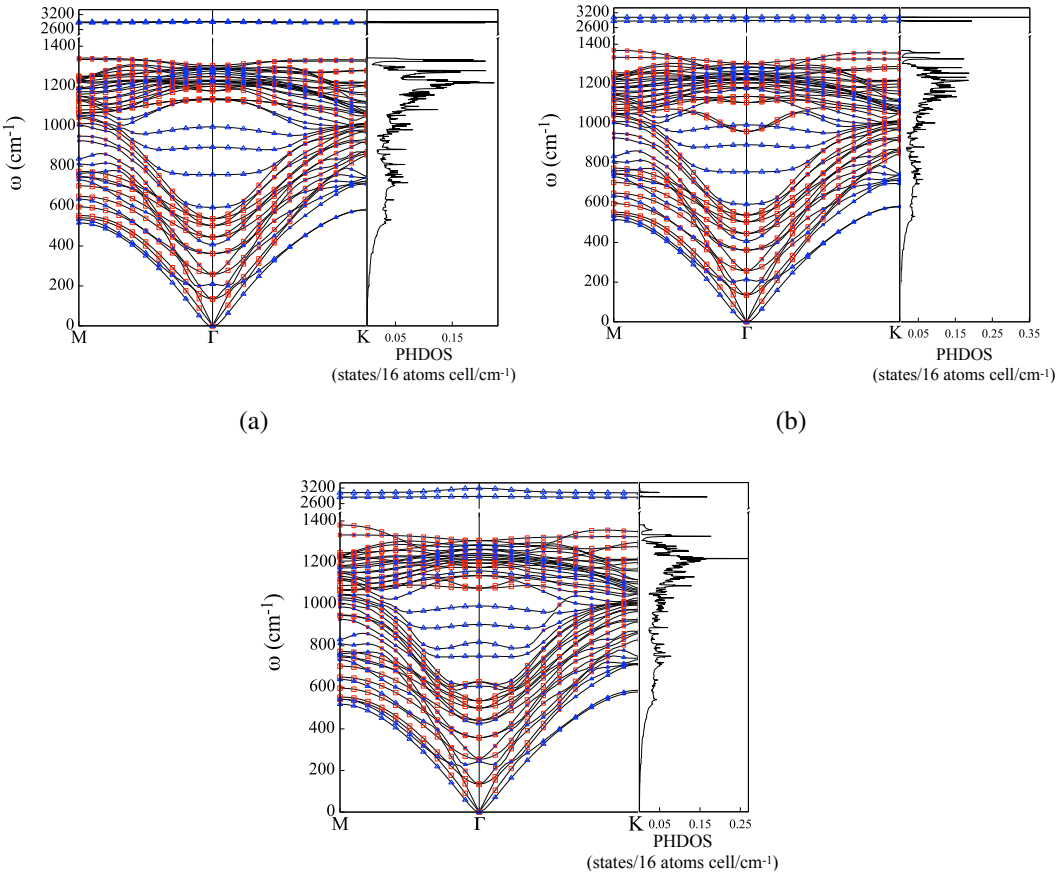

Fig. 4.8 Phonon dispersion relations and density of states (DOS) of the hydrogenated (111) diamond surface with (a) $n_{\mathrm{dop},1}$, (b) $n_{\mathrm{dop},2}$ and (c) $n_{\mathrm{dop},3}$. Red (blue) dots correspond to in-plane (out-of-plane) vibrational modes. The size of the dots correspond to the amount of [xy] or [z] nature of the phonon frequency. For example, the size of the dots for the modes at $\mathbf{\Gamma}$ corresponds to a 100% character, either [xy] or [z]. Figure taken from Ref. 281.

As I already have pointed out in Ch. 2, the many-body nature of the electron-phonon interaction is responsible for the renormalization of both electronic and vibration properties. In particular, when discussing the RPA approximation of the phonon self-energy, I have shown that the dressed phonon frequencies are related to the Lindhard function (Eq. 6.12) which in 3D and 2D has a logarithmic singularity in its first derivative when $\omega = 0$ and $\varepsilon^0_k = \varepsilon^0_{k\pm q}$: this can happen when there is perfect nesting of the Fermi surface, i.e. when a phonon with momentum $\mathbf{q}$ and energy ω scatters an electron from state $\mathbf{k}$ on the Fermi surface to another state $\mathbf{k} \pm \mathbf{q}$ on the Fermi surface ($\varepsilon^0_k = \varepsilon^0_{k\pm q}$). As a consequence, the logarithmic singularity in its first

derivative is mirrored on the discontinuity of the slope of the phonon branch (which gets sharper and sharper as we pass from a 3D to a 2D system).

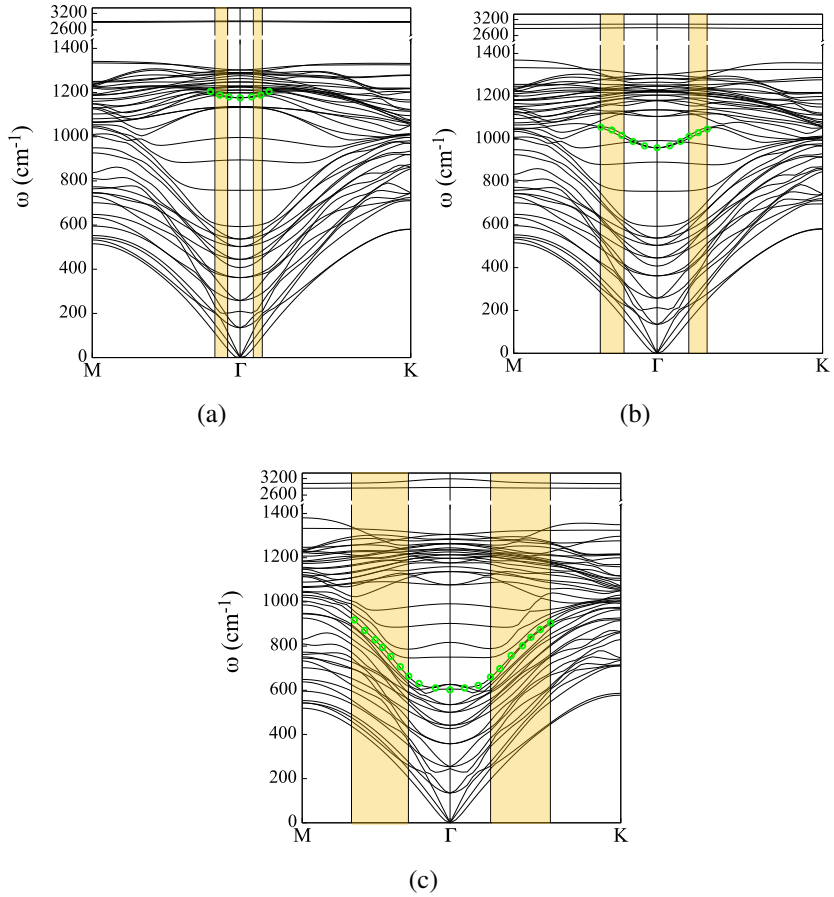

Fig. 4.9 Softening of phonon modes of the hydrogenated (111) diamond surface with (a) $n_{\mathrm{dop},1}$, (b) $n_{\mathrm{dop},2}$ and (c) $n_{\mathrm{dop},3}$. Green dots highlight the band which is actually being renormalized. Orange regions comprise the momenta interval $\mathbf{q} \in [2\mathbf{k}_{F,\mathrm{min}}, 2\mathbf{k}_{F,\mathrm{max}}]$, where $2\mathbf{k}_{F,\mathrm{min}}$ correspond to the smallest Fermi surface while $2\mathbf{k}_{F,\mathrm{max}}$ correspond to the biggest one. Figure taken from Ref. 281.

Assuming circular Fermi surfaces of radius $\mathbf{k}_{F,i}$ ($i = 1,2,3$), in the space of the phonon momenta, it is possible to identify cylindrical regions $\|\mathbf{q}\| \in [2\|\mathbf{k}_{F,\mathrm{min}}\|, 2\|\mathbf{k}_{F,\mathrm{max}}\|]$ ($\mathbf{k}_{F,\mathrm{min}}$ and $\mathbf{k}_{F,\mathrm{max}}$ are, respectively, the wavevectors corresponding to the smallest and largest Fermi surface) that can give rise to Kohn anomalies (Fig. 4.9, orange regions). With a very fine discretization of the reciprocal space, it would have been possible to observe a change in the slope of the phonon branch for each Fermi momentum, however this would be computationally expensive: in the present situation,

it is possible to observe a variation in the slope of the phonon mode in the orange region, which is very small for $n_{2D,1}$ but becomes more evident as we reach $n_{2D,3}$. From this discussion, it is already possible to state that this system is experiencing strong electron-phonon interactions.

4.5 Electron-Phonon Interactions

4.5.1 Computation of electron-phonon matrix elements at $\mathbf{q} = \Gamma$

I first computed the electron-phonon matrix elements for a phonon momentum at the center of the Brillouin zone, i.e. $\mathbf{q} = \mathbf{\Gamma}$, which is computationally inexpensive since it is possible to exploit all the symmetries of the system. The main approximation relies on the assumption that such electron-phonon matrix elements are constant (or nearly constant) in the portion of the phonon momenta phase space where the nesting factor:

$$N_f(\mathbf{q}) = \frac{1}{N_k} \sum_{\mathbf{k},nm} \delta(\varepsilon_{\mathbf{k}n}) \delta(\varepsilon_{\mathbf{k}+\mathbf{q}m}) \tag{4.7}$$

is non-zero (Fig. 4.10).

The summation over $\mathbf{q}$ is limited to those wave-vectors that scatter an electron from the n-th to the m-th Fermi surface thanks to the Dirac deltas appearing in Eq. 4.7 (recall that the Fermi level has been set to $E_F = 0$).

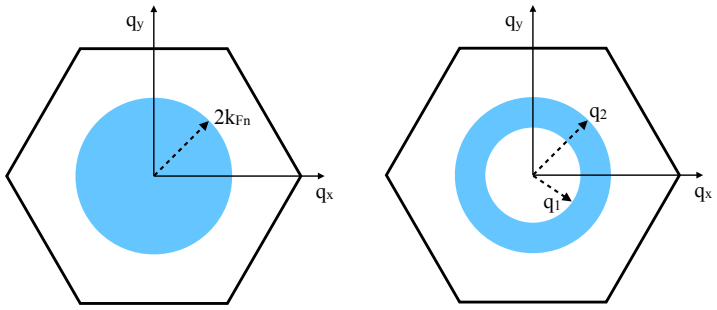

(a) (b)

Fig. 4.10 $\mathbf{q}$-space portions of the Brillouin zone (blue regions) over which the electron-phonon matrix elements are considered to be constant (and thus can be represented by their value at at $\mathbf{q} = 0$) in the case of $n = m$ (a) and $n \neq m$ (b). Figure taken from Ref. 281.

The first Dirac delta imposes that $|\mathbf{k}| = k_{Fn}$, while the second one sets $|\mathbf{k}'| = |\mathbf{k}+\mathbf{q}| = k_{Fm}$. Since the phonon momentum can be written as $\mathbf{q} = \mathbf{k}' - \mathbf{k}$, we get:

$$\begin{aligned} |\mathbf{q}| &= \sqrt{|\mathbf{k}|^2 + |\mathbf{k}'|^2 - 2|\mathbf{k}||\mathbf{k}'|\cos\theta} = \\ &= \sqrt{k_{Fn}^2 + k_{Fm}^2 - 2k_{Fn}k_{Fm}\cos\theta} \end{aligned} \tag{4.8}$$

where θ is the angle between $\mathbf{k}$ and $\mathbf{k}'$. Then electron-phonon matrix elements have been computed at $\mathbf{q} = \mathbf{\Gamma}$ and then considered them constant either in a circle of radius $|\mathbf{q}| = 2k_{Fn}$ (if $n = m$, Fig. 4.10(a)) or in an annulus of radii $|\mathbf{q}_1| = \sqrt{k_{Fn}^2 + k_{Fm}^2 - 2k_{Fn}k_{Fm}}$ and $|\mathbf{q}_2| = \sqrt{k_{Fn}^2 + k_{Fm}^2 + 2k_{Fn}k_{Fm}}$ (if $n \neq m$, Fig. 4.10(b)), with the assumption of spherical Fermi surfaces.

In order to classify the electron-phonon modes according to their strength, I computed the squared average of the electron-phonon matrix elements for each phonon mode ν:

$$\langle g_\nu^2 \rangle_{\mathbf{\Gamma}} = \sum_{n,m} \frac{\left| g^\nu_{\mathbf{\Gamma}n,\mathbf{\Gamma}m} \right|^2 N_{n\sigma}(0) N_{m\sigma}(0)}{N_\sigma^2(0)} \tag{4.9}$$

where $N_{n\sigma}(0)$ is the density of states per spin of band n at the Fermi level, $n,m = 1,2,3$ are band indices (labelling from Fig. 4.7) and ν is the mode index.

At low doping (i.e. $n_{2D,1}$), the strongest electron-phonon matrix elements are associated to two degenerate in-plane modes at $\omega_{\shortparallel} = 1176$ cm^{-1} whose squared average is equal to $\langle g_{\shortparallel}^2 \rangle = 0.167$ eV^2. At this doping there are only two Fermi surfaces and such modes are mainly concerned with intraband $1-1$ and interband $1-2$ scattering processes, while the $2-2$ channel is negligible.

Going to medium doping (i.e. $n_{2D,2}$), the strongest electron-phonon matrix elements still come from two degenerate in-plane modes $\omega_{\shortparallel} = 959.25$ cm^{-1} and a squared average value of $\langle g_{\shortparallel}^2 \rangle = 0.441$ eV^2. There are still only two Fermi surfaces, but this time also the intraband $2-2$ scattering process becomes relevant: this should not be surprising since the size of the second hole pocket has increased and is no longer negligible.

Finally, at high doping (i.e. $n_{2D,3}$), the strongest contributions to the electron-phonon interactions come from two degenerate in-plane modes at $\omega_{\shortparallel} = 626$ cm^{-1} ($\langle g_{\shortparallel}^2 \rangle = 1.105$ eV^2) and a single out-of-plane mode at $\omega_{\perp} = 817$ cm^{-1} ($\langle g_{\perp}^2 \rangle = 0.248$ eV^2). Intra-band scatterings are negligible for the in-plane mode, while they are

the only favored by the out-of-plane mode. The appearance of an out-of-plane phonon among the strongest electron-phonon matrix elements is not surprising due to the presence of the third Fermi hole pocket (which has an out-of-plane nature as discussed in Sec. 4.3, Fig. 4.4 (c)). Moreover, as discussed in Sec. 4.4, the two degenerate in-plane phonon modes are softened upon doping due to the Kohn anomaly (Fig. 4.9).

I then computed the electron-phonon coupling constant λ and the averaged logarithmic frequency $\omega_{\log}$ and, after that, I have used the McMillan/Allen-Dynes formula (Eq. 2.58) to estimate the superconducting critical temperature T_C. The formula for λ and $\omega_{\log}$ in this simplified approach are derived in App. C and are given by:

$$\lambda(\mathbf{\Gamma}) = \sum_{\nu} \frac{N_\sigma(0)\langle g^2_\nu\rangle_{\mathbf{\Gamma}}}{\omega_{\mathbf{\Gamma}\nu}} \tag{4.10}$$

$$\log\omega_{\log}(\mathbf{\Gamma}) = \frac{1}{2\lambda}\sum_{\nu} \frac{N_\sigma(0)\langle g^2_\nu\rangle_{\mathbf{\Gamma}}}{\omega_{\mathbf{\Gamma}\nu}} \log\omega_{\mathbf{\Gamma}\nu} \tag{4.11}$$

where $N_\sigma(0)$ is the electronic total density of states per spin at the Fermi level ($E_F = 0$) and $\omega_{\mathbf{\Gamma}\nu}$ are the phonon frequencies for mode ν computed at $\mathbf{q} = \mathbf{\Gamma}$.

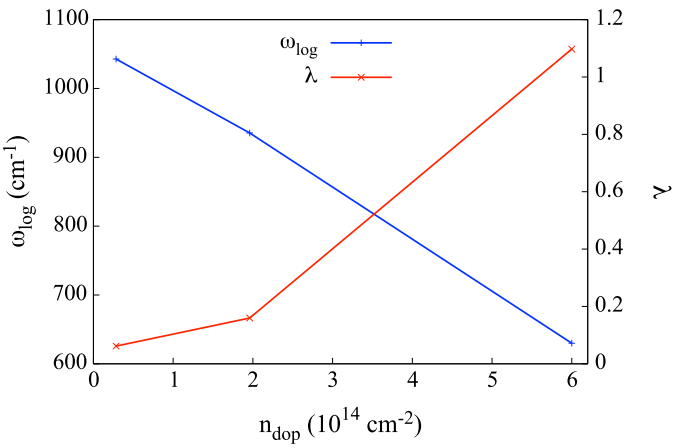

Fig. 4.11 Superconductive parameters (ω_{log} and λ) for the hydrogenated (111) diamond surface as a function of the induced charge density (n_{dop}) computed in the $\mathbf{q} = \mathbf{\Gamma}$ approximation. Figure taken from Ref. 281.

Going from low to large doping, the electron-phonon coupling constant increases while the logarithmic averaged phonon frequency decreases (Fig. 4.11). The phonon softening at $\mathbf{\Gamma}$ of the modes responsible for strongest electron-phonon matrix ele-

ments is responsible for the increase in λ: indeed, the e-ph matrix elements at low frequency are enhanced with respect to those at high frequencies and since $\lambda \propto \omega^{-1}$ their contribution is amplified. As a matter of fact, λ goes from ≈ 0.06 (at $n_{\mathrm{dop},1}$) to ≈ 1.09 (at $n_{\mathrm{dop},3}$). However, since the relevant frequencies become concentrated in the low part of the dispersion relation as they get softened upon doping, the logarithmic averaged phonon frequency ($\omega_{\log}$) decreases.

Inserting the calculated values of λ and $\omega_{\log}$ into the McMillan/Allen-Dynes formula (Eq. 2.58), it is now possible to estimate T_{c}. The only free parameter is the Morel-Anderson pseudopotential μ^*, which has been varied in the typical range of superconductive boron-doped bulk diamond: $\mu^* \in [0.13, 0.14]$ [18]. No superconductive phase transition is found either for $n_{2D,1}$ or for $n_{2D,2}$. On the other hand, only the high doping $n_{2D,3}$ allows for a possible superconductive phase transition with critical temperature in the range $T_{\mathrm{c}} \in [59.50 - 62.48]$ (with the maximum critical temperature obtained with the minimum value of μ^* and vice versa). The electron-phonon coupling constant λ computed for $n_{2D,3}$ is almost three times bigger than that of boron-doped diamond [18] ($\lambda_B = 0.43$): this is reasonable since the local density of holes on the first two carbon layers is one order of magnitude larger than the boron concentration responsible for a $T_{\mathrm{c}} = 4$ K. The striking difference with the low and medium doping regimes can be related to the presence of a third hole pocket in the Fermi surface, which doubles the density of states at the Fermi level. Nevertheless, this might also be an artifact of the simplified superconductive model at $\mathbf{q} = \mathbf{\Gamma}$ that I have employed and, therefore, a more accurate computation of λ and $\omega_{\log}$ is required for the high doping in order to better understand the origin of the superconductive phase transition.

4.5.2 Electron-Phonon computation through Wannier interpolation

In order to analyze the effect of high electrochemical doping on the hydrogenated diamond-(111) surface, I have performed an interpolation of the electron-phonon matrix elements over the whole Brillouin zone via Wannier functions [297], overcoming the limitations of the simplified superconductive model employed before.

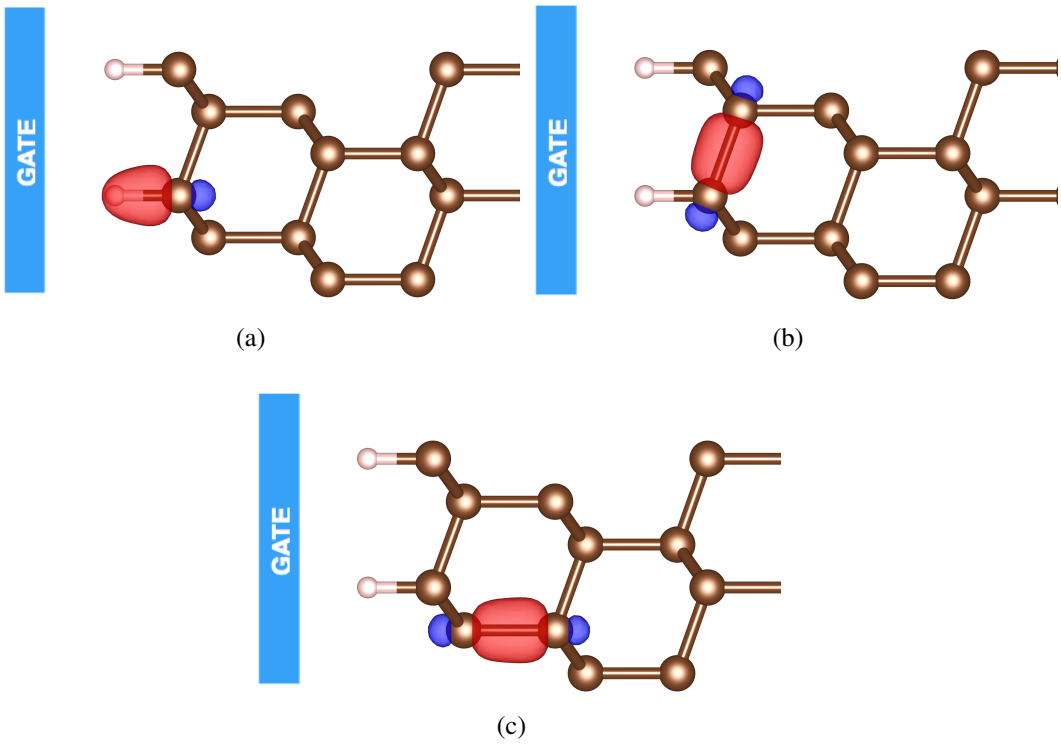

Fig. 4.12 Representative Wannier functions: (a) σ-bond between H 1s and and C(1) sp^3 orbitals; (b) σ-bond between C(1) and and C(2) sp^3 orbitals; (c) σ-bond between C(2) and and C(3) sp^3 orbitals. Red (blue) spheres represent positive (negative) phase of the bond.

It has been shown in Sec. 4.3 that the strongest contribution to the total electronic density of states comes from the first three carbon layers. Therefore, in order to correctly fit the first three electronic bands crossing the Fermi level I exploited Wannier functions with sp^3 symmetries centered on C(1), C(2) and C(3) (Fig. 4.12) for a total of 12 Wannier functions. As a result, the electronic bands computed via plane-wave DFT have been correctly fitted at the Fermi level (Fig. 4.13), i.e. the

Fermi velocities (or the first derivative of the energy bands computed at the Fermi level) have been correctly reproduced by the Wannierization process.

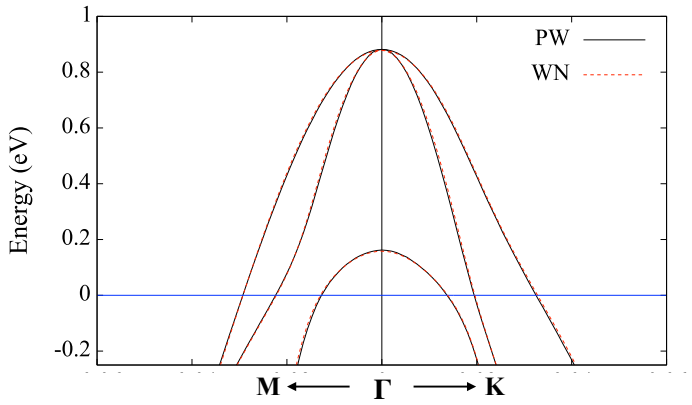

Fig. 4.13 Wannier-Interpolation (WN, red dashed line) of the electronic band structure computed via plane-wave density functional theory (PW, black solid line). The blue line represents the Fermi level, here set to $E_F = 0$.

The resulting electron-phonon coupling constant obtained from the Wannier-interpolation of the electron-phonon matrix elements is $\lambda = 0.81$, which is $\sim 35\%$ smaller with respect to the one obtained from the simplified approach at $\mathbf{q} = \mathbf{\Gamma}$. On the other hand the resulting logarithmic averaged phonon frequency is ~ 40 cm^{-1} larger with respect to the one computed at the center of the Brillouin zone. As a result, the superconductive phase transition occurs at a lower critical temperature $T_c \in [29.60 - 34.93]$ K (with $\mu^* \in [0.13; 0.14]$), i.e. ~ 30 K smaller than the one obtained by diagonalizing the dynamical matrices computed at $\mathbf{q} = \mathbf{\Gamma}$. These results are summarized in Tab. 4.4.

	λ	ω_{log} (cm^{-1})	T_C (K)
$\mathbf{\Gamma}$	1.09	629.94	$62.48 - 59.50$
Wannier	0.81	670.17	$34.93 - 29.60$

Table 4.4 Comparison between the electron-phonon coupling constant λ and logarithmic averaged phonon frequency computed only at $\mathbf{\Gamma}$ and obtained by Wannier interpolation on the whole Brillouin zone for the case at the highest doping. Table taken from Ref. 281.

Thanks to the Wannier interpolation of the electron-phonon matrix elements it is possible to get a further insight on the nature of the superconducting phase transition. Indeed, the total Eliashberg spectral function $\alpha^2F(\omega)$ and electron-phonon coupling constant λ can be directly obtained, as shown in Fig. 4.14 together with the in-plane and out-of-plane components of the phonon dispersion relation. The characteristic feature of the computed $\alpha^2F(\omega)$ is a peak due to softened in-plane modes, which make the λ acquires a jump in its correspondence: this agrees with what has been seen in the simplified superconductive model, since these modes were indeed the strongest in terms of electron-phonon matrix elements. However, thanks to the Wannierization scheme, it is possible to see that its intensity is comparable to the out-of-plane mode and this is in contrast to what has been found in the simple $\mathbf{q} = \mathbf{\Gamma}$ calculation.

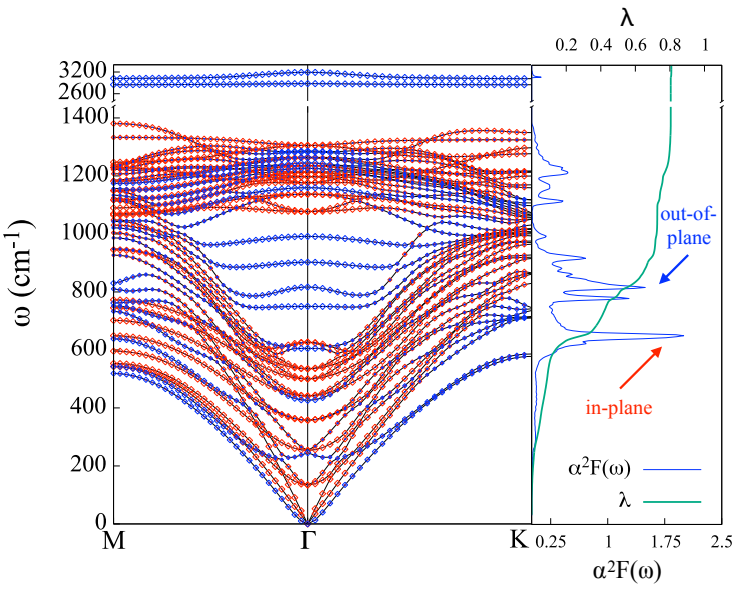

Fig. 4.14 Phonon dispersion relations, Eliashberg spectral function $\alpha^2F(\omega)$ and the electron-phonon coupling constant λ of the hydrogenated (111) diamond surface with $n_{\mathrm{dop},3}$. Red (blue) dots correspond to in-plane (out-of-plane) vibrational modes. The size of the dots correspond to the amount of [xy] or [z] nature of the phonon frequency. Figure taken from Ref. 281.

By decomposing over the Wannierized bands, it is also possible to study the different intra- and inter-band contributions to the final λ. In Fig. 4.15 I have plotted the band-resolved Eliashberg spectral function, from which the band-resolved electron-phonon coupling constant can be computed:

$$[\lambda] = \begin{pmatrix} \lambda_{11} & \lambda_{12} & \lambda_{13} \\ \lambda_{21} & \lambda_{22} & \lambda_{23} \\ \lambda_{31} & \lambda_{32} & \lambda_{33} \end{pmatrix} = \begin{pmatrix} 0.21 & 0.11 & 0.09 \\ 0.11 & 0.06 & 0.05 \\ 0.09 & 0.05 & 0.04 \end{pmatrix} \tag{4.12}$$

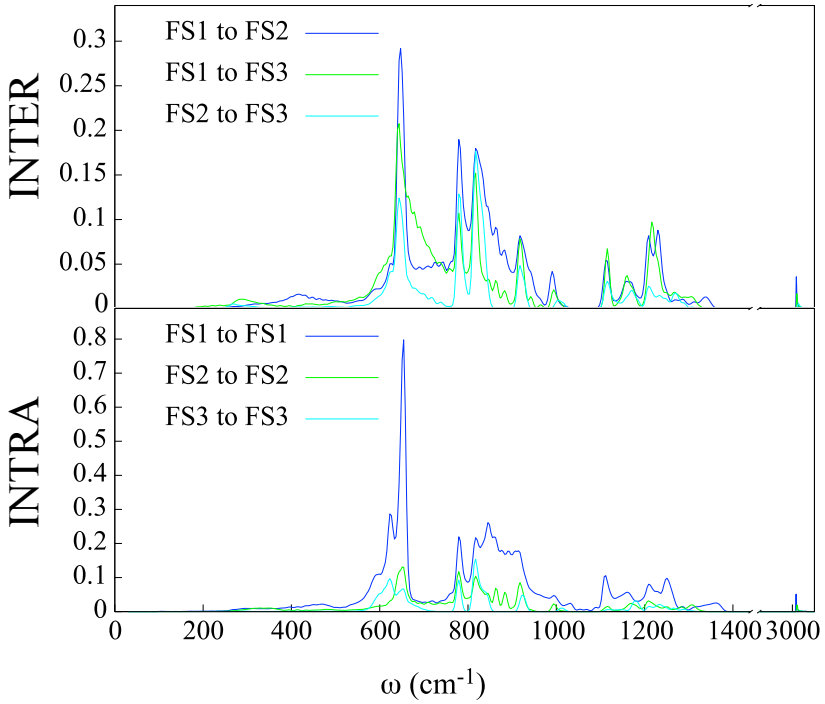

Fig. 4.15 Band resolved Eliashberg spectral function for the case at the highest doping. The label FS1, FS2 and FS3 correspond the the first, second and third crossed bands respectively as defined in Fig. 4.7. Figure taken from Ref. 281.

The relevant processes are related to the first Fermi surface. Indeed, the in-plane mode related to the intra-band scattering of the first band has the highest contribution to λ. On the other hand, the other two intra-band processes (i.e $2 \leftrightarrow 2$ and $3 \leftrightarrow 3$) are negligible. Moreover, also inter-band processes with the first band are relevant for the superconductive phase transition (i.e. $1 \leftrightarrow 2$, in-plane mode, and $1 \leftrightarrow 3$, out-of-plane mode): the second and third Fermi surfaces have a similar density of

states at the Fermi level, thus contributing in the same way since the electron-phonon coupling constant depends linearly on the DOS.

Finally, thanks to the Wannier interpolation scheme, it is also possible to obtain information on the electron-phonon coupling constant in the phase space of phonon momenta, i.e. for each **q**-point in the Brillouin zone:

$$\tilde{\lambda}_{nm}(\mathbf{q}) = \frac{\lambda_{nm}(\mathbf{q})}{N_f(\mathbf{q})} = \frac{\sum_{\mathbf{k},\nu}(\left|g^{\nu}_{\mathbf{k}n,\mathbf{k}+\mathbf{q}m}\right|^2/\omega^{\nu}_q)\delta(\varepsilon_{\mathbf{k}n})\delta(\varepsilon_{\mathbf{k}+\mathbf{q}m})}{\sum_{\mathbf{k}}\delta(\varepsilon_{\mathbf{k}n})\delta(\varepsilon_{\mathbf{k}+\mathbf{q}m})} \tag{4.13}$$

This quantity is the **q**-dependent electron-phonon coupling constant normalized by the nesting factor, which allows us to study how the electron-phonon interaction strength varies over the Brillouin zone and is depicted in Fig. 4.16, decomposed on the intra-band ($n = m$) and inter-band ($n \neq m$) process. The total λ is just an average of $\tilde{\lambda}_{nm}(\mathbf{q})$ over the **q**-points belonging to the FBZ:

$$\lambda = \sum_{nm}\sum_{\mathbf{q}}\frac{1}{N_q}\tilde{\lambda}_{nm}(\mathbf{q})\cdot N_f(\mathbf{q}) \tag{4.14}$$

The circle-like and annulus-like regions of the simplified superconductive model can be immediately identified, even if the Fermi surfaces are not actually circular-symmetric. Nevertheless, we can understand why the $\mathbf{q} = \mathbf{\Gamma}$ computation of the superconductive properties underestimates the T_c: the approximation of constant $\left|g^{\nu}_{nm,\mathbf{\Gamma}}\right|^2$ is wrong and high values of $\tilde{\lambda}$ can be reached in very localized parts of such regions, being therefore killed averaging over **q**.

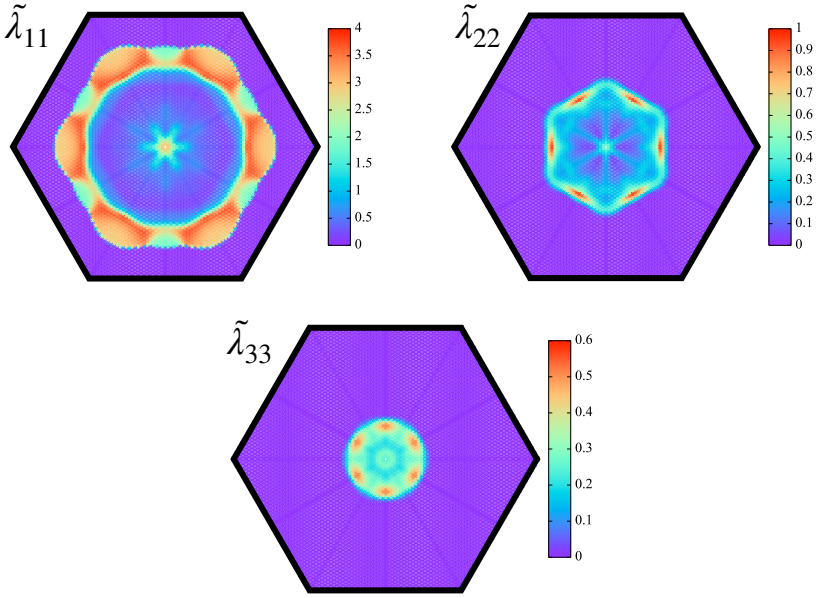

(a)

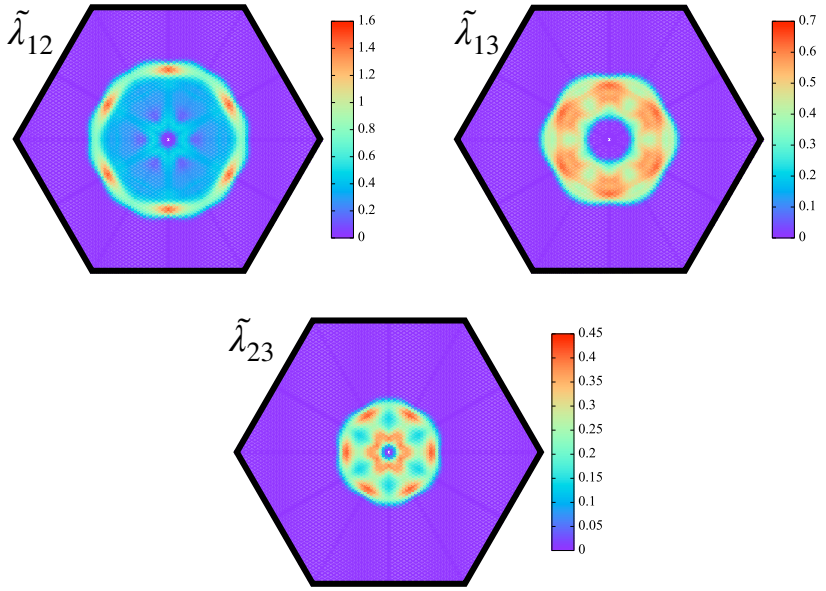

(b)

Fig. 4.16 **q**-dependent electron-phonon coupling constant normalized by the nesting factor, resolved per band as labelled by Fig. 4.7. This is a measure of how the electron-phonon interaction strength varies over the Brillouin zone. Figure taken from Ref. 281.

4.6 Migdal-Eliashberg theory of multi-band high-T_c superconductivity

While the McMillan/Allen-Dynes formula gives qualitative results, a more accurate estimate of the superconductive critical temperature for the highest doping value ($n_{2d,3}$) is obtained by solving the Migdal-Eliashberg (ME) equations. Since the system under study has a density of states typical of 2D systems, the approximation of constant DOS at E_F is satisfied. Moreover, since the Fermi surface are smooth and isotropic in **k** space, we will actually solve the isotropic ME equations. Finally, due to the multi-band nature of the hydrogenated diamond-(111) surface, I have solved both the single and multi-band equations in order to see whether the presence of scattering channels on different bands enhances the critical temperature or not.

4.6.1 Choice of the effective Coulomb pseudopotential

The Eliashberg spectral function has been computed from first principles via the Wannier interpolation of the electron-phonon matrix elements throughout the whole Brillouin zone, from which λ and $\omega_{\log}$ have been computed. The effective electron-electron Coulomb interaction μ^* is the only free parameter that had to be suitably chosen. However, the Morel-Anderson pseudopotential used in the McMillan/Allen-Dynes formula cannot be employed for the ME equations [197].

Therefore, in order to set μ^* to a suitable value, I have solved the single-band ME equations for bulk boron-doped diamond at a boron concentration $n_b \sim 1.85\%$, for which it is experimentally known that the system exhibits a superconductive phase transition at $T_c \approx 4$ K. In order to do so I have taken the corresponding Eliashberg spectral function from Ref. 18, computed via DFPT with in a a $3 \times 3 \times 3$ supercell and one substitutional boron atom (Fig. 4.17): the corresponding electron-phonon coupling constant is $\lambda = 0.43$. Then the single-band isotropic ME equations were solved varying μ^* until the superconducting gap closes at the experimental critical temperature $T_c = 4$ K: this happens when the Coulomb pseudopotential is $\mu^* = 0.17$ and then I assumed it to be also representative of the hydrogenated (111)-diamond surface doped via electrochemical gating.

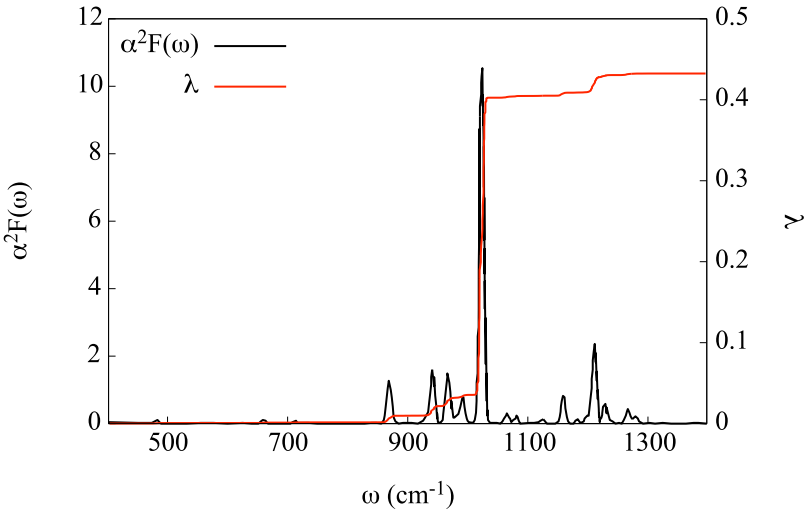

Fig. 4.17 Eliashberg spectral function $\alpha^2F(\omega)$ and electron-phonon coupling constant λ for boron-doped bulk diamond at a boron concentration of $n_b \sim 1.85\%$, whose superconductive transition temperature is $T_c = 4$ K. The picture is adapted from Ref. 18.

While in the single-band model the effective Coulomb pseudopotential is a scalar, when the multi-band model is taken into account the band-resolved $\mu^*_{jj'}$ is a 3×3 matrix. Since I no experimental measurements on the superconducting phase of this system are available for fixing the value of $\mu^*_{jj'}$, I made the following Ansatz [298]:

$$\begin{pmatrix} \mu^*_{11} & \mu^*_{12} = c \cdot \mu^*_{11} & \mu^*_{13} = c \cdot \mu^*_{11} \\ \mu^*_{21} = \frac{N_{\sigma,1}(0)}{N_{\sigma,2}(0)}\mu^*_{12} & \mu^*_{22} = \mu^*_{11} & \mu^*_{23} = c \cdot \mu^*_{11} \\ \mu^*_{31} = \frac{N_{\sigma,1}(0)}{N_{\sigma,3}(0)}\mu^*_{13} & \mu^*_{32} = \frac{N_{\sigma,2}(0)}{N_{\sigma,3}(0)}\mu^*_{23} & \mu^*_{33} = \mu^*_{11} \end{pmatrix}$$

with $c = 0.0, 0.5$ or 1.0 and the constraint that $\mu^*_{jj'}/\mu^*_{j'j} = N_{\sigma,j'}(0)/N_{\sigma,j}(0)$, as shown in Ref. 299. The parameter c controls the amount of inter-band scattering: for $c = 0$ only intra-band processes are admitted, while for $c = 0.5$ and $c = 1.0$ the possibility for electrons to be scattered on other bands is gradually taken into account.

Notice that a total Coulomb pseudopotential $\mu^*_{\rm tot}$ can be then retrieved as:

$$\mu^*_{\rm tot} = \frac{\sum_{jj'} N_{\sigma,j}(0)\mu^*_{jj'}}{\sum_j N_{\sigma,j}(0)} \tag{4.15}$$

which I required to be equal to the value of the single-band model, i.e. $\mu^*_{tot} = \mu^* = 0.17$ in order to determine the values of $\mu^*_{jj'}$ (which are summarized in Table 4.5 for the different values of c).

	Single-band	Multi-band		
		$c=0$	$c=1/2$	$c=1$
μ^*_{tot}	0.17	0.17	0.17	0.17
$\mu^*_{jj',j=j'}$	/	0.17	0.07785	0.05048
$\mu^*_{jj',j<j'}$	/	0	0.038925	0.05048

Table 4.5 Coulomb pseudopotentials employed in the solution of the single-band and multi-band Migdal-Eliashberg equations. All values are obtained under the condition that the total pseudopotential reproduces the experimental T_c of boron-doped bulk diamond. The indexes $j = 1,2,3$ are labelled in Fig. 4.3 (c). Table taken from Ref. 282.

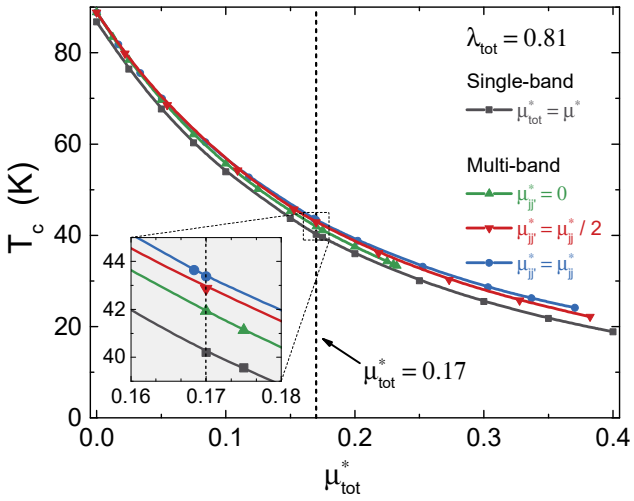

Fig. 4.18 Superconducting critical temperature T_c vs. the total effective Coulomb electron-electron interaction $\mu^*_{\rm tot}$. The black line corresponds to the solution of the isotropic single-band (j=j'=1 and μ^*=$\mu^*_{\rm tot}$) ME equations (Eq. 2.55). The green, red and blue lines correspond to the solution of the isotropic multi-band ($j, j' = 1,2,3$) Eliashberg equations with $c = 0.0, 0.5, 1.0$. Figure taken from Ref. 282.

4.6.2 Isotropic single-band solution

Starting from the single-band model, I computed the T-dependence of the superconducting gap on the imaginary axis ($\Delta(i\omega_{n=0})$) for a fixed value of μ^*: for each choice of the effective Coulomb potential, T_c is found as the temperature at which $\Delta(i\omega_n) \to 0$. In Fig. 4.19 the black line represents the superconducting critical temperature as a function of μ^*. For the representative value $\mu^* = 0.17$ that I have fixed starting from the boron-doped bulk diamond, I found $T_c = 40.3$ K which is higher with respect to the value obtained using the McMillan/Allen-Dynes formula, i.e. $T_c \in [29.6; 34.9]$ for $\mu^* \in [0.13; 0.14]$. I remind that, when analyzing the simplified superconductive, I computed the critical temperature with the McMillan/Allen-Dynes formula which requires a value of the Coulomb pseudopotential that is different from the one employed in the solution of the Migdal-Eliashberg equations [197] as explained at the beginning of the section.

The corresponding value of the superconducting order parameter as $T \to 0$ is $\Delta(i\omega_{n=0}; T{=}0) = 6.46$ meV. Even if the gap-to-T_c ratio requires the SC order parameter on the real axis, in this case the one obtained on the imaginary axis is not that different since we are in a weak-coupling limit. Therefore, I found:

$$r = \frac{2\Delta(i\omega_{n=0}; T = 0)}{k_B T_c} = 3.72 \tag{4.16}$$

which is close to the BCS value of $r_{\mathrm{BCS}} = 3.54$.

After that, I exploited Padé approximants to analytically continue the SC gap on the imaginary-axis at $T = T_c/10$ (i.e. $\Delta(i\omega_n; T = T_c/10)$) to the real-axis ($\Delta(\omega)$, Fig. 4.19(b)) and then I computed the quasiparticle DOS (see inset to Fig. 4.19(a)), which shows the typical shape of an s-wave superconductor.

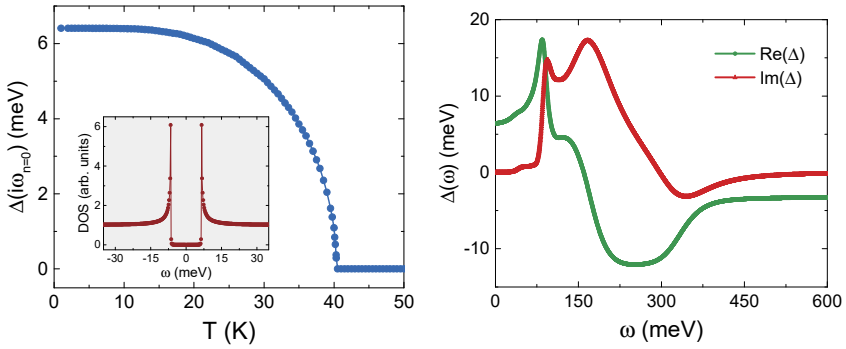

(a) (b)

Fig. 4.19 (a) Superconducting order parameter on the imaginary-axis, $\Delta(i\omega_{n=0})$, as a function of temperature T obtained from the solution of the isotropic single-band Migdal-Eliashberg equations with $\mu^* = 0.17$. The inset shows the single-band quasiparticle density of states (DOS) as a function of energy ω; (b) Real (Re) and Imaginary (Im) part of the superconducting order parameter on the real-axis, $\Delta(\omega)$, obtained from the analytic continuation of $\Delta(i\omega_n)$ computed at $T = T_c/10$. Figures taken from Ref. 282.

4.6.3 Isotropic multi-band solution

As for the multi-band model, the behavior of the system strongly depends on the structure of $\mu^*_{jj'}$, which depends on c according to our Ansatz.

For $c = 0$, I have neglected any electron-electron interaction between carriers belonging to different bands (inter-band repulsion): in Fig. 4.18 the T_c vs μ^*_{tot} dependence is shown with a solid green line and, with respect to the single-band model, the computed T_cs are slighlty higher. At $\mu^*_{tot} = 0.17$, $T_c = 41.9$ K. Notice that, for $c = 0$, the solution of ME equations is unstable for an equivalent $\mu^*_{\rm tot} \gtrsim 0.23 >> 0.17$, i.e. no solutions can be found.

For $c = 1/2$ I have included the inter-band repulsion with intermediate strength and the range of possible solutions extends up to $\mu^*_{tot} \approx 0.38$. The T_c vs μ^*_{tot} dependence is depicted in Fig. 4.18 with a solid red line: the critical temperature further increases both with respect to the single-band model and to the multi-band $c = 0$ case. Indeed, at $\mu^*_{tot} = 0.17$, $T_c = 42.9$ K.

Finally, by taking into account both inter- and intra-band electron-electron interactions with the same strenght (i.e. $c = 1$), solutions can be found up to $\mu^*_{tot} \approx 0.37$ and T_c is slightly higher with respect to that calculated at $c = 1/2$. This is shown in Fig. 4.18 with a solid blue line. In this case, $T_c = 43.4$ K at $\mu^*_{tot} = 0.17$.

Notice that, for all three cases, the multi-band critical temperature is higher than the single-band one: this means that the pairing between different bands strengthens the SC phase in this system, with an increase of T_c between $\approx 4-8\%$ at $\mu^*_{tot} = 0.17$ if compared to the single-band model. More specifically, moving from purely intra-band repulsion ($c = 0$ limit) to full inclusion of inter-band one ($c = 1$ limit) is beneficial to T_c. Notice that the multi-band increase of T_c is typical of other phonon-mediated superconductors [298, 300, 301].

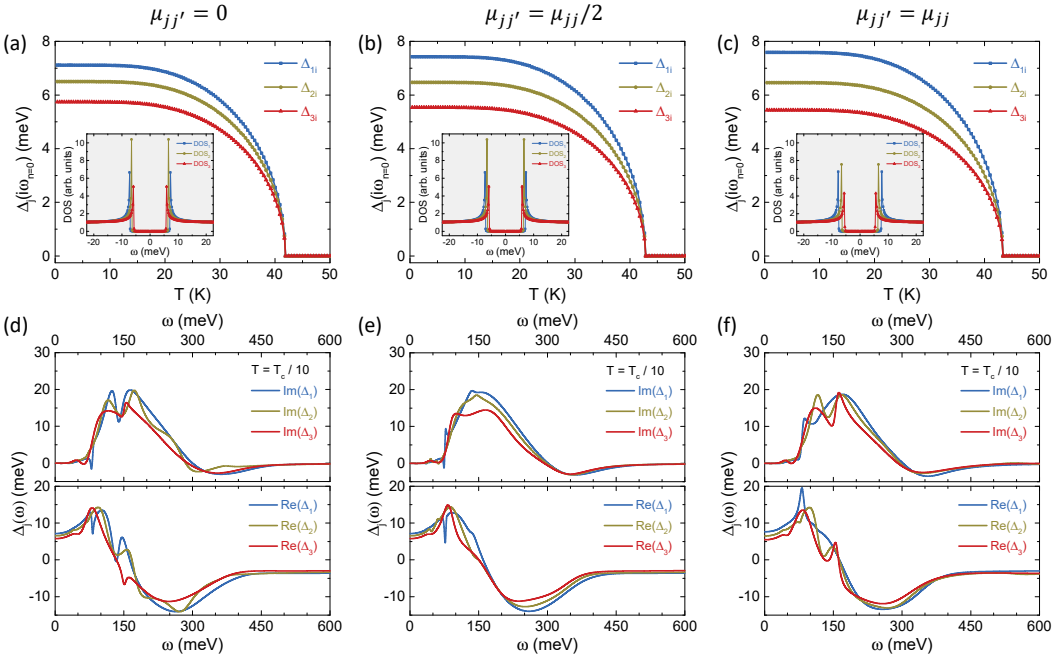

Fig. 4.20 (a-c) Band-resolved superconducting order parameters $\Delta_j(i\omega_{n=0})$ ($j = 1,2,3$ as labelled in Fig. 4.3 (c)) on the imaginary-axis as a function of temperature T obtained from the solution of the isotropic multi-band Migdal-Eliashberg equations at $\mu^*_{tot} = 0.17$ using (a) $c = 0$, (b) $c = 1/2$, and (c) $c = 1$ for $\mu^*_{jj'}$. In the inset we show the multi-band quasiparticle densities of states DOS$_j$ as a function of energy ω calculated at $T = T_c/10$; (d-f) Real (Re) and Imaginary (Im) part of the superconducting order parameters $\Delta_j(\omega)$ on the real-axis obtained from the analytic continuation of $\Delta_j(i\omega_n)$ computed at $T = T_c/10$ using $\mu^*_{tot} = 0.17$ and (d) $c = 0$, (e) $c = 1/2$, and (f) $c = 1$ for $\mu^*_{jj'}$. Figures taken from Ref. 282.

After that, I have studied how the multi-band pairing affects the SC order parameter (i.e. $\Delta_j(i\omega_n)$, $j = 1,2,3$ as labelled in Fig. 4.3 (c)), which is plotted in Fig. 4.20 (a-c). The superconducting gap has been computed solving the multi-band ME equations on the imaginary axis, setting $\mu^*_{tot} = 0.17$ and $c = 0$ (a), $c = 1/2$ (b), and $c = 1$ (c).

As $T \to 0$, multi-band pairing lifts the degeneracy among the three SC order parameters (i.e. their values are not equal if compared to the single-band case). Morevoer I found $\Delta_1(i\omega_{n=0};T{=}0) > \Delta_2(i\omega_{n=0};T{=}0) > \Delta_3(i\omega_{n=0};T{=}0)$ $\forall c$. As for the superconducting gap relative to the second Fermi surface, I found $\Delta(i\omega_{n=0};T{=}0) \lesssim \Delta_2(i\omega_{n=0};T{=}0)$ for $c = 0$ and that $\Delta(i\omega_{n=0};T{=}0) \approx \Delta_2(i\omega_{n=0};T{=}0)$ for $c = 0.5$ and $c = 1.0$ (where $\Delta(i\omega_{n=0};T{=}0)$ is the single-band value). Finally, it is also possible to notice that the degeneracy split between SC order parameters increases as the inter-band repulsion c increases.

As in the case of the single-band model, I computed the gap-to-T_c ratio for each SC gap:

$$r_j = \frac{2\Delta_j(i\omega_{n=0};T=0)}{k_B T_c} \tag{4.17}$$

This value on the second band is close to the BCS one, i.e. $r_2 \approx r_{BCS} = 3.54$, for every choice of c. On the other hand, r_1 and r_3 depart in a symmetric way from r_{BCS}: $r_1 > r_{BCS} > r_3$ and this is more and more accentuated as the inter-band repulsion increases. This is another typical behavior of multi-band superconductors [302].

Moreover, the multi-band model is consistent with the single-band one, as it can be seen by computing the weighted average of r_j over the DOS per band $N_{\sigma,j}$:

$$r = \frac{\sum_j N_{\sigma,j}(0) r_j}{\sum_j N_{\sigma,j}(0)} \tag{4.18}$$

obtaining $r = 3.62$ for $c = 0$, $r = 3.60$ for $c = 1/2$, and $r = 3.58$ for $c = 1$, slightly smaller with respect to the single-band ratio $r = 3.72$ computed before. All of the main parameters obtained from both the single- and multi-band isotropic ME equations are summarized in Table 4.6.

		Single-band	Multi-band		
			$c=0$	$c=1/2$	$c=1$
T_c	K	40.3	41.9	42.9	43.4
Δ	meV	6.46	/	/	/
Δ_1	meV	/	7.11	7.43	7.59
Δ_2	meV	/	6.50	6.47	6.46
Δ_3	meV	/	5.74	5.54	5.44
r		3.72	3.62	3.60	3.58
r_1		/	3.94	4.02	4.06
r_2		/	3.60	3.50	3.45
r_3		/	3.12	3.00	2.91

Table 4.6 Superconducting (SC) critical temperatures T_c, SC order parameters for $T\rightarrow 0$ on the imaginary-axis $\Delta_j(i\omega_{n=0};T=0)$, and gap-to-$T_c$ ratios r_j (Eq. 4.17), as obtained from the solution of the isotropic ME equations with μ^*_{tot}=0.17. The multi-band cases are calculated using $c=0.0$, $c=0.5$ and $c=1.0$ for $\mu^*_{jj'}$. The indexes $j=1,2,3$ are labelled in Fig. 4.3 (c). Table taken from Ref. 282.

Finally, the analytic continuations onto the real axis of the SC order parameter computed on the imaginary axis at $T=T_c/10$ (i.e. $\Delta_j(\omega)$, $j=1,2,3$ as labelled in Fig. 4.3 (c)) is plotted in Fig. 4.20 (d-f), for the three different choices of inter-band repulsion weight (i.e. $c=0$ (d), $c=1/2$ (e), and $c=1$ (f)). As done in the single-band case, I extracted the quasiparticle DOS for each band, as shown in the insets of Fig. 4.20 (a-c). The multi-band nature of hole-doped hydrogenated diamond-(111) can be seen as a splitting of the single-peaked quasiparticle DOS into three different peaks (which is more pronounced as the inter-band repulsion increases from $c=0$ to $c=1$), preserving the typical shape of s-wave superconductors. Experimentally, the measurement of a multi-peaked quasiparticle spectrum extracted from tunnelling spectroscopy [303] would be a direct evidence of the multi-band nature of the pairing and would allow us to determine the actual value of the inter-band repulsion weight c.

Summary

- Electrochemical gating (hole-doping) induces an electric exfoliation of the electronic band structure;
- Kohn anomalies soften in-plane phonon modes, which mainly contribute to the electron-phonon interaction;
- A multi-band superconductive phase transition occurs at a surface hole concentration $n_{2D} \sim 6 \times 10^{14}$ cm^{-2};
- The estimated critical temperature from the McMillan/Allen-Dynes formula is $T_c \sim 29 - 35$ K;
- Single-band isotropic Migdal-Eliashberg theory predicts a $T_c \sim 40$ K, while the inclusion of multi-band pairing increases it by $\sim 4 - 8\%$.

Chapter 5

Many-body Enhancement of Electron-Phonon Interactions in Gated Rhombohedral-Stacked Few-Layers Graphene

As stated in Ch. 1, the interesting property of rhombohedral multilayer graphene is the presence of extremely flat electronic bands [75, 80, 81] at the corner of the Brillouin zone (i.e. $\mathbf{K}$ and $\mathbf{K}' = -\mathbf{K}$, Fig. 1.8 (b)), which are surface states being spatially located on its top and bottom layers [304]. The presence of dispersionless electronic states favors the insurgence of strongly correlated phases of matter such as magnetism, high-T_c superconductivity, charge density waves or spin density waves: indeed the almost constant energy dispersion leads to a heavy Fermion system, thus quenching the electron kinetic energy and enhancing their long-range electron-electron interactions [305, 306].

This is confirmed in multilayer rhombohedral graphene, since it shows the opening of an energy gap at the Fermi level due to the stabilization of an antiferromagnetic ground-state at sufficiently low temperatures. As a matter of fact, in the case of a three layer system an energy gap of ~ 40 meV is opened for $T < T_c \approx 30 - 40$ K [83, 80, 84]. Moreover, upon field-effect doping it is possible to tune such magnetic phase: indeed by gradually increasing the doping of the system it is possible to go from an insulating antiferromagnetic state (undoped), to a half-metallic system

($n_{2D} \sim 10^{11}$ cm^{-2}) and finally to a conducting paramagnetic ground state ($n_{2D} > 10^{12}$ cm^{-2}) [82].

With the disappearance of a magnetically stable state, it would be interesting to understand whether a phonon-mediated superconductive phase transition is possible or not upon increment of the doping. Indeed, the Fermi level still crosses a non-dispersive electronic band which leads to a van Hove singularity in the electronic density of states [307] and therefore to a diverging value of the total DOS. This characteristic has been suggested to be promising for hosting high temperature superconductivity [85–88]. Indeed the critical temperature of a superconductive phase transition has an exponential dependence on the electronic density of states (i.e $T_c \sim e^{-1/N_\sigma(0)}$, where $N_\sigma(0)$ is the total electronic DOS at the Fermi level $E_F = 0$ per spin): as a consequence $N_\sigma(0) \to \infty$ would drastically increase T_c. Nevertheless, no superconductive phase transition has been observed experimentally up to $\sim 1.4 \times 10^{12}$ cm-2 [82].

Therefore in this chapter I will investigate if a phonon-mediated superconducting ground state can appear in an ABC three-layer system when the antiferromagnetic ground-state is no more present. I recall that such magnetic phase disappears at low temperatures for induced charge densities of $n_{2D} \sim 1.2 - 1.4 \times 10^{12}$ cm-2 [82], however in such case the Fermi level crosses no more a van Hove singularity. Nevertheless, a second divergency in the electronic density of states is present at higher energy and in order to pin there the Fermi level I have studied an induced electron charge density of $n_{2D} \sim 2 \times 10^{14}$ cm^{-2}: at this doping, a second flat band is crossed making the Fermi level fall in the proximity of a new van Hove singularity.

Moreover, due to the reduced dimensionality and the innate strong correlation of the electrons in the rhombohedral multilayer graphene, electron-electron interactions play a fundamental role: indeed it has been shown that electron-phonon interactions are severely underestimated in standard LDA/GGA DFPT computations, as exemplified by monolayer graphene. As a consequence, I will employ finite-difference computations of the electron-phonon interaction strength using hybrid functionals in order to quantify the correction to the e-ph matrix elements due to electron-electron interactions. Computational details can be found in App. A.

5.1 Electronic and vibrational properties

The starting point for the analysis of the electronic and vibrational properties is based on the PBE exchange-correlation potential, while the effects of exact exchange interactions among electrons on the electron-phonon matrix elements will be taken into account later on via both the PBE0 and B3LYP hybrid functionals.

5.1.1 Structural relaxation and electronic properties

Before electrochemically doping the rhombohedral stacked three-layer sample in the FET geometry, the three carbon planes are equally separated (with an interlayer distance $C(2)-C(3)=C(4)-C(5)=3.347$Å, with labelling of atoms given in Fig. 5.1) and the point group of the system (both in the unperturbed 1×1 and $\sqrt{3}\times\sqrt{3}$ unitary cell) is D_{3d}, which contains 6 symmetry operations:

- $\mathbb{I}$: identity;
- C_3: rotations of $2\pi/3$ about the threefold crystallographic axis $[0,0,1]$;
- C_2': rotations of π about the twofold crystallographic axes $[1,0,0]$, $[0,1,0]$ and $[1,1,0]$;
- i: inversion symmetry, i.e. rotations of π about the crystallographic axis $[0,0,1]$ followed by a reflection in a plane perpendicular to that axis;
- σ_d: rotations of π about the twofold crystallographic axes $[1,0,0]$, $[0,1,0]$ or $[1,1,0]$ followed by a reflection in a plane perpendicular to that axis;
- S_6: improper rotation, i.e. rotations of $\pi/3$ about the crystallographic axis $[0,0,1]$ followed by a reflection in a plane perpendicular to that axis;

It is also important to say that, due to symmetry properties, in rhombohedral-stacked graphene the forces acting on the atoms along z are non-zero even in absence of an external electric field. This is at odd with the Bernal stacking, in which interatomic forces along the out-of-plane direction exactly cancel out due to symmetry when no external electric field is applied.

However the further application of an electric field on the three-layer rhombohedral graphene breaks symmetry along the z direction (i.e. the one perpendicular to the carbon planes) and modifies the interlayer distances. In particular, for the considered doping of $n_{2D} \sim 2 \times 10^{14}$ cm^{-2}, $C(2) - C(3) = 2.792$ Å and $C(4) - C(5) = 2.807$ Å, with a variation on the interlayer spacing of $\sim 15\%$. The point group now is C_{3v} whose symmetry classes consist of:

- $\mathbb{I}$: identity;
- C_3: rotations of $2\pi/3$ about the threefold crystallographic axis $[0,0,1]$;
- $3\sigma_v$: rotations of π about the twofold crystallographic axes $[1,0,0]$, $[0,1,0]$ or $[1,1,0]$ followed by a reflection in a plane perpendicular to that axis;

Moreover, due to the out-of-plane perturbation, there is no more the inversion symmetry i along the z direction.

In Fig. 5.1 (a) I have plotted the planar averaged induced charge density $\rho_{||}^{ind}(z)$ in the FET configuration, as I have done before with the hydrogenated diamond-(111) surface (see Eqs. 4.1-4.3, with the difference that this time there is $\rho_{||}^{\mathrm{e}}(z)$ instead of $\rho_{||}^{\mathrm{h}}(z)$ since the system is electron-doped). In this way it is possible to see that the induced charge is mainly localized in the first carbon layer facing the metal gate, while the charge fluctuations rapidly decay on the second and third layers making them almost unperturbed.

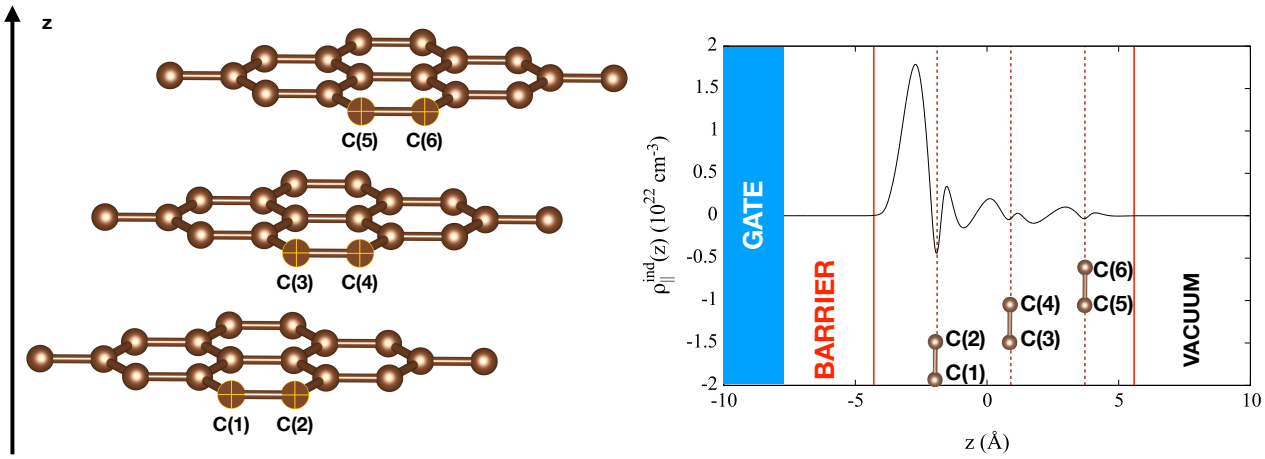

(a) (b)

Fig. 5.1 (b) 3D scheme of rhombohedral-stacked graphene; (a) Planar-averaged induced charge density ($\rho_{||}^{\text{ind}}(z)$) of the rhombohedral stacked three layer graphene at a surface electron charge density $n_{2D} = 2 \times 10^{14}$ cm^{-2}. The red solid lines indicates the location of the potential barrier which prevents charge spilling, while the red dashed lines identify the position of the carbon layers.

The electronic band structure and the electronic total density of states (DOS) are plotted in Fig. 5.2. First of all, I would like to stress that the energy gap of ~ 40 meV due to the antiferromagnetic phase [83, 84] is not present anymore but it is related to the out-of-plane external electric field (as it happens in the Bernal bilayer graphene [308]). Then, at the Fermi energy ($E_F = 0$) the dispersion relation of bands 1 and 2 (labels of band are shown in Fig. 5.2) leads to Van Hove singularities in the DOS [307]: the first one is due to the "Mexican hat" shape of band 1 (i.e. to a saddle point in the dispersion relation) and it was the one responsible for the magnetic phase, while the second one is due to a flat bottom of band 2. Both of this peculiarities in the dispersion relation are centered around the $\mathbf{K}$ (and $\mathbf{K}' = -\mathbf{K}$) point in the Brillouin zone. The two singularities are highlighted in the band-projected DOS and the densities of states at the Fermi energy ($E_F = 0$) are summarized in Tab. 5.1. This is an important point since, as I have stated before, singularities in the dispersion relation lead to a strong increase in the density of states at the Fermi level and this might be favorable for strongly correlated phases of matter, such as magnetism and high-T_c superconductivity [183, 309–313].

$N_\sigma(0)$	$N_{\sigma 1}(0)$	$N_{\sigma 2}(0)$
0.171	0.080	0.091

Table 5.1 Total density of states $N_\sigma(0)$ and band contributions to the total density of states $N_{\sigma \mathrm{i}}(0)$ (i $= 1,2$) at the Fermi level ($E_F = 0$), in units of states/eV/6 atoms cell/spin. Bands are labeled according to Fig. 5.2.

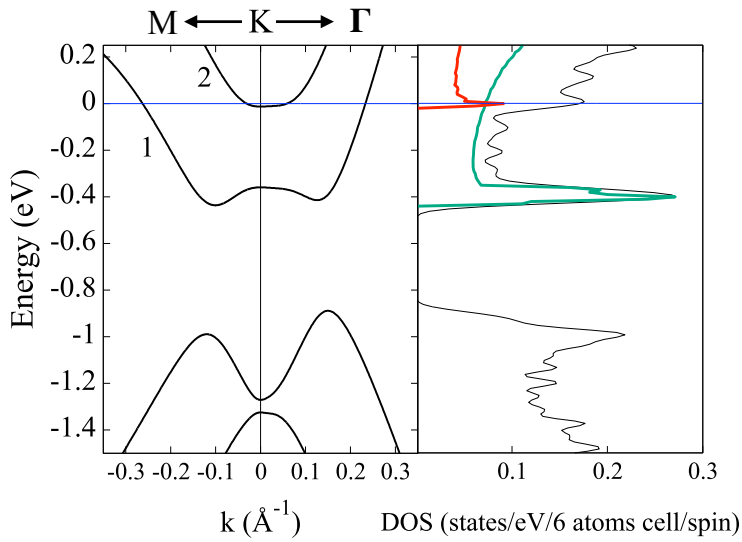

Fig. 5.2 Electronic band structure and density of states (DOS) of the ABC trilayer graphene at a surface electron charge density of $n_{2D} = 2 \times 10^{14}$ cm^{-2}. Green (red) solid line represents the contribution of band 1 (2) to the total density of states. The blue line is the Fermi Energy. The electronic band structure is shifted in k so that $\mathbf{K} \equiv \mathbf{0}$.

It is also interesting to know which atom is contributing to the total DOS at the Fermi energy and which one is giving rise to the Van Hove singularities. The six electronic bands around the Fermi level are due to the out-of-plane p_z orbitals of the carbon atoms of each layer [84, 75], therefore I have analyzed the projected density of states (PDOS) over the p_z-orbitals of the various carbon atoms (Fig. 5.3). Band 1 is no more entirely due to the electronic states coming from the sixth carbon atom (i.e. $C(6)$), as it was instead the case of undoped and slightly doped ABC three-layer [83]: there are some small contaminations coming from C(4), C(2) and C(1), nevertheless $C(6)$ is almost totally responsible for the saddle point singularity. On the other hand, band 2 is mostly due to the first three carbon atoms (i.e. $C(1)$, $C(2)$ and $C(3)$). However, while $C(1)$ shows a flat density of states, the van Hove

singularities of the second band are due to the third and the second carbon atoms. This is in agreement with what has been seen in the analysis of the induced charge density (Fig. 5.1): indeed, at the Fermi level the total density of states is almost totally due to the first carbon layer plus the third carbon atom, where the induced charge density is mostly localized.

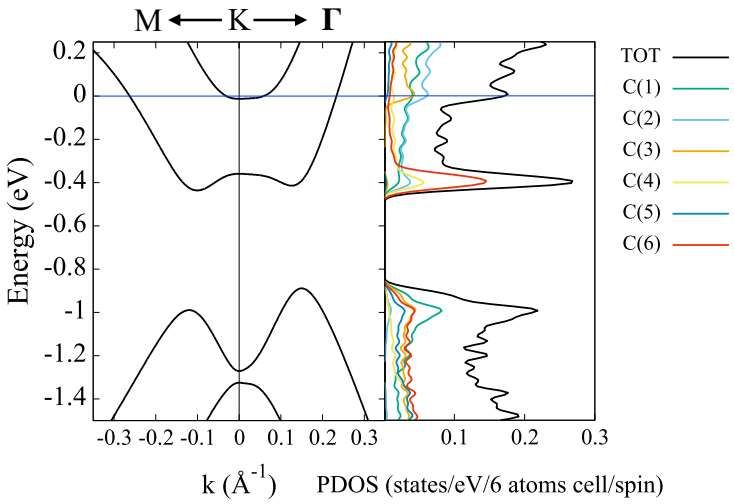

Fig. 5.3 Electronic band structure and density of states projected over p_z orbitals of the carbon atoms (PDOS) of the ABC trilayer graphene at a surface electron charge density of $n_{2D} = 2 \times 10^{14}$ cm^{-2}. Labelling of carbon atoms follow Fig. 5.1. The blue horizontal line is the Fermi Energy. The electronic band structure is shifted in k so that $\mathbf{K} \equiv \mathbf{0}$.

A further analysis on the nature of the van Hove singularities can be obtained from the k-resolved density of states. In particular, in Fig. 5.4 I have plotted the k-resolved projected densities of states over the p_z orbitals of atoms $C(2)$, $C(3)$ and $C(6)$ (the Fermi level is set to $E_F = 0$). First of all, the highest contribution to the total DOS at the Fermi level comes from the second and third carbon atoms and, more importantly, $C(3)$ is the main responsible for the singularity of the second band, while $C(2)$ contributes also to the electronic structure of the first band along the $\mathbf{\Gamma} - \mathbf{M}$ direction (i.e. where the trigonal warping is taking place). Finally, $C(6)$ is totally related to the saddle point of the first band centered around $\mathbf{K}$.

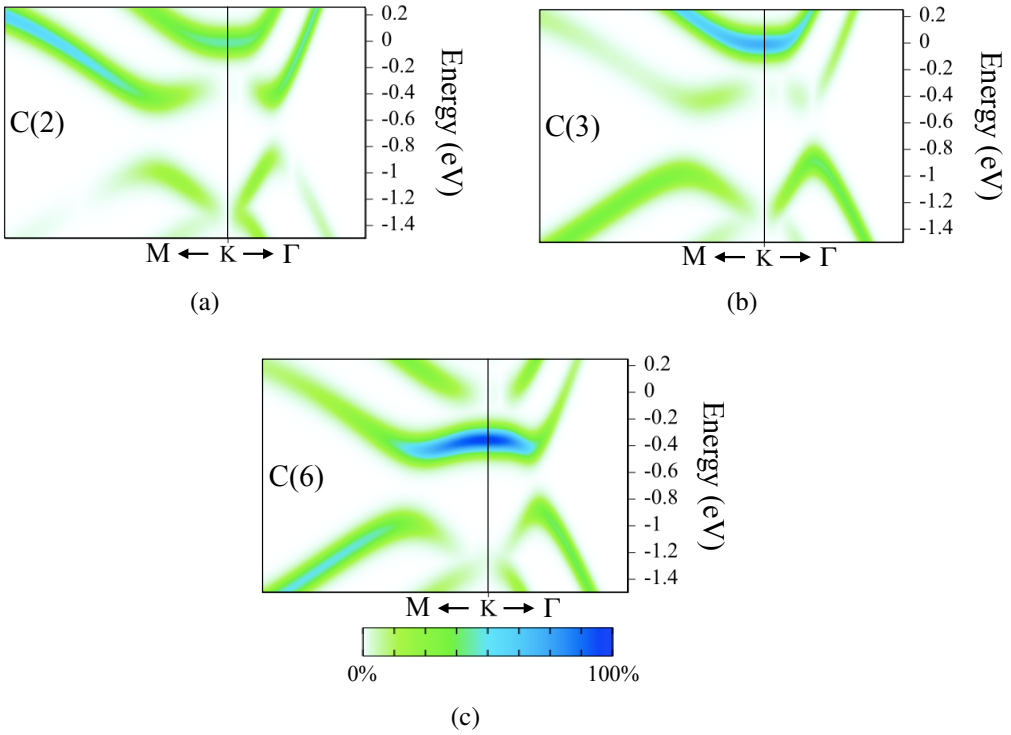

Fig. 5.4 k-resolved density of states projected over the p_z orbitals of carbon atoms C(2), C(3) and C(6), which are responsible for the van Hove singularities in the total density of states (Fig. 5.2) at a surface electron charge density of $n_{2D} = 2 \times 10^{14}$ cm^{-2}. Labelling of carbon atoms follows Fig. 5.1.

Finally, since two bands are crossed by the Fermi level there will be two Fermi surfaces (Fig. 5.5). They are concentric and centered at $\mathbf{k} = \mathbf{K}$ and $\mathbf{k} = \mathbf{K}'$ in the 1×1 Brillouin zone, with an almost circular shape except for the small deformation due to the trigonal warping of graphene systems along the $\mathbf{\Gamma} - \mathbf{M}$ direction in the reciprocal space. As a consequence the system is valley-degenerate, with a valley degeneracy $g_v = 2$. Therefore it is important to keep in mind that, when the electron-phonon interactions will be investigated, nesting between different portions of the Fermi surface is possible for phonon momenta $\mathbf{q}$ close to $\mathbf{\Gamma}$ and $\mathbf{K}$: indeed, due to the topology of the electronic band structure, lattice quasiparticles with almost zero-momentum (i.e. $\mathbf{q} \approx \mathbf{\Gamma}$) scatter electrons from Fermi surfaces belonging to the same valley, while phonons with momentum $\mathbf{q} \approx \mathbf{K}$ connect electrons belonging to two different valleys.

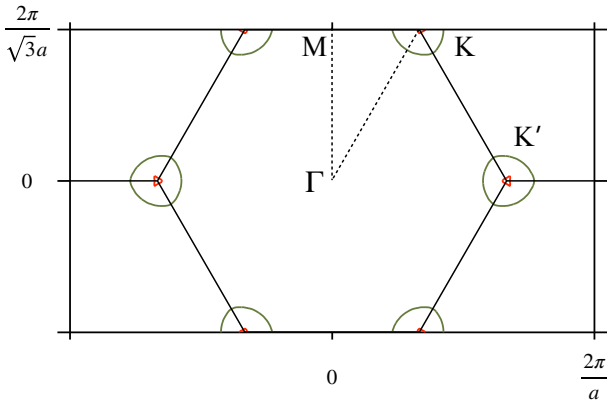

Fig. 5.5 2D Fermi surfaces of the ABC trilayer graphene at a surface electron charge density of $n_{2D} = 2 \times 10^{14}$ cm^{-2}. FS1 $\rightarrow$ green line and FS2 $\rightarrow$ red line, labelling in accordance with Fig. 5.2.

In view of the calculation of the e-ph matrix elements, it is good to anticipate the wannierization of the electronic bands in a range of 10 eV around the Fermi level as done before with the hydrogenated diamond-(111) surface. Therefore, I have fitted the first six electronic bands in an energy range of $\sim$ 10 eV around the Fermi level exploiting six Wannier functions with p_z symmetry, one for each carbon atom. As a result, the electronic bands computed via plane-wave DFT are correctly fitted at the Fermi level (Fig. 5.6), i.e. the Fermi velocities (or the first derivative of the energy bands computed at the Fermi level) are correctly reproduced by the Wannierization process.

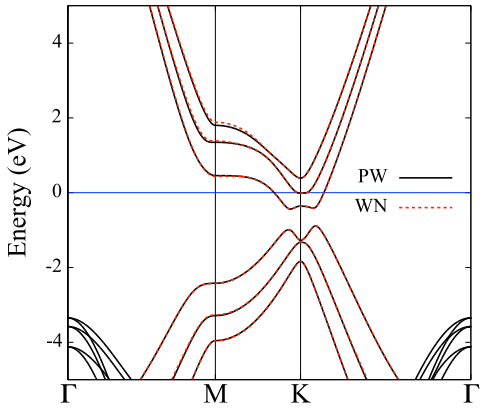

Fig. 5.6 Wannier-Interpolation (WN, red dashed line) of the electronic band structure computed via plane-wave density functional theory (PW, black solid line) at a surface electron charge density of $n_{2D} = 2 \times 10^{14}$ cm^{-2}. The blue line represent the Fermi level, here set to $E_F = 0$.

5.1.2 Vibrational properties

After the analysis of the electronic properties we move to study the dynamical properties of the lattice, looking for a possible superconducting phase transition.

In the first panel of Fig. 5.7, I have plotted the phonon dispersion relation of electrochemically doped ABC three-layer graphene at a surface electron charge density of $n_{2D} = 2 \times 10^{14}$ cm^{-2}. Notice that the phonon modes are divided into in-plane (red dots) and out-of-plane (blue dots), with the size of the dots dependent on the percentage of the $[xy]$ and $[z]$ character at a specific $\mathbf{q}$ point. The range of frequency goes from 0 to ~ 1600 cm^{-1}, with in-plane modes mostly concentrated around the high-energy part of the spectrum while the out-of-plane modes occupy the low energy part of it. It is also possible to observe the Kohn anomalies around $\mathbf{q} = \mathbf{\Gamma}$ and $\mathbf{q} = \mathbf{K}$ of the in-plane optical phonon modes, which are typical of graphene systems [68, 66]. Finally in the low-energy part of the spectrum around $\mathbf{q} = \mathbf{\Gamma}$, there are two in-plane acoustic modes with linear dispersion plus the out-of-plane quadratic flexural mode. As for the phonon density of states (shown in the second panel of Fig. 5.7, there are three van Hove singularities (i.e. sharp peaks in the phonon density of states): the first one is related to flat out-of-plane vibrational modes at ~ 800 cm^{-1}, while the other two are associated to the Kohn anomalies of the high-energy in-plane modes .

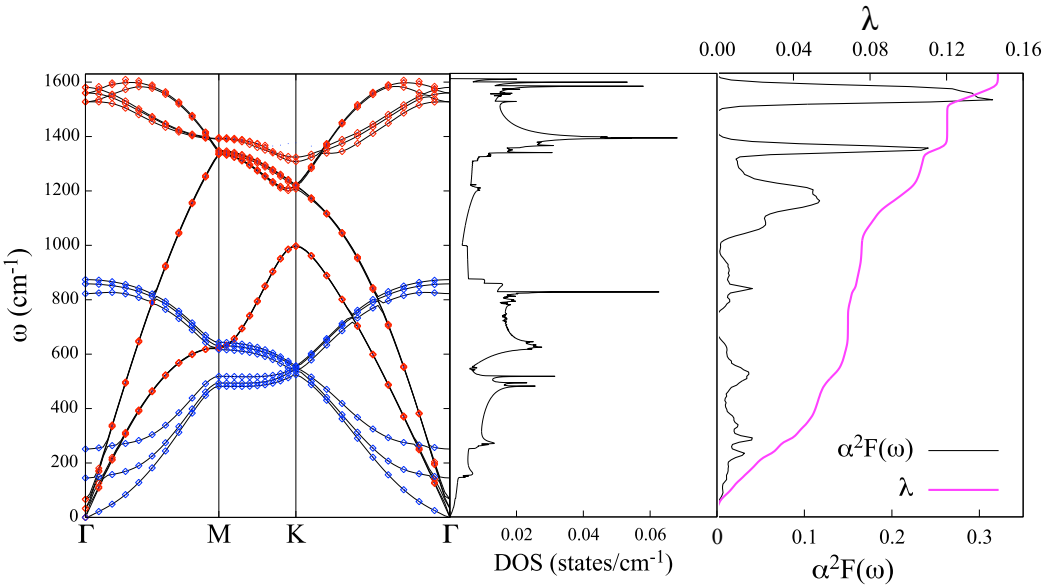

Fig. 5.7 Phonon dispersion relations, density of states (DOS), Eliashberg spectral function $\alpha^2F(\omega)$ (in arbitrary units) and electron phonon coupling constant λ of the rhombohedral stacked three layer graphene with n_{2D}. Red (blue) dots correspond to in-plane (out-of-plane) vibrational modes. The size of the dots correspond to the amount of [xy] or [z] nature of the phonon frequency. For example, the size of the dots for the modes at Γ corresponds to a 100% character, either [xy] or [z].

In Ch. 4 it was shown that the Wannier-interpolation of the electron-phonon matrix elements gives the most accurate estimate of both the electron-phonon coupling constant λ (Eq. 2.59) and of the logarithmic averaged phonon frequency $\omega_{\log}$ (Eq. 2.61). Therefore in the third panel of Fig. 5.7 I have plotted the Eliashberg spectral function (Eq. 2.60) obtained from the Wannier-interpolation of the electron-phonon matrix elements, and the associated electron-phonon coupling constant. The strongest contribution to λ comes from the low energy out-of-plane modes, representing $\sim 50\%$ of the total value of λ. It is also possible to observe two high-frequency peaks around the two Kohn anomalies of the in-plane modes: however, even if the associated deformation potential is very large, they are strongly suppressed due to the $1/\omega$ normalization (Eq. 2.59). As a result, $\lambda = 0.148$ is obtained together with a logarithmic averaged phonon frequency (Eq. 2.61) $\omega_{\log} = 74.27$ meV.

Moreover, since there are two possible phonon momenta that can give rise to Fermi surface nesting (i.e. $\mathbf{q} = \mathbf{\Gamma}$ and $\mathbf{q} = \mathbf{K}$, as explained before), the total electron-phonon coupling constant λ can be decomposed into two different contributions, i.e. $\lambda_{\mathbf{\Gamma}}$ and $\lambda_{\mathbf{K}}$ with $\lambda = \lambda_{\mathbf{\Gamma}} + \lambda_{\mathbf{K}}$. Therefore, in order to extract $\lambda_{\mathbf{\Gamma}}$ and $\lambda_{\mathbf{K}}$, the electron-phonon matrix elements can be interpolated via the Wannier functions only in limited regions of radius $2k_{F,\max}$ (where $k_{F,\max}$ is the maximum absolute value of the Fermi momentum, which in this case correspond to that of the first Fermi surface as shown in Fig. 5.5) centered around $\mathbf{q} = \mathbf{\Gamma}$ and $\mathbf{q} = \mathbf{K}$ in the phase space of phonon momenta (see Fig. 5.8 (a)).

By doing so the various contributions to the total $\alpha^2F(\omega)$ can be clearly recognized (Fig. 5.8 (b)): in particular, the $\mathbf{q} = \mathbf{K}$ phonon momenta are mainly responsible for the central part of the Eliashberg spectral function, while those $\mathbf{q}$ close to the center of the Brillouin zone $\mathbf{\Gamma}$ are related to the low-energy spectrum plus the high-frequency peak (i.e. the Kohn anomaly of the E_{2g} in-plane mode). The resulting electron-phonon coupling constant are $\lambda_{\mathbf{\Gamma}} = 0.095$ and $\lambda_{\mathbf{K}} = 0.053$, with the strongest electron-phonon interactions taking place thanks to the $\mathbf{q} = \mathbf{\Gamma}$ phonons.

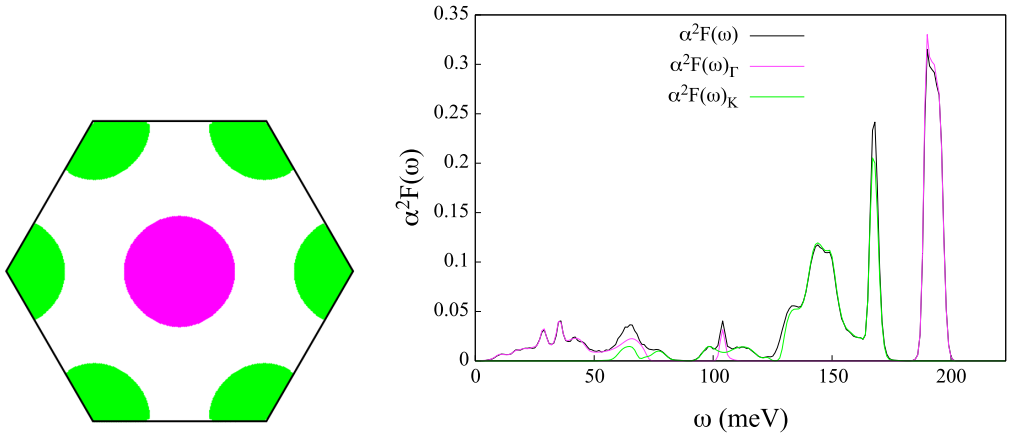

(a) (b)

Fig. 5.8 (a) $2k_{F,\max}$ regions in the phase space of phonon momenta $\mathbf{q}$, where $k_{F,\max}$ is the maximum absolute value of the Fermi momentum, which in this case correspond to that of the first Fermi surface (Fig. 5.5): the magenta region is centered around $\mathbf{q} = \Gamma$ while the green one is centered around $\mathbf{q} = \mathbf{K}$; (b) Comparison between the total Eliashberg spectral function ($\alpha^2F(\omega)$, black solid line) with those computed using $\mathbf{q} = \Gamma$ ($\alpha^2F(\omega)_{\Gamma}$, magenta solid line) and $\mathbf{q} = \mathbf{K}$ ($\alpha^2F(\omega)_{\mathbf{K}}$, green solid line) phonon momenta. The various Eliashberg spectral functions are given in arbitrary units.

If the computed λ and ω_{log} are used as input for the McMillan/Allen-Dynes formula (Eq. 2.58) setting the Morel-Anderson pseudopotential to $\mu^* = 0.1$ (which is typical of doped graphene systems [314–317]), no superconductive phase transition can be observed. This is due to the small electron-phonon coupling constant.

However, it is important to notice that linear response calculation are usually performed at the density functional perturbation theory (DFPT [172]) level with the aid of (semi)local exchange-correlation potential such as linear density approximated (LDA [318]) or generalized gradient approximated (GGA, in particular the most used is the PBE [319]) xc-functionals at the harmonic level. Nevertheless, approximate exchange-correlation functionals in standard density functional theory computations introduce errors in the calculation of electron-phonon interactions. Tipically, the electron-phonon coupling is severely underestimated [320], as shown in the case of monolayer graphene [64, 321], $TiSe_2$ [322], ZrNCl [323] and HfNCl [324], and the error gets higher and higher as the dimensionality of the system is reduced [325].

Corrections can be achieved either via hybrid exchange-correlation functionals [326] (which mix the standard LDA/GGA E_{xc} with a certain percentage of the exact Hartree-Fock exchange interaction among electrons, e.g. PBE0 [327, 328] or B3LYP [329]) or via *GW* computations [330–332] (which corrects the electron self-energy in a self-consistent way), however these techniques are computationally heavy and linear response is not feasible.

In many cases where only few modes give strong electron-phonon interactions, it is possible to employ a clever way to directly access the e-ph interaction strength, i.e. the finite-difference computation of electron-phonon interaction (that will be explained in more detail in Sec. 5.2). The main idea is to identify the vibrational modes that give the strongest electron-phonon interactions in the LDA/GGA picture and then find corrections due to exact electron-electron interactions via finite-differences computations and hybrid functionals.

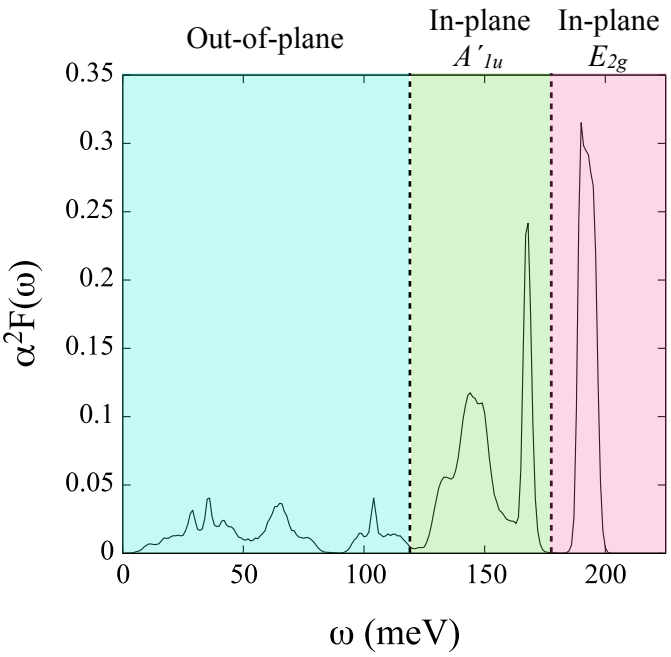

Fig. 5.9 Renormalization of the Eliashberg spectral function of electron-doped rhombohedral graphene. The contribution of the out-of-plane modes (blu shaded region) is not modified. The high-frequency part of the $\alpha^2F(\omega)$ related to $\mathbf{\Gamma}$ (pink shaded region) and $\mathbf{K}$ (green shaded region), are renormalized according to the electron-electron contribution to the e_{2g} and A'_{1u} vibrational modes respectively.

More precisely, in graphene system it is known that the vibratonal modes E_{2g} at $\mathbf{\Gamma}$ and the A'_1 at $\mathbf{K}$ are strongly renormalized due to electron-electron interaction [68, 70, 76, 321]. Such phonons are also responsible for the two Kohn anomalies of the optical branches at ~ 1550 cm^{-1} and ~ 1200 cm^{-1} respectively, which are a signature of a strong electron-phonon interaction as already widely discussed. Therefore I have computed the renormalization of the deformation potential of such vibrational modes due to the inclusion of electron-electron interactions in the field-effect electron-doped rhombohedral-stacked three-layer graphene at $n_{2D} = 2 \times 10^{14}$ cm^{-2}. As a first approximation, I have obtained an enhanced Eliashberg spectral function by applying such renormalization to the respective high-frequency portions of $\alpha^2F(\omega)$ as shown in Fig. 5.9, while leaving unperturbed the out-of-plane modes. After that I have computed the new λ and $\omega_{\log}$ in order to see if they can lead to a phonon-mediated superconductive phase transition.

5.2 Finite differences computations of the electron-phonon interactions

In Ch. 2 it was shown that the electron-phonon matrix elements are proportional to the variation of the effective potential felt by electrons ($v_{KS} = V_{KS}e^{-i\mathbf{q}\cdot\mathbf{r}}$) with respect to atoms displacement ($\mathbf{u^q}$) (Eq. 2.21). However, since the Kohn-Sham potential is the only term in the Kohn-Sham Hamiltonian which depends on the atoms' coordinates (the other being the electron kinetic energy) we can say that $\delta v_{KS}/\delta \mathbf{u^q} = \delta H_{KS}/\delta \mathbf{u^q}$. As a consequence:

$$g^{\nu}_{\mathbf{k}j,\mathbf{k}\pm\mathbf{q}j'} \propto \langle \mathbf{k}j| \frac{\delta H_{\mathrm{KS}}}{\delta \mathbf{u^q}} \left|j'\mathbf{k}\pm\mathbf{q}\right\rangle \tag{5.1}$$

i.e. the electron-phonon matrix elements will be proportional to the expectation value of the variation of the Kohn-Sham Hamiltonian with respect to phonon displacements. It is then possible to estimate the electron-phonon coupling of a certain vibrational mode when folded at the center of the Brillouin zone (i.e $\mathbf{q} = \mathbf{\Gamma} = \mathbf{0}$) via finite differences by looking at how electronic eigenvalues at the Fermi level vary as a function of the atomic displacement:

$$\begin{aligned} g^{\nu}_{\mathbf{k}j,\mathbf{k}j'} &\propto \left\langle \mathbf{k}j;(\mathbf{u^0}=0)\right| \frac{H_{\mathrm{KS}}(\mathbf{u^0}) - H_{\mathrm{KS}}(\mathbf{u^0}=0)}{\left|\mathbf{u^0}\right|} \left|j'\mathbf{k};(\mathbf{u^0}=0)\right\rangle \\ &= \frac{\left\langle \mathbf{k}j;(\mathbf{u^0}=0)\right| H_{\mathrm{KS}}(\mathbf{u^0}) \left|j'\mathbf{k};(\mathbf{u^0}=0)\right\rangle - \varepsilon^0_j \delta_{jj'}\delta_{\mathbf{k},\mathbf{k}}}{\left|\mathbf{u^0}\right|} \end{aligned} \tag{5.2}$$

where $\left|j\mathbf{k};(\mathbf{u^0}=0)\right\rangle$ is the Bloch-periodic part of the Kohn-Sham eigenfunction obtained from diagonalization of the Kohn-Sham Hamiltonian at non-displaced atoms' positions ($\mathbf{u^0}=0$) with eigenvalues ε^0_j. Therefore we just need to compute the eigenvalues of the Kohn-Sham Hamiltonian at displaced atoms' positions on top of undisplaced wavefunctions. The only drawback of this technique is that it becomes unfeasible for many band degeneracies or for phonon momenta that are not zone center or zone border and it is expensive for large supercells.

5.2.1 Example: application of the finite differences to a q = K lattice perturbation

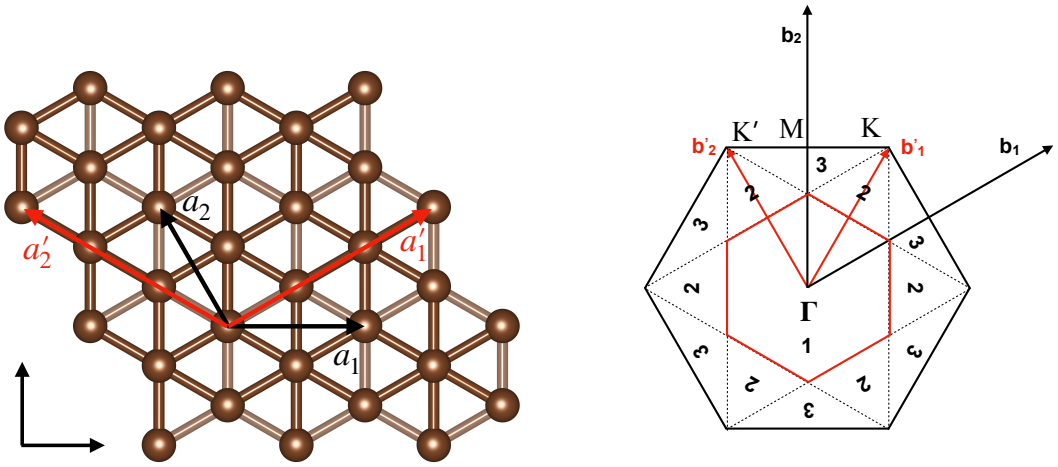

(a) (b)

Fig. 5.10 (a) Top view of the three-layer rhombohedral-stacked graphene: $\mathbf{a}_1$ and $\mathbf{a}_2$ represent the primitive vectors in the direct space for the 1×1 supercell, while $\mathbf{a}'_1$ and $\mathbf{a}'_2$ represent the primitive vectors in the direct space for the $\sqrt{3}\times\sqrt{3}$ supercell; (b) Reduction of the Brillouin zone for the $\sqrt{3}\times\sqrt{3}$ ABC graphene unit cell. The black BZ is the Brillouin zone for the 1×1 unit cell, with axes $\mathbf{b}_1$ and $\mathbf{b}_2$. The red BZ is the reduced Brillouin zone for the $\sqrt{3}\times\sqrt{3}$, with axes $\mathbf{b}'_1$ and $\mathbf{b}'_2$. 1, 2 and 3 label the first, second and third Brillouin zone in the reduced zone description of the $\sqrt{3}\times\sqrt{3}$ ABC graphene unit cell.

In order to show that this technique allows us to probe the strength of the electron-phonon interaction, consider the $\sqrt{3}\times\sqrt{3}$ supercell: since $\mathbf{K}=(\frac{1}{3},\frac{\sqrt{3}}{3})\frac{2\pi}{a}$ and $\mathbf{K}'=-\mathbf{K}$, such unit cell allows us to catch the correct periodicity of the atoms' displacement along the corresponding phonon modes. The hexagonal lattice (i.e. $\mathbf{R}_{n_1,n_2}=n_1\mathbf{a}_1+n_2\mathbf{a}_2$, with $n_1,n_2\in\mathbb{Z}$) is defined by the following primitive vectors (Fig. 5.10 (a)):

$$\mathbf{a}_1=(1,0)\cdot a \quad , \quad \mathbf{a}_2=\left(-\frac{1}{2},\frac{\sqrt{3}}{2}\right)\cdot a \tag{5.3}$$

where a is the lattice parameter.

From this, we can define the reciprocal vectors $\mathbf{G}_{m_1,m_2}=m_1\mathbf{b}_1+m_2\mathbf{b}_2$ (with $m_1,m_2\in\mathbb{Z}$ and $\mathbf{a}_i\cdot\mathbf{b}_j=2\pi\delta_{ij}$, $i,j=1,2$), where the reciprocal primitive vectors are

given by (Fig. 5.10 (b)):

$$\mathbf{b}_1 = \left(1, \frac{\sqrt{3}}{3}\right) \cdot \frac{2\pi}{a} \quad , \quad \mathbf{b_2} = \left(0, \frac{2\sqrt{3}}{3}\right) \cdot \frac{2\pi}{a} \tag{5.4}$$

However, we can choose larger primitive vectors in the direct space (i.e. $\mathbf{a}_1$ and $\mathbf{a}_2$), as long as they capture the overall periodicity of the system. Therefore, if we want to study the $\sqrt{3} \times \sqrt{3}$ supercell (Fig. 5.10), the axes in direct space will be multiplied by $\sqrt{3}$ while those in reciprocal space will be divided by $\sqrt{3}$. Moreover, they will be rotated by $\pi/6$ counter-clockwise. As a result, we have a unitary cell whose size is 3 times bigger than the original one while the First Brillouin zone will be three times smaller. The new primitive vectors will be given by:

$$\begin{cases} \mathbf{a}'_1 = (\frac{3}{2}, \frac{\sqrt{3}}{2}) \cdot a \\ \mathbf{a}'_2 = \left(-\frac{3}{2}, \frac{\sqrt{3}}{2}\right) \cdot a \end{cases} \quad , \quad \begin{cases} \mathbf{b}'_1 = \left(\frac{1}{3}, \frac{\sqrt{3}}{3}\right) \cdot \frac{2\pi}{a} \\ \mathbf{b}'_2 = \left(-\frac{1}{3}, \frac{\sqrt{3}}{3}\right) \cdot \frac{2\pi}{a} \end{cases} \tag{5.5}$$

In the new Brillouin zone, the original $\mathbf{K}$ and $\mathbf{K}' = -\mathbf{K}$ will be folded at the center of the reduced Brillouin zone ($\mathbf{\Gamma}' = \mathbf{0}$), where we will find doubly degenerate bands coming from the overlapping of the previously non-degenerate eigenvalues at $\mathbf{K}$ and $\mathbf{K}'$. This folded description of the electronic bandstructure for the system under study is shown in Fig. 5.11.

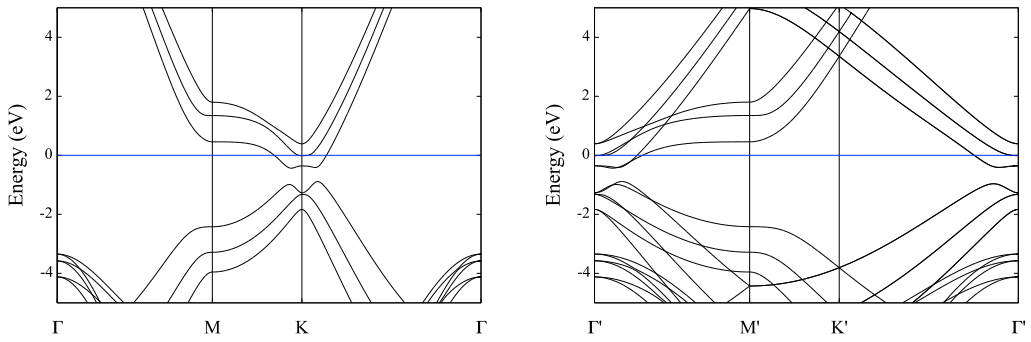

(a) (b)

Fig. 5.11 Electronic band structure in the FET geometry for the (a) unfolded (i.e. 1x1 unit cell) and (b) folded (i.e. $\sqrt{3} \times \sqrt{3}$) descriprion at surface electron doping $n_{2D} = \text{cm}^{-2}$. The blue line represents the Fermi energy ($E_F = 0$).

Indeed if $|\Psi\rangle$ is an eigenstate of a certain hamiltonian H and we apply a transformation A to it (such as a rotation, a reflection or a translation) we end up into another state $|\Psi'\rangle = A|\Psi\rangle$ which in principle is different from the previous one. However, if A is a symmetry of the system, the energy will not be altered by the transformation: $E_\Psi = E_{\Psi'}$. As a consequence, the presence of a symmetry determines the level of degeneracy of the eigenvalues which depends on how many states are connected among them via the symmetry group. As a consequence, since $\mathbf{K}$ and $\mathbf{K}'$ belong to the same symmetry group, eigenvalues will necessarily be degenerate when folded into $\mathbf{\Gamma}'$ and by removing suitable symmetry operations it will be possible to lift such energy degeneracies.

Therefore, the system will be defined by an unperturbed hamiltonian H with two degenerate states $|\phi_1\rangle$ and $|\phi_2\rangle$ (i.e. with the same eigenvalue $E_1 = E_2 = E$), respectively corresponding to the $\mathbf{K}$ and $\mathbf{K}'$ points in the original 1×1 Brillouin zone that are now folded at the new zone center $\mathbf{\Gamma}'$. Let us perturb the system with a static atom displacement corresponding to a specific phonon mode $\tilde{\nu}$ with momentum $\mathbf{q} = \mathbf{K}$, i.e.:

$$\Delta v_{KS} = \sum_{A\alpha} \sqrt{\frac{\hbar}{2M_A \omega_{\mathbf{K}\tilde{\nu}}}} e^{A\alpha}_{\mathbf{K}\tilde{\nu}} \frac{\delta v_{KS}}{\delta u^{\mathbf{K}}_{A\alpha}} \tag{5.6}$$

Due to momentum conservation we have $\langle 1|\Delta v_{KS}|1\rangle = \langle 2|\Delta v_{KS}|2\rangle = 0$, while $|\langle 1|\Delta v_{KS}|2\rangle| = \lambda_1$ and $|\langle 2|\Delta v_{KS}|1\rangle| = -\lambda_1$ since the perturbation matrix is hermitian. Moreover, thanks to quantum perturbation theory, at first order we can say that:

$$E'_1 = E_1 + \varepsilon\lambda_1 + O(\varepsilon^2) \quad , E'_2 = E_2 - \varepsilon\lambda_1 + O(\varepsilon^2) \tag{5.7}$$

where ε is a sufficiently small positive value. If we now take the difference between the perturbed eigenvalues we obtain:

$$\Delta E' = E'_1 - E'_2 = 2\varepsilon\lambda_1 + O(\varepsilon^2) = 2\varepsilon|\langle 1|\Delta v_{KS}|2\rangle| + O(\varepsilon^2) \tag{5.8}$$

Therefore, at first order in perturbation theory if we let $\varepsilon \to 0^+$ we have that:

$$\left| g^{\nu}_{\mathbf{k}j,\mathbf{k}\pm\mathbf{q}j'} \right|^2 \propto \left(\frac{d\Delta E'}{d\varepsilon} \right)^2 \tag{5.9}$$

The static perturbation lifts the degeneracy between eigenvalues in a symmetric way with respect to the unperturbed dispersion and such splitting is a measure of the strength of the electron-phonon interaction.

5.2.2 Finite-differences computation of the electron-phonon matrix elements in graphene systems

In order to see the effect of exact exchange on the electron-phonon interaction in field-effect doped rhombohedral graphene, I have deformed the atomic structure according to the phonon pattern generated by the vibrational modes of the E_{2g} and the A_1' vibrational modes. As a consequence of the lattice deformation, the electronic band structure will be modified removing degeneracies and changing the energies of the eigenvalues as described in Sec. 5.2.

In graphene-based systems it is possible to find analytical formulas for the evaluation of the deformation potential via finite differences methods. In this section I have summarized the procedure used in Ref. 321 in order to evaluate electron-phonon renormalization in graphene and graphite, which I then applied to the rhombohedral trilayer graphene. I have moved atoms with a variable displacement modulated by a parameter α, i.e atoms' positions have been varied in modulus by a quantity $\tilde{d} = \alpha \times d$, with d being the modulus of the highest atomic displacement. Within such "frozen-phonon" approach, it is possible to implicitly include the long-range electron-electron Coulomb interactions by computing the electronic structure via hybrid exchange-correlation functionals: in our case I have chosen the PBE (no exact exchange included), the PBE0 (which mixes 75% of the PBE exchange functional with 25% of the exact Hartree-Fock exchange interaction among electrons) and the B3LYP (which is a semi-empirical exchange-correlation functional) XC-functionals.

For $\mathbf{q} = \mathbf{\Gamma}$ I have studied the 1×1 cell where bands 1 and 2 are already separated at $\mathbf{k} = \mathbf{K}$ by an energy gap ΔE_K. However due to phonon pattern of the E_{2g} in-plane modes, such energy difference will be increased to $\Delta\varepsilon$. Thus, the electron phonon coupling interaction strength at $\mathbf{q} = \mathbf{\Gamma}$ can be computed as:

$$< D^2_{\mathbf{\Gamma}, E_{2g}} >= \lim_{d \to 0} \frac{1}{16} \left(\frac{\Delta\varepsilon^2 - \Delta E_K^2}{d^2} \right) \tag{5.10}$$

For $\mathbf{q} = \mathbf{K}$, I have moved to the $\sqrt{3} \times \sqrt{3}$ supercell which allows us to displace atoms according to the in-plane A'_{1u}. By doing so, eigenvalues at $\mathbf{q} = \mathbf{K}$ will overlap at the center of the reduced Brillouin zone $\mathbf{\Gamma'}$ (as explained in Sec. 5.2) and the atomic displacement will lift such degeneracy. This gives rise to an energy gap $\Delta E_{\mathbf{\Gamma'}}$ and we can compute the electron-phonon interaction strength at $\mathbf{q} = \mathbf{K}$ as:

$$< D^2_{\mathbf{K},A'_{1u}} >= \lim_{d\to 0} \frac{1}{8} \left(\frac{\Delta E_{\mathbf{\Gamma'}}}{d} \right)^2 \tag{5.11}$$

In both these expressions we take the limit of $\tilde{d} \to 0$ by actually letting $\alpha \to 0$.

In order to compare the effects of the different approximations on the exchange-correlation functionals I had to refer such electron-phonon interaction strengths to a fixed energy scale. More precisely, Eqs. 5.10-5.11 are referred to a displacement-independent energy scale $\Delta\varepsilon_g$ which is taken to be the distance between electronic bands at the highest symmetry point $\mathbf{q} = \mathbf{M}$ in the original Brillouin zone (1×1 cell). As a consequence, it can be defined:

$$\alpha^i_{\mathbf{q}} = \frac{< D^2_{\mathbf{q}} >}{\Delta\varepsilon_g} \tag{5.12}$$

with $\mathbf{q} = \mathbf{\Gamma}, \mathbf{K}$, i is the index for the type of exchange-correlation functional used (i.e PBE, PBE0 or B3LYP).

Finally, the parameter which gives the suppression or the enhancement of the electron-phonon interaction due to the inclusion of a certain percentage of exact exchange is given by the ratios of Eq. 5.12 computed for different choices of hybrid functionals with respect to the PBE xc-functional:

$$r^{\{\text{PBE0,B3LYP}\}}_{\mathbf{q}} = \frac{\alpha^{\{\text{PBE0,B3LYP}\}}_{\mathbf{q}}}{\alpha^{\text{PBE}}_{\mathbf{q}}} \tag{5.13}$$

5.3 Many-body enhancement of the electron-phonon coupling constant

5.3.1 Computation of the enhancement parameters

When displacing atoms according to the in-plane E_{2g} phonon pattern (Fig. 5.13 (a-b)) for $\mathbf{q} = \mathbf{\Gamma}$, no symmetry is found apart from the identity. Therefore such perturbation destroys all the rotational symmetries of the system.

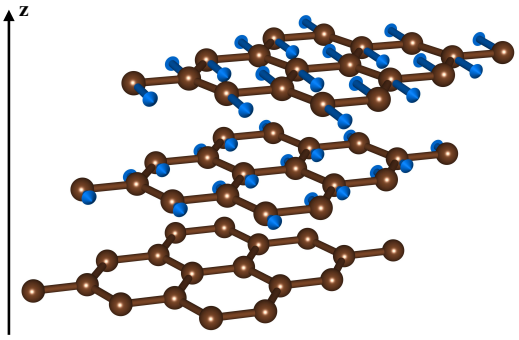

Fig. 5.12 In-plane E_{2g} phonon mode for $\mathbf{q} = \mathbf{\Gamma}$.

As it is possible to observe from Fig. 5.13 (a-c), this phonon displacement moves band 1 down in energy and band 2 up: therefore it affects both electronic bands at the Fermi energy, making it responsible for inter-band scattering. Passing from the PBE xc-functional to the hybrid functionals, the electron-phonon interaction is enhanced by the presence of a certain percentage of exact Hartree-Fock exchange interaction by:

$$r^{\mathrm{PBE0}}_{\Gamma,E_{2g}} = 4.97 \quad , \quad r^{\mathrm{B3LYP}}_{\Gamma,E_{2g}} = 3.72 \tag{5.14}$$

giving a boost of ~ 5 for the PBE0 exchange-correlation functional, while a factor ~ 4 for the B3LYP XC-functional. The relevant parameter for the evaluation of the electron-electron effects on the deformation potential are reported in Tab. 5.2.

	$\Delta\varepsilon_g$ (meV)	$< D^2_{\mathbf{\Gamma},E_{2g}} >$ (eV/Å)^2	$\alpha_{\mathbf{\Gamma}}$ (eV/Å^2)
PBE	890	2.536	2.849
PBE0	976	13.823	14.163
B3LYP	933	9.890	10.600

Table 5.2 Finite difference electron-phonon parameters computed with PBE, PBE0 and B3LYP XC-functionals for the E_{2g} in-plane phonon pattern at $\mathbf{q} = \mathbf{\Gamma}$ (Fig. 5.12).

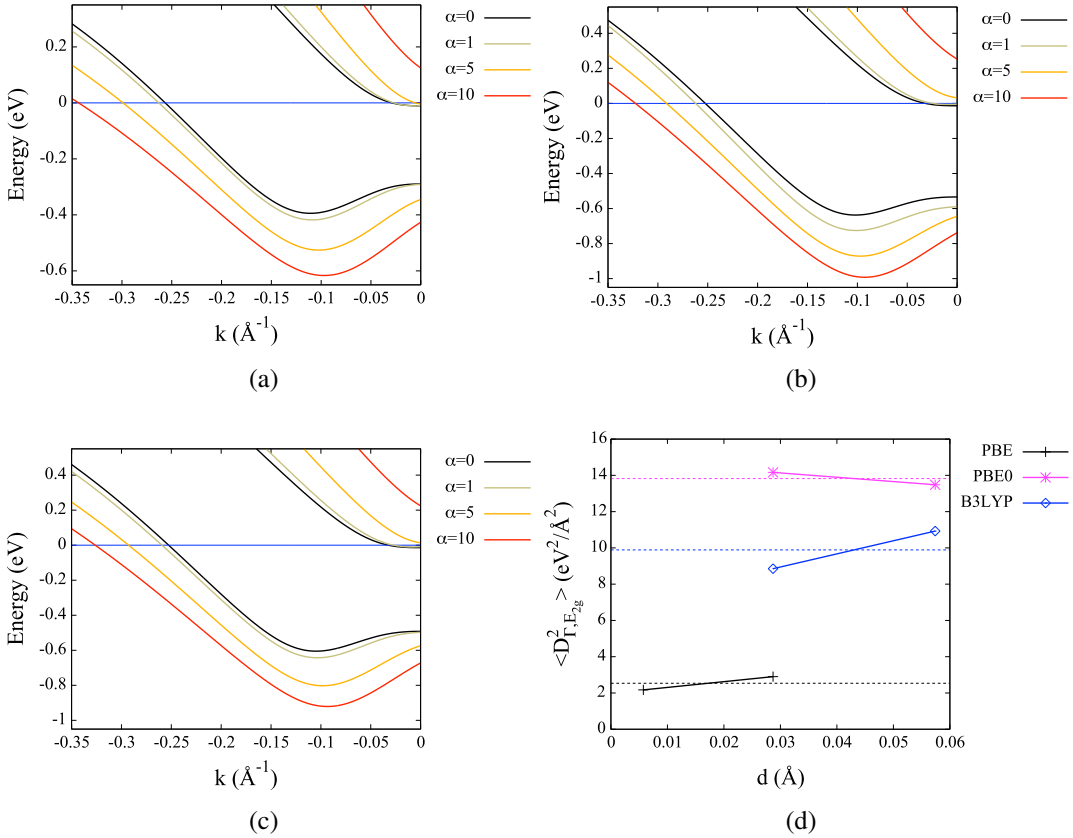

Fig. 5.13 (a-c) Degeneracy lifting of band 1 and 2 (label of bands according to Fig. 5.2) due to E_{2g} in-plane phonon mode obtained at $\mathbf{q} = \mathbf{\Gamma}$: (a) PBE, (b) PBE0 XC-functional (i.e. PBE + 25% of exact exchange) and (c) B3LYP XC-functional; (f) Deformation potential $< D^2_{\Gamma,E_{2g}} >$ as a function of the displacement d.

When displacing atoms according to the in-plane A_1' pattern (Fig 5.14) at $\mathbf{q} = \mathbf{K}$, the symmetry of the system is reduced: the point group is σ_v, leaving the the reflection in the vertical plane passing through the crystallographic axis of highest symmetry $[1,1,0]$ as the only symmetry operation that is still allowed.

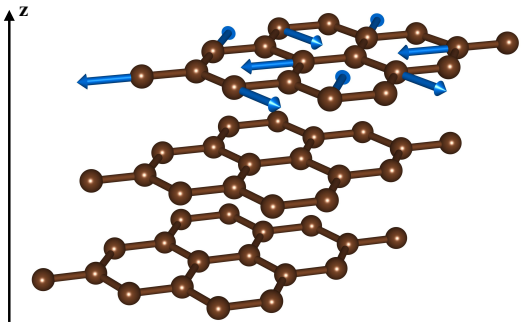

Fig. 5.14 In-plane A'_{1u} phonon mode for $\mathbf{q} = \mathbf{K}$.

This time, the displacement of carbon atoms perturbs only the first band, as it is shown in Fig. 5.13 (a-c): therefore, this phonon mode is responsible for intra-band scattering of electrons belonging to band 1. The electron-phonon interaction is enhanced by:

$$r^{\text{PBE0}}_{\mathbf{K},A'_{1u}} = 1.80 \quad , \quad r^{\text{B3LYP}}_{\mathbf{K},A'_{1u}} = 1.59 \tag{5.15}$$

giving a boost of ~ 2 for the PBE0 exchange-correlation functional, while a factor ~ 1.5 for the B3LYP XC-functional. The relevant parameter for the evaluation of the electron-electron effects on the deformation potential are reported in Tab. 5.3.

	$\Delta\varepsilon_g$ (meV)	$< D^2_{K,A'_{1u}} >$	α_K
PBE	890	3.104	3.488
PBE0	976	6.13	6.281
B3LYP	933	5.18	5.552

Table 5.3 Finite difference electron-phonon parameters computed with PBE, PBE0 and B3LYP XC-functionals for the A'_{1u} in-plane phonon pattern at $\mathbf{q} = \mathbf{K}$ (Fig. 5.14).

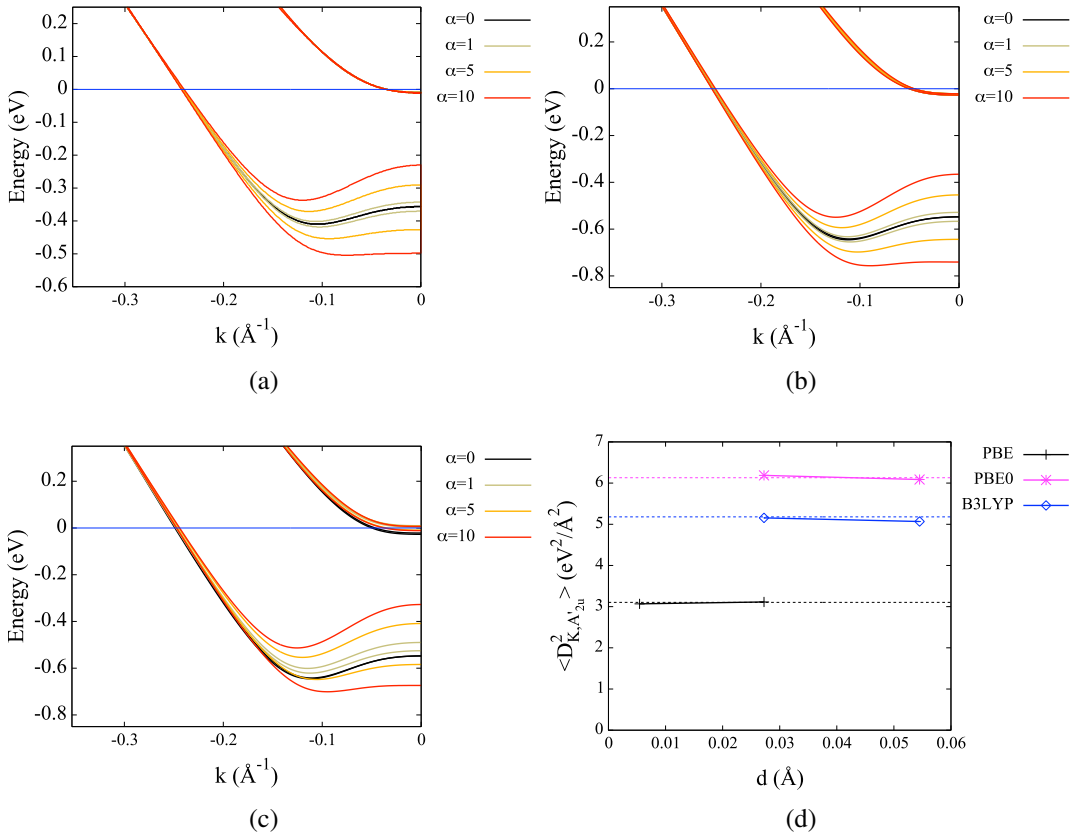

Fig. 5.15 (a-c) Degeneracy lifting of band 1 and 2 (label of bands according to Fig. 5.2) due to A'_{1u} in-plane phonon mode obtained at $\mathbf{q} = \mathbf{K}$: (a) PBE, (b) PBE0 XC-functional (i.e. PBE + 25% of exact exchange) and (c) B3LYP XC-functional; (f) Deformation potential $< D^2_{\Gamma,A'_{1u}} >$ as a function of the displacement d.

As a final remark on these atoms' displacements, I would like to point out the further connection between the electronic band structure and the phonon modes. Indeed in Sec. 5.1 I have studied which atom contributes the most to the total electronic density of states at the Fermi level and now the static perturbation of the lattice is affecting determined electronic bands, as discussed above.

In the case of the in-plane E_{2g} mode at $\mathbf{\Gamma}$, such phonon mode is responsible for inter-band scattering between bands 1 and 2: from the analysis of the projected DOS, all of the atoms contributes to the total density of states at the Fermi level and indeed the static perturbation is affecting mostly the second and the third carbon layers as it is shown in Fig. 5.12.

On the other hand, when the in-plane A'_{1u} mode at **K** is considered, intra-band scattering of electrons belonging to band 1 occurs (Fig. 5.15): I recall that while the first Fermi surface is mostly due to $C(6)$, the second one is mainly associated with $C(1)$, $C(2)$ and $C(3)$ and, as a matter of fact, the atoms displacement of the in-plane phonon mode mainly concerns the third carbon layer (which contains $C(6)$).

5.3.2 Renormalized Eliashberg spectral functions

I then applied these renormalizations to the Eliashberg spectral functions in order to compute the enhanced electron-phonon coupling constant λ and logarithmic averaged phonon frequency $\omega_{\log}$ (Fig. 5.16).

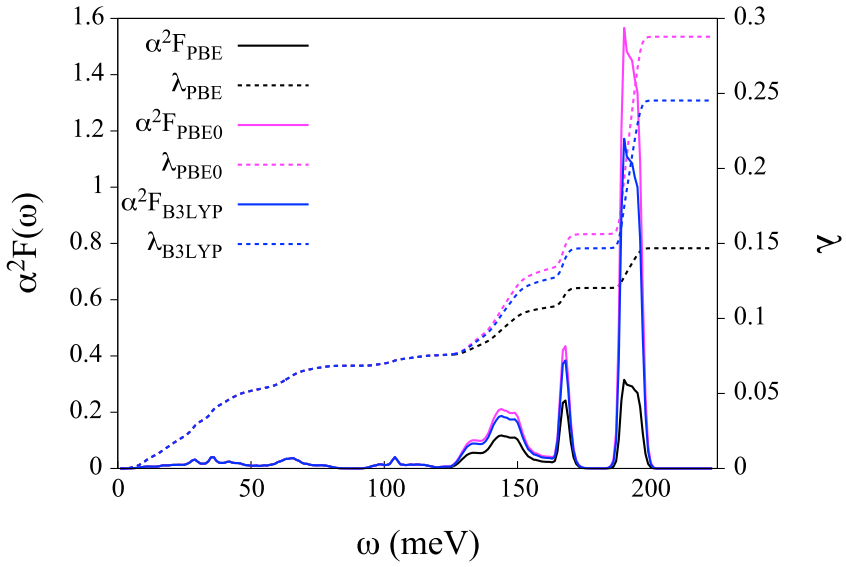

Fig. 5.16 Renormalized Eliashberg spectral function due to the inclusion of electronic interactions: black line PBE, magenta line PBE0 and blue line B3LYP.

The inclusion of the correlation between electrons enhances the total electron phonon coupling constant by a factor of ~ 2, with a greater boost if the PBE0 xc-functional is used with respect to the B3LYP one (see Tab. 5.4), confirming that standard LDA/GGA linear response computations severely underestimates the electron-phonon interactions. The in-plane E_{2g} phonon mode is the most affected by the (partial) inclusion of the electron-electron exact exchange, contributing the most to the total value of λ.

XCF	λ_{tot}	λ_{Γ}	$\lambda_{\mathbf{K}}$	ω_{log} (meV)
PBE	0.148	0.095	0.053	74.27
PBE0	0.288	0.196	0.092	114.09
B3LYP	0.245	0.163	0.082	106.20

Table 5.4 Comparison between the electron-phonon coupling constants and the logarithmic averaged phonon frequencies obtained from the enhanced Eliashberg spectral function using the three different exchange-correlation functionals (XCF): PBE, PBE0 and B3LYP.

Nevertheless, if the boosted parameters are now used as input for the McMillan/Allen-Dynes formula (keeping $\mu^* = 0.1$), no superconductive phase transition is observed yet. Clearly, this reasoning was meant to discuss the possibility of a phonon-mediated superconducting phase, and does not exclude that a superconducting phase with a different coupling mechanism can exist in this compound. Moreover, I have only analyzed the renormalization of the high-energy in-plane vibrational modes, however at the PBE level the out-of-plane displacement contributed for $\sim 50\%$ to the total value of λ: therefore, more accurate computations are needed in order to clearly establish whether a phonon mediated superconductivity is present or not at this surface doping.

Nevertheless, this discussion highlights the lack of precision when computing vibrational properties and electron-phonon interactions in the standard LDA/GGA approach. A more systematic and computationally achievable technique is needed for linear response computations including non-approximated electronic correlations.

Summary

- Standard LDA/GGA DFPT calculations severely underestimate the electron-phonon coupling;
- The strength of the electron-phonon interaction can be computed via finite differences including long-range electron-electron Coulomb correlations;
- The use of hybrid functionals boosts the electron-phonon coupling constant by a factor ~ 2 in the case of electron-doped ABC three-layer graphene;
- No phonon-mediated superconductivity is expected in rhombohedral three-layer graphene up to electron doping of $n_{2D} \sim 2 \times 10^{14}$ cm^{-2}.

Chapter 6

The Peierls Distortion in the Linear Acetylenic Carbon Chain

The linear acetylenic carbon chain (or carbyne) $(=C=C=)_\infty$ is the simplest example of a 1D carbon system. When atoms are equally spaced among them, they are connected by double bonds and the system is also called cumulene. However, at the harmonic approximation, the linear chain undergoes the Landau-Peierls [41, 43, 120] transition: carbon atoms get closer and we find sp-hybridized carbon dimers linked by triple bonds $(-C\equiv C-)_\infty$ and the new structure is called polyyne. As a result we have a metal-to-insulator phase transition due to a pure lattice instability [121–126] and, therefore, carbyne represents the prototypical example of a charge density wave (CDW) system.

The existence of carbyne is still controversial [114, 115]: indeed, due to the Mermin-Wagner-Hohenberg theorem [45, 46] and to the Coleman theorem [118], a long-range ordered phase in 1D cannot exist due to thermal fluctuations ($T \neq 0$ K) and quantum fluctuations (i.e. the zero-point motion of atoms [119] at $T = 0$ K). As a consequence, the dimerized polyyne structure should not be observed and cumulene should be the most stable phase. Nevertheless, Landau and Peierls showed that the long-range nature of interatomic forces stabilizes the distorted system.

Moreover, due to the light mass of carbon atoms and to the low dimensionality of such linear systems, zero-point (ZP) lattice motions are particularly relevant and the harmonic picture is no longer optimal for describing the vibrational properties: therefore the quantum nature of the carbon ion (i.e the fact that the carbon atom

has a wavefunction) and anharmonic phonon-phonon interactions have to be taken into account [127, 134]. The low dimensionality also favors the long-range electron-electron interaction, which plays a major role both in the electronic and in the vibrational properties as well as for the electron-phonon coupling as we discussed in Ch. 5 in the case the the rhombohedral graphene.

Therefore in this chapter I have analyzed the Peierls distortion of a linear acetylenic carbon chain taking into account both anharmonic phonon-phonon and electron-electron interactions. In particular, in Sec. 6.1 I will explain the standard Peierls distortion from an historical point of view using a tight-binding toy model of carbyne. Then, in Sec. 6.2 I will illustrate a way to go beyond the harmonic picture of the lattice dynamic, i.e the stochastic self-consistent harmonic approximation (SSHA). After that, in Sec. 6.3 I will analyze the structural instability of carbyne, studying the electronic and vibrational properties as well as the temperature dependence of the free energy of cumulene and polyyne. In Sec. 6.4.1 I will investigate the effect of quantum and thermal fluctuations of the lattice on the energy band gap. Finally in Sec. 6.4.2 I will analyze the excitonic effects on the energy band gap solving the Bethe-Salpeter equation. The computational details are given in App. A.

6.1 The Landau-Peierls distortion

6.1.1 Tight-binding description

The Peierls distortion of 1D system is the prototype of a charge density wave. Indeed, if the linear carbon chain with equidistant atoms (i.e. cumulene) at $T = 0$ K is considered, it shows a negative longitudinal phonon mode at $\mathbf{q} = 2\mathbf{k_F}$ (where k_F is the Fermi momentum) when computed using the harmonic approximation (see Fig. 6.1). As a consequence, the system is unstable and if the structure is distorted by moving carbon atoms according to the displacement of such vibrational mode, an energy gap is opened in the electronic dispersion: the linear acetylenic carbon chain is now insulating and the new ground state (polyyne) is more energetically favored and stable from the dynamical point of view.

If the system is assumed to be arranged along the x-axis of a cartesian coordinate system, cumulene has σ-bonds along the chain due to the sp^1 hybridization of the $2s$ and $2p_x$ orbitals. The remaining $2p_y$ and $2p_z$ orbitals form doubly degenerate π-bonds which are responsible for the metallicity of carbyne [121–126]. In order to qualitatively explain this metal-to-insulator phase transition induced by the lattice instability, I have employed a simple tight biding model.

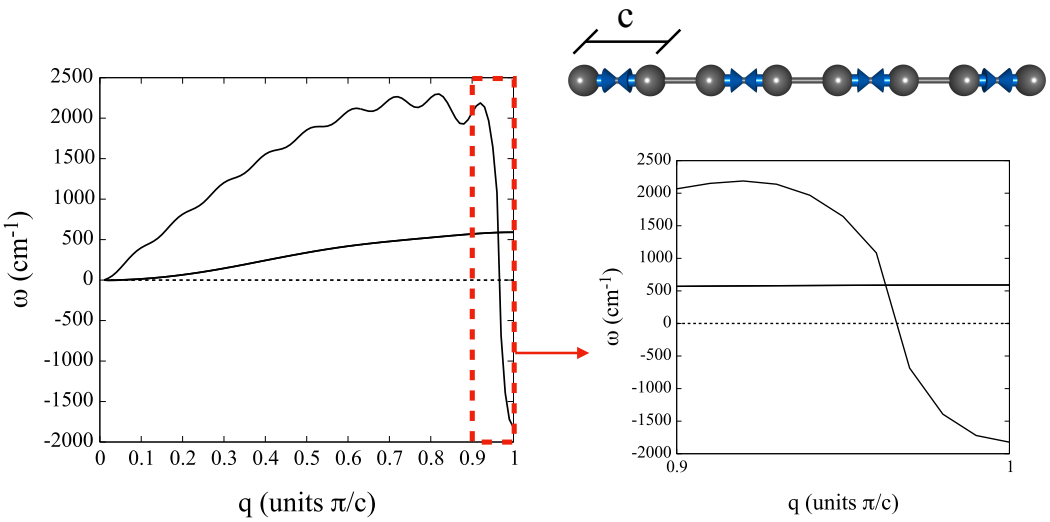

Fig. 6.1 Phonon dispersion relation of cumulene. We have zoomed around the border of the Brillouin zone in order to show the negative phonon mode. The corresponding atoms displacement is shown on top with blue arrow. The horizontal black dashed line is just a guide line for the zero frequency. Finally c is the lattice parameter of cumulene, which has only one atom per unit cell. This phonon dispersion relation has been computed via DFPT and with the aid of a PBE exchange-correlation functional within the harmonic approximation.

If only nearest-neighbor interaction are taken into account, the following secular equation has to be solved:

$$det\left[H^{(\mathbf{k})}_{nA,n'A'} - \varepsilon_{\mathbf{k}n} S^{(\mathbf{k})}_{nA,n'A'}\right] = 0 \tag{6.1}$$

where the tight-binding Hamiltonian and the overlap matrix are given by:

$$H^{(\mathbf{k})}_{nA,n'A'} = E^{nn'}_{0A}\,\delta_{A,A'} + \frac{1}{N}\sum_{<LA,L'A'>}(1-\delta_{A,A'}\delta_{L,L'})e^{i\mathbf{k}\cdot(\mathbf{R}_{LA}-\mathbf{R}_{L'A'})}t^{nn'}_{LA,L'A'} \tag{6.2a}$$

$$S^{(\mathbf{k})}_{nA,n'A'} = \delta_{n,n'}\delta_{A,A'} \tag{6.2b}$$

where N is the number of cells, $L = \{1,\dots,N\}$ is the cell index, $\mathbf{R}_{LA} = \mathbf{R}_L + \tau_A$ labels the A-th atom in the L-th unit cell and $\mathbf{R}_L$ is a direct lattice vector. Moreover, $E_{0A}^{nn'}$ is the on-site energy and n is the orbital index. Finally, the sum in the first equation is limited only to the nearest neighbor $< LA, L'A' >$. Notice that the Hamiltonian and the overlap matrix are matrices of dimension $\{\#\text{ of atoms per cell}\} \times \{\#\text{ of orbitals per atom}\}$.

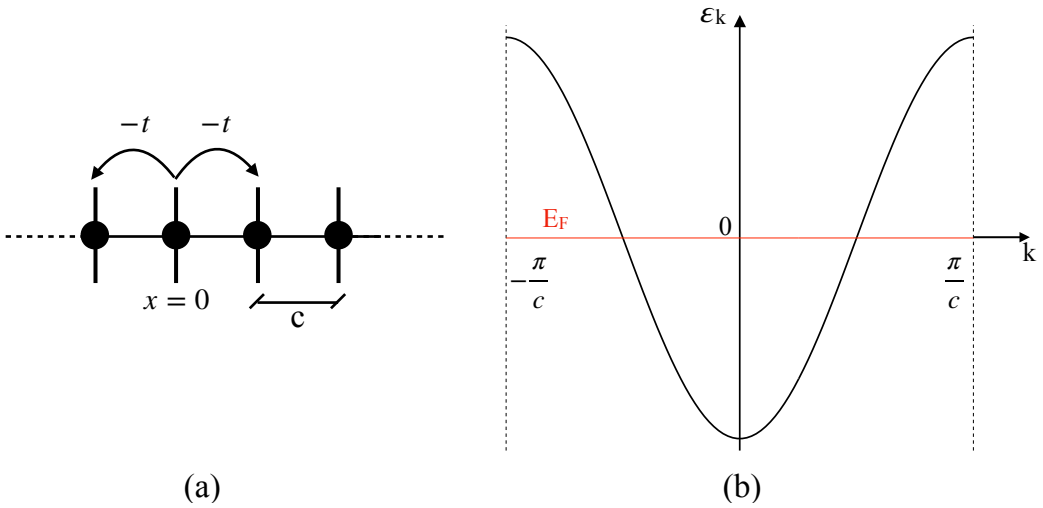

Fig. 6.2 (a) Toy model of cumulene. Black dots represent the carbon atoms and black vertical lines identify the unit cells; (b) Electronic dispersion relation of cumulene obtained from the tight-binding model in the nearest neighbor approximation. The red line represents the Fermi level ($E_F = 0$).

First of all, consider the undistorted chain, cumulene. There is only one atom per unit cell with a distance between nearest neighbors equal to c, therefore the unit cell of the direct lattice is $[0,c[$ (Fig. 6.2), and I considered one $2p_z$ orbital per atom. As a consequence $n = 1$ and $A = 1$, therefore $H^{(\mathbf{k})}_{nA,n'A'}$ and $S^{(\mathbf{k})}_{nA,n'A'}$ are 1×1 matrices. I also assumed that the the hopping matrix elements are:

$$t^{nn'}_{LA,L'A'} = \begin{cases} -t & \text{if } x = \pm c \\ 0 & \text{otherwise} \end{cases} \tag{6.3}$$

Therefore the following eigenvalue problem need to be solved:

$$E_0 - 2t\cos(kc) - \varepsilon_k = 0 \implies \varepsilon_k = E_0 - 2t\cos(kc) \tag{6.4}$$

and the resulting dispersion relation is shown in Fig. 6.2 (b). Notice that the on-site energy is just a simple energy shift, which can be set to zero without loss of generality. If every atom has one electron per orbital, the system is half filled: the Fermi level falls in the middle of the electronic band and, as such, cumulene is metallic.

If atoms are displaced according to the longitudinal imaginary phonon mode of Fig. 6.1 (assuming that the atom displacement is sufficiently small, i.e. $\delta << c$) the polyyne crystal structure is obtained. In order to correctly reproduce the system a unit cell which is twice as large as that of cumulene has to be taken into account, with two atoms per cell (Fig. 6.3 (a)). The unit cell of the direct lattice is now $[0, 2c[$ and $A = 1, 2$ and $n = 1$: therefore, $H^{(\mathbf{k})}_{nA,n'A'}$ and $S^{(\mathbf{k})}_{nA,n'A'}$ are 2×2 matrices. Moreover, I assumed that the overlap matrix is zero on different sites and that the hopping matrix elements are:

$$t^{nn'}_{LA,L'A'} = \begin{cases} -t_1 & \text{if } x = c + \delta \\ -t_2 & \text{if } x = c - \delta \\ 0 & \text{otherwise} \end{cases} \tag{6.5}$$

with $|t_1| < |t_2|$ if $\delta \neq 0$ and $t_1 = t_2 = t$ if $\delta = 0$. Indeed, the hopping parameter t depends on x like $t(x) \sim 1/x^3$ for p orbitals.

Therefore the following eigenvalue problem has to be solved:

$$\det \begin{bmatrix} E_0 - \varepsilon_k & H_{12} \\ H^*_{12} & E_0 - \varepsilon_k \end{bmatrix} = 0 \implies \varepsilon_k = \pm |H_{12}| \tag{6.6}$$

where I have set $E_0 = 0$ in the final result without loss of generality and $H_{21} = H^*_{12}$ since the Hamiltonian is Hermitian and:

$$H_{12} = -t_1 e^{-ik(c+\delta)} - t_2 e^{ik(c-\delta)} \tag{6.7}$$

The final dispersion relation for the polyyne is then:

$$\varepsilon_k = \pm \sqrt{\Delta^2 + 2\eta^2 \cos(2kc)} \tag{6.8}$$

where $\Delta^2 = t_1^2 + t_2^2$ and $\eta^2 = t_1 t_2$.

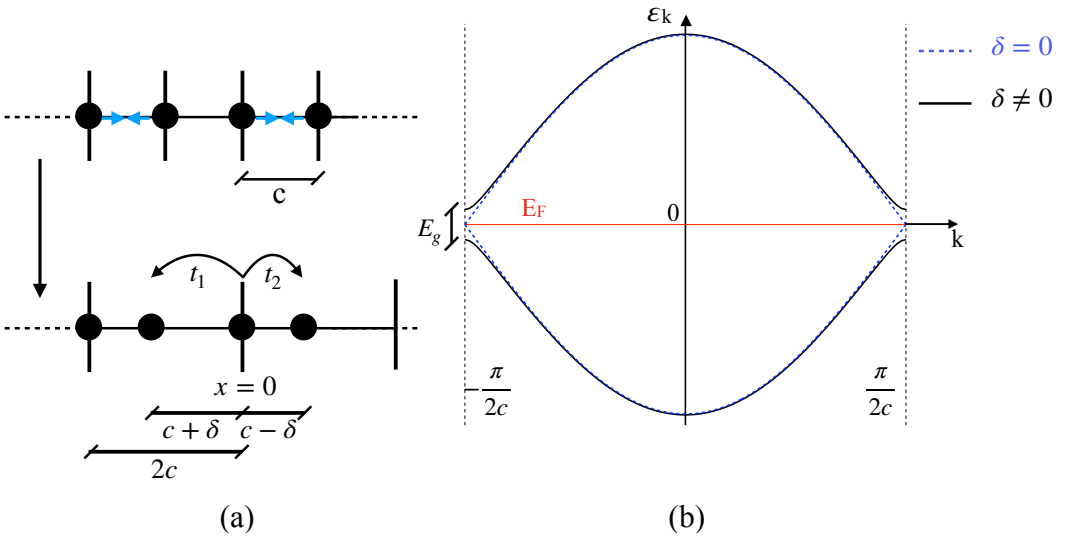

Fig. 6.3 (a) Toy model of polyyne. Black dots represent the carbon atoms and black vertical lines identify the unit cells. On the upper part of the panel we show the phonon displacement pattern applied to the cumulene. On the lower panel we show the distorted polyyne; (b) Electronic dispersion relation of polyyne obtained from the tight-binding model in the nearest neighbor approximation. Blue dashed lines represent the zero displacement case ($\delta = 0$), while the black solid line identifies the displaced-atoms picture ($\delta \neq 0$). The red line represents the Fermi level ($E_F = 0$). E_g is the energy gap which is opened due to the displacement of atoms.

The band structure is shown in Fig. 6.3 and for $\delta = 0$ (i.e. no atom displacement, cumulene) the system is metallic, while for $\delta \neq 0$ we have an insulator with an energy gap: indeed, in this latter case, $\varepsilon_{\pi/2c} = \pm\sqrt{\Delta^2 - 2\eta^2}$ and the whole lower band must be filled, so that the Fermi level ($E_F = 0$) falls in the middle of the band gap: the atomic displacement has opened a gap at the zone boundary.

The insulating phase is energetically favored over the metallic phase since the energy gap lowers the total energy of the polyyne structure. This can be seen by computing the total energy, which in an independent particle picture (such as the tight binding model) is defined as:

$$E = 2 \sum_{\substack{k \\ \varepsilon_k \leq E_F}} \varepsilon_k \tag{6.9}$$

where the factor 2 comes from spin degeneracy. Indeed, by fitting the electronic band structure of cumulene with Eq. 6.4 and that of polyyne with Eq. 6.8, at the level of PBE exchange-correlation functional I have obtained:

$$\begin{cases} t = 2.78 \text{ eV} \\ \Delta^2 = 15.64 \text{ eV}^2 \\ \eta^2 = 7.56 \text{ eV}^2 \end{cases} \tag{6.10}$$

Computing the total energy of both phases through Eq. 6.9 with such parameters it is possible to observe that, passing from the undistorted to the distorted structure, carbyne has an energy gain of ~ 0.42 eV. This is the insulator-to-metal phase transition due to the Peierls model for the charge density wave in carbyne at $T = 0$ K.

However, in this simple toy model, I have neglected both the electron-electron interactions and the anharmonic phonon-phonon interactions which can drastically alter the electronic band structure even at zero temperature. Therefore, in the remaining part of the thesis, I have studied the Peierls distortion from first principle by also taking into account interaction terms which were neglected in this simplistic description.

6.1.2 Many-body description

In the tight-binding description of the Landau-Peierls instability we have employed an energetic argument in order to show that the insulating phase is favored. Following Refs. 119,333 and334, we now want to derive the properties of a charge density wave in carbyne from a dynamical point of view using a many-body Green's function approach.

The starting point is the the Frölich hamiltonian [173] we have introduced in Sec. 2.2. We will focus on the unstable longitudinal phonon mode ($\nu = 1$) and we will consider a momentum-independent electron-phonon coupling constant ($g^{\nu}_{\mathbf{k}j,\mathbf{k}+\mathbf{q}j'}$=g). Moreover, for simplicity, we will consider spinless fermions and a single-band picture ($j = 1$):

$$\hat{H}_{\text{tot}} = \sum_{\mathbf{k}} \varepsilon^0_{\mathbf{k}} c^{\dagger}_{\mathbf{k}} c_{\mathbf{k}} + \sum_{\mathbf{q}} \hbar\omega^0_{\mathbf{q}} \left(b^{\dagger}_{\mathbf{q}} b_{\mathbf{q}} + \frac{1}{2} \right) + g \sum_{\mathbf{k},\mathbf{q}} c^{\dagger}_{\mathbf{k}} c_{\mathbf{k}+\mathbf{q}} \left[b_{\mathbf{q}\nu} + b^{\dagger}_{-\mathbf{q}\nu} \right] \tag{6.11}$$

where $c^{\dagger}_{\mathbf{k}}$ ($c_{\mathbf{k}}$) is the creation (destruction) operator for a fermion of momentum $\mathbf{k}$ with energy $\varepsilon^0_{\mathbf{k}}$ (i.e the Kohn-Sham eigenvalue measured with respect to the chemical potential, which is the Fermi level E_F at $T = 0$ K), while $b^{\dagger}_{\mathbf{q}}$ ($b_{\mathbf{q}}$) is the creation (destruction) operator for a phonon of unscreened frequency $\omega^0_{\mathbf{q}}$ of momentum $\mathbf{q}$.

Through this Hamiltonian we can derive the RPA approximated phonon self-energy ($\bar{\Pi}^{0,R}(q,\omega)$) as described in Sec. 2.3, which is related to the Lindhard function ($\chi^0(q,\omega)$) [186]:

$$\bar{\Pi}^{0,R}(q,\omega_q) = \frac{g^2}{N_k} \sum_k \frac{f(\varepsilon_k) - f(\varepsilon_{k+q})}{\omega_q - (\varepsilon^0_k - \varepsilon^0_{k+q})} = \frac{g^2}{N_k} \chi^0(q,\omega_q) \tag{6.12}$$

where N_k is the number of k-points used in the summation over k, ω_q is the complex frequency (such that $\Im\mathfrak{m}(\omega_q) > 0$) and $f(\varepsilon_k) = (\exp(\beta\varepsilon^0_k) + 1)^{-1}$ is the Fermi-Dirac distribution.

From the Dyson equation (Eq. 2.27) we can derive the exact phonon propagator as:

$$D(q,\omega_q) = \frac{2\omega^0_q}{\omega^2_q - (\omega^0_q)^2 - 2\omega^0_q \bar{\Pi}^{0,R}(q,\omega_q)} \tag{6.13}$$

from whose poles we can obtain the renormalized phonon frequencies:

$$\omega_q^2 = (\omega_q^0)^2 + 2\omega_q^0 \bar{\Pi}^{0,R}(q, \omega_q) \tag{6.14}$$

We thus need to find an analytical expression for the phonon self-energy. In order to do so we look at $q = 2k_F$ (where we already know that there is an instability) and, following Refs. 119 and333, we set $\omega_q = 0$ since the renormalized phonon frequency is typically smaller than any structure in the electron-hole continuum. Moreover, in order to simplify calculations, we consider $k/k_F << 1$ so that we can linearize the electronic dispersion relation:

$$\varepsilon_k^0 = v_F(|k| - k_F) \tag{6.15}$$

where $v_F = k_F/m_e$ is the Fermi velocity (and m_e is the electron mass). By doing so, it is possible to show [119, 333] that the phonon self-energy at $q = 2k_F$ is:

$$\bar{\Pi}^{0,R}(2k_F, 0) = -\frac{\omega_{2k_F}^0}{2} + \frac{\lambda\,\omega_{2k_F}^0}{2} \ln\left(\frac{T}{T_{CDW}}\right) \tag{6.16}$$

with $\lambda = g^2/\omega_q\varepsilon_F$ being the dimensionless electron-phonon coupling constant, ε_F is the Fermi energy and T is the temperature. Moreover, $k_B T_{CDW} = 1.14\varepsilon_F e^{-1/\lambda}$ is the critical temperature for the appearance of the charge density wave (where k_B is the Boltzmann constant).

The phonon softening at $q = 2k_F$ is thus described by:

$$\omega_{2k_F}^2 = \lambda(\omega_{2k_F}^0)^2 \ln\left(\frac{T}{T_{CDW}}\right) \tag{6.17}$$

For $T > T_{CDW}$ the undressed phonon frequency is suppressed until it vanishes for $T = T_{CDW}$. On the other hand, for $T < T_{CDW}$ there is a lattice instability (i.e. the Landau-Peierls instability): there is a continuous phase transition from an ordered metallic phase to a distorted insulating phase with the appearance of an energy gap Δ, which can be thought of as a phonon condensation into a coherent state.

The temperature dependence of the energy gap ($\Delta(T)$) can be derived by minimizing the free energy change due to the Peierls distortion with respect to Δ (which is proportional to the periodic lattice distortion in the mean-field picture) [335].

At $T = 0$ K we find an energy gap of:

$$\Delta(0) = 2\varepsilon_F e^{-1/\lambda} = 1.76 k_B T_{CDW} \tag{6.18}$$

and renormalized phonon frequencies:

$$\omega_{q,o}^2 = \lambda(\omega_{2k_F}^0)^2 + \tfrac{1}{3}\tfrac{m}{m^*}(v_F q)^2 \tag{6.19a}$$

$$\omega_{q,a}^2 = \tfrac{m}{m^*}(v_F q)^2 \tag{6.19b}$$

where $m^*/m = 1 + 4\Delta^2/\lambda(\omega_{2k_F}^0)^2$. Here $\omega_{q,o}^2$ and $\omega_{q,a}^2$ denotes the optical (Raman active) and acoustic phonon branches respectively. Moreover, $\omega_{q,a}$ and $\omega_{q,o}$ represent also the phase (phason) and amplitude (amplitudon) of the charge density wave, i.e. the time dependence of amplitude and phase fluctuations of the lattice distortion about the mean field value [119, 333].

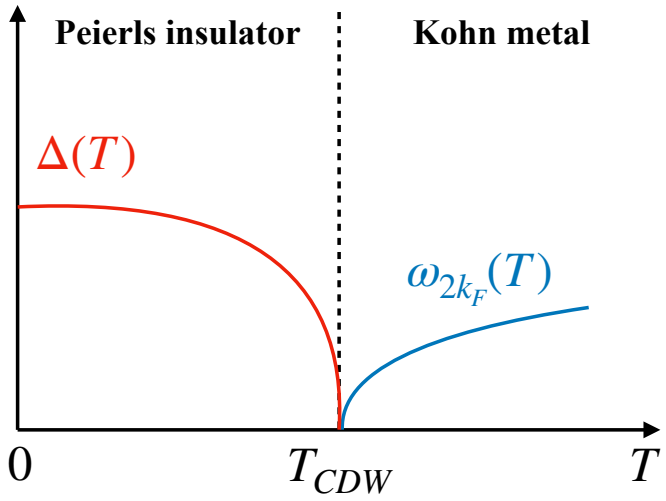

Fig. 6.4 Schematic representation of the temperature dependence of the unstable phonon mode $\omega_{2k_F}(T)$ and the Peierls gap $\Delta(T)$ arising from the RPA picture.

6.2 The Stochastic Self-Consistent Harmonic Approximation (SSCHA)

Phonon-phonon anharmonic interactions, i.e. those which were neglected when we truncated the expansion of the Born-Oppenheimer energy surface (harmonic approximation) in Eq. 2.15, introduce finite scattering rates and lifetimes in the quasiparticle picture of the thermally vibrating lattice. Usually, when the atom displacement is sufficiently small, a perturbative approach is employed to treat anharmonicity [336]. However, when we deal with light atoms [337–343] or when the system is on the verge of a phase transition [344–346] the perturbative approach fails and we need to go beyond it.

Usually this is accomplished either within classical molecular dynamics methods [347–350] or via path-integral molecular dynamics[351]. However, while the first doesn't take into account quantum effects, the latter is computationally expensive. Such difficulties can be overcome with the aid of several methods [337, 338, 352–357] based on the self-consistent harmonic approximation (SCHA), first proposed by D. J. Hooton [358]: thanks to this effective harmonic theory it is possible to obtain the free energy of strongly anharmonic systems.

Consider the Hamiltonian of a crystal lattice, defined in Eq. 2.7:

$$H = \sum_{A=1}^{N_{\text{atom}}} \sum_{\alpha=1}^{3} \frac{P_{A,\alpha}^2}{2M_A} + E(\mathbf{R}) \tag{6.20}$$

where we recall that N_{atom} is the number of atoms, A is the atom label and α are the cartesian coordinates. M_A is the A-th atomic mass, $R^{A,\alpha}$ and $P_{A,\alpha}$ are the position and the momentum operators respectively and $E(\mathbf{R})$ is the Born-Oppenheimer energy surface. The free energy of the lattice hamiltonian at a certain temperature T is a sum between its total energy and the entropic contribution:

$$F = \text{Tr}[\rho H] + \frac{1}{\beta}\text{Tr}[\rho \log(\rho)] \tag{6.21}$$

where $\beta = k_B T$ is the inverse temperature and the trace is taken on the atomic Hilbert space. The equilibrium density matrix is defined as:

$$\rho = e^{-\beta H}/\text{Tr}[e^{-\beta H}] \tag{6.22}$$

However, when dealing with many interacting atoms, the computation of the free energy can become complicated. Therefore the main idea of the self-consistent harmonic approximation is to use a variational approach with the aid of a trial hamiltonian and minimize the free energy of the system.

First of all we define a trial harmonic hamiltonian, which is parametrized in terms of a generic square positive-definite trial matrix $\boldsymbol{\phi}$ of order $3N_{\text{atom}}$ and a vector $\boldsymbol{\mathcal{R}}$ of dimension $3N_{\text{atom}}$ (i.e. our variational parameters):

$$\tilde{H}_{\boldsymbol{\mathcal{R}},\boldsymbol{\phi}} = \sum_a \frac{P_a^2}{2M_a} + \tilde{E}(\boldsymbol{\mathcal{R}},\boldsymbol{\phi}) \tag{6.23a}$$

$$\tilde{E}(\boldsymbol{\mathcal{R}},\boldsymbol{\phi}) = \frac{1}{2}\sum_{ab}\phi_{ab}(R-\mathcal{R})^a(R-\mathcal{R})^b \tag{6.23b}$$

where we have grouped the atom and cartesian coordinate label in $a = A,\alpha$ and $\tilde{E}(\boldsymbol{\mathcal{R}},\boldsymbol{\phi})$ is the harmonic trial potential respecting the symmetry of the system. As such, we can define a generic density matrix $\tilde{\rho}_{\boldsymbol{\mathcal{R}},\boldsymbol{\phi}}$ and a corresponding free energy:

$$\tilde{\rho}_{\boldsymbol{\mathcal{R}},\boldsymbol{\phi}} = e^{-\beta\tilde{H}_{\boldsymbol{\mathcal{R}},\boldsymbol{\phi}}}/\text{Tr}[e^{-\beta\tilde{H}_{\boldsymbol{\mathcal{R}},\boldsymbol{\phi}}}] \tag{6.24a}$$

$$\mathcal{F}[\tilde{\rho}_{\boldsymbol{\mathcal{R}},\boldsymbol{\phi}}] = \text{Tr}[\tilde{\rho}_{\boldsymbol{\mathcal{R}},\boldsymbol{\phi}}\tilde{H}_{\boldsymbol{\mathcal{R}},\boldsymbol{\phi}}] + \frac{1}{\beta}\text{Tr}[\tilde{\rho}_{\boldsymbol{\mathcal{R}},\boldsymbol{\phi}}\log\big(\tilde{\rho}_{\boldsymbol{\mathcal{R}},\boldsymbol{\phi}}\big)] \tag{6.24b}$$

Thanks to the Gibbs-Bogoliubov variational principle [359] we know that the free energy computed for the exact Hamiltonian is always smaller than the one computed with the trial Hamiltonian:

$$F[\rho] \leq \mathcal{F}[\tilde{\rho}_{\boldsymbol{\mathcal{R}},\boldsymbol{\phi}}] \tag{6.25}$$

We can define the average, with respect to the density matrix, of the observables that are functions of the position only $\mathbf{R}$ as:

$$\langle\mathbb{O}\rangle_{\tilde{\rho}_{\boldsymbol{\mathcal{R}},\boldsymbol{\phi}}} = \text{Tr}[\mathbb{O}\tilde{\rho}_{\boldsymbol{\mathcal{R}},\boldsymbol{\phi}}] = \int \mathbb{O}(\mathbf{R})\tilde{\rho}_{\boldsymbol{\mathcal{R}},\boldsymbol{\phi}}(\mathbf{R})d\mathbf{R} \tag{6.26}$$

with $\tilde{\rho}_{\boldsymbol{\mathcal{R}},\boldsymbol{\phi}}(\mathbf{R})$ being the diagonal part of the density matrix. Therefore, we can see that $\boldsymbol{\mathcal{R}}$ is a vector that contains the coordinates of the average position of the atoms

(centroids) for the trial density matrix:

$$\langle \mathbf{R} \rangle_{\tilde{\rho}_{\boldsymbol{\mathcal{R}},\boldsymbol{\phi}}} = \boldsymbol{\mathcal{R}} \tag{6.27}$$

The best approximation to the free energy within the self-consistent harmonic approximation ($F^{(s)}(\boldsymbol{\mathcal{R}}_{eq})$), according to the Gibbs-Bogoliubov variational principle, is obtained by minimizing the trial free energy:

$$F^{(s)}(\boldsymbol{\mathcal{R}}_{eq}) = \min_{\boldsymbol{\mathcal{R}}}(\min_{\boldsymbol{\phi}} \mathcal{F}[\tilde{\rho}_{\boldsymbol{\mathcal{R}},\boldsymbol{\phi}}]) \tag{6.28}$$

where $\boldsymbol{\mathcal{R}}_{eq}$ is the SCHA equilibrium configuration of the centroids at a given temperature T. We also define the square matrix $\boldsymbol{\Phi}(\boldsymbol{\mathcal{R}})$ as that matrix that minimizes $\mathcal{F}[\tilde{\rho}_{\boldsymbol{\mathcal{R}},\boldsymbol{\phi}}]$ with respect to $\boldsymbol{\phi}$ and which satisfies the self-consistent equation:

$$\Phi_{ab}(\mathcal{R}) = \langle \frac{\partial^2 E}{\partial R^a \partial R^b} \rangle_{\tilde{\rho}_{\boldsymbol{\mathcal{R}},\boldsymbol{\Phi}}} \tag{6.29}$$

We now have access to the free energy of the system as a function of the centroids (i.e. the average atomic positions) and we can use it to study both quantum and thermal lattice instabilities as well as first-order phase transitions.

As a matter of fact, the centroids can be used to define an order parameter (e.g. the relative position of atoms at a certain temperature) to study second-order phase transitions such as charge-density-waves or ferroelectric instabilities. Indeed, at a certain temperature, the equilibrium configuration $\boldsymbol{\mathcal{R}}_{eq}$ corresponds to a minimum of the free energy $F^{(s)}(\boldsymbol{\mathcal{R}}_{eq})$: its first derivative is zero, i.e. $\partial F^{(s)}(\boldsymbol{\mathcal{R}})/\partial \mathcal{R}^a \Big|_{\boldsymbol{\mathcal{R}}_{eq}} = 0$, while the Hessian matrix is positive definite, i.e. $\partial^2 F^{(s)}(\boldsymbol{\mathcal{R}})/\partial \mathcal{R}^a \partial \mathcal{R}^b \Big|_{\boldsymbol{\mathcal{R}}_{eq}} > 0$. According to the Landau's theory of second-order (or continuous) phase transitions [360], for $T > T_c$ the equilibrium configuration coincides with a high-symmetry phase of the system but for T approaching the critical temperature the minimum of the free energy becomes less and less pronounced until, for $T = T_c$, $\partial^2 F^{(s)}(\boldsymbol{\mathcal{R}})/\partial \mathcal{R}^a \partial \mathcal{R}^b \Big|_{\boldsymbol{\mathcal{R}}_{eq}}$ develops at least one null eigenvalue. Finally, for $T < T_c$ the zero eigenvalue of the free energy hessian becomes negative, i.e. we obtain a saddle point, and the system collapses to a lower symmetry equilibrium configuration (spontaneous symmetry breaking).

Therefore, in order to correctly describe the second order phase transitions within the self-consistent harmonic approximation, we have to compute the Hessian of the free energy: for $T > T_c$ such quantity is positive definite, while for $T < T_c$ it develops at least one negative eigenvalue which gives the atomic distortion that lowers the free energy of the system. We define the n-th order SCHA tensor as:

$$\Phi^{(n)}_{a_1 \dots a_n}(\boldsymbol{\mathcal{R}}) = \langle \frac{\partial^n E}{\partial R^{a_1} \cdots \partial R^{a_n}} \rangle_{\tilde{\rho}_{\boldsymbol{\mathcal{R}},\boldsymbol{\Phi}}} \tag{6.30}$$

The Hessian matrix of the free energy is given by [361]:

$$\frac{\partial^2 F^{(s)}(\boldsymbol{\mathcal{R}})}{\partial \boldsymbol{\mathcal{R}} \partial \boldsymbol{\mathcal{R}}} = \boldsymbol{\Phi} + \boldsymbol{\Phi}^{(3)} \boldsymbol{\Lambda} [\mathbb{I} - \boldsymbol{\Phi}^{(4)} \boldsymbol{\Lambda}]^{-1} \boldsymbol{\Phi}^{(3)} \tag{6.31}$$

where the dependence on $\boldsymbol{\mathcal{R}}$ is understood and we have defined:

$$\Lambda^{abcd} = -\frac{\hbar^2}{8} \sum_{\nu\mu} \frac{F(0,\omega_\mu,\omega_\nu)}{\omega_\mu \omega_\nu} \frac{e^a_\nu}{\sqrt{M_a}} \frac{e^b_\mu}{\sqrt{M_b}} \frac{e^c_\nu}{\sqrt{M_c}} \frac{e^d_\mu}{\sqrt{M_d}} \tag{6.32a}$$

$$F(0,\omega_\mu,\omega_\nu) = \begin{cases} \frac{2}{\hbar}\left(\frac{2n_\nu+1}{2\omega_\nu} - \frac{dn_\nu}{d\omega_\nu}\right) & \text{if } \omega_\nu = \omega_\mu \\ \frac{2}{\hbar}\left(\frac{n_\nu+n_\mu+1}{\omega_\nu+\omega_\mu} - \frac{n_\mu-n_\nu}{\omega_\mu-\omega_\nu}\right) & \text{if } \omega_\nu \neq \omega_\mu \end{cases} \tag{6.32b}$$

Here, e^a_ν and ω^2_ν are respectively the eigenvectors and eigenvalues of $\Phi_{ab}/\sqrt{M_a M_b}$ and n_ν is the Bose-Einstein distribution for mode ν. Notice that while $\boldsymbol{\Phi}$ is a positive definite matrix, $\boldsymbol{\Lambda}$ is a negative definite matrix making the quantity $\boldsymbol{\Phi}^{(3)}\boldsymbol{\Lambda}\boldsymbol{\Phi}^{(3)}$ semi-negative definite and thus allowing for the possibility of a negative eigenvalue and therefore a correct description of the second-order phase transitions within the SCHA framework.

Finally, we can define a generalization of the harmonic dynamical matrix (Eq. 2.17) based on the temperature-dependent free-energy:

$$D^{(F)}_{ab} = \frac{1}{\sqrt{M_a M_b}} \left. \frac{\partial^2 F^{(s)}}{\partial \mathcal{R}^a \partial \mathcal{R}^b} \right|_{\boldsymbol{\mathcal{R}}_{eq}} \tag{6.33}$$

such that:

$$\det\left| D^F_{a,b}(\mathbf{q}) - \Omega^2_{\mathbf{q}\nu} \mathbb{I} \right| = 0 \tag{6.34}$$

and $\Omega_{\mathbf{q}\nu}$ are free-energy based anharmonic phonons: a dynamical instability of the system would lead to negative eigenvalues of the dynamical matrix and therefore to imaginary phonon frequencies.

The stochastic implementation of the self-consistent harmonic approximation (SSCHA) [337, 338, 361] has proved to be a useful tool to explicitly probe the (approximated) anharmonic free energy of a system in a non-perturbative way. The free energy functional $\mathcal{F}[\tilde{\rho}_{\boldsymbol{\mathcal{R}},\boldsymbol{\phi}}]$ and its derivatives are expressed as averages with respect to $\tilde{\rho}_{\boldsymbol{\mathcal{R}},\boldsymbol{\phi}}$ of observables that are functions of the Born-Oppnheimer energy surface, $E(\mathbf{R})$, and of the forces acting on atoms, $\mathbf{f}(\mathbf{R}) = -\partial E/\partial \mathbf{R}$, i.e. $\mathbb{O}(\mathbf{R}) = \mathbb{O}(E(\mathbf{R}),\mathbf{f}(\mathbf{R}))$.

The procedure goes as follow:

- We generate a sufficiently large population of finite size $\mathcal{N}_\mathcal{I}$, with elements $\mathbf{R}_{(\mathcal{I})} = \boldsymbol{\mathcal{R}} + \mathbf{u}_\mathcal{I}$: $\mathbf{u}_\mathcal{I}$ are the displacements from the centroids $\mathcal{R}$ generated according to an initially fixed probability distribution $\tilde{\rho}_{in}(\mathbf{R}_{(\mathcal{I})})$;
- Forces and energies are calculated for each atomic distortion, i.e. $\mathbf{f}(\mathbf{R}_{(\mathcal{I})})$ and $E(\mathbf{R}_{(\mathcal{I})})$. Notice that this step can be performed with many different techniques, such as DFT, molecular dynamic or quantum montecarlo;
- Averages are computed via importance sampling, making the technique stochastic and leading to the exact value in the thermodynamic limit (i.e. $\mathcal{N}_\mathcal{I} \to \infty$):

$$\langle \mathbb{O} \rangle_{\tilde{\rho}_{\boldsymbol{\mathcal{R}},\boldsymbol{\phi}}} \approx \frac{1}{\mathcal{N}_\mathcal{I}} \sum_{\mathcal{I}=1}^{\mathcal{N}_\mathcal{I}} \frac{\tilde{\rho}_{\boldsymbol{\mathcal{R}},\boldsymbol{\phi}}(\mathbf{R}_{(\mathcal{I})})}{\tilde{\rho}_{in}(\mathbf{R}_{(\mathcal{I})})} \mathbb{O}(E(\mathbf{R}_{(\mathcal{I})}),\mathbf{f}(\mathbf{R}_{(\mathcal{I})})) \tag{6.35}$$

- Minimize the free energy functional $\mathcal{F}[\tilde{\rho}_{\boldsymbol{\mathcal{R}},\boldsymbol{\phi}}]$ with respect to $\boldsymbol{\mathcal{R}}$ and $\boldsymbol{\phi}$ with a conjugate-gradient method;
- Recompute the probability distribution $\tilde{\rho}_{\boldsymbol{\mathcal{R}},\boldsymbol{\phi}}(\mathbf{R}_{(\mathcal{I})})$;
- Iterate until convergence.

6.3 Structural instability of carbyne

6.3.1 Cumulene

First of all consider cumulene, where carbon atoms are equally spaced and connected by double bonds. From the tight-biding toy model I have discussed in Sec. 6.1, it is known that this system in unstable at $T = 0$ K, due to the presence of an unstable longitudinal mode at $\mathbf{q} = 2\mathbf{k}_F$ (with $\mathbf{k}_F$ being the Fermi momentum). In order to understand if there is a true lattice instability, I have performed linear response calculations on cumulene taking also into account both anharmonic lattice terms in the expansion of the Born-Oppenheimer energy surface and electron-electron correlation.

Usually, carbyne is studied in DFT via hybrid functionals [121, 124, 362–364] with better results obtained through the PBE0 and the HSE06 hybrid functionals [362, 364] (the latter being a generalization of the PBE0 XC functional enhancing short-range interactions). In order to lighten the computational load, I have taken into account electron-electron correlation via the PBE0 hybrid exchange-correlation functional and later on I will show that this choice compares well with more accurate computations within the G_0W_0 approximation.

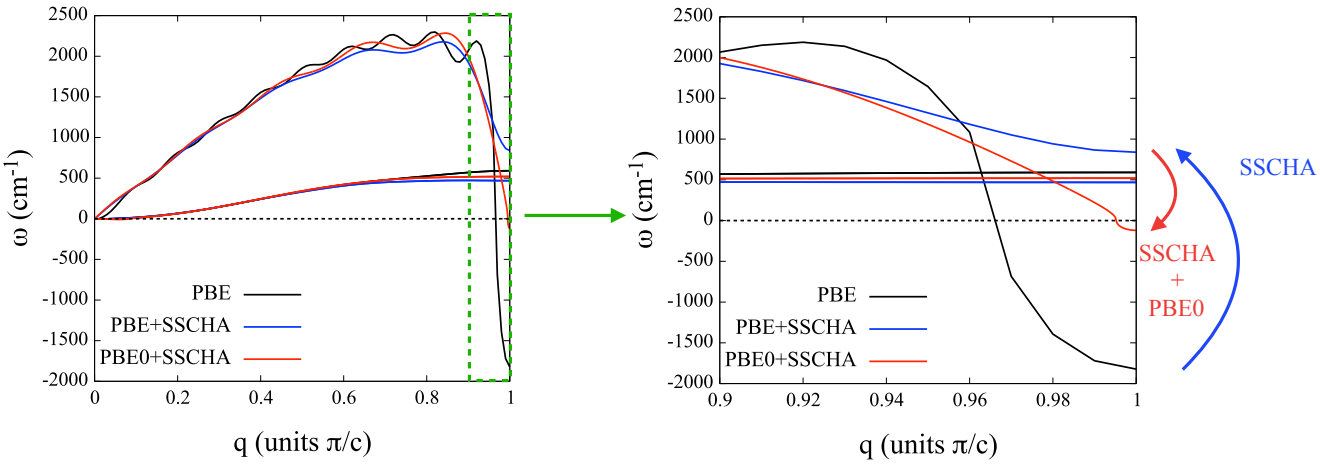

Fig. 6.5 Comparison of the phonon dispersion relation of cumulene computed with the PBE exchange-correlation functional (black line), adding anharmonic contribution via the SSCHA approach (blue line) and taking into account both anharmonic phonon-phonon interaction and electron-electron interaction via the PBE0 hybrid exchange-correlation functional (red line).

In Fig. 6.5 I have plotted a comparison of the phonon dispersion relation computed at $T = 0$ K with the PBE exchange-correlation (XC) functional (black line), adding anharmonic contribution via the SSCHA approach (blue line) and taking into account both anharmonic phonon-phonon interaction and electron-electron correlations via the PBE0 hybrid XC functional (red line). At the harmonic level and with the PBE XC functional, there is an instability at the border of the Brillouin zone of frequency $\omega^{(C)}_{\text{PBE}} \sim -1800$ cm^{-1} confirming the result of the simple tight-binding model.

However, departing from the harmonic picture and taking into account the anharmonic phonon-phonon interactions, such instability is removed and the longitudinal vibrational mode is stabilized at $\omega^{(C)}_{\text{PBE+SSCHA}} \sim 840$ cm^{-1} making cumulene stable. Notice that SSCHA computations of the free energy Hessian are performed by also taking into account the third-order SSCHA tensor $\mathbf{\Phi}^{(3)}$ which allows us to detect a dynamical instability if present, as explained in Sec. 6.2. This result shows that carbyne is a strongly anharmonic system since there is an energy gain of ~ 0.3 eV, as expected due to the light mass of carbon atoms and to the low dimensionality of the system (i.e. 1D) [132, 134].

Nevertheless, as soon as electronic correlations are included together with the SSCHA evaluation of the phonon frequencies, the longitudinal vibrational mode becomes again negative with a value of $\omega^{(C)}_{\text{PBE0+SSCHA}} \sim -120$ cm^{-1}. Therefore cumulene is actually unstable at zero temperature: I have shown that the instability is not purely due to the zero-point motion of the atoms but also electron-electron correlations are important. Results are summarized in Tab. 6.1.

	PBE	PBE+SSCHA	PBE0+SSCHA
$\omega^{(C)}$ (cm^{-1})	-1800	840	-120

Table 6.1 Comparison of the unstable longitudinal phonon frequency at $T = 0$ K computed with the PBE exchange-correlation functional, adding anharmonic contribution via the SSCHA approach and taking into account both anharmonic phonon-phonon interaction and electron-electron interaction via the PBE0 hybrid exchange-correlation functional.

While the anharmonic effects can be understood as a positive shift of the harmonic frequencies due to the zero-point motion of atoms, electronic correlations modify the electron-phonon coupling constant and as a consequence increase the magnitude

of the instability. In order to do so, I make use of the mean-field picture discussed in Sec. 6.1.2. In Fig. 6.6 (a) I have plotted the renormalization of the longitudinal mode due to the electron-phonon interaction (Eq. 6.17) as a function of the dimensionless electron-phonon coupling constant λ: it is possible to observe that by increasing (decreasing) such parameter, the instability tends to be highlighted (suppressed).

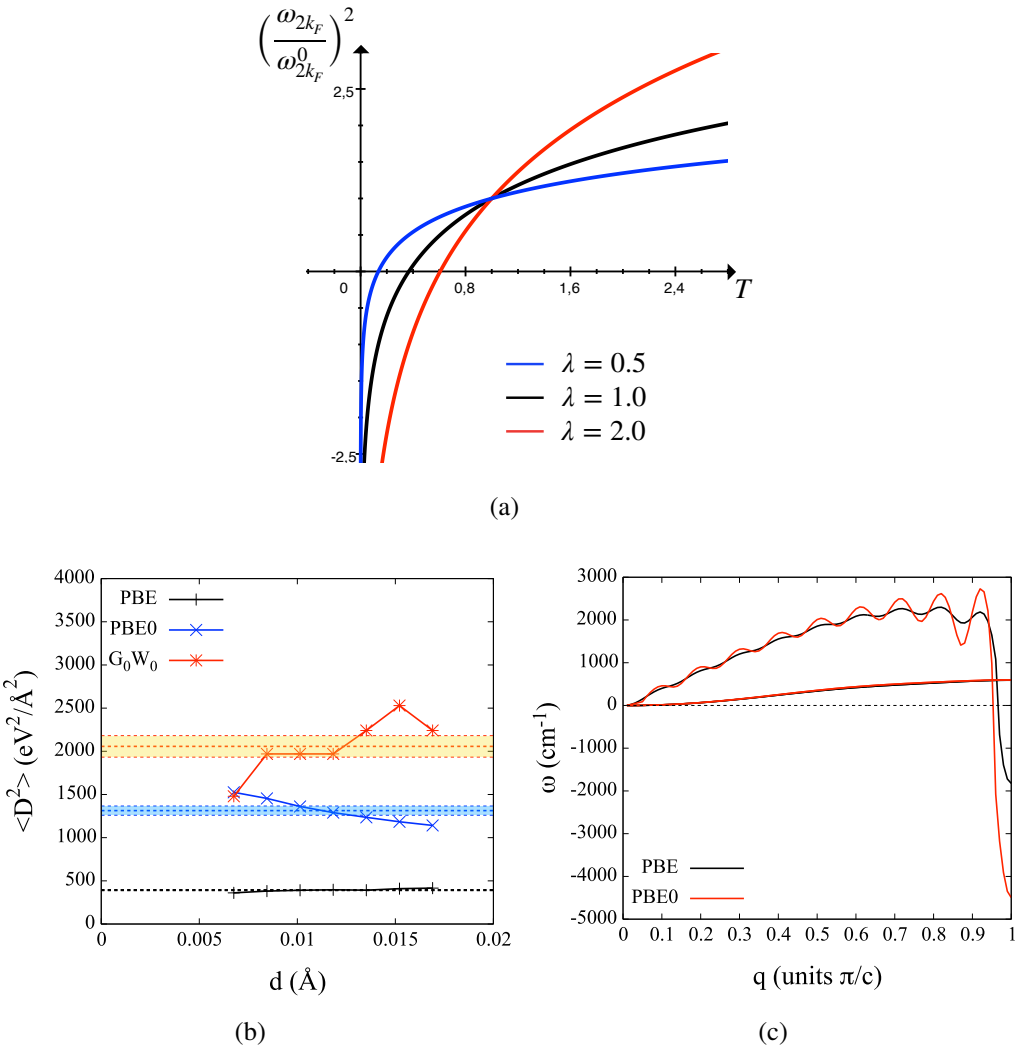

Fig. 6.6 (a) Electron-phonon renormalization of the longitudinal mode (Eq. 6.17) as a function of the dimensionless electron-phonon coupling constant λ; (b) Deformation potential of the longitudinal mode as a function of the displacement d: the shaded regions represent the uncertainty of the fitting process; (c) Harmonic dispersion relation of cumulene using both PBE and PBE0 xc-functionals.

In Ch. 5, I have shown in te case of rhombohedral graphene, that the inclusion of the electronic correlations boosts the electron-phonon coupling constant. In order to establish the magnitude of the electron-phonon boosting factor due to the PBE0 xc-functional I have used the fact that the deformation potential (and, as a consequence, the strength of the electron-phonon interaction) is proportional to the degeneracy lifting of energy eigenvalues due to the atomic displacement along the phonon mode pattern (Eq. 5.9). In Fig. 6.6 (b) I have plotted the Deformation potential of the longitudinal mode as a function of the displacement d: it is possible to see that when passing from the PBE to the PBE0 xc-functional, electronic correlations boost the deformation potential by a factor ~ 3.3 (and by a factor of ~ 5.2 with G_0W_0). Therefore, according to the mean-field picture of CDW in carbyne, the instability is highlighted due to electronic correlations and this can be observed in the harmonic dispersion relation of cumulene: the frequency of the unstable phonon mode goes from $\omega^{(C)}_{\text{PBE}} \sim -1800$ cm^{-1} to $\omega^{(C)}_{\text{PBE0}} \sim -4000$ cm^{-1}. On the other hand, electronic correlations also boost the anharmonic phonon-phonon interactions, since there is an energy gain of 0.48 eV, however it is not sufficient to stabilize the undistorted phase of carbyne.

It is then interesting to know whether cumulene might become stable or not as temperature is increased. I have therefore studied its dynamical properties as a function of temperature and observed how the longitudinal unstable mode evolves. In Fig. 6.7 (a) I have plotted the phonon dispersion relation of cumulene as a function of temperature computed within the SSCHA framework and taking also into account the third-order SSCHA tensor $\mathbf{\Phi}^{(3)}$ (D3V). Electronic correlations are still included through the PBE0 XC functional. As temperature is increased from $T = 0$ K to $T = 1800$ K, the unstable phonon mode becomes positive, going from $\omega^{(C)}_{T=0\text{K}} \sim -120$ cm^{-1} to $\omega^{(C)}_{T=1800\text{K}} \sim 460$ cm^{-1}.

As a consequence, it is possible to extract at which temperature cumulene becomes unstable, i.e. the critical temperature T_{CDW} at which the charge-density-wave (CDW) occurs. In order to do it, I have started from a sufficiently high temperature and cooled down cumulene ($T \to 0$): in Fig. 6.7 (b) I have plotted the squared longitudinal phonon frequencies multiplied by their sign (i.e. $\text{Sign}(\omega) \cdot \omega^2$) as a function of temperature since it is known that, close to a phase transition, $\omega \sim \sqrt{T/T_{CDW}}$. Then, by linearly interpolating such plot close to the region where it changes sign, I estimated a critical temperature of $T_{CDW} \sim 75$ K. As a consequence, for $T > T_{CDW}$

the ordered high-symmetry cumulenic phase is stabilized by thermal fluctuations, while for $T < T_{CDW}$ the system is distorted into a low-symmetry phase (i.e. polyyne) where carbon atoms gets closer forming triply bonded couples connected among them by single bonds.

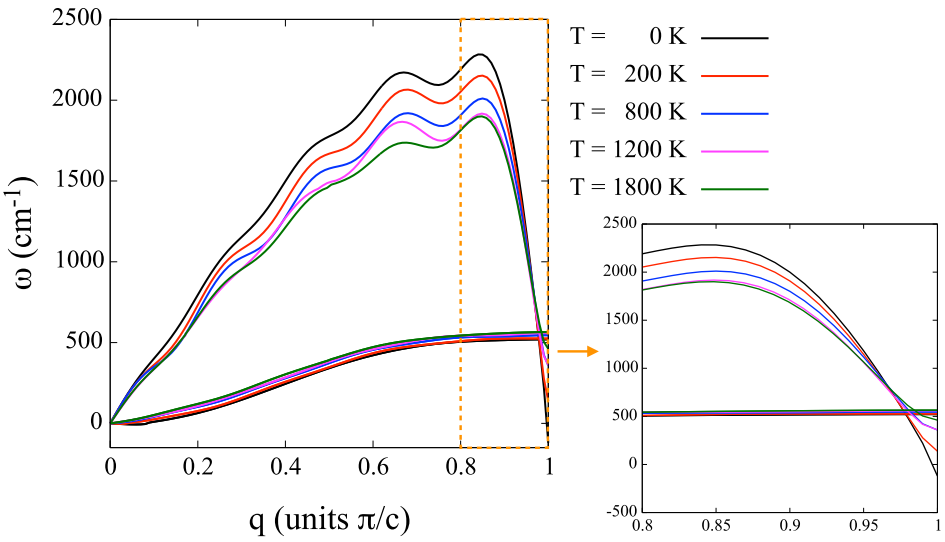

(a)

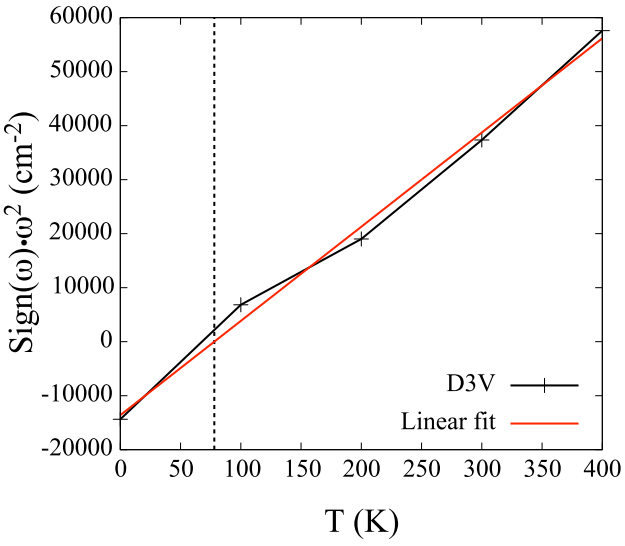

(b)

Fig. 6.7 (a) Temperature dependence of the phonon dispersion relation of cumulene computed via the SSCHA and with the PBE0 exchange-correlation functional; (b) Squared frequency of the unstable mode times their sign as a function of temperature, taking into account the third-order SSCHA tensor $\mathbf{\Phi}^{(3)}$ (D3V). Such squared phonon frequency are linearly interpolated in order to see at which temperature cumulene is stable.

6.3.2 Polyyne

I now turn the attention to the low-temperature and low-symmetry phase, i.e. polyyne. According to the Peierls picture, the phase transition from cumulene to polyyne should be of second order: starting from the distorted phase, when the temperature is increased carbon atoms should get more and more far apart in a continuous way until at T_{CDW} they become equidistant. A natural order parameter for studying such phase transition in carbyne is the bond-length alternation (BLA) defined as the difference between the single and the triple bonds, i.e. BLA=$r_1 - r_3$ (Fig. 6.8 (a)); polyyne corresponds to a BLA$\neq 0$, while cumulene is associated to BLA$= 0$. According to the Peierls model, the BLA is expected to be maximum at $T = 0$ K and that BLA$\rightarrow 0$ continuously as $T \rightarrow T_{CDW}$.

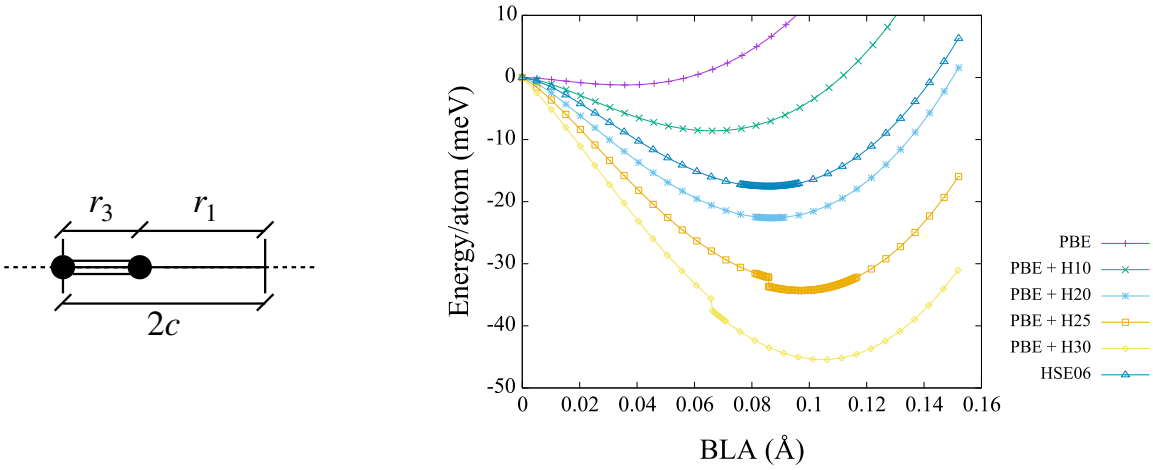

(a) (b)

Fig. 6.8 (a) Relevant parameters of polyyne: $2c$ represents the length of the unit cell (where c was the length of cumulene's unit cell) and r_3 (r_1) is the length of the triple (single) bond. As such, we can define the order parameter of carbyne as BLA$= r_1 - r_3$; (b) Total energy per atom of carbyne as a function of the order parameter BLA computed via DFT employing different exchange-correlations functionals: PBE, PBE plus different percentage of exact electron-electron exchange (HX, with $X = 10, 20, 25, 30$) and HSE06. Notice that PBE+H25 corresponds to the PBE0 exchange-correlation functional. All of the curves have been shifted in such a way to have zero energy when BLA$= 0$.

In Fig. 6.8 (b) I have plotted the total energy per atom of polyyne as a function of the BLA at $T = 0$ K without anharmonic interactions but with different degrees of electronic correlations. Each curve has a minimum in correspondence of the equilibrium value of the BLA, i.e. at the equilibrium distance between two carbon atoms inside the unitary cell of polyyne, meaning that the distorted phase is energetically stable at $T = 0$ K in the harmonic picture. As the percentage of the Hartree-Fock exchange interaction among electrons is increased, going from 0% (PBE) to 30% (PBE+H30), the system gains more and more energy due to the deformation and the equilibrium value of the BLA increases. Therefore, electronic correlations seem to favor the distorted structure. Results of the BLA as a function of the exchange-correlation functional are summarized in Tab. 6.2.

	PBE	PBE+H10	PBE+H20	PBE+H25 (PBE0)	PBE+H30	HSE06
BLA (Å)	0.035	0.066	0.087	0.097	0.106	0.087
$\lvert E_P - E_C \rvert$ (meV/atom)	1.2	8.6	22.6	34.3	45.4	17.6

Table 6.2 Comparison of the equilibrium BLA and of the energy gain per atom ($E_P - E_C$, where E_P and E_C are the energy per atom of polyyne and cumulene respectively) computed with different exchange-correlations functionals: PBE, PBE plus different percentage of exact electron-electron exchange (HX, with $X = 10, 20, 25, 30$) and HSE06.

From the simple tight-binding model I have shown that, as soon as atoms are displaced according to the pattern of the unstable phonon mode, a direct energy gap is opened in the energy spectrum of carbyne. Since from experiments it is possible to measure the optical band-gap [130, 131], I have computed the electronic dispersion relation of polyyne at the equilibrium BLA obtained with the PBE0 XC-functional. In order to show the effect of electronic correlation, in Fig. 6.9 I have plotted the electronic dispersion relation obtained both with PBE and with PBE0 exchange-correlation functional at $T = 0$ K. The energy gap is already opened at the PBE level, as expected from the tight-binding model, with a value of $\Delta_{PBE} = 0.93$ eV, however the partial inclusion of electron-electron exchange interaction (i.e. at the PBE0 level) makes the energy gap more than twice as large with a value of $\Delta_{PBE0} = 2.02$ eV.

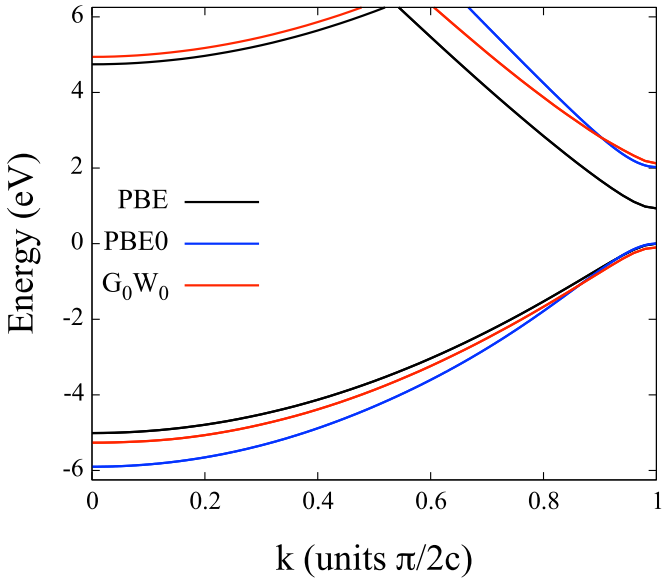

Fig. 6.9 Electronic band structure of polyyne at $T = 0$ K and at BLA$= 0.097$ Å computed with different degrees of electronic correlation: with the PBE and PBE0 xc-correlation functionals and within the G_0W_0 approximation.

Moreover, it is important to understand how good the results obtained with the PBE0 XC-functional are when compared to techniques that take care of electronic correlations in a more accurate way, such as the G_0W_0 approximation. Indeed, I recall that standard density functional theory deals with electronic correlations in an approximate way through exchange-correlations energy functionals which give quite good results in the calculation of equilibrium properties, even if they introduce some errors as I have shown for the computation of the electron-phonon matrix elements. Moreover, they surely underestimate excitation properties of materials such as optical absorptions. While the use of hybrid functionals surely improves the results of standard DFT calculations, in order to properly take into account electronic correlations in the system it is possible to exploit the GW approximation, which is a many-body technique.

Usually, quasiparticle excitations are found by computing the poles of the electron self-energy Σ by solving the Hedin's set of non-linear coupled equations [330] schematically given by:

$$\begin{cases} \Sigma = iGW \\ G = G_0 + G_0 \Sigma G \\ P = -iGG \\ W = v + vPW \end{cases} \tag{6.36}$$

where G (G_0) is the exact (free) electron Green's function at $T = 0$, W (v) is the dressed (undressed) Coulomb interaction and P is the polarization part.

In the G_0W_0 approximation [365], we assume that:

- the exact electron Green's function coincides with the free propagator, i.e. $G = G_0$;
- the Kohn-Sham eigenvalues and wavefunctions are a good starting point, so that $G_0 = G_0^{KS}$;
- the polarization of the medium is computed in the RPA approximation, i.e. $P = -iG_0^{KS}G_0^{KS}$, so that we actually have $W = W_0$.

By doing so, the quasiparticle energies can be computed by solving the non-linear equation:

$$\begin{cases} E_{n\mathbf{k}}^{QP} = \varepsilon_{n\mathbf{k}}^0 + Z_{nk} \langle n\mathbf{k}| \Sigma(\varepsilon_{n\mathbf{k}}^0) - V_{XC} |n\mathbf{k}\rangle \\ Z_{n\mathbf{k}} = \left[1 - \frac{d\Sigma_{n\mathbf{k}}(\omega)}{d\omega}\Big|_{\omega=\varepsilon_{n\mathbf{k}}^0}\right]^{-1} \end{cases} \tag{6.37}$$

where n is the band index, $\mathbf{k}$ is the electron momentum, $\varepsilon_{n\mathbf{k}}^0$ and $|k\rangle$ are the single-particle eigenvalues and Bloch-periodic eigenvectors of the Kohn-Sham Hamiltonian, V_{XC} is the exchange-correlation potential, $\Sigma(\varepsilon_{n\mathbf{k}}^0)$ is the electron self-energy computed at the single-particle energy.

Notice that the electron self-energy is made up of an exchange (Σ^x) and a correlation (Σ^c) part, schematically given by:

$$\Sigma = \Sigma^x + \Sigma^c = iG_0v + iG_0(W_0 - v) \tag{6.38}$$

the role of Σ^x, i.e the part related to the Hartree-Fock exchange interaction, is to open the energy gap, while the correlation part tends to close it. However, the overall effect of the G_0W_0 approximation is to increase the value of the energy band gap.

In Fig. 6.9 I also reported the electronic band structure of polyyne computed within the G_0W_0 approximation, which gives an energy bad gap of $\Delta_{G_0W_0} = 2.22$ eV. If it is compared to the PBE0 one, it is possible to see that the energy band gap difference is just of 0.2 eV: I can then conclude that the PBE0 hybrid XC-functional agrees quite well with the more accurate G_0W_0 approximation, the only error being in the slope of the energy bands. Results are summarized in Tab. 6.3.

	PBE	PBE0	G_0W_0
Δ (eV)	0.93	2.03	2.22

Table 6.3 Comparison of the energy band gap Δ computed at the PBE, PBE0 and G_0W_0 level.

In Fig. 6.10 I have also plotted the imaginary part of the macroscopic polarizability both at the PBE and G_0W_0 level. For one-dimensional systems, such quantity is defined as:

$$\alpha(\omega) = \lim_{\mathbf{q}\to 0} \frac{L}{2\pi\mathbf{q}} \chi_{00}(\mathbf{q},\omega) \tag{6.39}$$

where L is the size of the cell in the non-periodic direction, $\mathbf{q}$ (ω) is the polarization vector (frequency) of an applied electric field and $\chi_{00}(\mathbf{q},\omega)$ is the $\mathbf{G} = \mathbf{G}' = 0$ component of the polarizability $\chi_{\mathbf{GG}'}(\mathbf{q},\omega)$ (i.e. the response function of the system due to an applied oscillating electric field). The imaginary part of the macroscopic polarizability is directly related to the absorbance of a system, which can be measured.

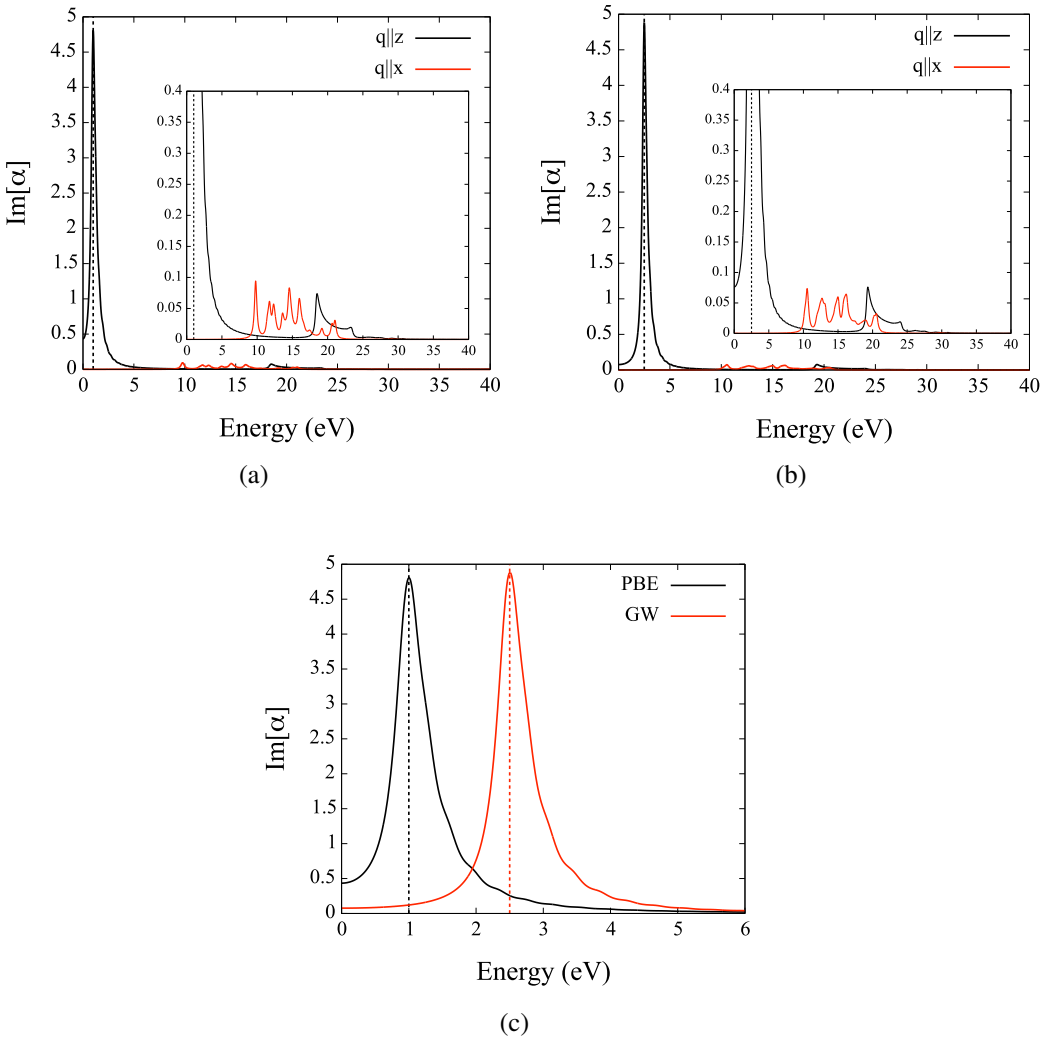

Fig. 6.10 Imaginary part of the macroscopic polarizability along the periodic ($q||z$) and non-periodic ($q||x$) direction computed with the (a) PBE exchange-correlation functional and in the (b) G_0W_0 approximation; (c) Comparison of the macroscopic polarizabilities along the periodic ($q||z$) direction computed with the PBE exchange-correlation functional (PBE) and in the G_0W_0 approximation (GW).

In both cases, along the periodic direction of polyyne (i.e. $\mathbf{q}||z$), the first peak of $\alpha(\omega)$ is the more intense of the spectrum and is located in energy at the value of the energy gap. If the two spectra are compared (Fig. 6.10 (c)), the effect of the electronic correlation can be clearly seen: the peak in the G_0W_0 approximation is shifted to higher frequencies, meaning that the energy gap is opened even more due to electron-electron interactions.

The analysis of the imaginary part of the macroscopic polarizability would be particularly useful later on, when the excitonic effects on the electronic band structure of polyyne will be considered. Indeed, by looking at how much the peak of $Im[\alpha]$ is shifted in energies the excitonic binding energy can be directly estimated.

I now move to the dynamical properties of polyyne. In Fig. 6.11 (a) I have plotted the phonon dispersion relation of the distorted phase as a function of temperature obtained from the SSCHA code and with the inclusion of the third order SSCHA tensor $\mathbf{\Phi}^{(3)}$. Notice that now the unit cell of the distorted phase is twice as large of that of cumulene, therefore the first Brillouin zone of polyyne is twice as small and the unstable phonon mode is folded at the center of the Brillouin zone (i.e. $\mathbf{q} = \mathbf{0}$). At $T = 0$ K, polyyne is dynamcally stable as the longitudinal phonon mode is now positive with a frequency of $\omega^{(P)}_{T=0\text{K}} \sim 1825$ cm^{-1}. As a consequence polyyne appears to be dynamically stable at zero temperature.

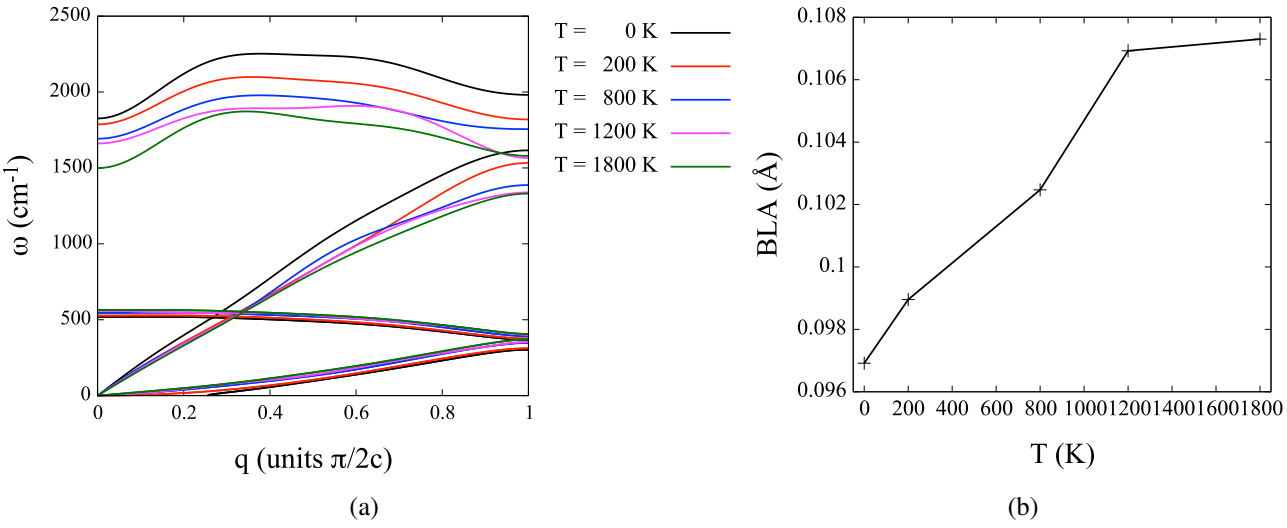

Fig. 6.11 (a) Temperature dependence of the phonon dispersion relation of polyyne computed via the SSCHA and with the PBE0 exchange-correlation functional, taking into account the third-order SSCHA tensor $\mathbf{\Phi}^{(3)}$ (D3V); (b) BLA as a function of temperature obtained from the minimization process of the stochastic self-consistent approximation.

However, if temperature is increased, polyyne always shows positive frequencies meaning that it is always stable from the dynamical point of view. Indeed, at a temperature well above the T_{CDW} that I have estimated for cumulene (≈ 75 K), $\omega^{(P)}_{T=1800\text{K}} \sim 1580$ cm^{-1} is found. I would have expected that $\omega^{(P)} \to 0$ as $T \to T_{CDW}$, becoming negative for $T > T_{CDW}$. Moreover, being a second order phase transition

in principle, I would also have expected the order parameter to continuously go to zero as $T \rightarrow T_{CDW}$: however, if the equilibrium *BLA* obtained from the SSCHA minimization process is computed as a function of temperature, the order parameter increases as T increases (Fig. 6.11 (b)). This means that as the temperature gets higher and higher, atoms tend to get closer and closer stabilizing the distorted structure even more.

From this analysis it appears that polyyne is always stable, even at temperatures $T >> T_{CDW}$ and this is clearly in contrast with the Landau-Peierls model.

6.3.3 First-order phase transition

In order to shed some light on whether or not a phase transition from polyyne to cumulene should be expected and in order to understand the nature of such phase transition, I have analyzed the free energy evolution of carbyne as a function of temperature. Indeed, I have shown above that the phase transition cannot be of second order since atoms get closer and closer stabilizing the distorted structure at temperature greater than T_{CDW}.

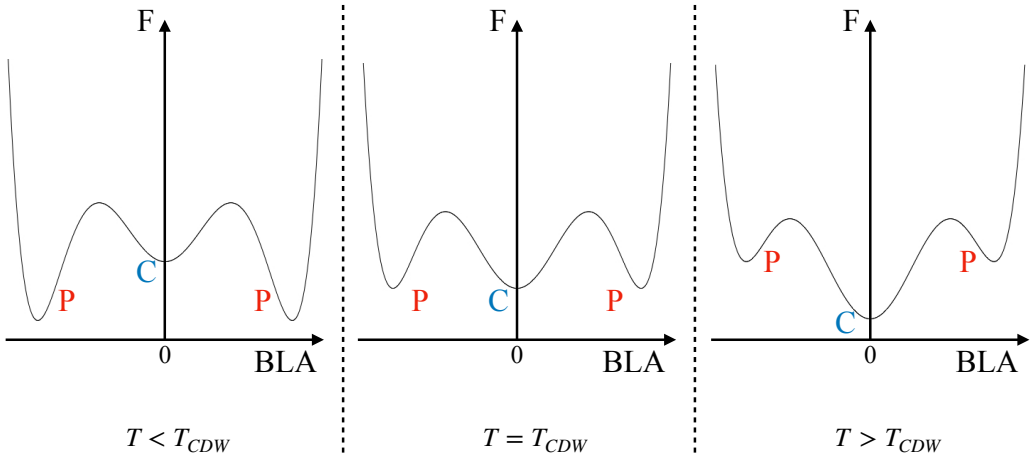

Fig. 6.12 Schematic representation of a first order phase transition in carbyne. Here we see the free energy (F) as a function of the order parameter (BLA) in three different cases: $T < T_{CDW}$, $T = T_{CDW}$ and $T > T_{CDW}$, where T_{CDW} is the critical temperature of the charge-density-wave. Here C stands for cumulene (BLA$= 0$), while P corresponds to polyyne (BLA$\neq 0$).

The only possible alternative is that the phase transition, if present, is of first order (Fig. 6.12). If this is the case, the free energy must display two minima: the absolute minimum would correspond to polyyne, while the relative one would correspond to cumulene. As the temperature is increased, the difference in energy between the two minima would become smaller and smaller until the two extremal point of the free energy are swapped at a temperature T'_{CDW}: cumulene now is the absolute minimum, while polyyne is the relative one.

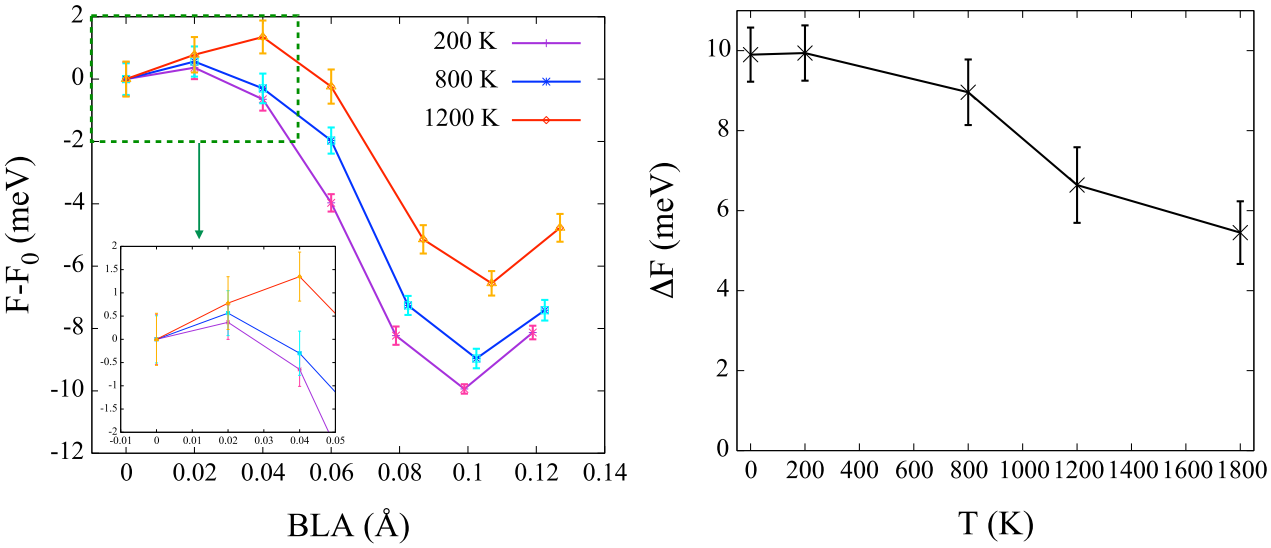

(a) (b)

Fig. 6.13 (a) Anharmonic free energy per atom of carbyne computed via the stochastic self-consistent approximation as a function of BLA and for three different temperatures (i.e. $T = 200$ K, $T = 800$ K and $T = 1800$ K). All of the curves are shifted so that the free energy of the undistorted phase (BLA$= 0$) is set to 0; (b) Free energy difference ΔF between the distorted (BLA$\neq 0$) and undistorted (BLA$= 0$) phase as a function of temperature.

In Fig. 6.13 (a) I have plotted the anharmonic free energy per atom of carbyne computed via the stochastic self-consistent approximation as a function of BLA and for three different temperatures (i.e. $T = 200$ K, $T = 800$ K and $T = 1200$ K), with their error bars. It is possible to observe the presence of two minima, the relative one being at BLA$= 0$ (i.e. cumulene) while the absolute one being at BLA$\neq 0$ (i.e. polyyne). Moreover, as temperature is increased, the distance between the two extrema (ΔF defined as the difference between the free energy of polyyne and cumulene) gets smaller and smaller (Fig. 6.13 (b)).

The free energy landscape is thus typical of a first order phase transition, which is in contrast with the second-order phase transition usually expected according to the Landau-Peierls mode since the passage from polyyne to carbyne occurs abruptly. Nevertheless, the distorted structure is always stable up to $T = 1800$ K. If the last part of the ΔF vs. T plot is linearly interpolated taking also into account the errorbars, a first order phase transition at $T'_{CDW} \sim 3000$ K is expected.

Moreover, from the analysis of the free energy at $T = 0$ K it is possible to understand how much the zero-point motion of atoms affects the linear acetylenic carbon. Indeed at $T = 0$ K, the free energy coincides with the total energy of the system and it is known from the discussion above that at the PBE0 level $\Delta F_{PBE0} =$ 34.3 meV/atom (Tab. 6.2). If the PBE0 free energy is now computed taking also into account anharmonic phonon-phonon interactions through the SSCHA method, $\Delta F_{PBE0+SSCHA} = 9.90$ meV/atom is found. Therefore, the zero point motion of atoms gives an energy correction of ~ 24 meV/atom making carbyne a strongly anharmonic system.

6.4 Quasiparticle energy gap renormalization

6.4.1 Quantum and thermal fluctuations

Since polyyne is the most stable system up to very large temperatures, it makes sense to study the temperature dependence of the energy gap, since it is a quantity that can be directly measured. Up to know I have analyzed the effects of electronic correlations on the energy band gap, however both quantum and thermal fluctuations of atoms can renormalize its value. Indeed, in Ch. 2 I have shown that electron-phonon interactions dress the electrons adding quasiparticle corrections to the electronic band structure.

The quasiparticle correction due to the zero-point motion of atoms ($T = 0$ K) and due to thermal fluctuations ($T \neq 0$ K) can be computed stochastically [366]. At a certain temperature T, in order to minimize the free energy of carbyne with the SSCHA method, I have generated a number $\mathcal{N}_\mathcal{I}$ of elements $\mathbf{R}_{(\mathcal{I})} = \boldsymbol{\mathcal{R}} + \mathbf{u}_\mathcal{I}$, where $\mathbf{u}_\mathcal{I}$ are the displacements from the centroids $\mathcal{R}$ generated according to a probability distribution $\tilde{\rho}_{in}(\mathbf{R}_{(\mathcal{I})})$ (which incorporates the symmetries of the dynamical matrix of the system). The displacements of atoms from their equilibrium positions are

then performed according to the possible phonon eigenmodes, altering the electronic band structure (similarly to the finite difference method explained in Ch. 5) and taking into account non-linear electron-phonon interactions thanks to the inclusion of anharmonicity. Therefore, for each configuration I have computed the quasiparticle band gap and then I have mediated over them: the result is expected to be exact in the thermodynamical limit (i.e. $\mathcal{N}_{\mathcal{I}} \to \infty$).

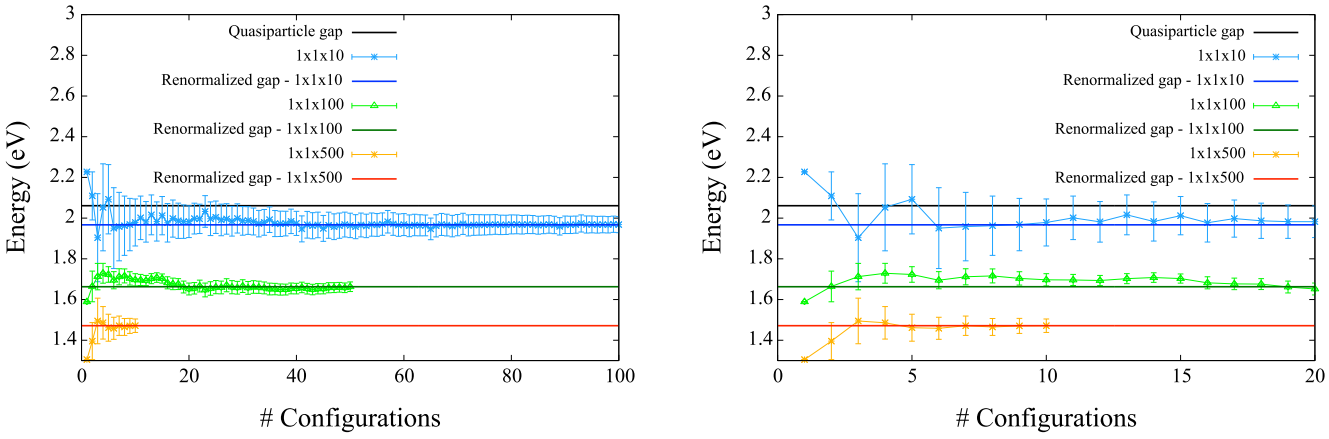

Fig. 6.14 (a) Convergence of the quasiparticle gap as a function of the number of SSCHA configurations, for three different sizes of the supercell and at $T = 200$ K. Black solid line refers to the quasiparticle gap computed without anharmonic effects at the PBE0 level and at $T = 0$ K; (b) Zoom around the first 20 configurations.

In order to show this, I have taken as an example the case of $T = 200$ K so that it is possible to take into account both quantum and thermal fluctuations. In Fig. 6.14 I have plotted the convergence of the quasiparticle gap as a function of the number of SSCHA configurations, for three different sizes of the supercell: $1 \times 1 \times 10$, $1 \times 1 \times 100$ and $1 \times 1 \times 500$ with 20, 200 and 1000 atoms per cell respectively. With 20 atoms ($1 \times 1 \times 10$, blue solid line) the quasiparticle gap is reduced with respect to the one computed at the PBE0 level and at $T = 0$ K ($1 \times 1 \times 10$, black solid line): indeed anharmonic effects reduce the band gap from 2.03 eV to 1.97 eV. However, as soon as the number of atoms in the supercell is increased, anharmonic effects are more and more evident, giving converged results of 1.65 ± 0.03 eV and 1.47 ± 0.03 eV at 200 and 1000 atoms per cell respectively. Since the error committed between the 200 and 1000 atoms system is just ~ 0.1 eV, I can say to have a converged result

on the renormalized quasiparticle gap already for the $1 \times 1 \times 100$ supercell (thus lightening the computational workload).

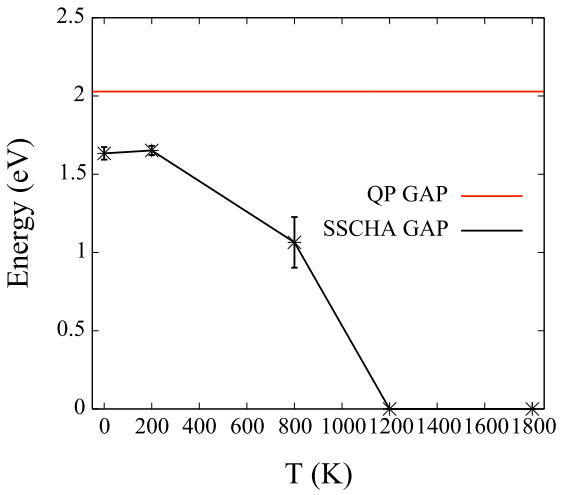

Fig. 6.15 Quasiparticle gap renormalized by quantum and thermal fluctuations (SSCHA GAP) as a function of temperature, showing metallicity of polyyne at $T = 1200$ K. Red solid line refers to the quasiparticle gap computed at the PBE0 level without anharmonic effects (QP GAP) and at $T = 0$ K.

In Fig. 6.15 I have plotted the quasiparticle (QP) gap renormalized by quantum ($T = 0$ K) and thermal ($T \neq 0$ K) fluctuations (SSCHA GAP) as a function of temperature. If compared to the the pure PBE0 QP gap at $T = 0$ K (Fig. 6.15, red solid line), it is possible to observe that as temperature increases the band gap is reduced more and more until it is null for $T \geq 1200$ K. Therefore the distorted structure, polyyne, becomes metallic for $T \geq 1200$ K due to anharmonic phonon-phonon interactions, which is something that could be probed experimentally.

6.4.2 Excitonic effects

When an electron is excited from the valence to the conduction band, it leaves behind an empty state which can be seen as a positive particle or a hole. As such, the negative electron in the conduction band and the positive hole in the valence band are attracted to each other creating an electron-hole pair ($e^- - h$) or exciton (Fig. 6.16). This quasiparticle introduces a binding state in the original band gap,

thus renormalizing the quasiparticle gap merely due to many-body electron-hole interactions (excitonic shift [187, 367–370]).

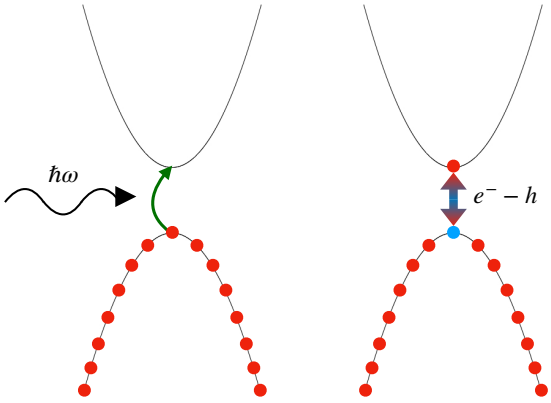

Fig. 6.16 Schematic representation of an exciton, i.e. the quasiparticle related to the attractive interaction between an excited electron (e^-) in the conduction band and the associated hole (h) in the valence band.

In order to describe this two-particle interaction from a many-body point of view, the two-particle Green's function is required [176, 370], from which it is possible to derive the Bethe-Salpeter equation (BSE) which allows us to compute optical and dielectric properties of extended systems including the electron-hole interaction (excitonic effects). The BSE equation is just a Dyson equation for the four-point polarizability, i.e. the four point (or two-body) response function to an oscillating electric field, which is schematically reproduced with Feynman diagrams in Fig. 6.17 [371].

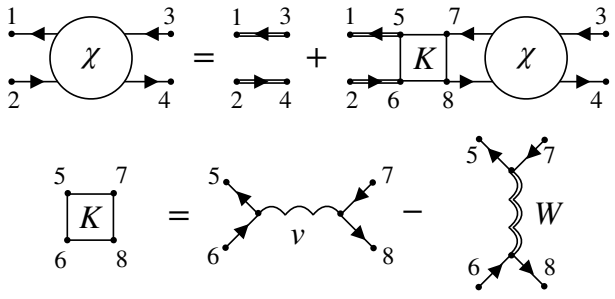

Fig. 6.17 Diagrammatic representation of the Bethe-Salpeter equation for the four-point polarization. Straight single (double) lines are free (exact) single-particle electron Green's functions, while wiggle single (double) lines are bare (dressed) electron-electron Coulomb interactions.

In the space of transitions between valence and conduction states, the Bethe-Salpeter equation can be rewritten as a (pseudo-)eigenvalue problem for a two-particle Hamiltonian. If we have a non spin-polarized system in the $\mathbf{q} \to 0$ limit, the electron-hole hamiltonian is given by [371]:

$$H^{\mathbf{k}}_{n_1 n_2 \atop n_5 n_6 \mathbf{k}'} = (\varepsilon_{n_2\mathbf{k}} - \varepsilon_{n_1\mathbf{k}})\delta_{n_1 n_5}\delta_{n_2 n_6}\delta_{\mathbf{k}\mathbf{k}'} + (f(\varepsilon_{n_2\mathbf{k}'}) - f(\varepsilon_{n_1\mathbf{k}}))[2v^{\mathbf{k}}_{n_1 n_2 \atop n_5 n_6 \mathbf{k}'} - W^{\mathbf{k}}_{n_1 n_2 \atop n_5 n_6 \mathbf{k}'}] \quad (6.40)$$

that is the sum of an independent particle part (diagonal) and a static interaction part ($K(\omega = 0)$) made of the electron-hole exchange part v (i.e. the Hartree potential) and the electron-hole attraction part W (i.e. the screened exchange potential). Here $n_1 n_2 \mathbf{k}$ and $n_5 n_6 \mathbf{k}'$ (with $\mathbf{k}' = \mathbf{k} + \mathbf{q}$) label the pair of quasiparticle states $n_1\mathbf{k}$, $n_2\mathbf{k}$, $n_5\mathbf{k}'$ and $n_6\mathbf{k}'$. Moreover, notice that the diagonal part of the interaction kernel shifts the eigenvalue differences while the non-diagonal part couples them. Excitations energies, such as excitonic energies, can then be found as the eigenvalues of such Hamiltonian [371].

It is therefore interesting to study the excitonic effects in polyyne at zero temperature, to see how much they affect the quasiparticle band gap. In order to do so, I solved the Bethe-Salpeter equation on top of the DFT-G_0W_0 approximation as it is represents the state-of-the-art approach from first principles to compute the excitations of solid-state systems [372].

In Fig. 6.18 I have plotted a comparison of the imaginary parts of the macroscopic polarizabilities along the periodic ($q||z$) direction computed with in the pure G_0W_0 approximation (G_0W_0) and by solving the Bethe-Salpeter equation on top of the DFT-G_0W_0 approximation (BSE). The first peak, corresponding to the measurable quasiparticle band gap, is shifted down in energy to 1.44 eV from the 2.03 eV of the pure G_0W_0 QP gap: I can therefore estimate an excitonic binding energy of ~ 0.6 eV. Moreover, also the high-energy part of the spectrum is shifted down in energy toward the first peak.

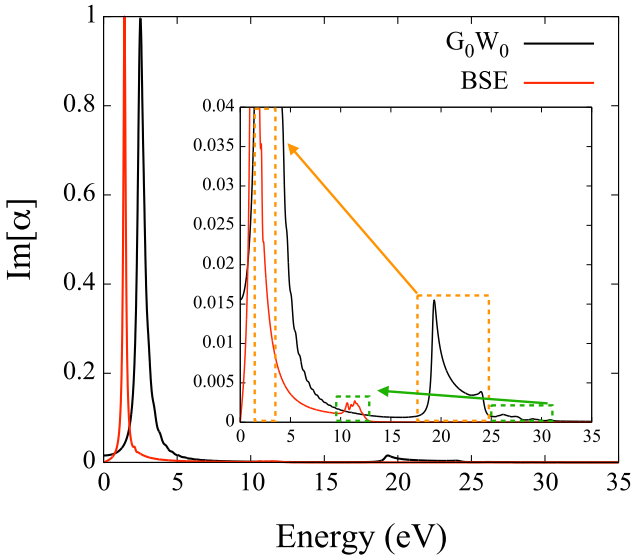

Fig. 6.18 Imaginary parts of the macroscopic polarizabilities along the periodic ($q||z$) direction computed with in the pure G_0W_0 approximation (G_0W_0) and by solving the Bethe-Salpeter equation on top of the DFT-G_0W_0 approximation (BSE). In the Inset we have highlighted the excitonic shifts in the absorption spectra.

Summary

- The insulator-to-metal phase transition is due to both electron-electron and electron-phonon interactions together with anharmonic phonon-phonon interactions;
- The phase transition from the ordered to the distorted phase (and vice-versa) is of first order, in contrast with the Landau-Peierls model;
- We estimate a $T_{CDW} = 75$ K for the cumulene-to-polyyne transition, while a $T'_{CDW} = 3300$ K for the opposite;
- Both quantum and thermal fluctuations, together with excitonic effects, strongly renormalize the quasiparticle band gap.

Chapter 7

Conclusions

In this work I have investigated the role of dimensionality and electronic correlations on the electron-phonon interactions in carbon allotropes. More precisely, I focused on the possible emergence of strongly correlated phases of matter such as high temperature superconductivity and charge-density-waves.

This has been accomplished thanks to density functional theory (DFT) and its linear response extension (DFPT). I have also dealt with different techniques for including electronic correlations, such as hybrid functionals and the many-body GW approximation. Finally, I have studied the lattice dynamic beyond the simple harmonic picture, making use of the stochastic self-consistent harmonic approximation (SSCHA).

I have shown that field effect doping can be used as a way to modify electronic and vibrational properties of a material. In particular, I have shown that in principle in hole-doped hydrogenated diamond (111) thin films it is possible to induce a high-temperature multi-band superconducting phase transition with a $T_c \approx 40$ K for relatively high doping regimes ($n_{2D} \sim 6 \times 10^{14}$ holes/cm^2).

In order to show this I have computed the Eliashberg spectral function by interpolating the electron-phonon matrix elements over the whole Brillouin zone via Wannier functions, which also allowed us to analyze the $\mathbf{q}$-dependence of the electron-phonon interactions, and I then solved the multi-band Migdal-Eliashberg equations.

Thanks to this first example I showed that electron-phonon interactions renormalize phonon frequencies due to their many-body nature, giving rise to Kohn anomalies in the phonon spectra (i.e. a sharp variation in the slope of the phonon branches).

After that I have also analyzed the possibility of inducing a high-T_c superconducting phase in rhombohedral few-layer graphene by means of field-effect doing. ABC graphene has been shown to host an antiferromagnetic ground state at low temperature and for moderate induced charge densities thanks to dispersionless electronic bands at the Fermi level.

Thus, I tried to exploit the presence of van Hove singularities in the electronic density of states at the Fermi energy in order to see if a superconductive phase for sufficiently high dopings (i.e. when the magnetic gap is closed) could be obtained. Unfortunately, no superconducting transition was found. However thanks to this system I showed that standard density functional theory computations severely underestimate the magnitude of the electron-phonon strength.

Indeed, the error relies on the approximation we employ for treating electronic correlations (i.e. on the exchange correlation functionals). Electron-electron interactions affect the linear response of a system: indeed the partial inclusion of exact exchange interaction among electrons via hybrid functionals boosts the electron-phonon matrix elements.

Finally, I put together the information on the many-body nature of electron-electron and electron-phonon interactions I collected in the preceding systems in order to study the Landau-Peierls transition in the linear acetylenic carbon. Indeed when carbon atoms are equally spaced among them an imaginary longitudinal phonon mode at the border of the Brillouin zone is present, signaling an instability of the crystal structure.

As a matter of fact carbyne is the prototype of the charge-density-wave instability which give rise to a metal-to-insulator second order phase transition according to the Landau-Peierls model. However electronic correlations play a crucial role in carbyne as well as anharmonic phonon-phonon interactions due to its low dimensionality and light mass of carbon atoms. Indeed I showed that if anharmonicity is carefully taken into account when dealing with the lattice dynamic and electron-electron

correlations are fully included in the computations, the phase transition from the ordered (cumulene) to the distorted (polyyne) phase is first order in nature.

This is then in contrast with the usual picture of the Landau-Peierls phase transition. Moreover, I showed that both quantum and thermal fluctuations of the lattice, as well as excitonic effects coming from many-body interactions among electrons, strongly reduce the energy gap of polyyne making it metallic at a certain temperature.

With this work I have shown that apparently simple systems such as carbon allotropes can host strongly correlated phases of matters such as charge-density-waves (CDW) and high-temperature superconductivity. Indeed, the light mass of carbon and low dimensionality enhance the relevance of the many-body nature of electron-electron, electron-phonon and anharmonic phonon-phonon interactions. An accurate description of such systems requires theoretical models and computational tools beyond the state of the art, underlying the necessity of an efficient and computationally affordable method for the linear response of materials together with non-approximated electronic correlations.

References

[1] Falcao, E. H. & Wudl, F. Carbon allotropes: beyond graphite and diamond. *Journal of Chemical Technology & Biotechnology* **82**, 524–531 (2007).

[2] Hirsch, A. The era of carbon allotropes. *Nature Materials* **9**, 868–871 (2010).

[3] Roth, S. & Carroll, D. *One-Dimensional Metals: Conjugated Polymers, Organic Crystals, Carbon Nanotubes and Graphene* (Wiley, 2015).

[4] Pauling, L., University, C. & Press, C. U. *The Nature of the Chemical Bond and the Structure of Molecules and Crystals: An Introduction to Modern Structural Chemistry*. George Fisher Baker Non-Resident Lecture Series (Cornell University Press, 1960).

[5] Harrison, W. *Electronic Structure and the Properties of Solids: The Physics of the Chemical Bond*. Dover Books on Physics (Dover Publications, 1989).

[6] Streitwieser, A., Heathcock, C. & Kosower, E. *Introduction to Organic Chemistry*. A series of books in organic chemistry (Macmillan, 1992).

[7] Saito, R., Dresselhaus, G. & Dresselhaus, M. *Physical Properties of Carbon Nanotubes* (Imperial College Press, 1998).

[8] Sólyom, J. *Fundamentals of the Physics of Solids: structure and dynamics*, vol. 1 (Springer-Verlag Berlin Heidelberg, 2007).

[9] Dresselhaus, M., Dresselhaus, G. & Eklund, P. Fullerenes. *Journal of Materials Research* **8**, 2054–2097 (1993).

[10] Rao, C., Seshadri, R., Govindaraj, A. & Sen, R. Fullerenes, nanotubes, onions and related carbon structures. *Materials Science and Engineering: R: Reports* **15**, 209 – 262 (1995).

[11] Dresselhaus, M. S. & Endo, M. *Relation of Carbon Nanotubes to Other Carbon Materials*, 11–28 (Springer Berlin Heidelberg, Berlin, Heidelberg, 2001).

[12] Yu, O., Jing-Cui, P., Hui, W. & Zhi-Hua, P. The rehybridization of electronic orbitals in carbon nanotubes. *Chinese Physics B* **17**, 3123–3129 (2008).

[13] Pan, L. & Kania, D. *Diamond: Electronic Properties and Applications*. Electronic Materials: Science & Technology (Springer US, 2013).

[14] Ekimov, E. A. *et al.* Superconductivity in diamond. *Nature* **428**, 542–545 (2004).

[15] Bustarret, E. *et al.* Dependence of the superconducting transition temperature on the doping level in single-crystalline diamond films. *Phys. Rev. Lett.* **93**, 237005 (2004).

[16] Yokoya, T. *et al.* Origin of the metallic properties of heavily boron-doped superconducting diamond. *Nature* **438**, 647–650 (2005).

[17] Bustarret, E. Superconducting diamond: an introduction. *Phys. Status Solidi A* **205**, 997–1008 (2008).

[18] Blase, X., Adessi, C. & Connetable, D. Role of the dopant in the superconductivity of diamond. *Phys. Rev. Lett.* **93**, 237004 (2004).

[19] Boeri, L., Kortus, J. & Andersen, O. K. Electron-phonon superconductivity in hole-doped diamond: a first-principles study. *J. Phys. Chem. Solids* **67**, 552–556 (2006).

[20] Giustino, F., Yates, J. R., Souza, I., Cohen, M. L. & Louie, S. G. Electron-phonon interaction via electronic and lattice wannier functions: superconductivity in boron-doped diamond reexamined. *Phys. Rev. Lett.* **98**, 047005 (2007).

[21] Moussa, J. E. & Cohen, M. L. Constraints on T_c for superconductivity in heavily boron-doped diamond. *Phys. Rev. B* **77**, 064518 (2008).

[22] Calandra, M. & Mauri, F. High-T_c superconductivity in superhard diamondlike BC_5. *Phys. Rev. Lett.* **101**, 016401 (2008).

[23] Caruso, F. *et al.* Nonadiabatic kohn anomaly in heavily boron-doped diamond. *Phys. Rev. Lett.* **119**, 017001 (2017).

[24] Solozhenko, V. L., Kurakevych, O. O., Andrault, D., Le Godec, Y. & Mezouar, M. Ultimate metastable solubility of boron in diamond: Synthesis of superhard diamondlike BC_5. *Phys. Rev. Lett.* **102**, 015506 (2009).

[25] Bhaumik, A., Sachan, R., Gupta, S. & Narayan, J. Discovery of high-temperature superconductivity (T_c = 55 K) in B-doped Q-carbon. *ACS Nano* **11**, 11915–11922 (2017).

[26] Kerrien, G. *et al.* Ultra-shallow, super-doped and box-like junctions realized by laser-induced doping. *Appl. Surf. Sci.* **186**, 45–51 (2002).

[27] Piatti, E., Romanin, D., Daghero, D. & Gonnelli, R. S. Two-dimensional hole transport in ion-gated diamond surfaces: A brief review (review article). *Low Temperature Physics* **45**, 1143–1155 (2019).

[28] Mounet, N. & Marzari, N. First-principles determination of the structural, vibrational and thermodynamic properties of diamond, graphite, and derivatives. *Phys. Rev. B* **71**, 205214 (2005).

[29] Wallace, P. R. The band theory of graphite. *Phys. Rev.* **71**, 622–634 (1947).

[30] McClure, J. W. Band structure of graphite and de haas-van alphen effect. *Phys. Rev.* **108**, 612–618 (1957).

[31] Slonczewski, J. C. & Weiss, P. R. Band structure of graphite. *Phys. Rev.* **109**, 272–279 (1958).

[32] McClure, J. W. Energy band structure of graphite. *IBM Journal of Research and Development* **8**, 255–261 (1964).

[33] Nery, J. P., Calandra, M. & Mauri, F. Long-range rhombohedral-stacked graphene through shear. *Nano Letters* **20**, 5017–5023 (2020).

[34] Yang, Y. *et al.* Stacking order in graphite films controlled by van der waals technology. *Nano Letters* **19**, 8526–8532 (2019).

[35] Shi, Y. *et al.* Electronic phase separation in multilayer rhombohedral graphite. *Nature* **584**, 210–214 (2020).

[36] Baskin, Y. On the formation of the rhombohedral graphite modification. *Zeitschrift für Kristallographie - Crystalline Materials* **107**, 337–356 (1956).

[37] Roviglione, A. N. & Hermida, J. D. Rhombohedral graphite phase in nodules from ductile cast iron. *Procedia Materials Science* **8**, 924–933 (2015).

[38] Xu, R. *et al.* Direct probing of the stacking order and electronic spectrum of rhombohedral trilayer graphene with scanning tunneling microscopy. *Phys. Rev. B* **91**, 035410 (2015).

[39] Lenski, D. R. & Fuhrer, M. S. Raman and optical characterization of multilayer turbostratic graphene grown via chemical vapor deposition. *Journal of Applied Physics* **110**, 013720 (2011).

[40] Hart, A. G., Hansen, T. C. & Kuhs, W. F. A hidden Markov model for describing turbostratic disorder applied to carbon blacks and graphene. *Acta Crystallographica Section A* **75**, 501–516 (2019).

[41] Landau, L. D. Zur theorie der phasenumwandlungen ii. *Phys. Z. Sowjetunion* **11**, 26–35 (1937).

[42] Landau, L. D. & Lifshitz, E. M. *Statistical Physics, Part I* (Pergamon Press, Oxford, UK, 1980).

[43] Peierls, R. E. Quelques proprietes typiques des corpses solides. *Ann. I. H. Poincare* **5**, 177–222 (1935).

[44] Mermin, N. D. Crystalline order in two dimensions. *Phys. Rev.* **176**, 250–254 (1968).

[45] Mermin, N. D. & Wagner, H. Absence of ferromagnetism or antiferromagnetism in one- or two-dimensional isotropic heisenberg models. *Phys. Rev. Lett.* **17**, 1133–1136 (1966).

[46] Hohenberg, P. C. Existence of long-range order in one and two dimensions. *Phys. Rev.* **158**, 383–386 (1967).

[47] Burgess, C. Goldstone and pseudo-goldstone bosons in nuclear, particle and condensed-matter physics. *Physics Reports* **330**, 193 – 261 (2000).

[48] Novoselov, K. S. *et al.* Electric field effect in atomically thin carbon films. *Science* **306**, 666–669 (2004).

[49] Mariani, E. & von Oppen, F. Flexural phonons in free-standing graphene. *Phys. Rev. Lett.* **100**, 076801 (2008).

[50] Aseginolaza, U. *et al.* Bending rigidity and sound propagation in graphene (2020). 2005.12047.

[51] Das Sarma, S., Adam, S., Hwang, E. H. & Rossi, E. Electronic transport in two-dimensional graphene. *Rev. Mod. Phys.* **83**, 407–470 (2011).

[52] Bae, S. *et al.* Roll-to-roll production of 30-inch graphene films for transparent electrodes. *Nature Nanotechnology* **5**, 574–578 (2010).

[53] Reich, S., Maultzsch, J., Thomsen, C. & Ordejón, P. Tight-binding description of graphene. *Phys. Rev. B* **66**, 035412 (2002).

[54] Castro Neto, A. H., Guinea, F., Peres, N. M. R., Novoselov, K. S. & Geim, A. K. The electronic properties of graphene. *Rev. Mod. Phys.* **81**, 109–162 (2009).

[55] Semenoff, G. W. Condensed-matter simulation of a three-dimensional anomaly. *Phys. Rev. Lett.* **53**, 2449–2452 (1984).

[56] Liu, Y., Bian, G., Miller, T. & Chiang, T.-C. Visualizing electronic chirality and berry phases in graphene systems using photoemission with circularly polarized light. *Phys. Rev. Lett.* **107**, 166803 (2011).

[57] Fradkin, E. Critical behavior of disordered degenerate semiconductors. ii. spectrum and transport properties in mean-field theory. *Phys. Rev. B* **33**, 3263–3268 (1986).

[58] Haldane, F. D. M. Model for a quantum hall effect without landau levels: Condensed-matter realization of the "parity anomaly". *Phys. Rev. Lett.* **61**, 2015–2018 (1988).

[59] Elias, D. C. *et al.* Dirac cones reshaped by interaction effects in suspended graphene. *Nature Physics* **7**, 701–704 (2011).

[60] Damascelli, A., Hussain, Z. & Shen, Z.-X. Angle-resolved photoemission studies of the cuprate superconductors. *Rev. Mod. Phys.* **75**, 473–541 (2003).

[61] Zhou, S. Y. *et al.* Coexistence of sharp quasiparticle dispersions and disorder features in graphite. *Phys. Rev. B* **71**, 161403 (2005).

[62] Zhou, S. Y. *et al.* First direct observation of dirac fermions in graphite. *Nature Physics* **2**, 595–599 (2006).

[63] Bostwick, A., Ohta, T., Seyller, T., Horn, K. & Rotenberg, E. Quasiparticle dynamics in graphene. *Nature Physics* **3**, 36–40 (2007).

[64] Attaccalite, C. & Rubio, A. Fermi velocity renormalization in doped graphene. *physica status solidi (b)* **246**, 2523–2526 (2009).

[65] Pati, S., Enoki, T. & Rao, C. *Graphene and Its Fascinating Attributes* (World Scientific, 2011).

[66] Piscanec, S., Lazzeri, M., Mauri, F. & Ferrari, A. C. Optical phonons of graphene and nanotubes. *The European Physical Journal Special Topics* **148**, 159–170 (2007).

[67] Basko, D. M. & Aleiner, I. L. Interplay of coulomb and electron-phonon interactions in graphene. *Phys. Rev. B* **77**, 041409 (2008).

[68] Lazzeri, M. & Mauri, F. Nonadiabatic kohn anomaly in a doped graphene monolayer. *Phys. Rev. Lett.* **97**, 266407 (2006).

[69] Pisana, S. *et al.* Breakdown of the adiabatic born–oppenheimer approximation in graphene. *Nature Materials* **6**, 198–201 (2007).

[70] Piscanec, S., Lazzeri, M., Mauri, F., Ferrari, A. C. & Robertson, J. Kohn anomalies and electron-phonon interactions in graphite. *Phys. Rev. Lett.* **93**, 185503 (2004).

[71] Hwang, E. H., Hu, B. Y.-K. & Das Sarma, S. Inelastic carrier lifetime in graphene. *Phys. Rev. B* **76**, 115434 (2007).

[72] Profeta, G., Calandra, M. & Mauri, F. Phonon-mediated superconductivity in graphene by lithium deposition. *Nature Physics* **8**, 131–134 (2012).

[73] Emery, N. *et al.* Superconductivity of bulk CaC_6. *Phys. Rev. Lett.* **95**, 087003 (2005).

[74] Weller, T. E., Ellerby, M., Saxena, S. S., Smith, R. P. & Skipper, N. T. Superconductivity in the intercalated graphite compounds C_6Yb and C_6Ca. *Nature Physics* **1**, 39–41 (2005).

[75] Campetella, M. *et al.* Hybrid-functional electronic structure of multilayer graphene. *Phys. Rev. B* **101**, 165437 (2020).

[76] Ferrari, A. C. *et al.* Raman spectrum of graphene and graphene layers. *Phys. Rev. Lett.* **97**, 187401 (2006).

[77] Torche, A., Mauri, F., Charlier, J.-C. & Calandra, M. First-principles determination of the raman fingerprint of rhombohedral graphite. *Phys. Rev. Materials* **1**, 041001 (2017).

[78] Grigorenko, A. N., Polini, M. & Novoselov, K. S. Graphene plasmonics. *Nature Photonics* **6**, 749–758 (2012).

[79] Nam, Y., Ki, D.-K., Soler-Delgado, D. & Morpurgo, A. F. A family of finite-temperature electronic phase transitions in graphene multilayers. *Science* **362**, 324–328 (2018).

[80] Henck, H. *et al.* Flat electronic bands in long sequences of rhombohedral-stacked graphene. *Phys. Rev. B* **97**, 245421 (2018).

[81] Thomsen, C. & Reich, S. Double resonant raman scattering in graphite. *Phys. Rev. Lett.* **85**, 5214–5217 (2000).

[82] Lee, Y. *et al.* Gate tunable magnetism and giant magnetoresistance in abc-stacked few-layer graphene (2019). 1911.04450.

[83] Pamuk, B., Baima, J., Mauri, F. & Calandra, M. Magnetic gap opening in rhombohedral-stacked multilayer graphene from first principles. *Phys. Rev. B* **95**, 075422 (2017).

[84] Baima, J., Mauri, F. & Calandra, M. Field-effect-driven half-metallic multilayer graphene. *Phys. Rev. B* **98**, 075418 (2018).

[85] Esquinazi, P. *et al.* Indications for intrinsic superconductivity in highly oriented pyrolytic graphite. *Phys. Rev. B* **78**, 134516 (2008).

[86] Dusari, S., Barzola-Quiquia, J. & Esquinazi, P. Superconducting behavior of interfaces in graphite: Transport measurements of micro-constrictions. *Journal of Superconductivity and Novel Magnetism* **24**, 401–405 (2011).

[87] Kopnin, N. B., Ijäs, M., Harju, A. & Heikkilä, T. T. High-temperature surface superconductivity in rhombohedral graphite. *Phys. Rev. B* **87**, 140503 (2013).

[88] Kopnin, N. B. & Heikkila, T. T. *Carbon-based Superconductors : Towards High-Tc Superconductivity*, chap. 9 (Jenny Stanford Publishing, New York, NY, 2015).

[89] Chen, G. *et al.* Signatures of tunable superconductivity in a trilayer graphene moiré superlattice. *Nature* **572**, 215–219 (2019).

[90] Cao, Y. *et al.* Unconventional superconductivity in magic-angle graphene superlattices. *Nature* **556**, 43–50 (2018).

[91] Shallcross, S., Sharma, S., Kandelaki, E. & Pankratov, O. A. Electronic structure of turbostratic graphene. *Phys. Rev. B* **81**, 165105 (2010).

[92] Bistritzer, R. & MacDonald, A. H. Moiré bands in twisted double-layer graphene. *Proceedings of the National Academy of Sciences* **108**, 12233–12237 (2011).

[93] Sboychakov, A. O., Rakhmanov, A. L., Rozhkov, A. V. & Nori, F. Electronic spectrum of twisted bilayer graphene. *Phys. Rev. B* **92**, 075402 (2015).

[94] Fang, S. & Kaxiras, E. Electronic structure theory of weakly interacting bilayers. *Phys. Rev. B* **93**, 235153 (2016).

[95] Cao, Y. *et al.* Correlated insulator behaviour at half-filling in magic-angle graphene superlattices. *Nature* **556**, 80–84 (2018).

[96] Trambly de Laissardière, G., Mayou, D. & Magaud, L. Localization of dirac electrons in rotated graphene bilayers. *Nano Letters* **10**, 804–808 (2010).

[97] Lian, B., Wang, Z. & Bernevig, B. A. Twisted bilayer graphene: A phonon-driven superconductor. *Phys. Rev. Lett.* **122**, 257002 (2019).

[98] Gonzalez-Arraga, L. A., Lado, J. L., Guinea, F. & San-Jose, P. Electrically controllable magnetism in twisted bilayer graphene. *Phys. Rev. Lett.* **119**, 107201 (2017).

[99] Sboychakov, A. O., Rozhkov, A. V., Rakhmanov, A. L. & Nori, F. Externally controlled magnetism and band gap in twisted bilayer graphene. *Phys. Rev. Lett.* **120**, 266402 (2018).

[100] Kim, K. *et al.* Tunable moiré bands and strong correlations in small-twist-angle bilayer graphene. *Proceedings of the National Academy of Sciences* **114**, 3364–3369 (2017).

[101] Yankowitz, M. *et al.* Tuning superconductivity in twisted bilayer graphene. *Science* **363**, 1059–1064 (2019).

[102] Wu, F., MacDonald, A. H. & Martin, I. Theory of phonon-mediated superconductivity in twisted bilayer graphene. *Phys. Rev. Lett.* **121**, 257001 (2018).

[103] Hsu, Y.-T., Wu, F. & Sarma, S. D. Topological superconductivity, ferromagnetism, and valley-polarized phases in moire systems: An rg analysis for twisted double bilayer graphene (2020). 2003.02847.

[104] Iijima, S. Helical microtubules of graphitic carbon. *Nature* **354**, 56–58 (1991).

[105] Hirsch, A. & Vostrowsky, O. *Functionalization of Carbon Nanotubes*, 193–237 (Springer Berlin Heidelberg, Berlin, Heidelberg, 2005).

[106] Avouris, P. Molecular electronics with carbon nanotubes. *Accounts of Chemical Research* **35**, 1026–1034 (2002).

[107] Lin, Y. *et al.* Advances toward bioapplications of carbon nanotubes. *J. Mater. Chem.* **14**, 527–541 (2004).

[108] Liu, C. *et al.* Hydrogen storage in single-walled carbon nanotubes at room temperature. *Science* **286**, 1127–1129 (1999).

[109] Dresselhaus, M., Dresselhaus, G. & Saito, R. Physics of carbon nanotubes. *Carbon* **33**, 883 – 891 (1995). Nanotubes.

[110] Dai, H. Carbon nanotubes: Synthesis, integration, and properties. *Accounts of Chemical Research* **35**, 1035–1044 (2002).

[111] Saito, R., Fujita, M., Dresselhaus, G. & Dresselhaus, M. S. Electronic structure of chiral graphene tubules. *Applied Physics Letters* **60**, 2204–2206 (1992).

[112] Molina, J. M., Savinsky, S. S. & Khokhriakov, N. V. A tight-binding model for calculations of structures and properties of graphitic nanotubes. *The Journal of Chemical Physics* **104**, 4652–4656 (1996).

[113] Dresselhaus, M. S. & Eklund, P. C. Phonons in carbon nanotubes. *Advances in Physics* **49**, 705–814 (2000).

[114] Jansta, J. & Dousek, F. Some aspects of existence of elementary carbon with sp-hybridized bonds. *Carbon* **18**, 433 – 437 (1980).

[115] SMITH, P. P. K. & BUSECK, P. R. Carbyne forms of carbon: Do they exist? *Science* **216**, 984–986 (1982).

[116] WHITTAKER, A. G., WATTS, E. J., LEWIS, R. S. & ANDERS, E. Carbynes: Carriers of primordial noble gases in meteorites. *Science* **209**, 1512–1514 (1980).

[117] Henning, T. & Salama, F. Carbon in the universe. *Science* **282**, 2204–2210 (1998).

[118] Coleman, S. There are no goldstone bosons in two dimensions. *Communications in Mathematical Physics* **31**, 259–264 (1973).

[119] Böttger, H. *Principles of the Theory of Lattice Dynamics* (Akad.-Verlag, 1983).

[120] Peierls, R. E. *Quantum theory of solids* (Clarendon Press, Oxford, UK, 1955).

[121] Yang, S., Olishevski, P. & Kertesz, M. Bandgap calculations for conjugated polymers. *Synthetic Metals* **141**, 171 – 177 (2004). Michael J. Rice Memorial Festschrift.

[122] Tongay, S., Dag, S., Durgun, E., Senger, R. T. & Ciraci, S. Atomic and electronic structure of carbon strings. *Journal of Physics: Condensed Matter* **17**, 3823–3836 (2005).

[123] Yang, S. & Kertesz, M. Bond length alternation and energy band gap of polyyne. *The Journal of Physical Chemistry A* **110**, 9771–9774 (2006).

[124] Peach, M. J. G., Tellgren, E. I., Sałek, P., Helgaker, T. & Tozer, D. J. Structural and electronic properties of polyacetylene and polyyne from hybrid and coulomb-attenuated density functionals. *The Journal of Physical Chemistry A* **111**, 11930–11935 (2007).

[125] Milani, A., Tommasini, M., Del Zoppo, M., Castiglioni, C. & Zerbi, G. Carbon nanowires: Phonon and π-electron confinement. *Phys. Rev. B* **74**, 153418 (2006).

[126] Milani, A. *et al.* First-principles calculation of the peierls distortion in an infinite linear carbon chain: the contribution of raman spectroscopy. *Journal of Raman Spectroscopy* **39**, 164–168 (2008).

[127] Artyukhov, V. I., Liu, M. & Yakobson, B. I. Mechanically induced metal–insulator transition in carbyne. *Nano Letters* **14**, 4224–4229 (2014).

[128] Liu, M., Artyukhov, V. I., Lee, H., Xu, F. & Yakobson, B. I. Carbyne from first principles: Chain of c atoms, a nanorod or a nanorope. *ACS Nano* **7**, 10075–10082 (2013).

[129] Cazzanelli, E. *et al.* High-temperature evolution of linear carbon chains inside multiwalled nanotubes. *Phys. Rev. B* **75**, 121405 (2007).

[130] Shi, L. *et al.* Confined linear carbon chains as a route to bulk carbyne. *Nature Materials* **15**, 634–639 (2016).

[131] Shi, L. *et al.* Electronic band gaps of confined linear carbon chains ranging from polyyne to carbyne. *Phys. Rev. Materials* **1**, 075601 (2017).

[132] McKenzie, R. H. & Wilkins, J. W. Effect of lattice zero-point motion on electronic properties of the peierls-fröhlich state. *Phys. Rev. Lett.* **69**, 1085–1088 (1992).

[133] Polizzi, E. & Yngvesson, S. K. Universal nature of collective plasmonic excitations in finite 1d carbon-based nanostructures. *Nanotechnology* **26**, 325201 (2015).

[134] Bonini, N., Rao, R., Rao, A. M., Marzari, N. & Menéndez, J. Lattice anharmonicity in low-dimensional carbon systems. *physica status solidi (b)* **245**, 2149–2154 (2008).

[135] Tongay, S., Senger, R. T., Dag, S. & Ciraci, S. *ab-initio* electron transport calculations of carbon based string structures. *Phys. Rev. Lett.* **93**, 136404 (2004).

[136] Sorokin, P. B., Lee, H., Antipina, L. Y., Singh, A. K. & Yakobson, B. I. Calcium-decorated carbyne networks as hydrogen storage media. *Nano Letters* **11**, 2660–2665 (2011).

[137] Heeger, A. J. Nobel lecture: Semiconducting and metallic polymers: The fourth generation of polymeric materials. *Rev. Mod. Phys.* **73**, 681–700 (2001).

[138] Gibtner, T., Hampel, F., Gisselbrecht, J.-P. & Hirsch, A. End-cap stabilized oligoynes: Model compounds for the linear sp carbon allotrope carbyne. *Chemistry –A European Journal* **8**, 408–432 (2002).

[139] Su, W. P., Schrieffer, J. R. & Heeger, A. J. Solitons in polyacetylene. *Phys. Rev. Lett.* **42**, 1698–1701 (1979).

[140] Jackiw, R. & Rebbi, C. Solitons with fermion number ½. *Phys. Rev. D* **13**, 3398–3409 (1976).

[141] Heeger, A. J., Kivelson, S., Schrieffer, J. R. & Su, W. P. Solitons in conducting polymers. *Rev. Mod. Phys.* **60**, 781–850 (1988).

[142] Qi, X.-L. & Zhang, S.-C. Topological insulators and superconductors. *Rev. Mod. Phys.* **83**, 1057–1110 (2011).

[143] Weber, M., Assaad, F. F. & Hohenadler, M. Excitation spectra and correlation functions of quantum su-schrieffer-heeger models. *Phys. Rev. B* **91**, 245147 (2015).

[144] Dresselhaus, M., Dresselhaus, G. & Eklund, P. *Science of Fullerenes and Carbon Nanotubes: Their Properties and Applications* (Elsevier Science, 1996).

[145] Kroto, H. W., Heath, J. R., O'Brien, S. C., Curl, R. F. & Smalley, R. E. C60: Buckminsterfullerene. *Nature* **318**, 162–163 (1985).

[146] Krätschmer, W., Lamb, L. D., Fostiropoulos, K. & Huffman, D. R. Solid *C*60: a new form of carbon. *Nature* **347**, 354–358 (1990).

[147] Hirsch, A., Brettreich, M. & Wudl, F. *Fullerenes: Chemistry and Reactions* (Wiley, 2006).

[148] Dennler, G., Scharber, M. C. & Brabec, C. J. Polymer-fullerene bulk-heterojunction solar cells. *Advanced Materials* **21**, 1323–1338 (2009).

[149] Friedman, S. H. *et al.* Inhibition of the HIV-1 protease by fullerene derivatives: model building studies and experimental verification. *Journal of the American Chemical Society* **115**, 6506–6509 (1993).

[150] Saito, S. & Oshiyama, A. Cohesive mechanism and energy bands of solid C_{60}. *Phys. Rev. Lett.* **66**, 2637–2640 (1991).

[151] Holczer, K. *et al.* Alkali-fulleride superconductors: Synthesis, composition, and diamagnetic shielding. *Science* **252**, 1154–1157 (1991).

[152] Tanigaki, K. *et al.* Superconductivity at 33 K in Cs_xRb_yc60. *Nature* **352**, 222–223 (1991).

[153] Faber, C., Janssen, J. L., Côté, M., Runge, E. & Blase, X. Electron-phonon coupling in the C_{60} fullerene within the many-body *GW* approach. *Phys. Rev. B* **84**, 155104 (2011).

[154] Capone, M., Fabrizio, M., Castellani, C. & Tosatti, E. Strongly correlated superconductivity. *Science* **296**, 2364–2366 (2002).

[155] Paci, P., Cappelluti, E., Grimaldi, C., Pietronero, L. & Strässler, S. Nonadiabatic high-T_c superconductivity in hole-doped fullerenes. *Phys. Rev. B* **69**, 024507 (2004).

[156] Capone, M., Fabrizio, M., Castellani, C. & Tosatti, E. Colloquium: Modeling the unconventional superconducting properties of expanded A_3C_{60} fullerides. *Rev. Mod. Phys.* **81**, 943–958 (2009).

[157] Capone, M., Fabrizio, M., Giannozzi, P. & Tosatti, E. Theory of the metal-nonmagnetic mott-jahn-teller insulator transition in A_4c_{60}. *Phys. Rev. B* **62**, 7619–7624 (2000).

[158] Ziman, J. *Electrons and phonons: the theory of transport phenomena in solids* (Oxford University Press, Oxford, UK, 1960).

[159] Gosar, P. & Choi, S. Linear-response theory of the electron mobility in molecular crystals. *Phys. Rev.* **150**, 529 (1966).

[160] Bardeen, J., Cooper, L. N. & Schrieffer, J. R. Theory of superconductivity. *Phys. Rev.* 1175 (1957).

[161] Grüner, G. *Density waves in solids (frontiers in Physics)* (CRC Press, 1994).

[162] Lv, B., Qian, T. & Ding, H. Angle-resolved photoemission spectroscopy and its application to topological materials. *Nat. Rev. Phys.* **1**, 609–626 (2019).

[163] Kohn, W. Image of the fermi surface in the vibration spectrum of a metal. *Phys. Rev. Lett.* **2**, 393 (1959).

[164] Allen, P. B. Neutron spectroscopy of superconductors. *Phys. Rev. B* **6**, 2577–2579 (1972).

[165] Allen, P. B. & Cardona, M. Temperature dependence of the direct gap of Si and Ge. *Phys. Rev. B* **27**, 4760 (1983).

[166] Bernardi, M., Vigil-Fowler, D., Lischner, J., Neaton, J. B. & Louie, S. G. Ab initio study of hot carriers in the first picosecond after sunlight absorption in silicon. *Phys. Rev. Lett.* **112**, 257402 (2014).

[167] Sangalli, D. & Marini, A. Ultra-fast carriers relaxation in bulk silicon following photo-excitation with a short and polarized laser pulse. *Europhys. Lett.* **110**, 4 (2015).

[168] Born, M. & Oppenheimer, R. Zur quantentheorie der molekeln. *Annalen der Physik* **389**, 457–484 (1927).

[169] Hohenberg, P. & Kohn, W. Inhomogeneous electron gas. *Phys. Rev.* **136**, B864–B871 (1964).

[170] Kohn, W. & Sham, L. J. Self-consistent equations including exchange and correlation effects. *Phys. Rev.* **140**, A1133–A1138 (1965).

[171] Gonze, X., Allan, D. C. & Teter, M. P. Dielectric tensor, effective charges, and phonons in α-quartz by variational density-functional perturbation theory. *Phys. Rev. Lett.* **68**, 3603–3606 (1992).

[172] Baroni, S., de Gironcoli, S., Dal Corso, A. & Giannozzi, P. Phonons and related crystal properties from density-functional perturbation theory. *Rev. Mod. Phys.* **73**, 515–562 (2001).

[173] Frölich, H. Interaction of electrons with lattice vibrations. *Proc. Roy. Soc.* **A215**, 291 (1952).

[174] Matsubara, T. A new approach to quantum-statistical mechanics. *Prog. Theor. Phys.* **14**, 351 (1955).

[175] Abrikosov, A. A., Gorkov, L. P. & Dzyaloshinski, I. E. *Methods of quantum field theory in statistical physics* (Dover Publications Inc., Mineola, NY, 1975).

[176] Fetter, A. L. & Walecka, J. D. *Quantum theory of many-particle systems* (Dover Publications Inc., Mineola, NY, 2003).

[177] Dyson, F. J. The radiation theories of Tomonaga, Schwinger and Feynman. *Phys. Rev.* **75**, 486 (1949).

[178] Dyson, F. J. The s matrix in quantum electrodynamics. *Phys. Rev.* **75**, 1736 (1949).

[179] Engelsberg, S. & Schrieffer, J. R. Coupled electron-phonon systems. *Phys. Rev.* **131**, 3 (1963).

[180] Marini, A., Poncé, S. & Gonze, X. Many-body perturbation theory approach to the electron-phonon interaction with density-functional theory as a starting point. *Phys. Rev. B* **91**, 224310 (2015).

[181] Migdal, A. B. Interactions between electrons and lattice vibrations in a normal metal. *Sov. Phys. JETP* **5**, 333 (1957).

[182] Allen, P. B. & Mitrovic, B. Theory of superconducting t_c. In Ehrenreich, H., Seitz, F. & Trunbull, D. (eds.) *Solid State Physics*, vol. 37, 1–92 (Academic Press Inc., New York, NY, 1982).

[183] Sano, W., Koretsune, T., Tadano, T., Akashi, R. & Arita, R. Effect of van hove singularities on high-tc superconductivity in h3s. *Phys. Rev. B* **93**, 094525 (2016).

[184] Lehmann, H. Über eigenschaften von ausbreitungsfunktionen und renormierungskonstanten quantisierter felder. *Nuovo Cim.* **11**, 342–357 (1954).

[185] Grimvall, G. *The electron-phonon interaction in metals* (North-Holland Publishing Company, 1981).

[186] Lindhard, J. On the properties of a gas of charged particles. *Det Kongelige Danske Videnskabernes Selskab, Matematisk-fysike Meddlelser* **28**, 8 (1954).

[187] Giuliani, G. F. & Vignale, G. *Quantum theory of the electron liquid* (Cambridge university press, Cambridge, UK, 2005).

[188] Cooper, L. N. Bound electron pairs in a degenerate fermi gas. *Phys. Rev.* **104**, 1189 (1956).

[189] Pitaevskii, L. *Phenomenology and microscopic theory: theoretical fundations* (Springer, 2008).

[190] Eliashberg, G. M. Interactions between electrons and lattice vibrations in a superconductor. *Sov. Phys. JETP* **11** (1960).

[191] Eliashberg, G. M. Interactions between electrons and lattice vibrations in a superconductor. *Zh. Eksp. Teor. Fiz* **38** (1960).

[192] Scalapino, D. J., Schrieffer, J. R. & Wilkins, J. W. *The electron-phonon interaction and strong-coupling superconductor* (Dekker, New York, NY, 1969).

[193] Nambu, Y. Quasi-particles and gauge invariance in the theory of superconductivity. *Phys. Rev.* **117**, 648 (1960).

[194] Gorkov, L. P. On the energy spectrum of superconductors. *Sov. Phys. JETP* **7**, 505 (1958).

[195] Gorkov, L. P. On the energy spectrum of superconductors. *Zh. Eksp. Teor. Fiz* **34**, 735 (1958).

[196] Sanna, A. *et al.* Phononic self-energy effects and superconductivity in cac6. *Phys. Rev. B* **85**, 184514 (2012).

[197] Carbotte, J. P. Properties of boson-exchange superconductors. *Rev. Mod. Phys.* **62**, 1027 (1990).

[198] Ummarino, G. A. *Emergent Phenomena in Correlated Matter*, 13.1–13.36 (Forschungszentrum Jülich GmbH and Institute for Advanced Simulations, 2013).

[199] Margine, E. R. & Giustino, F. Anisotropic migdal-eliashberg theory using wannier functions. *Phys. Rev. B* **87**, 024505 (2013).

[200] Videberg, H. J. & Serene, J. W. Solving the eliashberg equations by means of n-point padé approximants. *J. Low Temp. Phys.* **29** (1977).

[201] Marsiglio, F., Schossmann, M. & Carbotte, J. P. Iterative analytic continuation of the electron self-energy to the real axis. *Phys. Rev. B* **37**, 4965–4969 (1988).

[202] McMillan, W. L. Transition temperature of strong-coupled superconductors. *Phys. Rev.* **167**, 331 (1968).

[203] Allen, P. B. & Dynes, R. C. Transition temperature of strong-coupled superconductors reanalyzed. *Phys. Rev. B* **12**, 905 (1975).

[204] Morel, P. & Anderson, P. W. Calculation of the superconducting state parameters with retarded electron-phonon interaction. *Phys. Rev. Lett.* **125**, 1263 (1962).

[205] Sze, S. *Physics of Semiconductor Devices*. Wiley-Interscience publication (John Wiley & Sons, 1981).

[206] R. E. Glover, I. & Sherrill, M. D. Changes in superconducting critical temperature produced by electrostatic charging. *Phys. Rev. Lett.* **5**, 248 (1960).

[207] Daghero, D. *et al.* Large conductance modulation of gold thin films by huge charge injection via electrochemical gating. *Phys. Rev. Lett.* **108**, 066807 (2012).

[208] Tortello, M. *et al.* Huge field-effect surface charge injection and conductance modulation in metallic thin films by electrochemical gating. *Appl. Surf. Sci.* **269**, 17–22 (2013).

[209] Nakano, M. *et al.* Collective bulk carrier delocalization driven by electrostatic surface charge accumulation. *Nature* **487**, 459–462 (2012).

[210] Yu, Y. *et al.* Gate-tunable phase transitions in thin flakes of 1t-tas2. *Nat. Nanotechnol.* **10**, 270–6 (2015).

[211] Li, L. J. *et al.* Controlling many-body states by the electric-field effect in a two-dimensional material. *Nature* **529**, 185–9 (2016).

[212] Saito, Y. & Iwasa, Y. Ambipolar insulator-to-metal transition in black phosphorus by ionic-liquid gating. *ACS Nano* **9**, 3192 (2015).

[213] Katase, T., Hiramatsu, H., Kamiya, T. & Hosono, H. Electric double-layer transistor using layered iron selenide mott insulator tlfe1.6se2. *PNAS* **11**, 3979–3983 (2014).

[214] Yamada, Y. *et al.* Electrically induced ferromagnetism at room temperature in cobalt-doped titanium dioxide. *Science* **332**, 1065–7 (2011).

[215] Xi, X., Berger, H., Forró, L., Shan, J. & Mak, K. F. Gate tuning of electronic phase transitions in two-dimensional nbse2. *Phys. Rev. Lett.* **117**, 106801 (2016).

[216] Yoshida, M., Ye, J., Nishizaki, T., Kobayashi, N. & Iwasa, Y. Electrostatic and electrochemical tuning of superconductivity in two-dimensional nbse2 crystals. *Appl. Phys. Lett.* **108**, 202602 (2016).

[217] Li, L. J. *et al.* Anomalous quantum metal in a 2d crystalline superconductor with electronic phase nonuniformity. *Nano Lett.* **6**, 4126–4133 (2019).

[218] Choi, J. *et al.* Electrical modulation of superconducting critical temperature in liquid-gated thin niobium films. *Appl. Phys. Lett.* **205**, 012601 (2014).

[219] Piatti, E. *et al.* Superconducting transition temperature modulation in nbn via edl gating. *J. Supercond. Nov. Magn.* **29**, 587 (2016).

[220] Piatti, E. *et al.* Control of bulk superconductivity in a bcs superconductor by surface charge doping via electrochemical gating. *Phys. Rev. B* **95**, 140501(R) (2017).

[221] Simoni, G. D., Paolucci, F., Solinas, P., Strambini, E. & Giazotto, F. Metallic supercurrent field-effect transistor. *Nat. Nanotechnol.* **13**, 802–805 (2018).

[222] Paolucci, F., Simoni, G. D., Strambini, E., Solinas, P. & Giazotto, F. Ultra-efficient superconducting dayem bridge field-effect transistor. *Nano Lett.* **7**, 4195–4199 (2018).

[223] Paolucci, F. *et al.* Magnetotransport experiments on fully metallic superconducting dayem-bridge field-effect transistors. *Phys. Rev. Appl.* **11**, 024061 (2019).

[224] Bollinger, A. T. *et al.* Superconductor–insulator transition in at the pair quantum resistance. *Nature* **472**, 458–460 (2011).

[225] Leng, X., Garcia-Barriocanal, J., Bose, S., Lee, Y. & Goldman, A. M. Electrostatic control of the evolution from a superconducting phase to an insulating phase in ultrathin films. *Phys. Rev. Lett.* **107**, 039901 (2011).

[226] Leng, X. *et al.* Indications of an electronic phase transition in two-dimensional superconducting thin films induced by electrostatic doping. *Phys. Rev. Lett.* **108**, 067004 (2012).

[227] Maruyama, A. *et al.* Reversible electrochemical modulation of the superconducting transition temperature of liti2o4 ultrathin films by ionic liquid gating. *Appl. Phys. Lett.* **107**, 142602 (2015).

[228] Jin, K. *et al.* Evolution of electronic states in n-type copper oxide superconductor via electric double layer gating. *Sci. Rep.* **6**, 26642 (2016).

[229] Fete, A., Rossi, L., Augieri, A. & Senatore, C. Ionic liquid gating of ultra-thin films. *Appl. Phys. Lett.* **109**, 192601 (2016).

[230] Burlachkov, L., Khalfin, I. B. & Shapiro, B. Y. Increase of the critical current by an external electric field in high-temperature superconductors. *Phys. Rev. B* **48**, 1156 (1993).

[231] Ghinovker, M., Sandomirsky, V. B. & Shapiro, B. Y. Abrikosov-vortex-energy change due to an electric-field effect. *Phys. Rev. B* **51**, 8404 (1995).

[232] Walter, J., Wang, H., Luo, B., Frisbie, C. D. & Leighton, C. Electrostatic versus electrochemical doping and control of ferromagnetism in ion-gel-gated ultrathin. *ACS Nano* **10**, 7799 (2016).

[233] Shiogai, J., Ito, Y., Mitsuhashi, T., Nojima, T. & Tsukazaki, A. Electric-field-induced superconductivity in electrochemically etched ultrathin fese films on srtio3 and mgo. *Nature Physics* **12**, 42–46 (2016).

[234] Lei, B. *et al.* Evolution of high-temperature superconductivity from a low- t c phase tuned by carrier concentration in fese thin flakes. *Phys. Rev. Lett.* **116**, 077002 (2016).

[235] Hanzawa, K., Sato, H., Hiramatsu, H., Kamiya, T. & Hosono, H. Electric field-induced superconducting transition of insulating fese thin film at 35 k. *PNAS* **113**, 3986–3990 (2016).

[236] Zhu, C. S. *et al.* Tuning electronic properties of fese 0.5 te 0.5 thin flakes using a solid ion conductor field-effect transistor. *Phys. Rev. B* **96**, 174513 (2017).

[237] Miyakawa, T. *et al.* Enhancement of superconducting transition temperature in fese electric-double-layer transistor with multivalent ionic liquids. *Phys. Rev. Materials* **2**, 031801 (2018).

[238] Kouno, S. *et al.* Superconductivity at 38 k at an electrochemical interface between an ionic liquid and fese0.8te0.2 on various substrates. *Scientific Reports* **8**, 14731 (2018).

[239] Piatti, E. *et al.* Ambipolar suppression of superconductivity by ionic gating in optimally doped $\mathrm{bafe_2(As,P)_2}$ ultrathin films. *Phys. Rev. Materials* **3**, 044801 (2019).

[240] Brumme, T., Calandra, M. & Mauri, F. Electrochemical doping of few-layer zrncl from first principles: Electronic and structural properties in field-effect configuration. *Phys. Rev. B* **89**, 245406 (2014).

[241] Brumme, T., Calandra, M. & Mauri, F. First-principles theory of field-effect doping in transition-metal dichalcogenides: Structural properties, electronic structure, hall coefficient, and electrical conductivity. *Phys. Rev. B* **91**, 155436 (2015).

[242] Sohier, T., Calandra, M. & Mauri, F. Density functional perturbation theory for gated two-dimensional heterostructures: Theoretical developments and application to flexural phonons in graphene. *Phys. Rev. B* **96**, 075448 (2017).

[243] Huang, A. P., Chu, P. K. & Yang, Z. C. Hafnium-based high-k gate dielectrics. In *Advances in Solid State Circuit Technologies*, chap. 16 (InTech, 2010).

[244] Yuan, H. *et al.* High-density carrier accumulation in zno field-effect transistors gated by electric double layers of ionic liquids. *Advanced Functional Materials* **19**, 1046–1053 (2009).

[245] Ueno, K. *et al.* Electric-field-induced superconductivity in an insulator. *Nature Materials* **7**, 855–858 (2008).

[246] Ueno, K. *et al.* Field-induced superconductivity in electric double layer transistors. *Journal of the Physical Society of Japan* **83**, 032001 (2014).

[247] Jeong, J. *et al.* Suppression of metal-insulator transition in vo2 by electric field–induced oxygen vacancy formation. *Science* **339**, 1402–1405 (2013).

[248] Schladt, T. D. *et al.* Crystal-facet-dependent metallization in electrolyte-gated rutile tio2 single crystals. *ACS Nano* **7**, 8074–8081 (2013). PMID: 23962081.

[249] Li, M. *et al.* Suppression of ionic liquid gate-induced metallization of srtio3(001) by oxygen. *Nano Letters* **13**, 4675–4678 (2013). PMID: 23978006.

[250] Shi, W. *et al.* Superconductivity series in transition metal dichalcogenides by ionic gating. *Scientific Reports* **5**, 12534 (2015).

[251] De Gennes, P. G. Boundary effects in superconductors. *Rev. Mod. Phys.* **36**, 225–237 (1964).

[252] Pannetier, B. & Courtois, H. Andreev reflection and proximity effect. *Journal of Low Temperature Physics* **118**, 599–615 (2000).

[253] Andreev, A. F. The thermal conductivity of the intermediate state in superconductors. *Sov. Phys. JETP* **19**, 1228 (1964).

[254] Chazalviel, J. *Coulomb Screening by Mobile Charges: Applications to Materials Science, Chemistry, and Biology* (Birkhäuser Boston, 1999).

[255] Kopnin, N. & Press, O. U. *Theory of Nonequilibrium Superconductivity*. International Series of Monographs on Physics (Clarendon Press, 2001).

[256] Ovchinnikov, Y. N. Penetration of an electrical field into a superconductor. *Journal of Low Temperature Physics* **28**, 43–60 (1977).

[257] McMillan, W. L. Tunneling model of the superconducting proximity effect. *Phys. Rev.* **175**, 537–542 (1968).

[258] Ummarino, G. A. *et al.* Proximity eliashberg theory of electrostatic field-effect doping in superconducting films. *Phys. Rev. B* **96**, 064509 (2017).

[259] Ummarino, G. A. & Romanin, D. Theoretical explanation of electric field-induced superconductive critical temperature shifts in indium thin films. *physica status solidi (b)* **257**, 1900651 (2020).

[260] Ummarino, G. A. & Romanin, D. Proximity two bands eliashberg theory of electrostatic field-effect doping in a superconducting film of MgB2. *Journal of Physics: Condensed Matter* **31**, 024001 (2018).

[261] Ummarino, G. Superconductive critical temperature of pb/ag heterostructures. *Physica C: Superconductivity and its Applications* **568**, 1353566 (2020).

[262] Eisenstein, J. Superconducting elements. *Rev. Mod. Phys.* **26**, 277–291 (1954).

[263] Matthias, B. T., Geballe, T. H. & Compton, V. B. Superconductivity. *Rev. Mod. Phys.* **35**, 1–22 (1963).

[264] Eichele, R., Kern, W. & Huebener, R. P. Superconductivity of thin films of lead, indium, and tin prepared in the presence of oxygen. *Applied physics* **25**, 95–103 (1981).

[265] Dolgov, O. V. *et al.* Extraction of the electron-phonon interaction from tunneling data in the multigap superconductor mgb_2. *Phys. Rev. B* **68**, 132503 (2003).

[266] Golubov, A. A. *et al.* Specific heat of MgB2in a one- and a two-band model from first-principles calculations. *Journal of Physics: Condensed Matter* **14**, 1353–1360 (2002).

[267] Brinkman, A. *et al.* Multiband model for tunneling in mgb_2 junctions. *Phys. Rev. B* **65**, 180517 (2002).

[268] Golubov, A. A., Brinkman, A., Dolgov, O. V., Kortus, J. & Jepsen, O. Multi-band model for penetration depth in mgb_2. *Phys. Rev. B* **66**, 054524 (2002).

[269] Piatti, E., Romanin, D., Gonnelli, R. S. & Daghero, D. Anomalous screening of an electrostatic field at the surface of niobium nitride. *Applied Surface Science* **461**, 17 – 22 (2018). 5th Progress in Applied Surface, Interface and Thin Film Science and Solar Renewable Energy News.

[270] Ueno, K. *et al.* Effective thickness of two-dimensional superconductivity in a tunable triangular quantum well of srtio3. *Phys. Rev. B* **89**, 020508 (2014).

[271] Valentinis, D. *et al.* Modulation of the superconducting critical temperature due to quantum confinement at the $laalo_3/srtio_3$ interface. *Phys. Rev. B* **96**, 094518 (2017).

[272] Romanin, D., Brumme, T., Daghero, D., Gonnelli, R. S. & Piatti, E. Strong band-filling-dependence of the scattering lifetime in gated mos2 nanolayers induced by the opening of intervalley scattering channels (2020). 2006.06063.

[273] Sohier, T., Calandra, M. & Mauri, F. Density-functional calculation of static screening in two-dimensional materials: The long-wavelength dielectric function of graphene. *Phys. Rev. B* **91**, 165428 (2015).

[274] Sohier, T., Gibertini, M., Calandra, M., Mauri, F. & Marzari, N. Breakdown of optical phonons'splitting in two-dimensional materials. *Nano Letters* **17**, 3758–3763 (2017).

[275] Sohier, T., Calandra, M. & Mauri, F. Two-dimensional fröhlich interaction in transition-metal dichalcogenide monolayers: Theoretical modeling and first-principles calculations. *Phys. Rev. B* **94**, 085415 (2016).

[276] Jarvis, M. R., White, I. D., Godby, R. W. & Payne, M. C. Supercell technique for total-energy calculations of finite charged and polar systems. *Phys. Rev. B* **56**, 14972–14978 (1997).

[277] Rozzi, C. A., Varsano, D., Marini, A., Gross, E. K. U. & Rubio, A. Exact coulomb cutoff technique for supercell calculations. *Phys. Rev. B* **73**, 205119 (2006).

[278] Ismail-Beigi, S. Truncation of periodic image interactions for confined systems. *Phys. Rev. B* **73**, 233103 (2006).

[279] Nagamatsu, J., Nakagawa, N., Muranaka, T., Zenitani, Y. & Akimitsu, J. Superconductivity at 39 k in magnesium diboride. *Nature* **410**, 63–64 (2001).

[280] Drozdov, A. P., Eremets, M. I., Troyan, I. A., Ksenofontov, V. & Shylin, S. I. Conventional superconductivity at 203 kelvin at high pressures in the sulfur hydride system. *Nature* **525**, 73–76 (2015).

[281] Romanin, D. *et al.* Electric field exfoliation and high-tc superconductivity in field-effect hole-doped hydrogenated diamond (111). *Applied Surface Science* **496**, 143709 (2019).

[282] Romanin, D., Ummarino, G. A. & Piatti, E. Migdal-eliashberg theory of multiband high-temperature superconductivity in field-effect-doped hydrogenated (111) diamond. *Applied Surface Science* **536**, 147723 (2021).

[283] Duke, C. B. Semiconductor surface reconstruction: The structural chemistry of two-dimensional surface compounds. *Chemical Reviews* **96**, 1237–1260 (1996).

[284] Pandey, K. C. New dimerized-chain model for the reconstruction of the diamond (111)-(2 × 1) surface. *Phys. Rev. B* **25**, 4338–4341 (1982).

[285] Pamuk, B. & Calandra, M. Competition between exchange-driven dimerization and magnetism in diamond (111). *Phys. Rev. B* **99**, 155303 (2019).

[286] Nakamura, K. *et al.* Electric-field-driven hole carriers and superconductivity in diamond. *Phys. Rev. B* **87**, 214506 (2013).

[287] Sano, K., Hattori, T. & Nakamura, K. Role of surface-bound hole states in electric-field-driven superconductivity at the (110)-surface of diamond. *Phys. Rev. B* **96**, 155144 (2017).

[288] Ristein, J. Diamond surfaces: familiar and amazing. *Applied Physics A* **82**, 377–384 (2006).

[289] Yamaguchi, T. *et al.* Low-temperature transport properties of holes introduced by ionic liquid gating in hydrogen-terminated diamond surfaces. *Journal of the Physical Society of Japan* **82**, 074718 (2013).

[290] Takahide, Y. *et al.* Quantum oscillations of the two-dimensional hole gas at atomically flat diamond surfaces. *Phys. Rev. B* **89**, 235304 (2014).

[291] Piatti, E., Pasquarelli, A. & Gonnelli, R. S. Orientation-dependent electric transport and band filling in hole co-doped epitaxial diamond films. *Applied Surface Science* **528**, 146795 (2020).

[292] Skocpol, W. J. & Tinkham, M. Fluctuations near superconducting phase transitions **38**, 1049–1097 (1975).

[293] Kosterlitz, J. M. & Thouless, D. J. Ordering, metastability and phase transitions in two-dimensional systems **6**, 1181–1203 (1973).

[294] Baldereschi, A., Baroni, S. & Resta, R. Band offsets in lattice-matched heterojunctions: A model and first-principles calculations for gaas/alas. *Phys. Rev. Lett.* **61**, 734–737 (1988).

[295] Boeri, L., Kortus, J. & Andersen, O. K. Three-dimensional mgb_2-type superconductivity in hole-doped diamond. *Phys. Rev. Lett.* **93**, 237002 (2004).

[296] Savini, G., Ferrari, A. C. & Giustino, F. First-principles prediction of doped graphane as a high-temperature electron-phonon superconductor. *Phys. Rev. Lett.* **105**, 037002 (2010).

[297] Calandra, M., Profeta, G. & Mauri, F. Adiabatic and nonadiabatic phonon dispersion in a wannier function approach. *Phys. Rev. B* **82**, 165111 (2010).

[298] Ummarino, G. A., Gonnelli, R. S., Massidda, S. & Bianconi, A. Two-band eliashberg equations and the experimental tc of the diboride mg1-xalxb2. *Physica C: Superconductivity* **407**, 121–127 (2004).

[299] Adrian, S. D., Wolf, S. A., Dolgov, O., Shulga, S. & Kresin, V. Z. Density of states and the energy gap in superconducting cuprates. *Phys. Rev. B* **56**, 7878–7881 (1997).

[300] Gonnelli, R. S. *et al.* Fermi-surface topological phase transition and horizontal order-parameter nodes in cafe2as2 under pressure. *Scientific Reports* **6**, 26394 (2016).

[301] Piatti, E. *et al.* Multi-valley superconductivity in ion-gated mos2 layers. *Nano Letters* **18**, 4821–4830 (2018).

[302] Inosov, D. S. *et al.* Crossover from weak to strong pairing in unconventional superconductors. *Phys. Rev. B* **83** (2011).

[303] Costanzo, D., Zhang, H., Reddy, B. A., Berger, H. & Morpurgo, A. F. Tunnelling spectroscopy of gate-induced superconductivity in mos2. *Nature Nanotechnology* **13**, 483–488 (2018).

[304] Koshino, M. & McCann, E. Multilayer graphenes with mixed stacking structure: Interplay of bernal and rhombohedral stacking. *Phys. Rev. B* **87**, 045420 (2013).

[305] Shaginyan, V. R., Amusia, M. Y., Msezane, A. Z. & Popov, K. G. Scaling behavior of heavy fermion metals. *Physics Reports* **492**, 31–109 (2010).

[306] Kopnin, N. B., Heikkilä, T. T. & Volovik, G. E. High-temperature surface superconductivity in topological flat-band systems. *Phys. Rev. B* **83**, 220503 (2011).

[307] Van Hove, L. The occurrence of singularities in the elastic frequency distribution of a crystal. *Phys. Rev.* **89**, 1189–1193 (1953).

[308] Zhang, Y. *et al.* Direct observation of a widely tunable bandgap in bilayer graphene. *Nature* **459**, 820–823 (2009).

[309] Radtke, R. J. & Norman, M. R. Relation of extended van hove singularities to high-temperature superconductivity within strong-coupling theory. *Phys. Rev. B* **50**, 9554–9560 (1994).

[310] Cappelluti, E. & Pietronero, L. Nonadiabatic superconductivity: The role of van hove singularities. *Phys. Rev. B* **53**, 932–944 (1996).

[311] Irkhin, V. Y., Katanin, A. A. & Katsnelson, M. I. Effects of van hove singularities on magnetism and superconductivity in the $t-t'$ hubbard model: A parquet approach. *Phys. Rev. B* **64**, 165107 (2001).

[312] Quan, Y. & Pickett, W. E. Van hove singularities and spectral smearing in high-temperature superconducting h_3S. *Phys. Rev. B* **93**, 104526 (2016).

[313] Liu, Y.-W. *et al.* Magnetism near half-filling of a van hove singularity in twisted graphene bilayer. *Phys. Rev. B* **99**, 201408 (2019).

[314] Si, C., Liu, Z., Duan, W. & Liu, F. First-principles calculations on the effect of doping and biaxial tensile strain on electron-phonon coupling in graphene. *Phys. Rev. Lett.* **111**, 196802 (2013).

[315] Margine, E. R. & Giustino, F. Two-gap superconductivity in heavily *n*-doped graphene: Ab initio migdal-eliashberg theory. *Phys. Rev. B* **90**, 014518 (2014).

[316] Margine, E. R., Lambert, H. & Giustino, F. Electron-phonon interaction and pairing mechanism in superconducting ca-intercalated bilayer graphene. *Scientific Reports* **6**, 21414 (2016).

[317] Profeta, G., Tresca, C. & Sanna, A. *Electron–Phonon Coupling in Two-Dimensional Superconductors: Doped Graphene and Phosphorene*, 31–45 (Springer International Publishing, Cham, 2017).

[318] Perdew, J. P. Density-functional approximation for the correlation energy of the inhomogeneous electron gas. *Phys. Rev. B* **33**, 8822–8824 (1986).

[319] Perdew, J. P., Burke, K. & Ernzerhof, M. Generalized gradient approximation made simple. *Phys. Rev. Lett.* **77**, 3865–3868 (1996).

[320] Faber, C. *et al.* Exploring approximations to the *gw* self-energy ionic gradients. *Phys. Rev. B* **91**, 155109 (2015).

[321] Lazzeri, M., Attaccalite, C., Wirtz, L. & Mauri, F. Impact of the electron-electron correlation on phonon dispersion: Failure of lda and gga dft functionals in graphene and graphite. *Phys. Rev. B* **78**, 081406 (2008).

[322] Hellgren, M. *et al.* Critical role of the exchange interaction for the electronic structure and charge-density-wave formation in $tise_2$. *Phys. Rev. Lett.* **119**, 176401 (2017).

[323] Pamuk, B., Baima, J., Dovesi, R., Calandra, M. & Mauri, F. Spin susceptibility and electron-phonon coupling of two-dimensional materials by range-separated hybrid density functionals: Case study of li_xZrNCl. *Phys. Rev. B* **94**, 035101 (2016).

[324] Pamuk, B., Mauri, F. & Calandra, M. High-T_c superconductivity in weakly electron-doped hfncl. *Phys. Rev. B* **96**, 024518 (2017).

[325] Calandra, M., Zoccante, P. & Mauri, F. Universal increase in the superconducting critical temperature of two-dimensional semiconductors at low doping by the electron-electron interaction. *Phys. Rev. Lett.* **114**, 077001 (2015).

[326] Martin, R. M. *Electronic structure: basic theory and practical methods* (Cambridge university press, Cambridge, UK, 2004).

[327] Perdew, J. P., Ernzerhof, M. & Burke, K. Rationale for mixing exact exchange with density functional approximations. *The Journal of Chemical Physics* **105**, 9982–9985 (1996).

[328] Adamo, C. & Barone, V. Toward reliable density functional methods without adjustable parameters: The pbe0 model. *The Journal of Chemical Physics* **110**, 6158–6170 (1999).

[329] Kim, K. & Jordan, K. D. Comparison of density functional and mp2 calculations on the water monomer and dimer. *The Journal of Physical Chemistry* **98**, 10089–10094 (1994).

[330] Hedin, L. New method for calculating the one-particle green's function with application to the electron-gas problem. *Phys. Rev.* **139**, A796–A823 (1965).

[331] Aryasetiawan, F. & Gunnarsson, O. The gw method **61**, 237–312 (1998).

[332] Li, Z., Antonius, G., Wu, M., da Jornada, F. H. & Louie, S. G. Electron-phonon coupling from ab initio linear-response theory within the *gw* method: Correlation-enhanced interactions and superconductivity in $ba_{1-x}k_xbio_3$. *Phys. Rev. Lett.* **122**, 186402 (2019).

[333] Berlinsky, A. J. One-dimensional metals and charge density wave effects in these materials. *Reports on Progress in Physics* **42**, 1243–1283 (1979).

[334] Horovitz, B., Weger, M. & Gutfreund, H. Phonon dispersion and instability in linear-chain crystals. *Phys. Rev. B* **9**, 1246–1260 (1974).

[335] Lee, P. A., Rice, T. M. & Anderson, P. W. Fluctuation effects at a peierls transition. *Phys. Rev. Lett.* **31**, 462–465 (1973).

[336] Maradudin, A. A. & Fein, A. E. Scattering of neutrons by an anharmonic crystal. *Phys. Rev.* **128**, 2589–2608 (1962).

[337] Errea, I., Calandra, M. & Mauri, F. First-principles theory of anharmonicity and the inverse isotope effect in superconducting palladium-hydride compounds. *Phys. Rev. Lett.* **111**, 177002 (2013).

[338] Errea, I., Calandra, M. & Mauri, F. Anharmonic free energies and phonon dispersions from the stochastic self-consistent harmonic approximation: Application to platinum and palladium hydrides. *Phys. Rev. B* **89**, 064302 (2014).

[339] Errea, I. *et al.* High-pressure hydrogen sulfide from first principles: A strongly anharmonic phonon-mediated superconductor. *Phys. Rev. Lett.* **114**, 157004 (2015).

[340] Errea, I. *et al.* Quantum hydrogen-bond symmetrization in the superconducting hydrogen sulfide system. *Nature* **532**, 81–84 (2016).

[341] Borinaga, M. *et al.* Anharmonic enhancement of superconductivity in metallic molecular cmca 4 hydrogen at high pressure: a first-principles study **28**, 494001 (2016).

[342] Rousseau, B. & Bergara, A. Giant anharmonicity suppresses superconductivity in alh_3 under pressure. *Phys. Rev. B* **82**, 104504 (2010).

[343] Monacelli, L., Errea, I., Calandra, M. & Mauri, F. Black metal hydrogen above 360 gpa driven by proton quantum fluctuations. *Nature Physics* (2020).

[344] Pawley, G. S., Cochran, W., Cowley, R. A. & Dolling, G. Diatomic ferroelectrics. *Phys. Rev. Lett.* **17**, 753–755 (1966).

[345] Calandra, M., Mazin, I. I. & Mauri, F. Effect of dimensionality on the charge-density wave in few-layer $2H$-$NbSe_2$. *Phys. Rev. B* **80**, 241108 (2009).

[346] Bianco, R., Calandra, M. & Mauri, F. Electronic and vibrational properties of $tise_2$ in the charge-density-wave phase from first principles. *Phys. Rev. B* **92**, 094107 (2015).

[347] Wang, C. Z., Chan, C. T. & Ho, K. M. Tight-binding molecular-dynamics study of phonon anharmonic effects in silicon and diamond. *Phys. Rev. B* **42**, 11276–11283 (1990).

[348] de Koker, N. Thermal conductivity of mgo periclase from equilibrium first principles molecular dynamics. *Phys. Rev. Lett.* **103**, 125902 (2009).

[349] Magdău, I. B. & Ackland, G. J. Identification of high-pressure phases iii and iv in hydrogen: Simulating raman spectra using molecular dynamics. *Phys. Rev. B* **87**, 174110 (2013).

[350] Zhang, D.-B., Sun, T. & Wentzcovitch, R. M. Phonon quasiparticles and anharmonic free energy in complex systems. *Phys. Rev. Lett.* **112**, 058501 (2014).

[351] Ceperley, D. M. Path integrals in the theory of condensed helium. *Rev. Mod. Phys.* **67**, 279–355 (1995).

[352] Errea, I., Rousseau, B. & Bergara, A. Isotope effect in the superconducting high-pressure simple cubic phase of calcium from first principles. *Journal of Applied Physics* **111**, 112604 (2012).

[353] Brown, S. E., Georgescu, I. & Mandelshtam, V. A. Self-consistent phonons revisited. ii. a general and efficient method for computing free energies and vibrational spectra of molecules and clusters. *The Journal of Chemical Physics* **138**, 044317 (2013).

[354] Monserrat, B., Drummond, N. D. & Needs, R. J. Anharmonic vibrational properties in periodic systems: energy, electron-phonon coupling, and stress. *Phys. Rev. B* **87**, 144302 (2013).

[355] Hermes, M. R. & Hirata, S. Stochastic algorithm for size-extensive vibrational self-consistent field methods on fully anharmonic potential energy surfaces. *The Journal of Chemical Physics* **141**, 244111 (2014).

[356] Tadano, T. & Tsuneyuki, S. Self-consistent phonon calculations of lattice dynamical properties in cubic srtio$_3$ with first-principles anharmonic force constants. *Phys. Rev. B* **92**, 054301 (2015).

[357] Patrick, C. E., Jacobsen, K. W. & Thygesen, K. S. Anharmonic stabilization and band gap renormalization in the perovskite cssni$_3$. *Phys. Rev. B* **92**, 201205 (2015).

[358] Hooton, D. J. Li. a new treatment of anharmonicity in lattice thermodynamics: I. *The London, Edinburgh, and Dublin Philosophical Magazine and Journal of Science* **46**, 422–432 (1955).

[359] Isihara, A. The gibbs-bogoliubov inequality dagger **1**, 539–548 (1968).

[360] Landau, L. & Lifshitz, E. *Statistical Physics: Volume 5*. v. 5 (Elsevier Science, 2013).

[361] Bianco, R., Errea, I., Paulatto, L., Calandra, M. & Mauri, F. Second-order structural phase transitions, free energy curvature, and temperature-dependent anharmonic phonons in the self-consistent harmonic approximation: Theory and stochastic implementation. *Phys. Rev. B* **96**, 014111 (2017).

[362] Ciofini, I., Adamo, C. & Chermette, H. Effect of self-interaction error in the evaluation of the bond length alternation in trans-polyacetylene using density-functional theory. *The Journal of Chemical Physics* **123**, 121102 (2005).

[363] Jacquemin, D. *et al.* Assessment of several hybrid dft functionals for the evaluation of bond length alternation of increasingly long oligomers. *The Journal of Physical Chemistry A* **110**, 5952–5959 (2006).

[364] Brémond, É., Pérez-Jiménez, Á. J., Adamo, C. & Sancho-García, J. C. sp-hybridized carbon allotrope molecular structures: An ongoing challenge for density-functional approximations. *The Journal of Chemical Physics* **151**, 211104 (2019).

[365] Hybertsen, M. S. & Louie, S. G. Electron correlation in semiconductors and insulators: Band gaps and quasiparticle energies. *Phys. Rev. B* **34**, 5390–5413 (1986).

[366] Zacharias, M., Patrick, C. E. & Giustino, F. Stochastic approach to phonon-assisted optical absorption. *Phys. Rev. Lett.* **115**, 177401 (2015).

[367] Hanke, W. & Sham, L. J. Dielectric response in the wannier representation: Application to the optical spectrum of diamond. *Phys. Rev. Lett.* **33**, 582–585 (1974).

[368] Hanke, W. & Sham, L. J. Local-field and excitonic effects in the optical spectrum of a covalent crystal. *Phys. Rev. B* **12**, 4501–4511 (1975).

[369] Hanke, W. & Sham, L. J. Many-particle effects in the optical spectrum of a semiconductor. *Phys. Rev. B* **21**, 4656–4673 (1980).

[370] del Castillo-Mussot, M. & Sham, L. J. Excitonic effect in the optical spectrum of semiconductors. In Chadi, J. D. & Harrison, W. A. (eds.) *Proceedings of the 17th International Conference on the Physics of Semiconductors*, 1125–1128 (Springer New York, New York, NY, 1985).

[371] Onida, G., Reining, L. & Rubio, A. Electronic excitations: density-functional versus many-body green's-function approaches. *Rev. Mod. Phys.* **74**, 601–659 (2002).

[372] Sangalli, D. *et al.* Many-body perturbation theory calculations using the yambo code **31**, 325902 (2019).

[373] Giannozzi, P. *et al.* QUANTUM ESPRESSO: a modular and open-source software project for quantum simulations of materials. *Journal of Physics: Condensed Matter* **21**, 395502 (2009).

[374] Giannozzi, P. *et al.* Advanced capabilities for materials modelling with quantum ESPRESSO. *Journal of Physics: Condensed Matter* **29**, 465901 (2017).

[375] Methfessel, M. & Paxton, A. T. High-precision sampling for brillouin-zone integration in metals. *Phys. Rev. B* **40**, 3616–3621 (1989).

[376] Rudin, S. P., Bauer, R., Liu, A. Y. & Freericks, J. K. Reevaluating electron-phonon coupling strengths: Indium as a test case for ab initio and many-body theory methods. *Phys. Rev. B* **58**, 14511–14517 (1998).

[377] Smith, J. & Schneider, V. Anisotropic thermal expansion of indium. *Journal of the Less Common Metals* **7**, 17 – 22 (1964).

[378] Wierzbowska, M., de Gironcoli, S. & Giannozzi, P. Origins of low- and high-pressure discontinuities of t_c in niobium (2005). cond-mat/0504077.

[379] Troullier, N. & Martins, J. L. Efficient pseudopotentials for plane-wave calculations. *Phys. Rev. B* **43**, 1993–2006 (1991).

[380] Perdew, J. P. *et al.* Restoring the density-gradient expansion for exchange in solids and surfaces. *Phys. Rev. Lett.* **100**, 136406 (2008).

[381] Lejaeghere, K. *et al.* Reproducibility in density functional theory calculations of solids. *Science* **351**, aad3000 (2016).

[382] Pizzi, G. *et al.* Wannier90 as a community code: new features and applications. *Journal of Physics: Condensed Matter* **32**, 165902 (2020).

[383] Dovesi, R. *et al.* Crystal14: A program for the ab initio investigation of crystalline solids. *International Journal of Quantum Chemistry* **114**, 1287–1317 (2014).

[384] Vilela Oliveira, D., Laun, J., Peintinger, M. F. & Bredow, T. Bsse-correction scheme for consistent gaussian basis sets of double- and triple-zeta valence with polarization quality for solid-state calculations. *Journal of Computational Chemistry* **40**, 2364–2376 (2019).

[385] Vosko, S. H., Wilk, L. & Nusair, M. Accurate spin-dependent electron liquid correlation energies for local spin density calculations: a critical analysis. *Canadian Journal of Physics* **58**, 1200–1211 (1980).

[386] Marini, A., Hogan, C., Grüning, M. & Varsano, D. yambo: An ab initio tool for excited state calculations. *Computer Physics Communications* **180**, 1392–1403 (2009).

[387] Padé, H. Sur la répresentation approchée d'une fonction pour des fractions rationelles. *Ann Sc. École Norm. Sup. Suppl.* **9**, 1–93 (1892).

[388] George A. Baker, J. *Essentials of Padé approximants* (Academic Press Inc., New York, NY, 1975).

Appendix A

Computational Details

A.1 Superconducting proximity effect in Indium thin films

Density functional theory (DFT) computations are carried out in the plane-wave pseudopotential framework as implemented in Quantum ESPRESSO [373, 374]. The exchange-correlation functional is approximated with the Perdew-Burke-Ernxerhof (PBE) generalized gradient approximation. The effective interaction between core and valence electrons is treated with a scalar relativistic ultrasoft pseudopotential. Completeness of the plane-wave basis is achieved with an energy cutoff of 48 Ry and a density cutoff of 190 Ry.

The self-consistent solution of the Kohn-Sham equations is achieved with a threshold on the total energy of 10^{-9} Ry. The Brillouin zone is discretized through the Monkhorst-Pack grid algorithm, with a uniform grid of $16 \times 16 \times 16$ k-points and a Methfessel-Paxton smearing [375] of 0.04 Ry for the self-consistent cycle, while the non-self-consistent computation is performed instead on a uniform grid of $32 \times 32 \times 32$ k-points with tetrahedra smearing. Such parameters are fixed by assuring convergence on the total energy per atom within a $\Delta E_{tot}/\text{atom} \leq 1$ mRy threshold for both the undoped and the doped cases. By doing so we can reproduce already existing computations for unperturbed bulk Indium [376] and study the doped bulk Indium which was still not yet investigated. Finally, by letting the structure relax toward zero interatomic forces and stresses, the theoretical lattice parameter of undoped bulk Indium is found to be $a_{th} = 3.30$ Å, which is 1.5% larger than the experimental value $a_{exp} = 3.25$Å [377].

Density functional perturbation theory (DFPT) computation are performed on a uniform grid of $8 \times 8 \times 8$ q-points. The electron-phonon matrix elements $g^{\nu}_{\mathbf{k},\mathbf{k}+\mathbf{q}}$ are first computed on the coarse q-grid for each phonon mode ν and then interpolated over the Brillouin zone as described in Ref. [378]. By doing so, the Eliashberg spectral functions are computed using:

$$\alpha^2_{s(b)}F(\Omega) = \frac{1}{N_{s(b)}(0)N_k N_q}\sum_{\mathbf{q}\nu}\delta(\hbar\omega - \hbar\omega_{\mathbf{q}\nu})\sum_{\mathbf{k}}\|g^{\nu}_{\mathbf{k},\mathbf{k}+\mathbf{q}}\|^2\delta(\varepsilon_{\mathbf{k}})\delta(\varepsilon_{\mathbf{k}+\mathbf{q}}) \quad \text{(A.1)}$$

where $N_{s(b)}$ is the total density of state per spin at the Fermi energy ($E_F = 0$) for the doped surface (s) and bulk (b) system, N_q and N_k are the number of q- and k-points considered in the first Brillouin zone for the computations and the energy ε is measured from the Fermi level. The $\delta(\hbar\omega - \hbar\omega_{\mathbf{q}\nu})$ is approximated with a Gaussian smearing of 0.05 Ry.

In order to solve the one-band s-wave Eliashberg equations, we assume a cutoff energy $\omega_c = 50$ meV and a maximum energy $\omega_{max} = 60$ meV.

A.2 Superconducting proximity effect in Magnesium Diboride thin films

Density functional theory (DFT) computations are carried out in the plane-wave pseudopotential framework as implemented in Quantum ESPRESSO [373, 374]. The exchange-correlation functional is approximated with the Perdew-Burke-Ernxerhof (PBE) generalized gradient approximation for both Mg and B. The effective interaction between core and valence electrons is treated with norm-conserving pseudopotentials built according to Troullier-Martins scheme[379] for both atomic species. Completeness of the plane-wave basis is achieved with an energy cutoff of 35 Ry and a density cutoff of 140 Ry.

The self-consistent solution of the Kohn-Sham equations is achieved with a threshold on the total energy of 10^{-9} Ry. The Brillouin zone is discretized through the Monkhorst-Pack grid algorithm, with a uniform grid of $16 \times 16 \times 12$ k-points and a Methfessel-Paxton smearing [375] of 0.025 Ry for the self-consistent cycle, while the non-self-consistent computation is performed instead on a uniform grid of $32 \times 32 \times 24$ k-points with tetrahedra smearing. Such parameters are fixed by assuring convergence on the total energy per atom within a $\Delta E_{tot}/\text{atom} \leq 1$ mRy threshold for both the undoped and the doped cases.

In order to solve the two-band s-wave Eliashberg equations, we assume a cutoff energy $\omega_c = 290$ meV and a maximum energy $\omega_{max} = 300$ meV.

A.3 Anomalous screening of an electric field at the surface of Niobium Nitride

NbN thin films are modelled as a slab structure made of 7 atomic layer, with ~ 20Å of vacuum between two successive repeated images of the system to avoid any unphysical interaction between them. The theoretical lattice parameter is found to be $a = 4.42$Å after bulk relaxation.

Density functional theory (DFT) computations are carried out in the plane-wave pseudopotential framework as implemented in Quantum ESPRESSO [373, 374]. The exchange-correlation functional is approximated with a revised Perdew-Burke-Ernxerhof (PBEsol[380]) generalized gradient approximation, which is particularly suited for densely packed solids and their surfaces, for both Nb and N. The effective interaction between core and valence electrons for Nb is treated with a projector-augmented plane-wave pseudopotential (PAW), while that of N with an ultrasoft pseudopotential, both obtained from the SSSP library[381]. Completeness of the plane-wave basis is achieved with an energy cutoff of 65 Ry and a density cutoff of 750 Ry.

The self-consistent solution of the Kohn-Sham equations is achieved with a threshold on the total energy of 10^{-9} Ry. The Brillouin zone is discretized through the Monkhorst-Pack grid algorithm, with a uniform grid of $32 \times 32 \times 1$ k-points and a Methfessel-Paxton smearing [375] of 0.025 Ry for the self-consistent cycle, while the non-self-consistent computation is performed instead on a uniform grid of $64 \times 64 \times 1$ k-points with tetrahedra smearing. Such parameters are fixed by assuring convergence on the total energy per atom within a $\Delta E_{tot}/\text{atom} \leq 1$ mRy threshold for both the undoped and the doped cases.

The screening of an electric field produced at the surface of NbN in the FET geometry is modelled as described in Refs. 240 -241, where the ions accumulated near the electrolyte-material interface are treated as a planar distribution of charges and a potential barrier is inserted in order to prevent charge spilling from NbN to the charge distribution. Moreover, since Quantum ESPRESSO exploits periodic boundary conditions (PBC), a dipole correction is needed in order to get rid of unphysical Coulomb interaction between the doped system and the planar charge distribution. If we call z the axis perpendicular to the surface of NbN and L the total length of the supercell, the planar charge distribution (hereafter called monopole) will be placed at $z_{\text{mono}} = 0.011L$. The dipole correction is placed at $z_{\text{dip}} = 0.005L$ and has a width of $d_{\text{dip}} = 0.01L$. Finally, the barrier of height 6.0 Ry and width $d_{\text{b}} = 0.1L$ starts at z_{dip}.

A.4 High-T_c superconductivity in field-effect doped hydrogenated (111)-diamond thin films

The hydrogenated (111)-diamond thin film is modelled as a slab made of 14 layers of C atoms, oriented along the (111) direction, terminated on both sides by a layer of H atoms, with ~ 30 of vacuum between two successive repeated images of the system to avoid any unphysical interaction between them. The theoretical in-plane lattice parameter is found to be equal to $a = 2.52$Å, which is obtained after a bulk relaxation. Ground state and linear response calculations are performed with the appropriate boundary conditions by truncating the Coulomb interaction in the non-periodic (z) direction, which is the one perpendicular to the slab surface, as described in Ref. 242. The FET configuration is similar to that described in Ref. 242 and the presence of the applied electric field is taken into account self-consistently both for the electronic and vibrational properties. We call z the axis perpendicular to the surface of the sample and we put the slab such that the slab is symmetric around the coordinate $z = 0$ of the supercell of length L. The layer of accumulated ions at the surface is simulated through a sheet of uniformly distributed charges placed at $z_{gate} = ?0.181L$. A potential barrier of height of $V_0 = 3.5$ Ry is set at $z_{barrier} = ?0.18L$ in order to avoid spilling of charges towards the planar charge distribution.

Density functional theory (DFT) computations are carried out in the plane-wave pseudopotential framework as implemented in Quantum ESPRESSO [373, 374]. The exchange-correlation functional is approximated with the Perdew-Burke-Ernzerhof (PBE) generalized gradient approximaton, for both H and C. The effective interaction between core and valence electrons for H is treated with a ultrasoft pseudopotential, while that of C with a norm-conserving pseudopotential. Completeness of the plane-wave basis is achieved with an energy cutoff of 65 Ry and a density cutoff of 600 Ry.

The self-consistent solution of the Kohn-Sham equations is achieved with a threshold on the total energy of 10^{-9} Ry. The Brillouin zone is discretized through the Monkhorst-Pack grid algorithm, with a uniform grid of $24 \times 24 \times 1$ k-points and a gaussian smearing of 0.004 Ry (for $n_{dop,1}$), 0.03 Ry (for $n_{dop,2}$) and 0.006 Ry (for $n_{dop,3}$) for the self-consistent cycle: their value is chosen in such a way that their magnitude is less then the energy difference between the top of the valence band and the Fermi level. The non-self-consistent computation is performed instead on a uniform grid of $48 \times 48 \times 1$ k-points with tetrahedra smearing. Such parameters are fixed by assuring convergence on the total energy per atom within a $\Delta E_{tot}/\text{atom} \leq 1$ mRy threshold for both the undoped and the doped cases.

Density functional perturbation theory (DFPT) calculations are performed after checking convergence of phonon modes at $\mathbf{q} = \mathbf{\Gamma}$: convergence is achieved with a $24 \times 24 \times 1$ uniformly distributed k-points grid and Gaussian smearing of width 0.003 Ry, 0.02 Ry and 0.004 Ry, for the three doping values respectively. Also for linear response calculations the smearing is always smaller than the energy difference between the top of the valence band and the Fermi level. Electron-phonon computations are initially performed only at $\mathbf{\Gamma}$ for all three doping regimes. For the highest surface charge densities, the electron-phonon matrix elements are interpolated

over the whole Brillouin zone through Wannier functions via the procedure described in Ref. 297. First of all, we Wannier-interpolate the electronic band structure[382] using a grid of $6 \times 6 \times 1$ k-points for the non-self consistent computation. We then interpolate the electron-phonon matrix elements to $75 \times 75 \times 1$ k-points and phonon momenta (q-points) grids, which ensures convergence of quantities of interests.

In order to solve the single-band and the three-bands s-wave Eliashberg equations, we assume a cutoff energy $\omega_c = 1290$ meV.

A.5 Many-body Renormalization of Electron-Phonon Interactions in Gated Rhombohedral-Stacked Few-Layers Graphene

We consider a graphene system made of 3 layers in the rhombohedral (ABC) stacking with a total of 6 carbon atoms in the unit cell. The lattice parameter is taken to be $a = 2.461$ Å while the interplane distance is $c = 3.347$ Å. In order to investigate the effects of Van-Hove singularities which arise due to flat bands, we dope our system with electrons in the field effect transistor (FET) geometry, in the single gate configuration, with an electron doping of $n_{dop,3L} = 2 \times 10^{14}$ cm^{-2} (which is simulated with a positive planar uniform charge distribution with density 2×10^{14} cm^{-2}).

Density functional computations are performed in the pseudopotential plane-wave approximation[373, 374, 242] using the Quantum ESPRESSO code. Exchange and correlation for carbon atoms are taken into account using the Perdew-Burke-Ernzerhof (PBE) functional and the effective interaction between core and valence electrons is included with a norm-conserving pseudopotential. The kinetic energy cut-off is set to 65 Ry, while that for the density is set to 650 Ry. In order to solve the Kohn-Sham equations self-consistently (with a threshold of 10^{-11} Ry on the total energy), the Brillouin zone is uniformly sampled with a 72×72 electron momenta (k-points) Monkhorst-Pack grid and a Gaussian smearing of 0.3 mRy for both doping regimes under study. When computing the electronic density of states we use a 144×144 k-points uniform grid with a Tetrahedron smearing in order to assure converged quantities. These parameters are chosen upon convergence of the total energy per atom (i.e. $E_{tot}/\text{atom} \leq 1$ mRy) and the value of the Gaussian smearing is such that it is always smaller than the energy difference between the Fermi level and the bottom of the last crossed conduction band. FET geometry is simulated with a recent implementation[242] which allows for the computation of electroni and vibrational properties as well as electron-phonon interactions. Since we work in periodic boundary condition (PBC), a vacuum of ≈ 20 Åand The Coulomb interaction is truncated along the non-periodic direction (z, i.e. the direction normal to the carbon layers).

Vibrational properties are computed with density functional perturbation theory (DFTP). Convergence of phonon modes is checked at $\mathbf{q} = \mathbf{\Gamma}$ and is found with a 144×144 k-points uniform grid and 0.0001 Gaussian smearing for both doping values. Also in this case the Gaussian smearing is required to be smaller than the energy difference between the Fermi energy and the last crossed conduction band. Electron-phonon interactions are accurately computed as described in Ref.297 by first interpolating the electronic dispersion relations[382] using 6 Wannier functions and a grid of 9×9 k-points and then, we interpolate the electron-phonon matrix elements on a 72×72 grid both for the electron (k-points) and phonon (q-points) momenta, assuring convergence of quantities of interest. Electron-phonon computations are then performed with a simplified model which requires dynamical matrices obtained at $\mathbf{q} = \mathbf{\Gamma}$ and $\mathbf{q} = \mathbf{K}$.

Finally, electron-electron correlation effects are investigated using the CRYSTAL code[383]. For carbon atoms we use the triple-ξ-polarized Gaussian type basis set[384] and we take into account exact exchange using the PBE0[328] and B3LYP[385] hybrid functionals. The Brillouin zone is sampled with a uniform grid of 96×96 k-points and Fermi-Dirac smearing. We used real space integration tolerances of 7-7-7-15-30 and an energy tolerance of 10^{-9} Ha for the total energy convergence.

A.6 Anharmonicity effects in one-dimensional carbon chain

Density functional theory calculations using the Perdew-Burke-Ernzerhof (PBE) and PBE0 (75% PBE + 25% of Hartree-Fock exchange interaction) exchange-correlation functionals are carried out using the CRYSTAL [383] and the Quantum ESPRESSO [373, 374] packages. Carbyne is modelled as a linear carbon chain disposed along the z direction, withe ~ 10 Å of vacuum along the non-periodic x and y directions in order to have a proper one-dimensional system. For the CRYSTAL code we use the triple-ξ-polarized Gaussian type basis set[384] with real space integration tolerances of 7-7-7-15-30 and an energy tolerance of 10^{-10} Ha for the total energy convergence. In the Quantum ESPRESSO code we use a norm-conserving pseudopotential with the kinetic energy cut-off set to 65 Ry, while that for the density is set to 650 Ry, and a threshold of 10^{-9} Ry on the total energy. The equilibrium lattice parameter has been computed with the PBE0 exchange-correlation functional and corresponds to 2.534 Å.

In both codes we have employed the same Brillouin zone sampling of $1 \times 1 \times 1000$ and $1 \times 1 \times 600$ **k**-points for the PBE and PBE0 exchange-correlation functionals respectively obtained in the $1 \times 1 \times 2$ supercell, with a Fermi-Dirac smearing of 0.0002 Ha, in order to properly converge the unstable longitudinal phonon mode. The **k**-points meshes are re-scaled according to the the supercell size (i.e. if we have $N_{k,z}$ **k**-points in the $1 \times 1 \times 2$ cell, then we will have $N_{k,z}/\delta$ **k**-points in the $1 \times 1 \times (2 \cdot \delta)$ supercell).

The input dynamical matrices for the SSCHA utility are computed with the Quantum ESPRESSO [373, 374] code, with a **k**-point sampling of $1 \times 1 \times 50$ and a Fermi-Dirac smearing of 0.01 Ry. The force engine of the SSCHA utility is the CRYSTAL [383] code, where forces and energies are computed on $1 \times 1 \times 10$ (10 atoms per cell) and $1 \times 1 \times 20$ (20 atoms per cell) supercells containing the unstable phonon mode at the border of the Brillouin zone of the the $1 \times 1 \times 1$ unit cell. Renormalization of the energy band gap due to anharmonic interactions has been computed on $1 \times 1 \times 20$ (20 atoms per cell), $1 \times 1 \times 200$ (200 atoms per cell) and $1 \times 1 \times 1000$ (1000 atoms per cell) supercells.

The G_0W_0 quasiparticle band structure and optical absorption spectra are computed with the Yambo [386, 372] code within the plasmon-pole approximation [365]. The cut-off parameters are set to:

- 50 Ry for the number of **G**-vectors in the exchange;
- 30 for the number of bands in the independent response function;
- 30 for tne number of bands in the polarization function;
- 3 Ry for number of **G**-vectors block in the dielectric constant;
- 100 bands for the expansion of the Green's function;
- 100 **k**-points in the Brillouin zone;

Finally, in order to converge the Bethe-Salpeter results for the excitonic effects we increased the number of **k**-points in the Brillouin zone to 400 and we took into account processes between the first two valence bands and the first four conduction bands.

Appendix B

Analytic continuation by means of N-point Padé approximants

Given a function $f(z)$ (with $z \in \mathbb{C}$) defined on some limited region of the complex plane we want to perform its analytic continuation, i.e. we want to extend its domain to the whole complex plane. The Padé approximants[387, 388] can be exploited to obtain quite accurate continuations starting from limited information, i.e. low number of leading terms in truncated Taylor expansions.

B.1 Padé approximants

The Padé approximants are an approximation to the value of a function obtained from a rational fraction. We denote the $[L,M]$ Padé approximant to $f(x)$ by:

$$[L/M] = P_L(x)/Q_M(x) \tag{B.1}$$

where $P_L(x)$ and $Q_M(x)$ are respectively a polynomial of degree at most L and M.

The power series of the function $f(x)$ is formally given by:

$$f(x) = \sum_{j=0}^{\infty} f_j x^j = f_j x^j \tag{B.2}$$

where in the last equality Einstein's summation is assumed.

We want to match the Taylor expansion of $f(x)$ with the Padé approximants. In order to do so we need to solve the equation:

$$f(x) = P_L(x)/Q_M(x) + O(x^{L+M+1}) \tag{B.3}$$

If we expand the polynomials $P_L(x)$ and $Q_M(x)$ and requiring the normalization condition $q_0 = 1$:

$$\begin{aligned} P_L(x) =& p_0 + p_1 x + p_2 x^2 + \cdots + p_L x^L \\ Q_M(x) =& 1 + q_1 x + q_2 x^2 + \cdots + q_M x^M \end{aligned} \tag{B.4}$$

Then multiplying Eq. B.3 by $Q_M(x)$ on both sides we obtain the following set of coefficient relations:

$$\begin{aligned} p_0 =& f_0 \\ p_1 =& f_1 + f_0 q_1 \\ p_2 =& f_2 + f_1 q_1 + f_0 q_2 \\ & \cdots \end{aligned} \tag{B.5}$$

Assuming that f_j is given, we have two new unknowns (p_j and q_j) for each line and therefore the system seems to be severely underdetermined. Nevertheless, by requiring the degree of the numerator, of the denominator and of the truncated Taylor expansion to be respectively N, M and $M+N$, we get as many equations as unknowns (to order $O(x^{M+N+1})$) and we can then obtain a solution of the linear system.

B.2 Relation between Padé approximants and continued fractions

We define a continued fraction to be the limit of successive truncations (or convergents):

$$G = b_0 + \cfrac{a_1}{b_1 + \cfrac{a_2}{b_2 + \cfrac{a_3}{b_3 + \ldots}}} = \lim_{n\to\infty} (A_n/B_n) \tag{B.6}$$

where the first few truncations (convergents) are:

$$\frac{A_0}{B_0} = \frac{b_0}{1}, \quad \frac{A_1}{B_1} = \frac{a_1 + b_1 b_0}{b_1}, \quad \frac{A_2}{B_2} = \frac{b_0 a_2 + a_1 b_2 + b_0 b_1 b_2}{a_2 + b_1 b_2} \tag{B.7}$$

Some important recursive relations for convergents of continued fraction are:

- $A_{n+1} = b_{n+1} A_n + a_{n+1} A_{n-1}$
- $B_{n+1} = b_{n+1} B_n + a_{n+1} B_{n-1}$
- $A_{n-1} B_n = (-1)^n a_1 a_2 \ldots a_n$

If $b_n \neq 0$, we can transform Eq. B.6 by multiplying successive numerators and denominators by non-zero numbers $c_n = b_n^{-1}$ (i.e. equivalence transformations):

$$G = b_0 + \cfrac{a_1'}{1 + \cfrac{a_2'}{1 + \cfrac{a_3'}{1+\ldots}}} \tag{B.8}$$

We would like to relate continued fractions to a Taylor series. Therefore we define the function:

$$G(z) = b_0 + \cfrac{a_1 z}{1 + \cfrac{a_2 z}{1 + \cfrac{a_3 z}{1+\ldots}}} = \sum_{n=0}^{\infty} g_n z^n \tag{B.9}$$

where the g_n depends on $b_0, a_1, a_2, \ldots, a_n$ and is given by the nth convergent to $G(z)$:

$$\frac{A_0(z)}{B_0(z)} = \frac{b_0}{1}, \quad \frac{A_1(z)}{B_1(z)} = \frac{b_0 + a_1 z}{1}, \quad \frac{A_2(z)}{B_2(z)} = \frac{b_0 + a_1 z + b_0 a_2 z}{1 + a_2 z} \tag{B.10}$$

In general:

$$\begin{aligned} A_{n+1}(z) &= A_n(z) + a_{n+1} z A_{n-1}(z) \\ B_{n+1}(z) &= B_n(z) + a_{n+1} z B_{n-1}(z) \end{aligned} \tag{B.11}$$

Where the degrees of $A_n(z)$ and $B_n(z)$ are respectively (n,n), if n even, or $(n+1,n)$, if n odd. Moreover the nth convergent produces the first n+1 coefficients of the Taylor expansion of $G(z)$.

B.3 Thiele's reciprocal difference method

Thanks to reciprocal differences we can obtain a general interpolation algorithm in terms of a rational function. Assume that we know the values of a function $f(x)$ for some distinct $x_0, x_1, x_2, \ldots, x_n$. We can define the reciprocal difference of $f(x)$ of arguments x_0, x_1 by:

$$\rho(x_0 x_1) = \frac{x_0 - x_1}{f(x_0) - f(x_1)} \tag{B.12}$$

The reciprocal difference of three arguments x_0, x_1, x_2 is defined by:

$$\rho_2(x_0 x_1 x_2) = \frac{x_0 - x_2}{\rho(x_0 x_1) - \rho(x_1 x_2)} + f(x_1) \tag{B.13}$$

The reciprocal differences of four arguments is defined as:

$$\rho_3(x_0 x_1 x_2 x_3) = \frac{x_0 - x_3}{\rho_2(x_0 x_1 x_2) - \rho_2(x_1 x_2 x_3)} + \rho(x_1 x_2) \tag{B.14}$$

We therefore obtain a general recursion relation for the reciprocal differences of n+1 arguments:

$$\rho_n(x_0x_1x_2\ldots x_n) = \frac{x_0 - x_n}{\rho_{n-1}(x_0x_1\ldots x_{n-1}) - \rho_{n-1}(x_1x_2\ldots x_n)} + \rho_{n-2}(x_1x_2\ldots x_{n-1}) \tag{B.15}$$

By writing x for x_0 we get:

$$\begin{aligned}
f(x) &= f(x_1) + \frac{x - x_1}{\rho(xx_1)} \\
\rho(xx_1) &= \rho(x_1x_2) + \frac{x - x_2}{\rho_2(xx_1x_2) - f(x_1)} \\
\rho_2(xx_1x_2) &= \rho_2(x_1x_2x_3) + \frac{x - x_3}{\rho_3(xx_1x_2x_3) - \rho(x_1x_2)} \\
\rho_3(xx_1x_2x_3) &= \rho_3(x_1x_2x_3x_4) + \frac{x - x_4}{\rho_4(xx_1x_2x_3x_4) - \rho_2(x_1x_2x_3)} \\
\rho_4(xx_1x_2x_3x_4) &= \rho_4(x_1x_2x_3x_4x_5) + \frac{x - x_5}{\rho_4(xx_1x_2x_3x_4x_5) - \rho_3(x_1x_2x_3x_4)} \\
&\ldots
\end{aligned}$$

Thus, for five interpolation points, the continued fraction of $f(x)$ is then:

$$f(x1) + \cfrac{x - x_1}{\rho(x_1x_2) + \cfrac{x-x_2}{\rho_2(x_1x_2x_3) - f(x_1) + \cfrac{x-x_3}{\rho_3(x_1x_2x_3x_4) - \rho(x_1x_2) + \cfrac{x-x_4}{\rho_4(x_1x_2x_3x_4x_5) - \rho_2(x_1x_2x_3) + \cfrac{x-x_5}{\rho_4(xx_1x_2x_3x_4x_5) - \rho_3(x_1x_2x_3x_4)}}}}}$$

A property of continued fractions, is that if a numerator of one of the constituent partial fractions vanish, this and all the following constituents do not affect the value and can be ignored. Therefore if we set $x = x_1, x_2, x_3, x_4, x_5$ we obtain $f(x_1), f(x_2), f(x_3), f(x_4), f(x_5)$ and in no case the last constituent partial fraction affect the result. Thus if we delete the last constituent partial fraction:

$$\frac{x - x_5}{\rho_4(xx_1x_2x_3x_4x_5) - \rho_3(x_1x_2x_3x_4)}$$

we obtain a rational function, which coincides with $f(x)$ at the points $x = x_1, x_2, x_3, x_4, x_5$.

Now we want to connect this technique with the above discussion on Padé approximants and continued fractions, using only the values at the points to be fitted. We seek:

$$f(z) = \cfrac{a_0}{1 + \cfrac{(z-z_0)a_1}{1 + \cfrac{(z-z_1)a_2}{1 + \cfrac{\ddots}{\cfrac{(z-z_{p-1})a_p}{\ddots \cfrac{}{1 + (z-z_p)g_{p+1}(z)}}}}}} \tag{B.16}$$

and $f(z_0) = a_0$. If we define:

$$g_0(z) = f(z), \quad g_p(z) = \frac{g_{p-1}(z_{p-1}) - g_{p-1}(z)}{(z - z_{p-1}) g_{p-1}(z)}, \quad p \geq 1 \tag{B.17}$$

then we can find: $a_p = g_p(z_p)$. We can then generate the function f_p for a fit on p points by means of the recursion formulas:

$$\begin{aligned} f_p &= \frac{A_p}{B_p}, \quad \frac{A_{n+1}}{B_{n+1}} = \frac{A_n + (z - z_n) a_{n+1} A_{n-1}}{B_n + (z - z_n) a_{n+1} B_{n-1}} \\ A_{-1} &= 0, \quad A_0 = a_0, \quad B_{-1} = 1, \quad B_0 = 1 \end{aligned} \tag{B.18}$$

The f_{2p+1} will be of the form $P_p(z)/Q_{p+1}(z)$ and f_{2p} of the form $P_p(z)/Q_p(z)$. The number of operations required to produce a fit this way is p^2.

B.4 N-point Padé approximants for the imaginary-axis superconducting gap

The complex gap function on the real axis $\Delta(\omega, T) = \Delta_1(\omega, T) + i\Delta_2(\omega, T)$ can be obtained using Vidberg and Serene's technique[200], which involves two steps:

- Solve the Eliashberg equations on the imaginary frequency axis, thus obtaining $\Delta(i\omega_n)$ for a large number of thermal frequencies $i\omega_n$;
- Obtain N-point Padé approximant using Thiele's reciprocal difference method starting from N points in the complex plane. By doing so, we analytically continue $\Delta(i\omega_n)$ to the real-frequency axis and we obtain $\Delta(N; \omega, T)$.

Notice however that this method is reliable only for $T << T_C$, therefore the number of thermal gaps $\Delta(i\omega_n)$ needed is quite high for very low temperature superconductors since the density of thermal frequencies $\sim T^{-1}$.

The N-point Padé approximant to $\Delta(\omega, T)$ is then given by:

$$\Delta(N; \omega, T) = \cfrac{a_1}{1 + \cfrac{a_2(\omega - z_1)}{1 + \cfrac{\ddots}{1 + a_N(\omega - z_{N-1})}}} \tag{B.19}$$

where $\{z_n : n = 1, \ldots, N\}$ is usually a set of the first N thermal frequencies. The coefficients a_n are given by:

$$\begin{aligned} g_1(z_n) &= \Delta(z_n) \\ g_p(z_n) &= \frac{g_{p-1}(z_{p-1}) - g_{p-1}(z_n)}{(z_n - z_{p-1}) g_{p-1}(z_n)} \quad p = 2, \ldots, n \\ a_n &= g_n(z_n) \quad n = 1, \ldots, N \end{aligned} \tag{B.20}$$

and the corresponding Padé approximant $\Delta(N;\omega,T) = P_N(\omega)/Q_N(\omega)$ is computed through:

$$\begin{aligned}
&P_1(\omega) = a_1 \quad , \quad P_2(\omega) = a_1 \quad , \\
&P_n(\omega) = P_{n-1}(\omega) + a_n(\omega - z_{n-1})P_{n-2}(\omega) \quad n = 3,\ldots,N \\
&Q_0(\omega) = 1 \quad , \quad Q_1(\omega) = 1 \\
&Q_n(\omega) = Q_{n-1}(\omega) + a_n(\omega - z_{n-1})Q_{n-2}(\omega) \quad n = 2,\ldots,N
\end{aligned} \tag{B.21}$$

Notice that If N is even then we obtain the $[\frac{N}{2}-1, \frac{N}{2}]$ Padé approximant, otherwise for odd N the $[\frac{N-1}{2}, \frac{N-1}{2}]$ Padé approximant is formed.

Appendix C

Simplified Superconductive Model

Consider the general case of two distinct spherical bands ($n \neq m$), centered around the center of the First Brillouin Zone (Γ). The electron-phonon coupling constant is given by Eq. 2.59, i.e.:

$$\lambda = 2\int \frac{\alpha^2 F(\omega)}{\omega} d\omega \tag{C.1}$$

The Eliashberg's spectral function is given by Eq. 2.60, i.e:

$$\alpha^2 F(\omega) = \frac{1}{N_\sigma(0) N_q N_k} \sum_{\nu,n,m} \sum_{\mathbf{k},\mathbf{q}} \left| g^{\nu}_{\mathbf{k}n,\mathbf{k}+\mathbf{q}m} \right|^2 \delta(\varepsilon_{\mathbf{k}n}) \delta(\varepsilon_{\mathbf{k}+\mathbf{q}m}) \delta(\omega - \omega_{\mathbf{q}\nu}) \tag{C.2}$$

where $N_\sigma(0)$ is the total density of states per spin at the Fermi level.

Inserting Eq. C.2 into Eq. C.1, gives:

$$\lambda = \frac{2}{N_\sigma(0)} \sum_{\nu,n,m} \frac{1}{N_{k'} N_k} \sum_{\mathbf{k},\mathbf{k}'} \frac{\left| g^{\nu}_{\mathbf{k}n,\mathbf{k}'m} \right|^2}{\omega_{\mathbf{k}'-\mathbf{k},\nu}} \delta(\varepsilon_{\mathbf{k}n}) \delta(\varepsilon_{\mathbf{k}'m}) \tag{C.3}$$

where $\mathbf{k}' = \mathbf{k} + \mathbf{q}$. Due to the Dirac deltas electrons can only scatter from states on the Fermi surface onto other states on the Fermi surface ($|\mathbf{k}| = k_{Fn}$ and $|\mathbf{k}'| = \tilde{k}_{Fm} = \tilde{k}_{Fm} \pm |Q|$), where $\mathbf{Q}$ is another vector in the reciprocal space. In the case of two Fermi surfaces both centered around the center of the Brillouin zone (as in the case of the hole doped hydrogenated diamond-(111) surface in Ch. 4), we have $\mathbf{Q} = \Gamma = \mathbf{0}$. On the other hand, if we take into account a multivalley system we have a phonon momentum $\mathbf{Q} \neq \mathbf{0}$ which can connect two Fermi surfaces belonging to different valleys (as in the case of the electron doped rhombohedral-stacked three layer graphene in Ch. 5, where $\mathbf{Q} = \mathbf{K}$).

As a consequence:

$$q^2 = k^2 + k'^2 - 2kk'\cos\theta = k_{Fn}^2 + \tilde{k}_{Fm}^2 - 2k_{Fn}\tilde{k}_{Fm}\cos\theta \tag{C.4}$$

Therefore the phonon momentum can range in the interval:

$$|\mathbf{q}| \in \left[\sqrt{k_{Fn}^2 + \tilde{k}_{Fm}^2 - 2k_{Fn}\tilde{k}_{Fm}}\,;\,\sqrt{k_{Fn}^2 + \tilde{k}_{Fm}^2 + 2k_{Fn}\tilde{k}_{Fm}}\right] = [q_1;q_2]$$

Assume now that we have :

$$\frac{\left|g^{\nu}_{\mathbf{k}n,\mathbf{k}'m}\right|^2}{\omega_{\mathbf{k}'-\mathbf{k},\nu}} = \frac{\left|g^{\nu}_{n,m}\right|^2_{\mathbf{Q}}}{\omega_{\mathbf{Q}\nu}}$$

in the region $|\mathbf{k}| \in [0, k_{Fn}]$ and $|\mathbf{q}| \in [q_1, q_2]$. Then, the electron-phonon coupling constant assume the form:

$$\lambda = \frac{2}{N_\sigma(0)} \sum_{\nu,n,m} \frac{\left|g^{\nu}_{n,m}\right|^2_{\mathbf{Q}}}{\omega_{\mathbf{Q}\nu}} N_{f,nm} \tag{C.5}$$

where $N_{f,nm}$ is the *Nesting factor*:

$$N_{f,nm} = \frac{1}{N_{k'}N_k} \sum_{\mathbf{k},\mathbf{k}'} \delta(\varepsilon_{\mathbf{k}n})\delta(\varepsilon_{\mathbf{k}'m}) \tag{C.6}$$

In its continuum form, Eq. C.6 becomes (cf. Grimvall [185], pp.12-13):

$$\begin{aligned} N_{f,nm} &= \frac{A}{(2\pi)^2}\frac{A}{(2\pi)^2}\int\int d^2k d^2k' \delta(\varepsilon_{\mathbf{k}n})\delta(\varepsilon_{\mathbf{k}'m}) = \\ &= N_{\sigma,n}(0)\frac{A}{(2\pi)^2}\int_{S_{E_{Fm}}} \frac{dS}{|\boldsymbol{\nabla}_{\mathbf{k}'}E(\mathbf{k}')|} \end{aligned} \tag{C.7}$$

where $N_{\sigma,n}(0)$ is the DOS per spin of band n at the Fermi level and A is the BZ area.

In 3D we can define a directional dependent DOS like:

$$N_\sigma(E;\mathbf{k}) = \frac{V}{(2\pi)^3}\frac{4\pi k^3}{\mathbf{k}\cdot\boldsymbol{\nabla}_{\mathbf{k}}E(\mathbf{k})} \tag{C.8}$$

So, in 2D we will have:

$$N_\sigma(E;\mathbf{k}) = \frac{A}{(2\pi)^2}\frac{2\pi k^2}{\mathbf{k}\cdot\boldsymbol{\nabla}_{\mathbf{k}}E(\mathbf{k})} \tag{C.9}$$

Therefore Eq. C.7 can be rewritten as:

$$N_{f,nm} = N_{\sigma,n}(0)\int \frac{d\Omega_{k'}}{2\pi} N_\sigma(E_{Fm};\mathbf{k}) = N_{\sigma,n}(0)N_{\sigma,m}(0)\int \frac{d\theta}{2\pi} \tag{C.10}$$

From Eq. C.4 we have that:

$$qdq = k_{Fn}\tilde{k}_{Fm}\sin\theta d\theta \Rightarrow d\theta = \frac{2qdq}{\sqrt{4k_{Fn}^2\tilde{k}_{Fm}^2 - [q^2-(k_{Fn}^2+\tilde{k}_{Fm}^2)]^2}} \tag{C.11}$$

Then:

$$\begin{aligned} N_{f,nm} =& \frac{N_{\sigma,n}(0)N_{\sigma,m}(0)}{\pi}\int_{q1}^{q2} \frac{qdq}{\sqrt{4k_{Fn}^2\tilde{k}_{Fm}^2 - [q^2-(k_{Fn}^2+\tilde{k}_{Fm}^2)]^2}} = \\ =& -\frac{N_{\sigma,n}(0)N_{\sigma,m}(0)}{2\pi}\arctan\left\{\frac{k_{Fn}^2+\tilde{k}_{Fm}^2-q^2}{\sqrt{4k_{Fn}^2\tilde{k}_{Fm}^2 - [q^2-(k_{Fn}^2+\tilde{k}_{Fm}^2)]^2}}\right\}\Bigg|_{q_1}^{q_2} = \\ =& \frac{N_{\sigma,n}(0)N_{\sigma,m}(0)}{2} \end{aligned} \tag{C.12}$$

Inserting Eq. C.12 in Eq. C.5, we arrive at the simplified electron-phonon coupling constant:

$$\lambda = \sum_{\nu,n,m} \frac{\left|g_{n,m}^{\nu}\right|_{\mathbf{Q}}^2}{\omega_{\mathbf{Q}\nu}} \frac{N_{\sigma,n}(0)N_{\sigma,m}(0)}{N_\sigma(0)} \tag{C.13}$$